

University of Louisville

ThinkIR: The University of Louisville's Institutional Repository


Electronic Theses and Dissertations

5-2017

Homogeneous ligand-centered hydrogen evolution and hydrogen oxidation : exploiting redox non-innocence to drive catalysis.

Andrew Z. Haddad
University of Louisville

Follow this and additional works at: <https://ir.library.louisville.edu/etd>

 Part of the [Analytical Chemistry Commons](#), [Environmental Chemistry Commons](#), [Inorganic Chemistry Commons](#), and the [Physical Chemistry Commons](#)

Recommended Citation

Haddad, Andrew Z., "Homogeneous ligand-centered hydrogen evolution and hydrogen oxidation : exploiting redox non-innocence to drive catalysis." (2017). *Electronic Theses and Dissertations*. Paper 2710.

<https://doi.org/10.18297/etd/2710>

This Doctoral Dissertation is brought to you for free and open access by ThinkIR: The University of Louisville's Institutional Repository. It has been accepted for inclusion in Electronic Theses and Dissertations by an authorized administrator of ThinkIR: The University of Louisville's Institutional Repository. This title appears here courtesy of the author, who has retained all other copyrights. For more information, please contact thinkir@louisville.edu.

HOMOGENEOUS LIGAND-CENTERED HYDROGEN EVOLUTION
AND HYDROGEN OXIDATION:
EXPLOITING REDOX NON-INNOCENCE TO DRIVE CATALYSIS

By

Andrew Z. Haddad
B.A. University of Louisville 2012
M.S. University of Louisville 2015

A Dissertation Submitted to the
Faculty of the College of Arts and Sciences
of the University of Louisville in Fulfillment
of the Requirements for the Degree of

Doctor of Philosophy in Chemistry

Department of Chemistry
University of Louisville
Louisville, KY

May 2017

© 2017 by Andrew Zahi Haddad

All Rights Reserved

HOMOGENEOUS LIGAND-CENTERED ELECTROCATALYTIC
HYDROGEN EVOLUTION AND HYDROGEN OXIDATION
EXPLOITING REDOX NON-INNOCENCE TO DRIVE CATALYSIS

By

Andrew Z. Haddad
B.A. University of Louisville, 2012
M.S. University of Louisville, 2014

A Dissertation Approved on

April 20, 2017

By the following Dissertation Committee

Advisor: Dr. Craig A. Grapperhaus

Dr. Robert M. Buchanan

Dr. Richard P. Baldwin

Dr. Gamini Sumanasekra

For Mom and Yaba

ACKNOWLEDGEMENTS

I would first like to thank Professor Craig Grapperhaus for accepting me into his group and providing me guidance over the last five years. Professor Grapperhaus has supported my growth as both a person and a scientist beyond my highest expectations, while also managing to be caring and sincere. I am very thankful for the numerous talks and conferences he has sent me to which have provided me the opportunity to grow outside of the lab by gaining exposure within the broader chemistry community. Additionally, he has provided countless opportunities for me to learn the intricacies of working in academia, and how to think pragmatically. Not only has he been a tremendous mentor to me, but he also gave me the opportunity to pursue my PhD, and for this I will forever be indebted. Professor Grapperhaus is one of the best at his profession that I know, and I so grateful that I've had an opportunity to learn as much as I have from him.

I would like to thank Professor Robert Buchanan for his support and advice over the last five years. I have learned so much from you and have enjoyed some of the most rewarding scientific discussions, in addition to enjoying the many emails, text messages, and general correspondence about research. Your unmatched knowledge of bio-inorganic chemistry and synthetic methods has been one of the most helpful things during the last five years. I also appreciate all the countless times you assisted me in the preparation of manuscripts and your guidance in helping me develop into a proper scientific writer. Most importantly, you showed me how to enjoy research and how to make it into something you love that's worthwhile.

I am extremely grateful to my computational collaborators, Professor Pawel Kozlowski and Brady Garabato. Professor Kozlowski shaped my entire understanding of computational chemistry, and we have enjoyed many fulfilling discussions over the last few years. Without your guidance, I would not have been able to achieve the level of theoretical understanding I currently have. I also owe much to Brady Garabato, who not only served as a sort of computational guide, but is one of my dearest friends. I want to thank you for the incredible support and patience you provided me; I could not have accomplished much of the theoretical work without your insight. You also provided me an outlet outside of lab, where we had fantastic safaris, great scientific debates, as well as thought provoking discussions on life and our future ambitions.

I would also like to thank Dr. Mark Mashuta, who solved many crystal structures for me and provided me with many ideas for growing crystals. Furthermore, I would like to him for welcoming me to his fantastic football tailgates, which provided a great getaway from lab over the last five years.

I would to thank Rajat Chauhan and Davinder Kumar who took me into the Grapperhaus Lab my first year and taught me almost everything I know about electrochemistry and Schlenk line synthesis. Often times, during the first few years when our group was very small, it would just be the three of us in the lab. Those times were incredibly influential, and that is when and where I learned the type of work ethic you need to complete a PhD, as well as how to maintain a lab. I also enjoyed the many discussions we had about world events and history of civilizations. I also would like to thank all of the other members of Grapperhaus Group, past and present. I am grateful for

their support and friendship over the years, in addition to making my work possible, as all science is built upon the work of those that came before.

I would also like to thank my undergraduate research mentor, Professor Mark Noble. Working in your lab as an undergraduate provided an excellent knowledge base and skill set, which was incredibly helpful while completing my PhD.

I would like to thank Professor Richard Baldwin and Professor Gamini Sumanasekera for serving on my dissertation committee. I would also like to thank Professor Baldwin for being a reliable source of knowledge on all things electrochemistry, and for talking me through various parts of my work and for providing me with insight into certain experimental designs.

Finally, I would like to thank my parents, Zahi and Deborah, and my older brother, David. You all have been the biggest influences on my life and without you I certainly would not be where I am today. I owe so much to you for making every dream I have ever had possible, and proving me with endless, loving support.

ABSTRACT
HOMOGENEOUS LIGAND-CENTERED HYDROGEN EVOLUTION
AND HYDROGEN OXIDATION:

EXPLOITING REDOX NON-INNOCENCE TO DRIVE CATALYSIS

Andrew Z. Haddad

April 20, 2017

Hydrogen is a promising carbon-free fuel / energy carrier and is an essential building block for many industrial and agricultural processes. Rising energy demands have ignited interest in the development of carbon-free and carbon neutral energy sources. In this context, hydrogen is an attractive candidate—being energy-dense, carbon-free—and easily accessible through a two-electron reduction of water. Accordingly, many electrochemical homogeneous catalyst systems have been studied, with a focus on understanding the mechanism of hydrogen evolution proceeding through metal-hydride intermediates. However, there has been a renaissance in hydrogen evolution reaction (HER) catalyst design, with many groups implicating ligand redox non-innocence as a crucial driving force for catalysis rather than metal-hydride formation. In this dissertation, using characterization techniques including, cyclic voltammetry, controlled potential coulometry, UV-visible spectroscopy, ^1H NMR, cyclic voltammetry modeling, x-ray crystallography, kinetic isotope effect studies, and density functional theory, we investigate ligand-centered electrocatalysts, which function without

the generation of metal-hydride intermediates, for the production and oxidation of dihydrogen.

Chapter three expands upon the previous work in the Grapperhaus Lab, and focus on ReL_3 (L = diphenylphosphinobenzenethiolate). ReL_3 reduces acids to H_2 in dichloromethane with an overpotential of 0.708 V and a turnover frequency (TOF) of 32 s^{-1} , and also oxidizes H_2 in the presence of base with an overpotential of 0.970 V and a TOF of 4 s^{-1} . The mechanism is supported by kinetic isotope effect (KIE) studies and density functional theory calculations (DFT). Chapters four and five will build on Chapter three, aiming to develop sustainable approaches for ligand-centered catalysis. The non-transition metal complex, ZnL^1 , the metal-free complex, H_2L^1 , and the transition metal complex, CuL^1 (L^1 = diacetyl-bis(N4-methyl-3-thiosemicarbazonato)), function as electrocatalysts for hydrogen evolution (ZnL^1 , H_2L^1 and CuL^1) and hydrogen oxidation (ZnL^1 and H_2L^1). H_2L^1 and ZnL^1 display TOF's of $1,320 \text{ s}^{-1}$ and $1,170 \text{ s}^{-1}$ at overpotentials of 1.43 and 0.756 V, respectively, while the CuL^1 complex demonstrates a TOF of $10,000 \text{ s}^{-1}$. H_2L^1 and ZnL^1 also display TOF values for H_2 oxidation of 32 s^{-1} and 72 s^{-1} at overpotentials of 0.328 and 0.315 V, respectively. Mechanisms for the HER were modeled using digital simulations and are further supported by DFT calculations.

ReL_3 , ZnL^1 , H_2L^1 , and CuL^1 represent a fundamentally new class of electrocatalysts. Contrary to traditional molecular electrocatalysts that employ a metal-hydride as the key mechanistic intermediate, this approach facilitates H_2 evolution through ligand-centered proton and electron-transfer events resulting in the evolution of H_2 through either ligand-centered H^\bullet radical coupling or ligand-centered hydride proton coupling.

TABLE OF CONTENTS

ACKNOWLEDGEMENTS	iv
Abstract	vii
LIST OF FIGURES.....	xiii
LIST OF TABLES	xxii
LIST OF SCHEMES.....	xxiii
CHAPTER I: INTRODUCTION	1
1.1. Hydrogen: Importance and Background	2
1.2. Hydrogenase and Biomimetic Hydrogenase Complexes	3
1.3. Mechanistic Features of H ₂ Evolution and Oxidation.....	9
1.4. Ligand-Centered HER Electrocatalysts	10
CHAPTER II: EXPERIMENTAL DETAILS.....	14
2.1. Materials and Physical Methods	15
2.2. Crystallographic Details.....	15
2.3. Chemical Synthesis	17
2.4. Electrochemical Methods.....	19
2.5. Overpotential Determination and Calculations	23
2.6. ReL ₃ : Determination and Calculation of Third-Order Rate Constant, <i>k</i> , from Pseudo First-Order Rate Constant <i>k_{obs}</i> , and estimation of Turnover Frequency (TOF) for H ₂ Evolution and Oxidation	25
2.7. ZnL ¹ and H ₂ L: Determination and Calculation of TOF for H ₂ Evolution and Oxidation.....	28
2.8. CuL ¹ : Determination and Calculation of TOF for H ₂ Evolution	29
2.9. ReL ₃ : Quantification of H ₂ from Controlled Potential Coulometry (CPC) and Calculation of Turnover Number and Faradaic Efficiency.....	30
2.10. ZnL ¹ : Quantification of H ₂ from CPC and Turnover Number and Faradaic Efficiency Calculations	32
2.11. CuL ¹ : Quantification of H ₂ from Controlled Potential Coulometry and Turnover Number and Faradaic Efficiency Calculations.....	33
2.12. Determination and Calculation of Diffusion Coefficients, D ₀ , for ZnL ¹ and CuL ¹	35
2.13. Kinetic Isotope Effect Calculations.....	36

2.14.	Digital Simulations using DigiElch	38
2.15.	Computational Methods	38
CHAPTER III: LIGAND-CENTERED ELECTROCATALYTIC HYDROGEN EVOLUTION AND HYDROGEN OXIDATION		42
3.1.	Introduction	43
3.2.	Results and Discussion.....	47
3.2.1.	Cyclic Voltammetry HER and HOR Studies and X-ray Crystallography.....	47
3.2.2.	Controlled Potential Coulometry and Gas Product Analysis	54
3.2.3.	Deuterated Acid Studies	55
3.2.4.	Mechanism Discussion and Theoretical Insight.....	56
3.3.	Conclusion.....	66
3.4.	Acknowledgement.....	67
CHAPTER IV: SUSTAINABLE METAL ALTERNATIVES FOR LIGAND-CENTERED H₂ EVOLUTION AND HYDROGEN OXIDATION		68
4.1.	Introduction	69
4.2.	Results and Discussion.....	72
4.2.1.	ZnL ¹ Cyclic Voltammetry Characterization.....	72
4.2.2.	ZnL ¹ Cyclic Voltammetry Hydrogen Evolution and Hydrogen Oxidation Studies	73
4.2.3.	H ₂ L ¹ Cyclic Voltammetry Hydrogen Evolution and Hydrogen Oxidation Studies	77
4.2.4.	ZnL ¹ Extended Stability and Gas Identification: Controlled Potential Coulometry Studies.....	79
4.2.5.	ZnL ¹ Mechanism Evaluation: Digital Simulations, Isotope Effect Studies ...	81
4.2.6.	ZnL ¹ Density Functional Theory Study.....	83
4.3.	Conclusion.....	88
4.4.	Acknowledgement.....	89
CHAPTER V: TRANSITION METAL ASSISTED LIGAND-CENTERED H₂ EVOLUTION		90
5.1.	Introduction	91
5.2.	Results and Discussion.....	93
5.2.1.	CuL ¹ Cyclic Voltammetry HER Studies	93

5.2.2. CuL ¹ Extended Stability: Controlled Potential Coulometry and Gas Identification	98
5.2.3. Mechanistic Insights	101
5.2.4. CuL ¹ Density Functional Theory Study	104
5.2.5. Overview of CuL ¹ and Comparison with ZnL ¹ , H ₂ L ¹ and Other HER Electrocatalysts.....	107
5.3. Conclusions	109
5.4. Acknowledgement.....	110
CHAPTER VI: CONCLUSIONS.....	111
6.1. Ligand-Centered Electrocatalytic Hydrogen Evolution and Hydrogen Oxidation	112
6.2. Sustainable Metal Alternatives for Ligand-Centered H ₂ Evolution Oxidation	114
6.3. Transition Metal Assisted Ligand-Centered H ₂ Evolution	117
REFERENCES	120
APPENDIX A: CYCLIC VOLTAMMETRY SIMULATION PARAMETER TABLES AND DIGIELCH GUIDE	128
APPENDIX B: EXPERIMENTAL AND SIMULATED CYCLIC VOLTAMMOGRAMS	140
APPENDIX C: ADDITIONAL ELECTROCHEMICAL AND UV-VIS DATA	161
APPENDIX D: ADDITIONAL DFT STRUCTURES AND ALL COMPUTATIONAL INPUT COORDINATES.....	190
CURRICULUM VITA	238

LIST OF FIGURES

Figure 1. Percent of global hydrogen use by industry. ¹⁷	3
Figure 2. (Top) Structures of the [NiFe] hydrogenase ²² and of the [FeFe] hydrogenase from Dd. ²³ (Bottom) the chemical structures of the active sites of the two types of hydrogenases are given; the arrows indicate the open metal coordination sites.....	4
Figure 3. Postulated catalytic mechanism for reversible H ⁺ reduction by [FeFe]-hydrogenases, the location of the proton in the H _{red} and H _{sred} state is undetermined, adapted from reference 53. ⁴⁰	7
Figure 4. Synthetic scheme for the preparation of [(μ -SEt) ₂ Fe(CO) ₆] (left), and precursor diiron hexacarbonyl complex (middle) used in route to the first true [FeFe] hydrogenase model [(μ -pdt)Fe ₂ (CO) ₄ (CN) ₂] ²⁻ (right). ⁴⁵⁻⁴⁷	8
Figure 5. Illustration of two potential routes for H ₂ evolution following either a homolytic or heterolytic pathway.	9
Figure 6. Illustration showing the four traditional reaction pathways observed with redox non-innocent ligands in catalysis (S = substrate).....	11
Figure 7. Double slope plot for evaluation of the third-order rate constant, <i>k</i>	27
Figure 8. Cyclic Voltammogram (CV) of 0.3 mM ReL ₃ in 0.1 M Bu ₄ NPF ₆ CH ₂ Cl ₂ solutions.....	45
Figure 9. (A) Calculated "p-type" lone-pair orientation of [M(SP) ₃] ⁿ enforced by meridional PS chelates. (B) Proposed interactions of [M(SP) ₃] ⁿ frontier orbitals with LUMO (top) and HOMO (bottom) of C ₂ H ₄ . (C) HOMO/LUMO symmetries of H ₂	46
Figure 10. CV of ReL ₃ with excess CH ₃ CO ₂ H added in 0.1 M Bu ₄ NPF ₆ CH ₂ Cl ₂ solution.	48
Figure 11. (Left) Labeled ORTEP ¹⁶² of [Re(LH)L ₂] ⁺ from [Re(LH)L ₂]PF ₆ . (Right) Labeled ORTEP ¹⁶² of [Re(LH)L ₂] ⁺ from [Re(LH)L ₂]O ₃ SCF ₃	48
Figure 12. Cyclic Voltammograms of 0.3 mM ReL ₃ in 0.1 M Bu ₄ NPF ₆ CH ₂ Cl ₂ solution showing H ₂ evolution upon successive additions of CH ₃ CO ₂ H. Inset: Plot of catalytic current vs CH ₃ CO ₂ H concentration, showing acid saturation above 0.4 M CH ₃ CO ₂ H. ..	50
Figure 13. Open circuit potential for the reduction of protons to acetic to H ₂ with 0.4 M CH ₃ COOH added to 0.1 M Bu ₄ NPF ₆ CH ₂ Cl ₂ solution.	51
Figure 14. Peak Current vs. [ReL ₃] using weak acid (CH ₃ CO ₂ H) at (A) 0.2, (B) 0.5, (C) 1 V/s, and using strong acid (H ₂ SO ₄) at (D) 0.2 (E) 0.5, (F) 1.0 V/s.....	52
Figure 15. CV showing H ₂ oxidation upon successive additions of triethylamine to 0.3 mM ReL ₃ in 0.1 M Bu ₄ NPF ₆ CH ₂ Cl ₂ solution under 1 atm of H ₂ gas.	53

Figure 16. Plot of charge vs time recorded during the controlled potential coulometry of 0.3 mM ReL_3 for 1.5 hours (blue) and 6 hours (red) in the presence of $\text{CH}_3\text{CO}_2\text{H}$. Inset: Gas chromatography thermal conductivity (GC-TCD) readout of headspace analysis during electrolysis.	54
Figure 17. Bond lengths (Å) and angles (°) for ReL_3 from $S = 0$ and $S = 1$ DFT optimizations (M06/LANL2DZ) and the experimental (Exp.) x-ray crystal structure. ¹⁵⁷ ΔG indicates relative zero-point free energy (kcal / mole) values of the $S = 0$ and $S = 1$ electronic states.	58
Figure 18. Bond lengths (Å) and angles (°) for $[\text{Re}(\text{LH})\text{L}_2]^+$ from $S = 0$ and $S = 1$ DFT optimizations (B3LYP/LANL2DZ) and the experimental (Exp.) x-ray crystal structure. ⁹ ΔG indicates relative zero-point free energy (kcal / mole) values of the $S = 0$ and $S = 1$ electronic states.	60
Figure 19. Bond lengths (Å), bond angles (°), and spin-density percentage contributions for the $S = 1/2$ DFT optimizations (M06/LANL2DZ) of (A) $[\text{ReL}_3]^-$, (B) $[\text{Re}(\text{LH})\text{L}_2]^0$, and (C) $[\text{Re}(\text{LH})_2\text{L}]^+$	62
Figure 20. Bond lengths (Å) and angles (°) for optimizations (M06/LANL2DZ) of (A) $[\text{Re}(\text{LH})_2\text{L}]^0$ ($S = 0$) DFT and (B) $[\text{HRe}(\text{LH})\text{L}_2]^0$ ($S = 1$). and (c) $[\text{Re}(\text{LH})_2\text{L}]^+$. ΔG indicates relative zero-point free energy (kcal / mole) values of the $S = 0$ and $S = 1$ electronic states (see appendix for analysis of the singlet $[\text{HRe}(\text{LH})\text{L}_2]^0$ species).	63
Figure 21. Transition states and energy profile for HER through Re-dithiol and Re-hydride pathways. (A) Representation of TS- $[\text{Re}(\text{LH})_2\text{L}]$ showing lengthening of two S-H bonds associated with H_2 evolution. (B) Representation of TS- $[\text{HRe}(\text{LH})\text{L}_2]$ showing H_2 evolution from Re-H and S-H. (C) Comparison of relative energies (ZPE corrected) for Re-dithiol and Re-hydride HER pathways using M06/LANL2DZ.	64
Figure 22. (A) Transition state geometry of $[\text{Re}(\text{LH})\text{L}_2]$ along the HER pathway, shown with active S-H bond dissociations and Re atom associated with the imaginary frequency, $i1113 \text{ cm}^{-1}$. (B) Transition State Analysis of H_2 Evolving Complex $[\text{Re}(\text{LH})_2\text{L}]$. Internal reaction coordinates (IRC) moving through the TS for $[\text{Re}(\text{LH})_2\text{L}]$ associated with the imaginary frequency $i1113 \text{ cm}^{-1}$. (C) Charge densities of sulfur and hydrogen atoms near H_2 evolution for $[\text{Re}(\text{LH})_2\text{L}]$ along the HER pathway with respect to IRC, associated with the imaginary frequency $i1113 \text{ cm}^{-1}$, S3 / S4 (cyan, magenta) and H5 / H105 (blue, purple). Transition State S-H bond lengths = 1.524 Å and 1.532 Å. (D) Charge densities of the Rhenium atom near H_2 evolution with respect to IRC, associated with the imaginary frequency $i1113 \text{ cm}^{-1}$, Re1 (red).	65
Figure 23. (A) Cyclic voltammogram of ZnL^1 in 0.1 M Bu_4NPF_6 methanol solution (B) Blow up of cathodic region of cyclic voltammogram of ZnL^1 in 0.1 M Bu_4NPF_6 methanol solution. (C) Cyclic voltammogram of ZnL^1 in 0.1 M Bu_4NPF_6 acetonitrile solution.....	72
Figure 24. (A) Cyclic voltammogram of ZnL^1 in 0.1 M Bu_4NPF_6 methanol solution scanned at 0.1 (black), 0.2 (dark blue), 0.3 (purple), 0.4 (blue), 0.5 (green), 0.6 (light	

green). 0.7 (yellow), 0.8 (orange), 0.9 (red) and, 1.0 (black) V/s. (B) Cottrell plot of the peak current plotted against the square root of the scan rate.	72
Figure 25. (A) Cyclic voltammograms of 3 mM ZnL ¹ in methanol with no added acid (black), 6 mM CH ₃ COOH (blue), 9 mM CH ₃ COOH (purple), and 12 mM CH ₃ COOH (red). Data collected at a scan rate of 0.5 V/s in the presence of 0.1 M Bu ₄ NPF ₆ as supporting electrolyte. (B) Plot of <i>i</i> _{cat} vs [CH ₃ COOH] for 3 mM ZnL ¹ (red) at scan rates of 0.2 (▲), 0.3 (●), 0.4 (■), and 0.5 (◆) V/s.	73
Figure 26. (A) Cyclic voltammograms of 3 mM ZnL ¹ in ACN with no added acid (black), 2.4 mM CH ₃ COOH (dark blue), 4.8 mM CH ₃ COOH (blue), 7.2 mM CH ₃ COOH (light blue), 9.6 mM CH ₃ COOH (green), 12.0 mM CH ₃ COOH (light green), 14.4 mM CH ₃ COOH (yellow), 16.8 mM CH ₃ COOH (orange), 19.2 mM CH ₃ COOH (red), and 21.6 mM CH ₃ COOH (dark red). Data collected at a scan rate of 0.5 V/s in the presence of 0.1 M Bu ₄ NPF ₆ as supporting electrolyte. (B) Plot of <i>i</i> _{cat} vs [CH ₃ COOH] for 3 mM ZnL ¹ (red) at scan rates of 0.2 (◆) V/s.	74
Figure 27. (A) Cyclic voltammograms of 0.3 mM ZnL in methanol under 1 atm. H ₂ with no added base (black), 3 mM (CH ₃ CH ₂) ₃ N (dark blue), 6 mM (CH ₃ CH ₂) ₃ N (light blue), 12 mM (CH ₃ CH ₂) ₃ N (light purple), 21 mM (CH ₃ CH ₂) ₃ N (dark purple), and 30 mM (CH ₃ CH ₂) ₃ N (red). Data collected at a scan rate of 0.5 V/s in the presence of 0.1 M Bu ₄ NPF ₆ as supporting electrolyte. (B) Plot of <i>i</i> _{cat} / <i>i</i> _p vs [(CH ₃ CH ₂) ₃ N] for 0.3 mM ZnL under 1 atm. H ₂ (red) at scan rates of 0.2 (▲), 0.5 (◆), and 1.0 (×) V/s.	75
Figure 28. (A) Cyclic Voltammograms of 1.0 mM (black), 1.5 mM (blue), 2.0 mM (light blue), 2.5 mM (magenta), 3.0 mM (red) ZnL ¹ with 12 mM CH ₃ COOH in 0.1 M Bu ₄ NPF ₆ methanol solution. (B) Plot of peak current versus [ZnL ¹] ²	76
Figure 29. (A) Cyclic Voltammogram of H ₂ L ¹ in 0.1 M Bu ₄ NPF ₆ solution collected at 0.5 V/s. (B) Blow up showing cathodic scan only of H ₂ L ¹	77
Figure 30. (A) Cyclic voltammograms of 3 mM H ₂ L ¹ with no added acid (black), 3 mM CH ₃ COOH (blue), 5.8 mM CH ₃ COOH (purple), and 7 mM CH ₃ COOH (light purple), 8.2 mM CH ₃ COOH (pink) and, 9.8 mM CH ₃ COOH (red) . Data collected at a scan rate of 0.5 V/s in the presence of 0.1 M Bu ₄ NPF ₆ as supporting electrolyte. (B) Plot of <i>i</i> _{cat} vs [CH ₃ COOH] for 3 mM H ₂ L ¹ (blue) at scan rates of 0.2 (▲), 0.5 (◆), and 1.0 (×) V/s. .	78
Figure 31. (A) Cyclic voltammograms of 0.3 mM H ₂ L in methanol under 1 atm. H ₂ with no added base (black), 0.75 mM (CH ₃ CH ₂) ₃ N (blue), 1.5 mM (CH ₃ CH ₂) ₃ N (cyan), 3 mM (CH ₃ CH ₂) ₃ N (light blue), 6 mM (CH ₃ CH ₂) ₃ N (light purple), 9 mM (CH ₃ CH ₂) ₃ N (purple), 12 mM (CH ₃ CH ₂) ₃ N (pink), 15 mM (CH ₃ CH ₂) ₃ N (rose), 18 mM (CH ₃ CH ₂) ₃ N (red) and, 21 mM (CH ₃ CH ₂) ₃ N (dark red). (B) Plot of <i>i</i> _{cat} / <i>i</i> _p vs [(CH ₃ CH ₂) ₃ N] for 0.3 mM ZnL under 1 atm. H ₂ (blue) at scan rates of 0.2 (▲), 0.5 (◆), and 1.0 (×) V/s.	79
Figure 32. (A) Plot of charge vs time recorded during bulk electrolysis of 0.1 mM ZnL ¹ and 12 mM CH ₃ COOH in methanol with 0.1M Bu ₄ NPF ₆ as supporting electrolyte. (B) Headspace readout of GC-TCD showing H ₂ as gaseous product at times 30, 60, 90, 120, and 150 minutes during electrolysis.	79

- Figure 33.** (A) UV spectra recorded every 15 minutes during the electrolysis of 1 mM ZnL¹ under applied potential of -1.7 V in 0.1 M Bu₄NPF₆ methanol solution. (B) CV of ZnL after electrolysis in 0.1 M Bu₄NPF₆ methanol solution with 12 mM acetic acid added. $v = 0.2$ V/s vs Fc⁺/Fc. 80
- Figure 34.** Comparisons of experimental (solid) and simulated (dotted) cyclic voltammograms for 3 mM ZnL¹ and 12 mM CH₃COOH in methanol with 0.1M Bu₄NPF₆ as supporting electrolyte at scan rates of 0.3 (blue), 0.4 (purple), and 0.5 (red) V/s..... 82
- Figure 35.** Concurrent catalytic pathways for hydrogen evolution through homocoupling of neutral Zn(HL•) radicals (red arrows) and heterocoupling of a neutral Zn(HL•) and cationic [Zn(H₂L•)]⁺ radicals (blue arrows)..... 83
- Figure 36.** Optimized Structure of [ZnLH]⁺ with protonation on the hydrazino nitrogen, B97-D/6-311G(d)..... 83
- Figure 37.** DFT optimized structures showing energetic stability of protonated species, [ZnL¹H]⁺. 84
- Figure 38.** Energy profile along with spin densities of species involved in catalyzed H₂ evolution. Spin-density profiles for (A) Zn(HL•) and (B) [Zn(H₂L•)]⁺. (C) Relative energies (ZPE corrected) for H₂ evolution through the heterocoupling of Zn(HL•) and [Zn(H₂L•)]⁺ using the B97-D/6-311G(d) level of theory. (D) Structure of the singlet [Zn₂(H₃L•₂)]⁺ transition state through the heterocoupling pathway. Analysis of the eigenvector associated with the imaginary frequency $i1572$ cm⁻¹, and the charge densities of atoms for H₂ evolution with respect to intrinsic reaction coordinate. 84
- Figure 39.** (Upper) Transition state geometry of [Zn₂H₃L•₂]⁺ along the HER pathway, shown with active N-H bond lengths associated with the imaginary frequency $i1572$ cm⁻¹, and equilibrium bond lengths in parentheses. (Lower) Charge densities of atoms near H₂ evolution with respect to IRC; N-H of [Zn(HL•)]⁺ (blue, and cyan), and N-H of Zn(H₂L•) (magenta, purple). 86
- Figure 40.** CVs of CuL¹ in 0.1 M Bu₄NPF₆ acetonitrile solution at scan rates of 0.1 (black), 0.2 (blue), 0.3 (light blue), 0.4 (green), 0.5 (light green), 0.6 (purple), 0.7 (yellow), 0.8 (orange), 0.9 (red) and 1.0 (black) V/s. CuL¹. Inset: Cottrell plot of peak current vs square root of scan rate. 94
- Figure 41.** (A) CVs of 0.6mM CuL¹ (black) in 0.1M Bu₄NPF₆ acetonitrile with 0.0244 (purple), 0.0448 (light purple), 0.0896 (light blue), 0.134 (pink), 0.179 (yellow), 0.244 (light green) and 0.269 (red) M CH₃COOH, Inset. Blow up of CV showing shift of Cu^{II/I} reduction event. (B) Plot of i_{cat}/i_p vs [CH₃COOH] for 0.60 mM CuL¹ (blue) at scan rates of 0.20 (X), 0.50 (●) and 1.00 (*) V/s (C) Catalytic Tafel Plot of CuL¹ (blue) with comparison of performance for hydrogen evolution with those of others reported in literature. Blue ◇: Co^{II}(dmgH)₂py; green ●: [Ni(P^{Ph}₂N^{Ph})₂]²⁺; red ■: NiL²; magenta ▲: ZnL¹; purple X: H₂L¹.¹⁹⁷ 95
- Figure 42.** (A) CVs of 0.6mM CuL¹ (black) in 0.1M Bu₄NPF₆ DMF with 0.0244 (light purple), 0.0448 (purple), 0.0896 (blue), 0.157 (green), 0.202 (light green), 0.246 (yellow),

0.269 (orange). And 0.292 (red) M CH ₃ COOH. (B) Plot of i_{cat}/i_p vs [CH ₃ COOH] concentration.....	96
Figure 43. (A) Bulk electrolysis showing plot of charge versus time of 0.6mM CuL ¹ in 0.1 M Bu ₄ NPF ₆ acetonitrile (pink and orange) and in 0.1 M Bu ₄ NPF ₆ DMF (red and blue) with 0.292M CH ₃ COOH added. Blank acetonitrile (green). (B) GC-TCD headspace readout of H ₂ from electrolysis. (C) Summary of CPE results.	98
Figure 44. Dip test post electrolysis in acetonitrile: After electrolysis working electrode was rinsed with water and immersed in a fresh solution of 0.1 M Bu ₄ NPF ₆ acetonitrile solution and a CV was recorded (blue). 0.269 M acetic acid was then added and a CV was obtained (red).....	99
Figure 45. (A) CVs of 0.6 mM CuL ¹ in 0.1 M Bu ₄ NPF ₆ acetonitrile solution with 0.269 M acetic acid, from 0-100% D-acetic acid use. (B) Plot of %D-Acetic acid use vs KIE.	101
Figure 46. UV-Visible spectrum of CuL ¹ titrated with acetic acid; 0.022 (dark red), 0.044 (red), 0.056 (light red), 0.067 (orange), 0.089 (light orange), 0.112 (yellow), 0.134 (light green), 0.157 (green), 0.202 (sky blue), 0.244 (blue), 0.269 (magenta), 0.292 (light blue), 0.337 (purple), and 0.382 (black) M.	102
Figure 47. (A) Cyclic Voltammograms run in 0.1 M Bu ₄ NPF ₆ acetonitrile solution with 0.269 M acetic acid added run with 0.1 (light blue), 0.2 (green), 0.3 (light green), 0.4 (yellow), 0.5 (orange), 0.6 (red), and 0.7 (dark red) mM CuL ¹ . (B) Plot of peak current versus catalyst concentration showing linear dependence and 1 st order relationship.	104
Figure 48. (A) Energetic stability of protonated species, [CuL ¹ H] ⁺ . (B) Energetic Stability of protonated and reduced species, CuL ¹ H.	105
Figure 49. Spin-density map of [CuL ¹ H] ⁺	106
Figure 50. Spin-density map of CuL ¹ (S=1/2).	106
Figure A51. Screenshot of a .use file used for import into DigiElch.....	133
Figure A52. (Left) Screenshot showing how to import files to DigiElch using import icon. (Right) Sample .use files to import.	134
Figure A53. Screenshot of simulation parameters. Setting under Model parameters, 2D Simulation and FEM-Simulation do not need to be changed at all.	136
Figure A54. Screenshot of the chemical reactions tab.	137
Figure A55. Screenshot of popup window obtained by double clicking on charge transfer reaction box.....	138
Figure B56. ZnL HER CV Simulations of experimental data; 12 mM [acid]; $v = 0.2 - 0.5$ V/s vs Fc ⁺ /Fc. Fit with mechanism parameters from Table A4.....	141
Figure B57. Comparison of experimental (black solid) and simulated (green dotted) cyclic voltammograms; ZnL ¹ HER. 12 mM [acid]; $v = 0.2$ V/s vs Fc ⁺ /Fc. Fit with mechanism parameters from Table A4.	142

Figure B58. Comparison of experimental (black solid) and simulated (green dotted) cyclic voltammograms; ZnL ¹ HER. 12 mM [acid]; $\nu = 0.3$ V/s vs Fc ⁺ /Fc. Fit with mechanism parameters from Table A4.	143
Figure B59. Comparison of experimental (black solid) and simulated (green dotted) cyclic voltammograms; ZnL ¹ HER. 12 mM [acid]; $\nu = 0.4$ V/s vs Fc ⁺ /Fc. Fit with mechanism parameters from Table A4.	144
Figure B60. Comparison of experimental (black solid) and simulated (green dotted) cyclic voltammograms; ZnL ¹ HER. 12 mM [acid]; $\nu = 0.5$ V/s vs Fc ⁺ /Fc. Fit with mechanism parameters from Table A4.	145
Figure B61. ZnL HER CV Simulations of experimental data; 12 mM [acid]; $\nu = 1.0 - 5.0$ V/s vs Fc ⁺ /Fc. Fit with mechanism parameters from Table A5.	146
Figure B62. Comparison of experimental (black solid) and simulated (red dotted) cyclic voltammograms; ZnL ¹ HER. 12 mM [acid]; $\nu = 1.0$ V/s vs Fc ⁺ /Fc. Fit with mechanism parameters from Table A5.	147
Figure B63. Comparison of experimental (black solid) and simulated (red dotted) cyclic voltammograms; ZnL ¹ HER. 12 mM [acid]; $\nu = 1.5$ V/s vs Fc ⁺ /Fc. Fit with mechanism parameters from Table A5.	148
Figure B64. Comparison of experimental (black solid) and simulated (red dotted) cyclic voltammograms; ZnL ¹ HER. 12 mM [acid]; $\nu = 2.0$ V/s vs Fc ⁺ /Fc. Fit with mechanism parameters from Table A5.	149
Figure B65. Comparison of experimental (black solid) and simulated (red dotted) cyclic voltammograms; ZnL ¹ HER. 12 mM [acid]; $\nu = 2.5$ V/s vs Fc ⁺ /Fc. Fit with mechanism parameters from Table A5.	150
Figure B66. Comparison of experimental (black solid) and simulated (red dotted) cyclic voltammograms; ZnL ¹ HER. 12 mM [acid]; $\nu = 3.0$ V/s vs Fc ⁺ /Fc. Fit with mechanism parameters from Table A5.	151
Figure B67. Comparison of experimental (black solid) and simulated (red dotted) cyclic voltammograms; ZnL ¹ HER. 12 mM [acid]; $\nu = 3.5$ V/s vs Fc ⁺ /Fc. Fit with mechanism parameters from Table A5.	152
Figure B68. Comparison of experimental (black solid) and simulated (red dotted) cyclic voltammograms; ZnL ¹ HER. 12 mM [acid]; $\nu = 4.0$ V/s vs Fc ⁺ /Fc. Fit with mechanism parameters from Table A5.	153
Figure B69. Comparison of experimental (black solid) and simulated (red dotted) cyclic voltammograms; ZnL ¹ HER. 12 mM [acid]; $\nu = 4.5$ V/s vs Fc ⁺ /Fc. Fit with mechanism parameters from Table A5.	154
Figure B70. Comparison of experimental (black solid) and simulated (red dotted) cyclic voltammograms; ZnL ¹ HER. 12 mM [acid]; $\nu = 5.0$ V/s vs Fc ⁺ /Fc. Fit with mechanism parameters from Table A5.	155
Figure B71. ZnL ¹ HER. ZnL HER CV Simulations of experimental data; 6 mM [acid]; $\nu = 0.2-0.5$ V/s vs Fc ⁺ /Fc. Fit with mechanism parameters from Table A6.	156

Figure B72. Comparison of experimental (black solid) and simulated (green dotted) cyclic voltammograms; ZnL ¹ HER. 6 mM [acid]; $\nu = 0.2$ V/s vs Fc ⁺ /Fc. Fit with mechanism parameters from Table A6.	157
Figure B73. Comparison of experimental (black solid) and simulated (green dotted) cyclic voltammograms; ZnL ¹ HER. 6 mM [acid]; $\nu = 0.3$ V/s vs Fc ⁺ /Fc. Fit with mechanism parameters from Table A6.	158
Figure B74. Comparison of experimental (black solid) and simulated (green dotted) cyclic voltammograms; ZnL ¹ HER. 6 mM [acid]; $\nu = 0.4$ V/s vs Fc ⁺ /Fc. Fit with mechanism parameters from Table A6.	159
Figure B75. Comparison of experimental (black solid) and simulated (green dotted) cyclic voltammograms; ZnL ¹ HER. 6 mM [acid]; $\nu = 0.5$ V/s vs Fc ⁺ /Fc. Fit with mechanism parameters from Table A6.	160
Figure C76. ZnL ¹ HER cyclic voltammograms in 0.1 M Bu ₄ NPF ₆ methanol solution with increasing concentrations of CH ₃ COOH added; $\nu = 0.2$ V/s.	162
Figure C77. Plot of CH ₃ COOH concentration versus catalytic current for ZnL ¹ in 0.1 M Bu ₄ NPF ₆ methanol solution; $\nu = 0.2$ V/s.	163
Figure C78. ZnL ¹ HER cyclic voltammograms in 0.1 M Bu ₄ NPF ₆ methanol solution with increasing concentrations of CH ₃ COOH added; $\nu = 0.3$ V/s.	164
Figure C79. Plot of CH ₃ COOH concentration versus catalytic current for ZnL ¹ in 0.1 M Bu ₄ NPF ₆ methanol solution; $\nu = 0.3$ V/s.	165
Figure C80. ZnL ¹ HER cyclic voltammograms in 0.1 M Bu ₄ NPF ₆ methanol solution with increasing concentrations of CH ₃ COOH added; $\nu = 0.4$ V/s.	166
Figure C81. Plot of CH ₃ COOH concentration versus catalytic current for ZnL ¹ in 0.1 M Bu ₄ NPF ₆ methanol solution; $\nu = 0.4$ V/s.	167
Figure C82. ZnL ¹ HER cyclic voltammograms in 0.1 M Bu ₄ NPF ₆ methanol solution with increasing concentrations of CH ₃ COOH added; $\nu = 0.5$ V/s.	168
Figure C83. Plot of CH ₃ COOH concentration versus catalytic current for ZnL ¹ in 0.1 M Bu ₄ NPF ₆ methanol solution; $\nu = 0.5$ V/s.	169
Figure C84. ZnL ¹ HOR cyclic voltammograms in 0.1 M Bu ₄ NPF ₆ methanol solution, under an H ₂ atmosphere, with increasing concentrations of (CH ₂ CH ₃) ₃ N added; $\nu = 0.2$ V/s.	170
Figure C85. ZnL ¹ HOR cyclic voltammograms in 0.1 M Bu ₄ NPF ₆ methanol solution, under an H ₂ atmosphere, with increasing concentrations of (CH ₂ CH ₃) ₃ N added; $\nu = 0.5$ V/s.	171
Figure C86. ZnL ¹ HOR cyclic voltammograms in 0.1 M Bu ₄ NPF ₆ methanol solution, under an H ₂ atmosphere, with increasing concentrations of (CH ₂ CH ₃) ₃ N added; $\nu = 1.0$ V/s.	172
Figure C87. H ₂ L ¹ HER cyclic voltammograms in 0.1 M Bu ₄ NPF ₆ methanol solution with increasing concentrations of CH ₃ COOH added ; $\nu = 0.5$ V/s.	173

Figure C88. H ₂ L ¹ HER cyclic voltammograms in 0.1 M Bu ₄ NPF ₆ methanol solution with increasing concentrations of CH ₃ COOH added; $\nu = 1.0$ V/s.	174
Figure C89. Cyclic Voltammogram of H ₂ L ¹ in 0.1 M Bu ₄ NPF ₆ methanol solution; $\nu = 0.2$ V/s.	175
Figure C90. H ₂ L ¹ HOR cyclic voltammograms in 0.1 M Bu ₄ NPF ₆ methanol solution, under an H ₂ atmosphere, with increasing concentrations of (CH ₂ CH ₃) ₃ N added; $\nu = 0.2$ V/s.	175
Figure C91. H ₂ L ¹ HOR cyclic voltammograms in 0.1 M Bu ₄ NPF ₆ methanol solution, under an H ₂ atmosphere, with increasing concentrations of (CH ₂ CH ₃) ₃ N added; $\nu = 0.5$ V/s.	176
Figure C92. H ₂ L ¹ HOR cyclic voltammograms in 0.1 M Bu ₄ NPF ₆ methanol solution, under an H ₂ atmosphere, with increasing concentrations of (CH ₂ CH ₃) ₃ N added; $\nu = 1.0$ V/s.	177
Figure C93. CuL ¹ HER cyclic voltammograms in 0.1 M Bu ₄ NPF ₆ acetonitrile solution with increasing concentrations of CH ₃ COOH added; $\nu = 0.2$ V/s.	178
Figure C94. CuL ¹ HER cyclic voltammograms in 0.1 M Bu ₄ NPF ₆ acetonitrile solution with increasing concentrations of CH ₃ COOH added; $\nu = 0.5$ V/s.	179
Figure C95. CuL ¹ HER cyclic voltammograms in 0.1 M Bu ₄ NPF ₆ acetonitrile solution with increasing concentrations of CH ₃ COOH added; $\nu = 1.0$ V/s.	180
Figure C96. 0.6 mM CuL ¹ in 0.1 M Bu ₄ NPF ₆ DMF; HER CVs scanned at 0.5 V/s.	181
Figure C97. Plot of i_{cat}/i_p vs [CH ₃ COOH]; $\nu = 0.5$ V/s.	181
Figure C98. 0.6 mM CuL ¹ in 0.1 M Bu ₄ NPF ₆ DMF; HER CVs scanned at 1.0 V/s.	182
Figure C99. Plot of i_{cat}/i_p vs [CH ₃ COOH]; $\nu = 1.0$ V/s.	182
Figure C100. Scan Rate Dependence: CVs of 0.6 mM CuL ¹ in 0.1 M Bu ₄ NPF ₆ DMF solution with 0.292 M acetic acid added scanned from 0.1 – 1.0 V/s.	183
Figure C101. Plot of scan rate vs TOF for CuL ¹ in DMF.	183
Figure C102. Plot of scan rate vs catalytic current for CuL ¹ in DMF.	184
Figure C103. CVs run in 0.1 M Bu ₄ NPF ₆ acetonitrile solutions, showing blank acetonitrile (blue), with 0.0672 M acetic acid added (black dashed), and with 0.0672 M acetic acid and 0.6 mM CuL ¹ (red).	184
Figure 104. CVs run in 0.1 M Bu ₄ NPF ₆ DMF solutions, showing blank DMF (blue), with 0.0224 M acetic acid added (black dashed), and with 0.0224 M acetic acid and 0.6 mM CuL ¹ (red).	185
Figure C105. CVs run in 0.1 M Bu ₄ NPF ₆ DMF solutions with 0.292 M acetic acid (blue) and upon addition of 0.6 mM CuL ¹ (purple).	185
Figure C106. OCP measurement for ZnL ¹ HER 0.1M Bu ₄ NPF ₆ methanol solution with 12 mM acetic acid added.	186
Figure C107. OCP measurement for ZnL ¹ HOR 0.1M Bu ₄ NPF ₆ methanol solution with 30 mM triethylamine added.	186

Figure C108. OCP measurement for H_2L^1 HER 0.1M Bu_4NPF_6 methanol solution with 10 mM acetic acid added.	187
Figure C109. OCP measurement for H_2L^1 HOR 0.1M Bu_4NPF_6 methanol solution with 10 mM acetic acid added.	187
Figure C110. OCP measurement for ZnL^1 HER in Acetonitrile 0.1M Bu_4NPF_6 acetonitrile solution with 21 mM acetic acid added.	188
Figure C111. OCP measurement for CuL^1 HER 0.1 M Bu_4NPF_6 acetonitrile solution with 0.269 M acetic acid added	188
Figure C112. OCP measurement for CuL^1 HER 0.1 M Bu_4NPF_6 DMF solution with 0.292 M acetic acid added.	189
Figure C113. UV-Vis absorbance's measured during titration of ReL_3 with increasing equivalents of HCl.	189
Figure D114. DFT (M06 / LANL2DZ) optimized geometric parameters with bond lengths (Å) and angles (°) for $[\text{HRe}(\text{LH})\text{L}_2]^0$ with free energy energies (kcal / mole) of singlet (S = 0) and triplet (S = 1) electronic states.....	191

LIST OF TABLES

Table 1. Comparison of selected bond distances and bond angles between ReL_3 , $[\text{Re}(\text{LH})\text{L}_2]\text{PF}_6$, $[\text{Re}(\text{LH})\text{L}_2]\text{O}_3\text{SCF}_3$ and, $[\text{ReL}_3\cdot\text{C}_2\text{H}_4][\text{PF}_6]_2$. ^a	49
Table 2. Bond length comparison of calculated HER intermediates	87
Table 3. Bond angle comparison of calculated HER intermediates	88
Table A4. ZnL^1 Optimized parameters of data fitting, 12 mM [acid]; $v = 0.2 - 0.5$ V/s vs Fc^+/Fc	129
Table A5. ZnL^1 Optimized parameters of data fitting, 12 mM [acid]; $v = 1.0 - 5.0$ V/s vs Fc^+/Fc	130
Table A6. ZnL^1 Optimized parameters of data fitting, 6 mM [acid]; $v = 0.2 - 0.5$ V/s vs Fc^+/Fc	131
Table D8. Computational input coordinates for ZnL^1 and related compounds.	192
Table D9. Computational input coordinates for ReL_3 and related compounds.	203
Table D10. Computational input coordinates for CuL^1 and related compounds.	233

LIST OF SCHEMES

Scheme 1. Stick representation of ReL_3 (L = diphenylphosphinobenzenethiolate).....	45
Scheme 2. Proposed Mechanism for Electrocatalytic H_2 evolution and oxidation by ReL_3	56
Scheme 3. Proposed Mechanism of H_2 Evolution by ReL_3	57
Scheme 4. Comparison of first and second generation Ligand-Centered HER Electrocatalysts.	69
Scheme 5. Representation of ZnL^1 and H_2L^1	70
Scheme 6. Selected ligand-centered HER/HOR electrocatalysts, taken from references 71, 99 and 100. ^{71,99,100}	71
Scheme 7. Representation of thiosemicarbazone based electrocatalysts.	93
Scheme 8. Comparison of thiosemicarbazone HER electrocatalysts.	107
Scheme 9. ReL_3 HER mechanism	112
Scheme 10. Representation of homolytic S-H bond cleavage leading to H_2 evolution via radical coupling and calculated transition state for H_2 evolution.	113
Scheme 11. Proposed mechanism for H_2 evolution by ZnL^1	115
Scheme 12. Mechanism for H_2 evolution for ZnL^1 showing evolution through heterolytic N-H bond cleavage resulting in deprotonation of neighboring hydrogen and (right) the calculated transition state for H_2 evolution.	116

CHAPTER I: INTRODUCTION

1.1. Hydrogen: Importance and Background

Energy is an essential requirement for the development of any society, and therefore should be a key consideration in discussions of sustainable development. Yet, reliable and practical renewable energy sources remain a paramount challenge as we continue into the 21st century.¹ Current energy needs are largely met by fossil fuels, but these sources are non-renewable and their use releases billions of tons of the greenhouse gas CO₂ annually.^{2,3} Long range predictions suggest a tripling of global energy needs by 2100, while also suggesting depletion of all fossil fuel reserves other than coal by 2042.⁴ Clearly, the current energy use is unsustainable, and researchers are going to great lengths to develop renewable resources capable of meeting energy demands.^{2,3,5}

In this context, hydrogen can be viewed as being a promising alternative carbon-free fuel/energy carrier, in addition to currently being an essential building block for industrial and agricultural processes. Estimates suggest that a hydrogen based economy would require as much as 150 million tons of H₂ annually, demonstrating the need for efficient electrolytic and/or photochemical catalysts that generate H₂ from carbon-free sources.⁶ As such, the development of both heterogeneous and homogeneous catalysts for hydrogen evolution reactions (HER) from water/acid for H₂ production and hydrogen oxidation reactions(HOR) for H₂ utilization have received significant attention.⁷⁻¹⁴

Not only is hydrogen an attractive energy carrier candidate, but there is also a great demand for hydrogen in other industrial sectors. Industrial production of ammonia via the Haber-Bosch process currently accounts for 54% of all hydrogen use; coming in a close second is the chemical industry/refineries, accounting for a substantial 35% of its use (Figure 1). Even more, 95% of industrial H₂ production derives from fossil-fuel

cracking, which is environmentally unsustainable due to the aforementioned perpetual increases in atmospheric CO₂ levels and continual lowering of global carbon reserves,^{5,15,16} further indicating the need to develop alternative, carbon neutral methods for hydrogen production.¹⁷

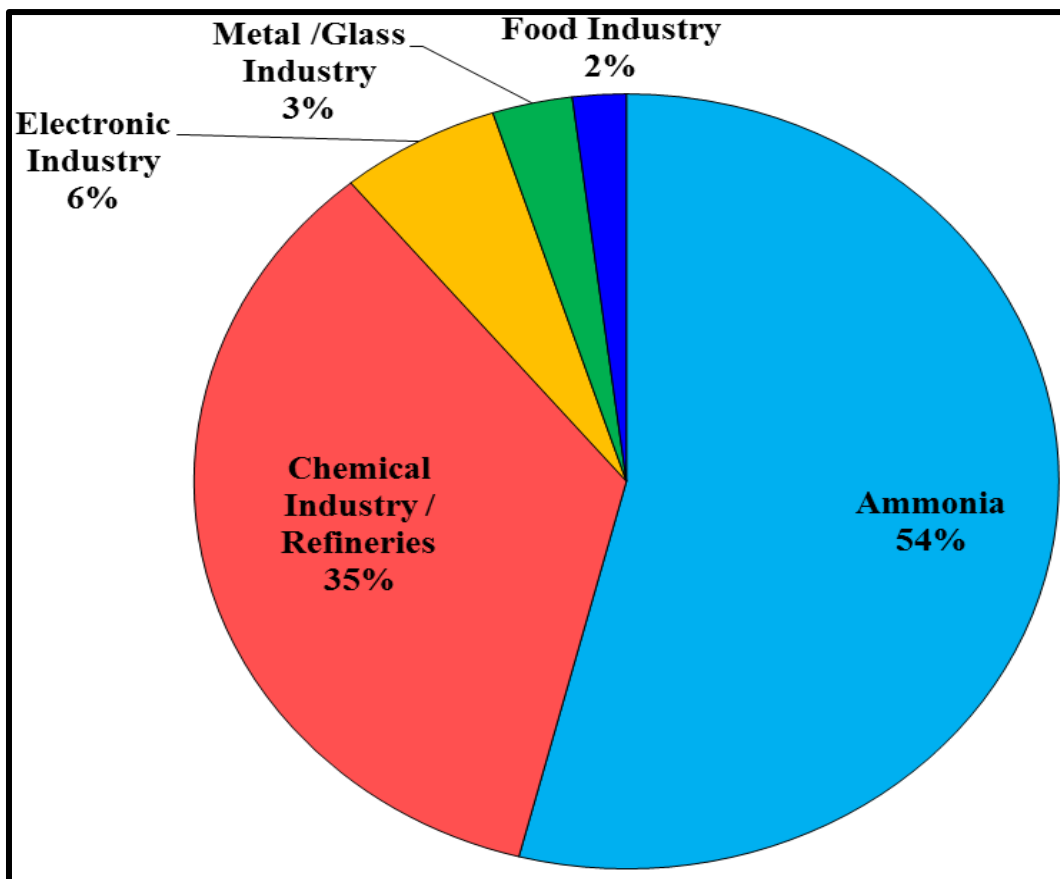


Figure 1. Percent of global hydrogen use by industry.¹⁷

1.2. Hydrogenase and Biomimetic Hydrogenase Complexes

Hydrogenases are a diverse group of metalloenzymes that catalyze one of the simplest molecular reactions, the oxidation of dihydrogen to protons and electrons and the reverse reaction, the formation of H₂.^{18,19} The term hydrogenase was first suggested by Stephenson and Strickland in 1931^{20,21} when observing activity in anaerobically grown *Escherichia Coli* cells which mediated the reversible reduction of dyes with H₂. The

observation that the dye reduction was reversibly inhibited by CO indicated the involvement of a transition metal in H₂ activation. The hydrogenase reaction takes place at either an iron or nickel center, which utilize specific ligands to increase the acidity of H₂ leading to a heterolytic splitting of the molecule. This process is strongly accelerated by the presence of a nearby base. The reverse reaction, the evolution of H₂, involves the respective coupling of H⁺ and H⁻ ions.

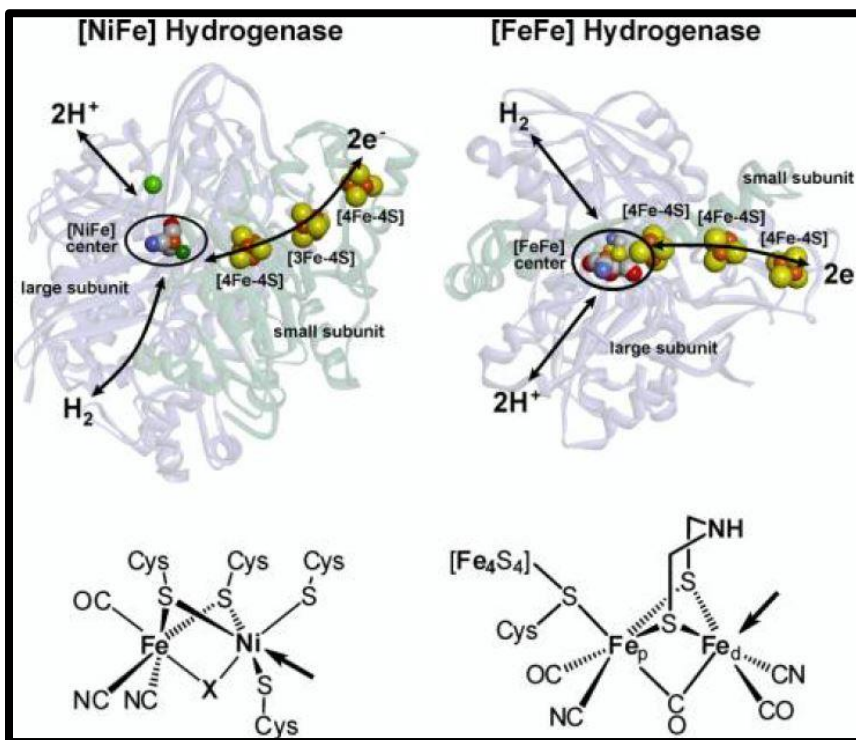


Figure 2. (Top) Structures of the [NiFe] hydrogenase²² and of the [FeFe] hydrogenase from Dd.²³ (Bottom) the chemical structures of the active sites of the two types of hydrogenases are given; the arrows indicate the open metal coordination sites.

Hydrogenases are widespread in nature, occurring in bacteria, archaea, and some eukarya.^{18,19,24,25} They can be divided into three groups, according to the metal ion composition of their active sites, as either [NiFe], [FeFe], or [Fe] hydrogenase, with H₂ evolution favored in [FeFe]-hydrogenase, and H₂-oxidation preferential at [NiFe]-

hydrogenase.²⁶⁻³⁰ A characteristic feature of two of the classes, [NiFe] and [FeFe] hydrogenases, is that the iron atoms are ligated by small inorganic ligands such as CO and CN⁻, which were first detected by FTIR spectroscopy.³¹⁻³³ They also exhibit sulfur bridged bimetallic centers, with an open coordination site on one of the metal centers (Figure 2). The third class, [Fe] hydrogenase, contains only a single iron atom³⁴⁻³⁷ with CO ligands on the iron center, in addition to its cofactor.

A combination of crystallographic and spectroscopic data has provided a clear view of the enzymatic mechanism for the [FeFe] hydrogenase (Figure 3). The initial state of hydrogenase is a dianion, termed H_{ox}. In this state, the proximal iron site (Fe_p) is Fe(I) and is in an octahedral coordination environment, containing two thiolate bridging ligands with a pendant amine, two CO ligands with one terminal and one bridging, a terminal CN⁻ ligand and a thiolate which is associated with [Fe₄S₄] cluster. The distal iron, (Fe_d) is five coordinate with a free coordination site and is Fe(II).³⁸ Upon one-electron reduction and protonation, the Fe(II) center is reduced to Fe(I) giving the H_{red} state. Here, the cubane subcluster is still in the oxidized state, while the di-iron subcluster is still in the Fe(I)/Fe(I) state, with Fe_p in a square pyramidal geometry bearing a free coordination site. It is important to point out that the location of the added proton has not been determined, but it is thought to be either on the right five-coordinate iron center or on one of the bridging sulfurs.³⁹ The formation of H_{red} from H_{ox} is additionally described as a proton-coupled electron transfer process. Very recently a third paramagnetic redox state, H_{sred} (super-reduced), has been experimentally observed and characterized by EPR and FTIR spectroscopy.⁴⁰ H_{sred} contains one more electron than H_{red}, which is located on the [4Fe-4S] cluster, and is characterized by a Fe(I)/Fe(I)/[4Fe-

$4S]^+$ configuration. It is suggested that H_{sred} forms part of the catalytic cycle as an additional intermediate.^{40,41} It was then proposed, on this basis, that H_2 oxidation, catalyzed by [FeFe]-hydrogenases, proceeds *via* initial binding of H_2 to the exchangeable/free coordination site of H_{ox} , followed by heterolytic cleavage of the H—H bond assisted by the bridgehead amine function, and finally transfer of two individual electrons from the Fe-bound hydride to the [4Fe—4S] cluster and the Fe_p of the [FeFe] subsite. Ejection of the protons and the electrons from H_{sred} regenerates H_{ox} to complete the catalytic cycle. Each step is reversible, and proton reduction to H_2 is proposed to use the same catalytic steps and intermediates, but in the opposite direction. The structure for [NiFe] hydrogenase was first structurally characterized by the Fontecilla-Camp Group in 1995.^{33,42} Several H_2 uptake mechanisms have been proposed for [NiFe] hydrogenases, but a consensus has yet to be reached.⁴³

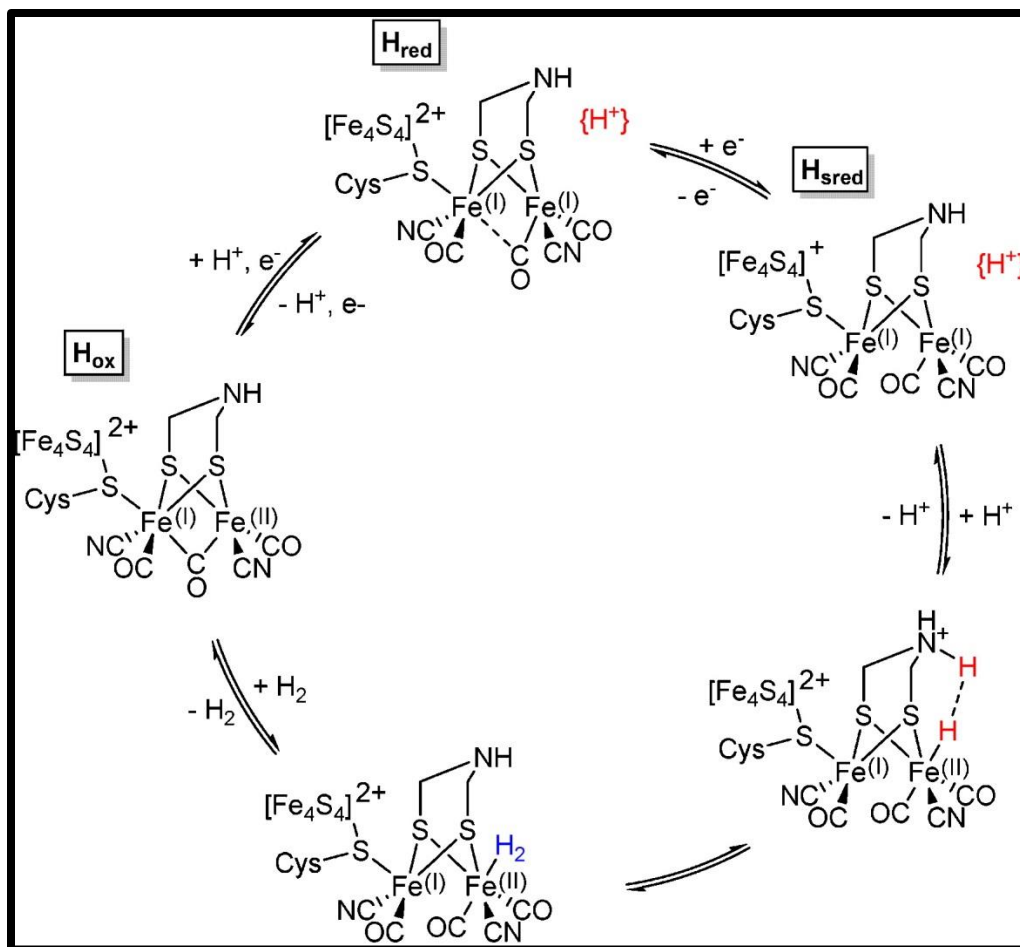


Figure 3. Postulated catalytic mechanism for reversible H⁺ reduction by [FeFe]-hydrogenases, the location of the proton in the H_{red} and H_{sred} state is undetermined, adapted from reference 53.⁴⁰

To provide further insight into the active site and reaction mechanism of [FeFe] and [NiFe] hydrogenase synthetic inorganic chemists began to make model complexes of hydrogenase in order to mimic its bifunctional behavior and high activity for H₂ evolution and oxidation. A number of biomimetic hydrogenase models have been explored. Interestingly—prior to the structural elements of [FeFe] hydrogenases active site being known—in 1929 Reihlen *et al.* reported the preparation of analogous dithiolate-bridged hexacarbonyl di-iron complexes, [(μ-SEt)₂Fe(CO)₆] (Figure 4).⁴⁴

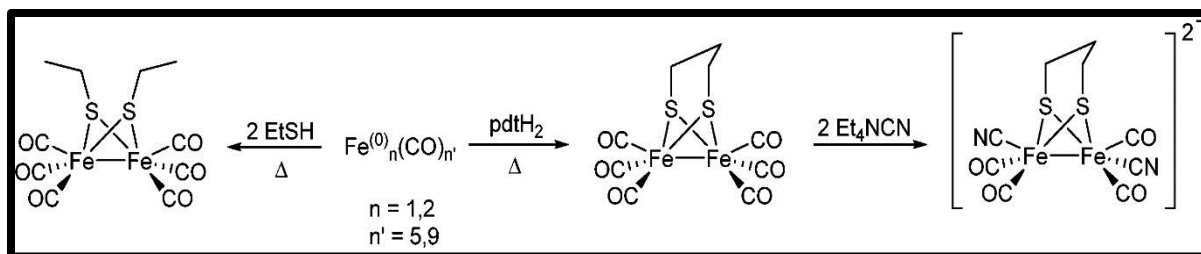


Figure 4. Synthetic scheme for the preparation of $[(\mu\text{-SEt})_2\text{Fe}(\text{CO})_6]$ (left), and precursor diiron hexacarbonyl complex (middle) used in route to the first true $[\text{FeFe}]$ hydrogenase model $[(\mu\text{-pdt})\text{Fe}_2(\text{CO})_4(\text{CN})_2]^{2-}$ (right).⁴⁵⁻⁴⁷

The structural characterization of the H-cluster in 1998-1999 by Peters *et al.*,^{23,48} served as an inspiration to many groups who desired to create synthetic hydrogenase analogues. Three groups, Pickett, Rauchfuss, and Darensbourg, replaced two CO groups with two CN ligands in order to generate the water soluble dianion, $[(\mu\text{-pdt})\text{Fe}_2(\text{CO})_4(\text{CN})_2]^{2-}$ (Figure 4).⁴⁵⁻⁴⁷ These first-generation $[\text{FeFe}]$ hydrogenase mimics initiated further synthetic inorganic chemistry research. Currently, there are over 300 model systems reported.^{39,49}

Interest in $[\text{FeFe}]$ hydrogenase has continued to the present day, with close to 100 new papers in the last five years.⁵⁰⁻⁵⁸ Much of this second-generation work has been directed to the bridging group ligands, to overcome limitations such as large overpotential requirements. Strategies included using higher group chalcogens such as selenide to replace the bridging dithiolates⁵⁹, inclusion of a suitably substituted aromatic dithiolate bridgehead,⁶⁰ substitution of the CN ligands to phosphines,³⁹ and addition of benzene rings bearing strong electron withdrawing groups like chloride.^{60,61} These approaches led to moderate success, reducing overpotentials by roughly 150 mV, although at the expense of catalytic efficiency in terms of turnover frequencies.

1.3. Mechanistic Features of H₂ Evolution and Oxidation

The investigation into the production or oxidation of H₂, as discussed above, has long been a fundamental interest of energy research. In addition to better understanding hydrogenase, research in this area does have a double incentive—that is to understand completely, whether the reaction follows a homolytic or a heterolytic pathway (Figure 5). This has been a long held question^{62,63} and continues to be a hotly debated issue.^{10,13,64-90}

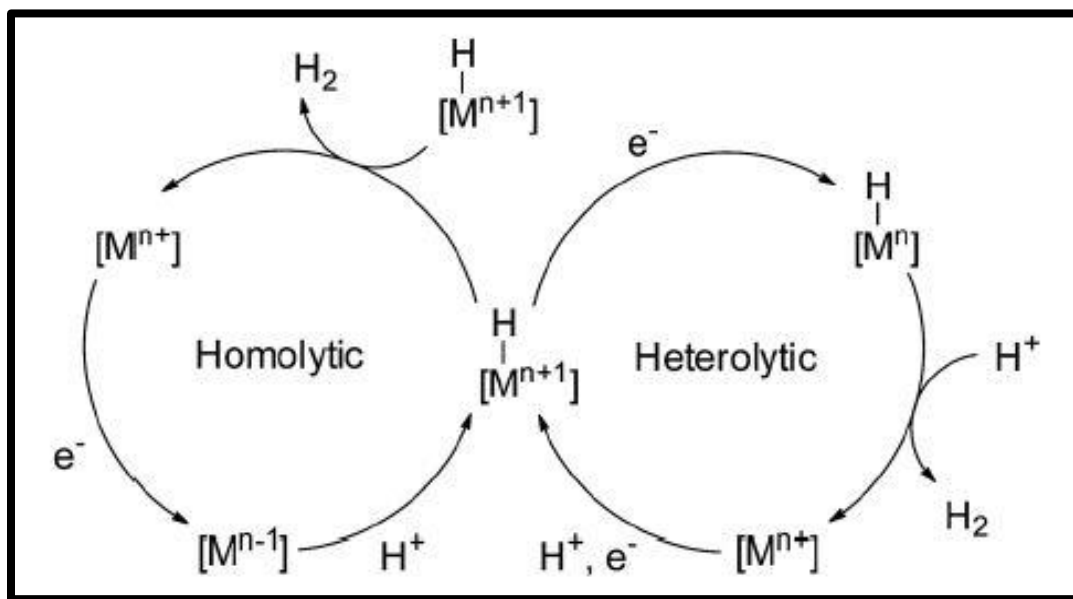


Figure 5. Illustration of two potential routes for H₂ evolution following either a homolytic or heterolytic pathway.

One common and well-studied class of H₂ evolution catalysts is the cobaloxime family of complexes. Initial reports by both Peters *et al.*¹⁰ and Dempsey *et al.*⁹¹ suggested a homolytic pathway involving a bi-molecular mechanism, where homolytic bond cleavage of two Co^I-H species results in the evolution of hydrogen.^{10,64,91} However, further research by Muckerman *et al.*⁷² and Fontecave *et al.*^{73,74} tend to favor a heterolytic pathway, which was further supported by an array of computational reports that also favor the heterolytic pathway.^{72,92} Recently, even more light has been shed onto the

mechanism of H₂ evolution with these complexes with Artero *et al.* suggesting *in situ* formation of catalytic nanoparticles as the active species for catalysis.⁹³ Dubois and Bullock have extensively evaluated the reactivity of nickel and iron bis(diamine) complexes.^{14,94} The complexes mimic nature by employing a pendant amine as a proton relay group, in order to lower overpotential and increase turnover frequency and achieve some of the fastest reported homogeneous HER TOFs. Furthermore, Eisenberg and Holland reported a series of metal-dithiolene complexes with the highest TOFs and lowest overpotentials of synthetic transition metal-sulfur electrocatalysts under homogeneous conditions.^{7,11,95} Each of these systems are thought to follow a metal-hydride pathway and it is widely regarded that transition metals capable of forming metal-hydride intermediates are essential to the HER mechanism. Naturally, most HER electrocatalysts reported to date closely follow the archetypal mechanism of ligand protonation, metal reduction, proton to hydride migration, and subsequent chemical/electrochemical steps leading to H₂ release.⁹⁴

While the metal-hydride approach has led to significant advances, catalyst candidates that fall into this paradigm are limited to economically viable first-row transition metals complexes capable of stabilizing hydrides. Moreover, few complexes of this type are reported to catalyze both HERs and HORs.¹³ This has led to a renaissance in hydrogen evolution or oxidation electrocatalyst design and thought, stimulating researchers to probe ligand-centered homolytic routes for catalysis.

1.4. Ligand-Centered HER Electrocatalysts

Classical behavior of transition complexes which involve a redox process encompasses oxidation or reduction of the metal, leaving the ligand unaffected. However, ligands can

also participate in the redox process. In these cases, the ligand is referred to as being *redox non-innocent* or *redox active*.^{96,97} These types of ligands and their metal complexes have attracted substantial attention over the past decade and longer, since they offer a unique opportunity to modify the reactivity of transition metal complexes. Within traditional redox non-innocence, four different strategies can

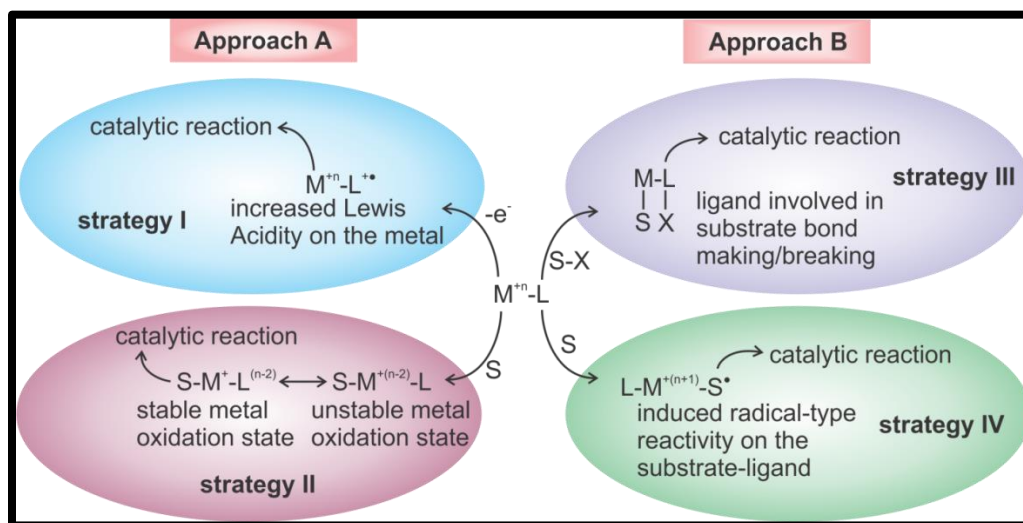


Figure 6. Illustration showing the four traditional reaction pathways observed with redox non-innocent ligands in catalysis (S = substrate).

be employed. The first is the modification of the Lewis acidity of the metal via reduction/oxidation of the ligand. Doing so strongly influences the substrate affinity and lowers reaction barriers for subsequent reaction steps. The second approach involves exploiting an *electron-reservoir* in the redox active ligand. This allows the metal to work with the ligand and store extra reducing or oxidizing equivalents on the ligand in elementary steps, avoiding uncommon oxidation states of the metal. The third strategy essentially forces/generates a reactive ligand-radical. These reactive ligand radicals can then actively participate in the making and breaking of chemical bonds during catalysis,

allowing reactions to be performed that are difficult to achieve otherwise. The final strategy is similar to the third, but uses radical-type activation of the substrates or modification of the substrate reactivity in cases where the substrate itself acts as a redox non-innocent ligand, as demonstrated previously in the Grapperhaus group.⁹⁸ In general terms, a redox active non-innocent ligand can either participate in the catalytic cycle by (A) accepting/releasing electrons (strategies I and II) or by (B) forming/breaking chemical bonds of the substrate (strategies III and IV) (Figure 6).

The first non-transition metal homogeneous HER catalyst reported was an aluminum-bis(imino)pyridine complex by Thompson *et al.* that evolved H₂ with a TOF of 3.3 hr⁻¹ at an overpotential of 0.5 V, via ligand-centered reduction and protonation.⁹⁹ As shown later in Chapter three, Haddad *et al.* reported a rhenium dithiolate complex as the first reversible, ligand-centered catalyst for both HER and HOR, which proceeds through a radical coupling mechanism.⁷⁷ Subsequently, Solis *et al.* reported a nickel phlorin intermediate with a hydridic C-H bond that reacts with an external acid to produce H₂ in a purely ligand-centered process.⁷¹ Following these reports, Zarkadoulas *et al.* reported DFT computations that suggested Ni-dithiolene HER catalysts may proceed via metal-hydrides or a ligand-centered mechanism.⁸⁹

Recently, we reported the first examples of HER/HOR activity with the non-innocent bis(thiosemicarbazone) ligand framework, Chapter four.⁷⁶ The zinc complex of diacetyl-bis(N-4-methyl-3-thiosemicarbazone), ZnL¹, catalyzes HER with a maximum TOF of 1170 s⁻¹, and the HOR in the presence of triethylamine with a maximum TOF of 72 s⁻¹. Unlike many prior homogeneous catalysts that rely on oxidation state changes of transition metals associated with the generation of a metal-hydride intermediate, the non-

transition metal Zn(II) is redox inactive, requiring redox processes to be mediated by the ligand. Results of that work indicate a ligand-centered process involving a binuclear transition state with evolution of H₂ via ligand hydride-proton coupling. Notably, the free ligand H₂L¹ also demonstrates similar HER activity. In addition to homogeneous catalysis, transition metal-free HER electrocatalysts have been reported in heterogeneous systems, based on N-doped graphene (NG) with graphitic-carbon nitride (G-C₃N₄),¹⁰⁰ as well as metal-free and zinc-phthalocyanines.¹⁰¹⁻¹⁰⁶ Furthermore, a heterogeneous metal-free frustrated Lewis pair¹⁰⁷ HOR electrocatalyst has been reported and is proposed to operate via a hydride intermediate, similar to Ni^{13,108} and Fe^{86,109} homogeneous HOR catalysts.

Clearly, the use of redox non-innocent ligands provides a variety of new and versatile tools that can be used to control reactivity of transition metal complexes. The principal of non-innocent ligands are rapidly being applied to HER and HOR electrocatalysis, leading to the pursuit of new catalysts for small molecule activation where reactivity occurs exclusively on the ligand. This type of reactivity leads to mechanisms for hydrogen evolution or oxidation in which the H—H bond is either split or formed in either a ligand-centered homolytic fashion through the coupling of two H[•] radicals, or in a ligand-centered heterolytic fashion via recombination of H⁺ and H⁻. The study of these two types of ligand-centered catalysis for HER and HOR will be presented in the following chapters of this dissertation.

CHAPTER II: EXPERIMENTAL DETAILS

2.1. Materials and Physical Methods

All chemicals were purchased from commercial sources (Aldrich, VWR Chemicals, TCI, Acros, Alfa Aesar) and used without purification unless noted otherwise stated. AgPF_6 was obtained from Aldrich and stored in an argon filled dry box. The ligand, LH, and the ReL_3 and $[\text{ReL}_3 \cdot \text{C}_2\text{H}_4][\text{PF}_6]_2$ metal complexes were synthesized by the modification as described below.¹¹⁰ The H_2L ligand and the CuL^1 and ZnL^1 and metal complex were made according to published literature methods^{111,112} as described below. All solvents were purified with an MBraun solvent purification system or prepared (methanol) utilizing standard methods and were freshly distilled immediately before use.¹¹³ All reactions were performed under anaerobic conditions via standard Schlenk line techniques unless otherwise noted. X-ray crystallography was conducted by Dr. Mark Mashuta at the University of Louisville's X-ray diffraction. X-ray crystallographic data were collected on a Bruker SMART APEX CCD diffractometer. CCDC-1403507 and 1410091 contains the supplementary crystallographic data for this dissertation. Data can be obtained free of charge from The Cambridge Crystallographic Data Center via www.ccdc.cam.ac.uk/data_request.cif.

2.2. Crystallographic Details

A purple prism $0.27 \times 0.27 \times 0.12 \text{ mm}^3$ crystal of $[\text{Re}(\text{LH})\text{L}_2]\text{PF}_6$ was mounted on a glass fiber for collection of x-ray data on an Agilent Technologies Gemini CCD diffractometer. The CrysAlis PRO (CCD)5 software package (v 1.171.36.28) was used to acquire a total of 562 thirty-second frame ω -scan exposures of data at $100.0(1) \text{ K}$ to a $2\theta \text{ max} = 56.20^\circ$ using monochromated $\text{MoK} \alpha$ radiation (0.71073 \AA) from a sealed tube. Frame data were processed using CrysAlis PRO (RED)5 (v 1.171.34.36) to determine final unit cell

parameters: $a = 9.59553(9) \text{ \AA}$, $b = 33.0018(3) \text{ \AA}$, $c = 15.41951(15) \text{ \AA}$, $\alpha = 90^\circ$, $\beta = 97.5416(10)^\circ$, $\gamma = 90^\circ$, $V = 4840.66(8) \text{ \AA}^3$, $D_{\text{calc}} = 1.663 \text{ Mg/m}^3$, $Z = 4$ to produce raw hkl data that were then corrected for absorption (transmission min./max. = 0.743/1.00; $\mu = 2.834 \text{ mm}^{-1}$) using SCALE3 ABSPACK. The structure was solved by Patterson methods in the space group $P 2_1/c$ using SHELXS-907 and refined by least squares methods on F2 using SHELXL-977 incorporated into the SHELXTL8 (v 6.14) suite of programs. All non-hydrogen atoms were refined anisotropically. The H atom bonded to S3 was located in difference maps; its geometric parameters were refined with $U(\text{H}) = 1.2 \times U_{\text{eq}}$ (attached S atom). Phenyl hydrogen atoms were placed in their geometrically generated positions and refined as a riding model that were included as fixed contributions with $U(\text{H}) = 1.2 \times U_{\text{eq}}$ (attached C atom). For 13,986 unique reflections ($R(\text{int}) 0.0281$) the final anisotropic full matrix least-squares refinement on F2 for 598 variables converged at $R_1 = 0.033$ and $wR_2 = 0.078$ with a GOF of 1.09.

Preparation of $[\text{Re}(\text{LH})\text{L}_2]\text{PF}_6$ Crystal:

$[\text{Re}(\text{LH})\text{L}_2]\text{PF}_6$ crystals were prepared as follows: A 7.5mg sample of $[\text{ReL}_3 \cdot \text{C}_2\text{H}_4][\text{PF}_6]_2$ was placed in a test tube and 1 mL of dry methanol was added via syringe to yield a burgundy red solution. The sample was sealed with a rubber stopper secured with copper wire. After thirteen days, dark purple crystals of $[\text{Re}(\text{LH})\text{L}_2]\text{PF}_6$ were obtained. Crystallographic data can be obtained free of charge from The Cambridge Crystallographic Data Center (CCDC 1403507).

Preparation of $[\text{Re}(\text{LH})\text{L}_2]\text{O}_3\text{SCF}_3$ Crystal:

$[\text{Re}(\text{LH})\text{L}_2]\text{O}_3\text{SCF}_3$ crystals were prepared as follows: A 3 mM solution of ReL_3 in dry degassed chlorobenzene was sealed in a vacuum/flame dried test tube and under a

hydrogen atmosphere with 7 μL of triflic acid. The solution was carefully layered with dry, degassed cyclohexane. After ten days dark purple crystals of $[\text{Re}(\text{LH})\text{L}_2]\text{O}_3\text{SCF}_3$ were obtained. Crystallographic data can be obtained free of charge from The Cambridge Crystallographic Data Center (CCDC 1410091).

2.3. Chemical Synthesis

(2-diphenylphosphinobenzenethiol), (LH): Benzenethiol (6.6 mL, 7 g, 0.064 mol) was added dropwise slowly to n-butyllithium solvent (57 mL, 0.142 mol) and N, N, N', N'-tetramethylethylenediamine (22 mL, 0.14 mol) in 100 mL (0.142 mol) in cyclohexane at room temperature under nitrogen atmosphere. The reaction mixture was heated to 70°C for four hours under reflux, it was filtered and then the precipitate was washed with hexane (100 mL). Tetrahydrofuran (100 mL) in acetone dry ice bath at -78°C dissolved the resultant lithium precipitate (lithium 2-lithiobenzenethiolate). Chlorodiphenylphosphine (8.41 mL, 0.045 mol) was then added dropwise to the THF solution in at 0° C over 2 hours. The mixture was stirred for 24 hours at room temperature. The reaction mixture, diphenylphosphine 2-lithiobenzenethiolate, was quenched with aqueous hydrochloric acid (30 mL HCl and 170 mL distilled water) and dried in vacuo. Distilled water (150 mL) and 300 mL diethyl ether was then added. The water layer was extracted with ether (3X). The ether layer was then dried with MgSO_4 and then the ether was using an external trap to give the indicated products (2-diphenylphosphinobenzenethiol). Yield: 1.208 g. ^1H NMR (CD_2Cl_2): (ppm) = 7.3-6.7 (14H, m), 4.00 (1H, SH). ^{31}P NMR (CD_2Cl_2) (ppm) = -11.73.

[tris(2-diphenylphosphinobenzenethiolato)rhenium(III)], (ReL_3): 0.11 g (0.036 mmol) LH (2-diphenylphosphinobenzenethiol) in 0.7 mL triethylamine was added to 0.1

g (0.12 mmol) $[\text{ReOCl}_3 (\text{PPh}_3)_2]$ in methanol (25 mL). The mixture was heated and stirred under reflux for 30 minutes. The precipitate was filtered under gravity. The burgundy product was washed with ethanol and diethyl ether and dried in vacuo. Yield: 75 % (0.096 g, 0.09 mmol). The square wave voltammetry showed events at 427 mV, -357 mV and -1600 mV vs Fc^+/Fc .

[(ethane-1,2-diylbis((thio-2,1-phenylene)diphenylphosphine)]-(2-

diphenylphosphinobenzenethiolato)rhenium(III)) hexafluorophosphate,

($[\text{ReL}_3 \cdot \text{C}_2\text{H}_4][\text{PF}_6]_2$): To a burgundy solution of ReL_3 (30 mg, 28 μmol) in $\text{C}_6\text{H}_5\text{Cl}$ (5 mL) was added AgPF_6 (14 mg, 56 μmol). The resulting solution was bubbled with ethylene during which an orange color developed. The mixture was then filtered through cotton wool to remove Ag (s). Within 10 minutes a fine orange microcrystalline product precipitates. The $\text{C}_6\text{H}_5\text{Cl}$ was removed via cannula and the product dissolved in a mixture of CH_2Cl_2 (1.0 mL) and $\text{C}_6\text{H}_5\text{Cl}$ (0.6 mL) under an ethylene atmosphere. Slow evaporation of the solvent yields x-ray quality needles.

Diacetyl-bis(N4-methyl-3-thiosemicarbazone), (H_2L^1): 4-methylthiosemicarbazide (2.40g, 22.8 mmol) was dissolved in ethanol (50 mL) and butane-2,3-dione (1.0 mL, 11.4 mmol) and concentrated H_2SO_4 (5 drops) were added. The reaction stirred at room temperature for 16 hours. The white precipitate was filtered, rinsed with ethanol and diethyl ether. (93.0%). $^1\text{H-NMR}$ (DMSO-d_6) δ 10.23 (s, 2H) NH, 8.38 (m, 2H) NHCH_3 , 3.02 (d, 6H, $J = 4.5$ Hz) NHCH_3 , 2.20 (s, 6H) $2 \times \text{CH}_3$.

Diacetyl-bis(N4-methyl-3-thiosemicarbazonato) zinc(II), (ZnL^1): H_2L^1 (1.50 g, 5.8 mmol) was suspended in methanol (50 mL) and $\text{Zn}(\text{OAc})_2 \cdot 2\text{H}_2\text{O}$ (1.39 g, 6.3 mmol) was added. The reaction stirred at reflux for 4 hours. The yellow precipitate was filtered,

rinsed with methanol and diethyl ether. ^1H NMR (DMSO- d_6): δ / ppm 7.21 (2H, br s, CH_3NH); 2.83 and 2.81 (6H, two overlapping singlets, CH_3NH); 2.20 (6H, s, $\text{CH}_3\text{C}=\text{N}$).

Diacetyl-bis(N4-methyl-3-thiosemicarbazonato) copper(II), (CuL^1): H_2L^1 (0.50g, 1.9 mmol) was suspended in methanol (25 mL) and $\text{Cu}(\text{OAc})_2 \cdot \text{H}_2\text{O}$ (0.42g, 2.09 mmol) was added. The reaction was stirred at reflux for four hours, and the red-brown precipitate was filtered, and rinsed with methanol and diethyl ether.

Diacetyl-bis(N4-methyl-3-thiosemicarbazonato) Copper(I),

Bis(cyclopentadienyl)cobalt(III), [CuL^1]: In a the glove box, 6 μmoles (2 mg) of CuL^1 was dissolved in 2 mL DMSO- d_6 and stirred. To this was added 1 equivalent of cobaltocene (6 μmoles / 1 mg) and stirred for 15 minutes. Upon addition of cobaltocene, the solution color changes from red to purple. ^1H NMR (DMSO- d_6): δ / ppm 7.94 (1H, s, CH_3NH); 2.86 (3H, CH_3NH); 2.72 (3H, s, $\text{CH}_3\text{C}=\text{N}$).

2.4. Electrochemical Methods

Cyclic voltammetry is a technique involving sweeping the electrode potential between limits E_{initial} and E_{final} at a predetermined sweep rate or scan rate, v . Once the electrode potential reaches E_{final} , it is switched and returned to E_{initial} .^{114,115} The observed peaks in cyclic voltammetry are the result of oxidation or reduction at the electrode surface, which is known as the Nernstian diffusion layer process. As the reduction potential (E_{pc}) is reached for a system, current is produced by the reduction of the analyte.

All cyclic voltammetry (CV) and controlled potential coulometry (CPC) measurements for experiments with ReL_3 were recorded using a Par 273 potentiostat, while all cyclic voltammetry (CV) and controlled potential coulometry (CPC) measurements for experiments with H_2L^1 , ZnL^1 , and CuL^1 were recorded using a Gamry

Interface potentiostat/galvanostat. All CV experiments were performed using a glassy carbon working electrode (6.5 mm diameter, surface area = 0.07 cm²), a platinum wire counter electrode, and Ag/AgCl reference electrode. Potentials are reported versus ferrocenium/ferrocene (Fc⁺/Fc), which was measured as an internal reference for each sample. The working electrode was polished with alumina slurry prior to use. Working and counter electrodes were both cleaned before use by sonication in water, methanol, isopropanol, acetone and experimental solvent (dichloromethane/methanol/acetonitrile). All electrochemical experiments were conducted under a N₂ atmosphere (except for H₂ oxidation studies). CV measurements were conducted using a three-neck electrochemical cell that was washed and dried in oven over night before use.

CPC measurements with ReL₃ were conducted using a custom cell described previously¹¹⁶ with a volume of ~ 10 mL, which was washed and dried in oven over night before use. The working compartment was fitted with a glassy carbon working electrode (surface area = 0.07 cm²) and an Ag/AgCl reference electrode. The auxiliary compartment was fitted with a Pt wire counter electrode. The working compartment was filled with 10 mL of 0.05 M acetic acid in a 0.1 M Bu₄NPF₆ dichloromethane solution, while the auxiliary compartment was filled with 2 mL of 0.1 M Bu₄NPF₆ dichloromethane solution. Solution diffusion across the glass frit was slow under static pressure. Both compartments were purged for 15 min with N₂. A control (blank) CPC study over 6 hours resulted in a total charge accumulation of 614 μC. Electrolysis was then measured with the addition of the 0.3 mM ReL₃. Electrolysis was conducted for 6 hours and the headspace samples were subjected to gas chromatographic analysis. A Gow-Mac series 400 GC-TCD with molecular sieve column was used for product

detection. The column was heated to 130 °C under N₂ gas flow with 250 μL injection samples injected onto the column. The integrated area of the H₂ peak was then compared to the calibration curve made in order to calculate the moles of H₂ generated.

CPC measurements for experiments with ZnL¹ and CuL¹ were conducted using a two-compartment glass electrolysis cell with working and auxiliary compartments separated by a frit, with a volume of 10 mL in each, washed and dried the night before use. The working compartment was fitted with a glassy carbon working electrode and an Ag/AgCl reference electrode. The auxiliary compartment was fitted with a Pt wire counter electrode.

For CPC experiments with ZnL¹ the working compartment contained 12 mM acetic acid added to a 0.1 M Bu₄NPF₆ methanol solution, while the auxiliary compartment was filled with 0.1 M Bu₄NPF₆ methanol solution. Both compartments were purged for 15 min with N₂. A control (blank) CPC study was conducted and subtracted from experimental results. Electrolysis was then measured with the addition of the 0.1 mM ZnL, and run for 2.5 hours. Headspace samples were extracted and subjected to gas chromatographic analysis every 30 minutes. A Gow-Mac series 400 GC-TCD with molecular sieve column was used for product detection. The column was heated to 130 °C under N₂ gas flow with 250 μL injection samples injected onto the column. The integrated area of the H₂ peak was then compared to the pre-made H₂ calibration curve in order to calculate the volume and moles of H₂ generated.

For CPC experiments with CuL¹ the working compartment contained 0.226 M acetic acid added to a 0.1 M Bu₄NPF₆ acetonitrile / dimethylformamide (DMF) solution, while the auxiliary compartment was filled with 0.1 M Bu₄NPF₆ acetonitrile / DMF

solution. Both compartments were purged for 15 min with N_2 prior to electrolysis. A control (blank) CPC study was conducted and subtracted from experimental results. Electrolysis was then measured with the addition of the 0.6 mM CuL^1 and conducted various time intervals, then subjected to GC-TCD analysis at the end of the electrolysis in the same manner as described above.

Blank and control experiments were performed for ReL_3 , CuL^1 , ZnL^1 and H_2L^1 HER CV studies. Blank runs consisted of 0.1 M Bu_4NPF_6 methanol, dichloromethane, or acetonitrile, depending on experiment, which had been purged with N_2 gas for 10 minutes. Control CVs run in 0.1 M Bu_4NPF_6 methanol, dichloromethane, or acetonitrile with acetic acid showed minimal currents when compared to currents observed after addition of either CuL^1 , ZnL^1 or H_2L^1 electrocatalysts.

Blank and control experiments were performed for ReL_3 , ZnL^1 and H_2L^1 HOR CV studies. Blank runs consisted of 0.1 M Bu_4NPF_6 methanol or dichloromethane solutions, which had been purged with N_2 gas for 10 minutes. Control CVs in the absence of catalyst were performed. CVs were run under an H_2 atmosphere in solutions of 0.1 M Bu_4NPF_6 methanol with increasing concentrations of triethylamine, added until reaching base saturated concentrations. The current observed was significantly lower when compared to the current observed after the addition of the ReL_3 , ZnL^1 or H_2L^1 electrocatalysts. Additionally control experiments were performed with ReL_3 , ZnL^1 or H_2L^1 in 0.1 M Bu_4NPF_6 methanol solutions under an N_2 atmosphere. Application of an N_2 atmosphere resulted in no catalytic currents. After introduction of an H_2 atmosphere and purging the solution with H_2 for 15 minutes, catalytic current was observed.

Post electrolysis dip tests experiments were performed on the working electrode after electrolysis in 0.1 M Bu_4NPF_6 acetonitrile / DMF solutions with 0.6 mM CuL^1 with 0.292 M acetic acid added. After completion of electrolysis, the working electrode was taken from the solution and rinsed with DI water. In both DMF and acetonitrile solvents, a thin film was persisted, coving the working electrode surface. This film-covered electrode was then immersed into a fresh solution of 0.1 M Bu_4NPF_6 acetonitrile / DMF solution and CVs were recorded. Both CVs showed irreversible reductions and irreversible oxidations. Upon addition of 0.292 M acetic acid, an increase of catalytic current was observed at -1.7 V vs Fc^+/Fc , consistent with data observed from homogeneous CV experiments, and also implying that the film is an active catalyst for HER either acting dependently, independently, or in conjunction with homogenous catalysis. Efforts are currently underway to better understand this development.

2.5. Overpotential Determination and Calculations

Overpotential can be defined as the difference between the thermodynamic and equilibrium potentials for a given reaction and the potential at which the reaction occurs under a set of specific conditions. In the case of H_2 evolution or oxidation, when either the equilibrium potential for the standard state H^+/H_2 couple ($E^\circ_{\text{H}^+}$) is not known for some particular solvent or a reliable pKa scale is unavailable, the direct measurement of the equilibrium potential for the reduction of protons (E_{H^+}) can be accomplished through an open circuit potential (OCP) measurements, as described by Bullock, Appel and Helm.¹¹⁷ Using this method this method provides an accurate determination of the equilibrium potential for the H^+/H_2 couple under a wide range of acids and bases, as well as solvents or mixtures of solvents. For example, recent reports using this method have

appeared in the literature for the determination of E_{H^+} of protic ionic liquids¹¹⁸ and various acid base pairs in acetonitrile and/or water.⁸⁷ The accurate determination of overpotential requires an estimation of $E_{cat/2}$ and E_{H^+} , each of which can change, depending on the reaction conditions. The value for the potential for catalysis should be related to the catalytic current, and therefore, we use $E_{cat/2}$. This combined with a value for E_{H^+} , obtained through OCP measurements allows for calculation of the overpotential (η) for proton reduction or H_2 oxidation under specific experimental conditions. This can be estimated as: $\eta = |(E_{OCP} - E_{cat/2})|$, where E_{OCP} is the measured open circuit potential measured under catalytic conditions specific for each reaction, and $E_{cat/2}$ is the potential at one-half the maximum of the catalytic current measured for the catalyzed reduction of protons or oxidation of H_2 . (see appendix for OCP plots)

Overpotential Calculation: ReL₃ HER:

$$\eta = \text{Overpotential} = |(E_{BH^+(OCP)}) - (E_{cat/2})|$$

$$\eta = |[-0.222 \text{ V} - (-0.930 \text{ V})]|$$

$$\eta = 0.708 \text{ V vs } Fc^+/Fc$$

Overpotential Calculation; ReL₃ HOR:

$$\eta = \text{Overpotential} = |(E_{BH^+(OCP)}) - (E_{cat/2})|$$

$$\eta = |[-1.18 - (-0.210)]|$$

$$\eta = 0.970 \text{ V vs } Fc^+/Fc$$

Overpotential calculation; ZnL¹ HER:

$$\eta = \text{Overpotential} = |(E_{BH^+(OCP)}) - (E_{cat/2})|$$

$$\eta = |[-0.924 - (-1.68)]|$$

$$\eta = 0.756 \text{ V vs } Fc^+/Fc$$

Overpotential calculation; ZnL¹ HOR:

$$\eta = \text{Overpotential} = |(E_{\text{BH}^+(\text{OCP})}) - (E_{\text{cat}/2})|$$

$$\eta = |(0.190 - 0.505)|$$

$$\eta = 0.315 \text{ V vs Fc}^+/\text{Fc}$$

Overpotential calculation; H₂L¹ HER:

$$\eta = \text{Overpotential} = |(E_{\text{BH}^+(\text{OCP})}) - (E_{\text{cat}/2})|$$

$$\eta = |[-0.37 - (-1.80)]|$$

$$\eta = 1.43 \text{ V vs Fc}^+/\text{Fc}^0$$

Overpotential calculation; H₂L¹ HOR:

$$\eta = \text{Overpotential} = |(E_{\text{BH}^+(\text{OCP})}) - (E_{\text{cat}/2})|$$

$$\eta = |(0.177 - 0.505)|$$

$$\eta = 0.328 \text{ V vs Fc}^+/\text{Fc}$$

Overpotential Calculation; CuL¹ HER

$$\eta = \text{Overpotential} = |(E_{\text{BH}^+(\text{OCP})}) - (E_{\text{cat}/2})|$$

$$\eta = |[-0.50 - (-2.20 \text{ V})]|$$

$$\eta = 1.7 \text{ V vs Fc}^+/\text{Fc}^0$$

2.6. ReL₃: Determination and Calculation of Third-Order Rate Constant, *k*, from Pseudo First-Order Rate Constant *k_{obs}*, and estimation of Turnover Frequency (TOF) for H₂ Evolution and Oxidation

Calculations were performed using the method described by Dubois *et al.*⁸⁴ A summary of the methods with respect to our specific data is provided below. Equation 1 details the relationship between the catalytic current *i_c*, the catalyst concentration [*cat*], and the acid concentration [*H*⁺] for a catalytic reaction that is second-order in acid, and first-order in catalyst. The terms *n*, *F*, *A*, and *D*, are the normal electrochemical terms related to the

number of electrons transferred, Faraday's constant, area of the electrode, and diffusion constant, respectively.

$$i_{cat} = nFA[cat]\sqrt{Dk[H^+]^2} \quad (1)$$

Equation 2 (Randle-Sevcik eq.)¹¹⁴ provides the relationship between the peak current i_p , catalyst concentration, and scan rate (ν) in the absence of acid. The factor of 0.4463 is related to the diffusion equations,¹¹⁴ R is the gas constant, and T is temperature in K. The other terms are the same as in equation 1.

$$i_p = 0.4463FA[cat]\sqrt{\frac{F\nu D}{RT}} \quad (2)$$

Thus, the ratio of i_{cat}/i_p (equation 3) is obtained from equations S1 and S2

$$\frac{i_{cat}}{i_p} = \frac{n}{0.4463} \sqrt{\frac{RTk[H^+]^2}{F\nu}} \quad (3)$$

Under pseudo first-order conditions where $k_{obs} = k[H^+]^2$, equation 3 simplifies to 4.^{79,119}

$$\frac{i_{cat}}{i_p} = \frac{n}{0.4463} \sqrt{\frac{RTk_{obs}}{F\nu}} \quad (4)$$

It should be noted that from equations 3 and 4 that the ratio of i_{cat}/i_p should be directly proportional to the acid concentration at lower acid concentrations and independent of acid concentrations under pseudo first-order conditions as shown in our experimental results.

Equation 4 can be rewritten to solve for k_{obs} under scan rate independent conditions.

Using numerical values of constants at 298 K, equation 5 is obtained.

$$k_{obs} = \nu * 1.94 \left(\frac{i_{cat}}{i_p}\right)^2 \quad (5)$$

At a scan rate of 0.2 V, our currents of 149 μ A and 17 μ A for i_{cat} and i_p yield $k_{obs} = 29.8$ s⁻¹.

From equation 3, a straight line in a plot of i_{cat}/i_p versus $[H^+]$ in the acid-dependent region is indicative of a second-order dependence on acid concentration. As shown in later in chapter 3 for scan rates of 0.2, 0.5, and 1.0 V/s, respectively, our data is consistent with this interpretation.

Further, the third-order order rate constant, k , can be obtained from the scan rate dependence of the slopes of the current vs $[H^+]$ plots in order to provide a double slope plot for which the slope can be used to solve for k , described by equations 6 and 7.

$$\frac{i_{cat}}{i_p} = \frac{n}{0.4463} \sqrt{\frac{RTk}{Fv}} [H^+]^2 \quad (6)$$

$$slope = \frac{n}{0.4463} \sqrt{\frac{RTk}{Fv}} \quad (7)$$

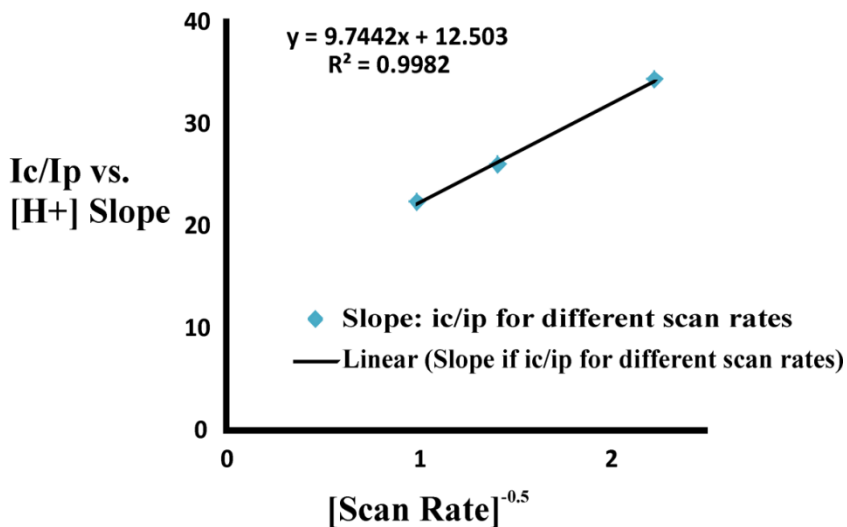


Figure 7. Double slope plot for evaluation of the third order rate constant, k .

A plot of slopes from Figures S7 – S9 versus $\sqrt{\frac{1}{v}}$ yields a linear relationship (Figure 7).

The slope of this line (the double slope) allows quantification of the third order rate constant k using equation 8 at 298K.

$$\text{double slope} = 0.72\sqrt{k} \quad (8)$$

Using our data, $k = 184 \text{ M}^{-2} \text{ s}^{-1}$.

2.7. ZnL^1 and H_2L : Determination and Calculation of TOF for H_2 Evolution and Oxidation

As stated above equation 4 is obtained by taking the ratio for catalytic current, equation 1, and peak current (equation 2).

$$\frac{i_{cat}}{i_p} = \frac{n}{0.4463} \sqrt{\frac{RTk_{obs}}{Fv}} \quad (4)$$

Equation 4 can further be simplified to equation 5 under scan rate independent conditions, when $n=1$ for bimolecular processes. An n value of 1 was used due to the bimolecular nature of the mechanism involving ZnL^1 and H_2L^1 .

$$k_{obs} = v \times \left[\frac{i_{cat}}{0.35 i_p} \right]^2 \quad (9)$$

Since no peak current for ZnL^1 was observed in the absence of substrate in methanol, the experimentally determined diffusion coefficient (described below), 1.15×10^{-7} , was used to calculate the value for i_p . This gave an i_p of $43 \mu\text{A}$ when run at 5 V/s (the scan rate in which catalytic current becomes independent of scan rate). Furthermore, the value of i_p was confirmed through simulations using DigiElch, which agree with the calculated i_p values. Using equation 5, the TOF or k_{obs} can be calculated using the experimentally determined i_p value as well as the i_{cat} observed at 5 V/s , $230 \mu\text{A}$. This results in a TOF of 1170 s^{-1} .

We then calculated the TOF using Eq. 10, which is Eq. 1 under pseudo first-order conditions, to compare both calculated values, which are in agreement with each other.

$$i_{cat} = nFA[cat]\sqrt{Dk_{obs}} \quad (10)$$

Sample Calculations ZnL¹ TOF/k_{obs}:

Using Eq. 10:

$$\begin{aligned} i_{cat} &= 230 \mu\text{A}; i_p = 43 \mu\text{A}; v = 5.0 \text{ V/s} \\ &= k_{obs} / \text{TOF} = 1170 \text{ s}^{-1} \end{aligned}$$

Using Eq. 9:

$$\begin{aligned} i_{cat} &= 230 \mu\text{A}; n = 1 \text{ mole e}^- / \text{mole of ZnL}; F = 96485 \text{ C / mol e}^-; A = \\ &0.071 \text{ cm}^2; [\text{cat}] = 3\text{E-}6 \text{ moles / cm}^3; D_{cat} = 1.15\text{E-}7 \text{ cm}^2 / \text{s}. \\ &= k_{obs} / \text{TOF} = 1100 \text{ s}^{-1} \end{aligned}$$

HOR TOF ZnL and H₂L Sample Calculation when v = 1.0 V/s:

ZnL¹:

$$\begin{aligned} \text{TOF} &= k_{obs} = v * 1.94(i_{cat}/i_p)^2 \text{ when } i_{cat} = -712 \mu\text{A} \text{ and } i_p = -117 \mu\text{A} \text{ at } 1.0 \\ &\text{V/s} \end{aligned}$$

$$\text{TOF} = 72 \text{ s}^{-1}$$

H₂L¹:

$$\begin{aligned} \text{TOF} &= k_{obs} = v * 1.94(i_{cat}/i_p)^2 \text{ when } i_{cat} = -475 \mu\text{A} \text{ and } i_p = -117 \mu\text{A} \text{ at } 1.0 \\ &\text{V/s} \end{aligned}$$

$$\text{TOF} = 32 \text{ s}^{-1}$$

2.8. CuL¹: Determination and Calculation of TOF for H₂ Evolution

Using equation 5 as described above we can calculate the estimated TOF for the CuL¹ electrocatalyst. The i_p of Cu^{II/I} reduction event, 14.0 μA , and the i_{cat} max of 2.25 mA correspond with a maximum i_{cat} / i_p value of 161, affording a TOF of 10000 s^{-1} in

acetonitrile.¹²⁰⁻¹²³ Following the same procedure for CVs run in DMF, we get a TOF of 5140 s⁻¹.

CuL¹ HER TOF Sample Calculations

TOF_{max} Sample Calculation for CuL¹ in acetonitrile:

Using equation 5, at scan-rate independent conditions, when $\nu = 0.2$ v/s and when $i_{cat} = 2250 \mu\text{A}$ and $i_p = 14 \mu\text{A}$

$$\frac{i_{cat}}{i_p} = 160.71$$

$$\text{TOF}_{\text{max}} / k_{\text{obs}} = 10000 \text{ s}^{-1}$$

TOF_{max} Sample Calculation for CuL¹ in dimethylformamide:

Using equation 5, at scan rate independent conditions, when $\nu = 1.0$ v/s, and when $i_{cat} = 1490 \mu\text{A}$ and $i_p = 29 \mu\text{A}$

$$\frac{i_{cat}}{i_p} = 51.44$$

$$\text{TOF}_{\text{max}} / k_{\text{obs}} = 5140 \text{ s}^{-1}$$

2.9. ReL₃: Quantification of H₂ from Controlled Potential Coulometry (CPC) and Calculation of Turnover Number and Faradaic Efficiency

Theoretical Moles of Hydrogen Made via Total Charge:

$$(Q_{\text{net}}) \times (1 \text{ mol e}^- / 96485 \text{ C}) \times (1 \text{ mol H}_2 / 2 \text{ mol e}^-) = \text{liberated moles H}_2$$

$$Q_{\text{net}} = Q_{\text{with cat}} - Q_{\text{w/o cat}} = 31.2202635 - 0.0002635 = 31.22 \text{ C}$$

$$(31.22) \times (1 \text{ mol e}^- / 96485 \text{ C}) \times (1 \text{ mol H}_2 / 2 \text{ mol e}^-) = 0.000162 \text{ mol}$$

H₂

$$\text{TON} = (\text{mol of H}_2 \text{ produced} / \text{mol of catalyst used})$$

$$= (0.000162 / 0.000003) = 54.0$$

% Headspace Calculation

Assumptions

1. Henry's constant (k_H) for hydrogen in dichloromethane is 0.00151 M/atm
2. Bulk electrolysis occurs in a closed, gas tight cell.

- The volume of the solution is 10.0 mL and it remains constant.
- The headspace above the reaction prior to bulk electrolysis is 1 atm of nitrogen.
- The reaction takes place at 298 K.
- Ideal gas behavior

Calculation Procedure

- Calculate moles of H₂ based on total charge at 100% Faradaic efficiency.
- Divide by the volume of the solution to obtain [H₂] in solution.
- Convert k_H to the dimensionless form k_H^{cc} by multiplying by RT.

a. $k_H = [H_2]_{sln}/P_{H_2}$

b. $P_{H_2}/RT = n_{H_2g}/V_g = [H_2]_g$

c. multiply both sides of "a": $k_H RT = RT[H_2]_{sln}/P_{H_2}$

d. combine "c" and "d": $k_H RT = [H_2]_{sln} / [H_2]_g = k_H^{cc}$

- Use k_H^{cc} to calculate equilibrium [H₂]_g assuming an initial [H₂]_g = 0 and initial [H₂]_{sln} from step 2.
- Calculate the equilibrium P_{H_2} using ideal gas law and the equilibrium $[H_2]_g = n/V$.
- Calculate the total pressure as the sum of the partial pressures of N₂ and H₂.
- Calculate the % H₂ in the headspace from the values in 5 and 6.

Sample Calculation: 6 hour electrolysis

$$31.22 \text{ C} \times (\text{mol e}^-)/(96485 \text{ C}) \times (1 \text{ mol H}_2)/(2 \text{ mol e}^-) = 0.000162 \text{ moles H}_2$$

$$(0.000162 \text{ moles H}_2)/(0.010 \text{ L}) = 0.0162 \text{ M H}_2$$

$$k_H^{cc} = (0.00151 \text{ M/atm}) \times (0.08214 \text{ L atm/mol K}) \times (298 \text{ K}) = 0.03696$$

$[\text{H}_2]_{\text{sln}}$	\rightarrow	$[\text{H}_2]_{\text{g}}$
initial	0.0162	0
delta	-x	+x
final	0.0162-x	x

$$0.03696 = (0.0162 - x)/x$$

$$0.03696x = 0.0162 - x$$

$$1.03696x = 0.0162$$

$$x = [\text{H}_2]_{\text{g}} = 0.01562 \text{ M}$$

$$P_{\text{H}_2} = nRT/V = RT[\text{H}_2]_{\text{g}} = (0.08214 \text{ L atm/mol K}) \times (298 \text{ K}) \times 0.01562 \text{ M} = 0.3824 \text{ atm}$$

$$P_T = 1 + 0.3824 = 1.3824 \text{ atm}$$

$$\% \text{ H}_2 = 100 \times (0.3824/1.3824) = 27.7\%$$

Observed actual value is lower 21.8%. This indicates either 1) some H_2 escaped the cell as it was not gas tight and/or 2) Faradaic efficiency is less than 100%.

Results are consistent with a *minimum*

= Faradaic efficiency of 73%.

2.10. ZnL¹: Quantification of H_2 from CPC and Turnover Number and Faradaic Efficiency Calculations

Theoretical Moles of Hydrogen Made via Total Charge:

$$19.8 \text{ C} \times (1 \text{ mol e}^- / 96485 \text{ C}) \times (1 \text{ mol H}_2 / 2 \text{ mol e}^-) = \text{moles H}_2 \text{ theoretical}$$

$$\text{Moles H}_2 \text{ theoretical} = 0.00011 \text{ moles H}_2$$

Faradaic Efficiency Calculation:

To quantify H_2 production, the output gas was sampled, 250 μL , every 30 minutes and analyzed by the GC-TCD described in electrochemical methods section. After sampling,

the chromatographic peak area of hydrogen is obtained. The GC-TCD calibration curve was prepared by sampling known hydrogen concentrations, made with known volumes of hydrogen, from the working compartment, with a constant known N₂ flow rate, and then measured by the same procedure described above. A linear relationship between the chromatographic peak areas of the hydrogen sampled and the specific amounts of hydrogen used was established, defined by $y = mx + b$, where y is the peak area and x is the amount of hydrogen. Using this linear relationship, the amount of hydrogen produced during experimental electrolysis can be calculated from the integrated peak areas obtained.

$$\text{Faradaic Efficiency} = (\text{Moles H}_2 \text{ Quantified} / \text{Moles of H}_2 \text{ Theoretical}) \times 100\%$$

$$\text{Faradaic Efficiency} = (0.000093 \text{ moles}) / (0.00011 \text{ moles}) \times 100\%$$

$$\text{Faradaic Efficiency} = 85\%$$

TON Calculations:

$$\text{TON} = \text{Moles of H}_2 \text{ Produced} / \text{Moles of ZnL Used}$$

$$\text{TON} = (0.00011 \text{ moles H}_2 \text{ produced}) / (0.000003 \text{ moles ZnL used})$$

$$\text{TON} = 36.7$$

2.11. CuL¹: Quantification of H₂ from Controlled Potential Coulometry and Turnover Number and Faradaic Efficiency Calculations

Sample Calculations CuL¹ Electrolysis in Acetonitrile:

$$\begin{aligned} \text{Trial 1: Total charge} &= Q_{\text{with cat}} - Q_{\text{blank}} = Q_{\text{net}} \\ 60.49 \text{ C} - 0.0576 \text{ C} &= 60.43 \end{aligned}$$

Theoretical Moles of Hydrogen Made via Total Charge:

$$60.43 \text{ C} \times (1 \text{ mol e}^- / 96485 \text{ C}) \times (1 \text{ mol H}_2 / 2 \text{ mol e}^-) = \text{moles H}_2 \text{ theoretical}$$

Moles H₂ theoretical = 0.00031 moles H₂ based on charge from electrolysis

Trial 1: CuL¹ TON Calculation:

$$\text{TON} = \text{Moles of H}_2 \text{ Produced} / \text{Moles of CuL}^1 \text{ Used}$$

$$\text{TON} = (0.00031 \text{ moles H}_2 \text{ produced}) / (0.000006 \text{ moles CuL}^1 \text{ used})$$

$$\text{TON} = 51.7$$

Trial 2: Total Charge = Q_{with cat} - Q_{blank} = Q_{net}

$$84.74 \text{ C} - 0.0576 \text{ C} = 84.68$$

Theoretical moles of Hydrogen made via Total Charge

$$84.68 \text{ C} \times (1 \text{ mol e}^- / 96485 \text{ C}) \times (1 \text{ mol H}_2 / 2 \text{ mol e}^-) = \text{moles H}_2 \text{ theoretical}$$

Moles H₂ Theoretical = 0.00044 moles H₂ based on charge from electrolysis

Trial 2: CuL¹ TON Calculation:

$$\text{TON} = \text{Moles of H}_2 \text{ Produced} / \text{Moles of CuL}^1 \text{ Used}$$

$$\text{TON} = (0.00044 \text{ moles of H}_2 \text{ produced}) / (0.000006 \text{ moles CuL}^1 \text{ used})$$

$$\text{TON} = 73.3$$

Sample Calculations CuL¹ Electrolysis in DMF

Trial 1: Total charge = Q_{with cat} - Q_{blank} = Q_{net}

$$67.03 \text{ C} - 0.0682 \text{ C} = 66.96 \text{ C}$$

Theoretical Moles of Hydrogen made via total Charge:

$$66.96 \times (1 \text{ mol e}^- / 96485 \text{ C}) \times (1 \text{ mol H}_2 / 2 \text{ mol e}^-) = \text{moles of H}_2 \text{ theoretical}$$

Moles H₂ Theoretical = 0.00035 moles H₂ based on charge from electrolysis

Trial 1: CuL¹ TON Calculation:

$$\text{TON} = \text{Moles of H}_2 \text{ Produced} / \text{Moles of CuL}^1 \text{ Used}$$

$$\text{TON} = (0.00035 \text{ moles of H}_2 \text{ produced}) / (0.000006 \text{ moles CuL}^1$$

used)

$$\text{TON} = 58.3$$

Trial 2: Total Charge = Q_{with cat} - Q_{blank} = Q_{net}

$$85.06 \text{ C} - 0.682 \text{ C} = 85 \text{ C}$$

Theoretical Moles of Hydrogen made via total Charge:

$$85 \times (1 \text{ mol e}^- / 96485 \text{ C}) \times (1 \text{ mol H}_2 / 2 \text{ mol e}^-) = \text{moles of H}_2 \text{ theoretical}$$

Moles H₂ Theoretical = 0.00044 moles H₂ based on charge from electrolysis

Trial 2: CuL¹ TON Calculation:

$$\text{TON} = \text{Moles of H}_2 \text{ Produced} / \text{Moles of CuL}^1 \text{ Used}$$

$$\text{TON} = (0.00044 \text{ moles of H}_2 \text{ produced}) / (0.000006 \text{ moles CuL}^1 \text{ used})$$

$$\text{TON} = 73.3$$

Trial 2: CuL¹ Faradaic Efficiency Calculation:

$$\text{Faradaic efficiency} = (\text{moles of H}_2 \text{ quantified}) / (\text{moles of H}_2 \text{ theoretical based on charge}) \times 100\%$$

$$= (0.00038 \text{ moles}) / (0.00044 \text{ moles}) \times 100\%$$

$$= 86 \% \text{ Faradaic Efficiency}$$

Faradaic Efficiency Determination: Evolved gas from the cathode compartment displaced water in a cylinder with radius 1.12 cm by a height of 2.16 cm. Using the equation for the volume of a cylinder, $V = \pi(r)^2h$, we can calculate the volume displaced. This is calculated to be 8.513 mL. Using the conversion factor of 22.4 L of any ideal gas per one mole of gas allows us to quantify the number of moles of H₂ evolved as 3.8×10^{-4} moles. This value can then be compared to the theoretical number of moles of H₂ evolved based on charge determined earlier, 4.4×10^{-4} . Faradaic efficiency is defined as moles of H₂ quantified/moles of H₂ theoretical based on charge x 100%. This corresponds with a 86% Faradaic efficiency.

2.12. Determination and Calculation of Diffusion Coefficients, D₀, for ZnL¹ and CuL¹

CV data were collected at multiple scan rates from 0.1 to 1.0 V/s establishing that reduction is diffusion limited. Using the Randles-Sevcik equation (Eq. 2) and plotting peak current vs the square root of the scan rate allows for accurate calculation of the diffusion coefficient, D₀.

Determination of ZnL¹ Diffusion Coefficient (D₀):

$$\text{Slope (Figure 24B)} \equiv 1.94\text{E-}5 = 0.4463FA[\text{cat}][(\text{FD}_0/\text{RT})]^{0.5}$$

$$A = 0.071 \text{ cm}^2$$

$$[\text{cat}] = 3\text{E-}6 \text{ moles/cm}^3$$

$$F = 96485 \text{ C/mole e}^-$$

R = ideal gas constant

$$T = 298 \text{ K}$$

$$D_0 = 1.15 \times 10^{-7} \text{ cm}^2/\text{s in MeOH for ZnL}^1$$

Determination of CuL¹ Diffusion Coefficient (D₀):

$$\text{Slope (Figure 40 inset)} \equiv 3.22\text{E-}5 =$$

$$0.4463FA[\text{cat}][(\text{FD}_0/\text{RT})]^{0.5}$$

$$A = 0.071 \text{ cm}^2$$

$$[\text{cat}] = 6\text{E-}7 \text{ moles/cm}^3$$

$$F = 96485 \text{ C/mole e}^-$$

R = ideal gas constant

$$T = 298 \text{ K}$$

$$D_0 = 2.3 \times 10^{-5} \text{ cm}^2/\text{s in acetonitrile for CuL}^1$$

2.13. Kinetic Isotope Effect Calculations

ReL₃

Using equation (5) we can calculate k_{obs} for experiments using D-acetic acid and D-triflic acid.

D-Acetic Acid: At a scan rate of 0.2 V/s, $i_{cat} = 63.17 \mu\text{A}$ and $i_p = 22.48 \mu\text{A}$ giving a $k_{obs} = 3.06 \text{ s}^{-1}$.

$$\text{KIE} = k_H/k_D = 29.8 \text{ s}^{-1} / 3.06 \text{ s}^{-1} = 10$$

D-Triflic Acid: At a scan rate of 0.2 V/s, $i_{cat} = 115 \mu\text{A}$ and $i_p = 38 \mu\text{A}$ giving a $k_{obs} = 3.55 \text{ s}^{-1}$.

$$\text{KIE} = k_H/k_D = 29.8 \text{ s}^{-1} / 3.55 \text{ s}^{-1} = 9$$

*ZnL*¹

Following same procedure above but instead using equation (10) we can calculate KIE for *ZnL*¹ using D-acetic acid.

Scan Rate	$k_H \text{ (s}^{-1}\text{)}$	$k_D \text{ (s}^{-1}\text{)}$	$k_H / k_D \text{ (s}^{-1}\text{)}$
5 V/s	1170	975	1.2

*CuL*¹

Following same procedure above, using equation (5) we can calculate KIE for *CuL*¹ using D-acetic acid. KIE studies on *CuL*¹ were performed from 0-100% mole D-Acetic acid use. The results are summarized below.

%D-Acid	$i_{cat} \text{ (}\mu\text{A)}$	TOF (s ⁻¹)	KIE
0.00	2250	10021.68	1
20.00	1837	6680.269	1.500192
40.00	1257	3127.852	3.204015
60.00	1045	2161.764	4.635883
80.00	910	1639.3	6.113392
100.00	819	1327.833	7.547398

2.14. Digital Simulations using DigiElch

Digital simulations of voltammetric data were performed using commercially available DigiElch Pro software package (v.7) ¹²⁴. ZnL¹ models were fit using an experimentally determined ZnL¹ diffusion coefficient and fitted values of α and k_s , which were based on experimental CVs of the electrocatalysts run from 0.1 to 1.0 V/s. The consistency of the mechanism over a broad set reaction conditions was confirmed through models employing multiple scan rates and acid concentrations, all which agree with experimental results (See Appendix for additional simulation data).

2.15. Computational Methods

General Considerations

Hybrid Hartree-Fock density functional theory (hybrid DFT) has long been of great interest for computational thermochemistry, saddle point analysis, and general computational structure optimizations. One main advantage is its low computational cost with respect to *ab initio* methods. Many hybrid DFT functionals have been shown to be very promising for calculation of reaction barrier heights as well as optimization of transition state geometries.

Generally speaking, hybrid DFT involves mixing various amounts of the Hartree-Fock (HF) nonlocal exchange operator with DFT exchange correlation functionals. A few promising hybrid DFT functionals are B3LYP,¹²⁵ M06,¹²⁶ and mPW1PW91.¹²⁷ These hybrid DFT methods have been shown to be effective for obtaining accurate molecular structures, vibrational frequencies, and bond energies. The most important variable that varies in these types of functionals is the fraction of the HF exchange set. For B3LYP the HF exchange set is 20%, for mPW1PW91 it is 25% and for M06 it is 27%. Other

important parameters of functionals include local spin density approximation (LSDA), density-gradient expansion, constraint satisfaction, modeling the exchange-correlation hole, and empirical fits. The constraint satisfaction factor refers to having the correct limit for a uniform electron gas. The M06 family of functionals, in general, is better at improving this parameter, relative to first generation hybrid DFT functionals like B3LYP or BLYP. M06 also improves upon LSDA factor by including a spin density gradient and a spin kinetic energy density, in addition to local spin density. When using the term, *local*, this means that there has been replacement of a small fraction of the local density-functional exchange by *exactly computed exchange*.¹²⁸ Hybrid functionals allow one to use density functional algorithms,¹²⁹⁻¹³⁷ and plane wave algorithms¹³⁸ which require much less computation when compared to the best algorithms for nonlocal functionals.

ReL₃

All reported calculations were performed in the gas phase using Density Functional Theory (DFT) employing the M06 exchange correlation functional¹²⁶ and the LANL2DZ basis set for all atoms as implemented in the Gaussian09 suite of programs.¹³⁹ LANL2DZ was chosen rather than 6-311g(d) due to it being a double zeta basis. Contrary to minimum basis where there are only enough functions used to contain the electrons of the neutral atoms (usually core plus valence orbitals), a double zeta (DZ) basis double the number of all basis functions. For example consider hydrogen with two 1s functions, *1s* and *1s'*. 1s and 1s' can be thought of as inner and outer functions. The inner function has a larger zeta, ζ , and is therefore tighter. The outer function has a smaller ζ , and is therefore more diffuse. This enables DZ basis sets to be more computationally flexible when describing charge distribution in both parts of a molecule (the metal and the

ligand), whereas minimum basis sets do not. Other positives of DZ basis sets include doubling the number of functions. This provides a much better description of bonding in the valence region as well as improving the description of energetically important but chemically uninteresting core electrons.

Initially, the restricted formalism using a restricted Hartree-Fock (RHF) wave function was invoked, and subsequently unrestricted calculations based on an unrestricted Hartree-Fock (UHF)-type wave function were carried out for complexes with even electron counts. Furthermore, the B3LYP functional was used to obtain broken symmetry solutions.^{125,140-143} Frequency calculations were performed for all optimized stationary points to ensure they were true minima. Transition states (TS) were determined using the Berny algorithm with GEDIIS, and verified by intrinsic reaction coordinate (IRC) calculations with forward and reverse step sizes of 40. TS structures were constructed manually based on their optimized reactants and products under tight constraints, with no symmetry imposed. Chemcraft software was used for graphics visualization.¹⁴⁴

ZnL^I

All calculations were performed in the gas phase using density functional theory (DFT) employing the B97-D exchange correlation functional, and the 6-311G(d) basis set for all atoms as implemented in the Gaussian09 suite of programs for electronic structure¹⁴⁵ and ChemCraft was used for graphics visualization¹⁴⁴. Transition states were determined locally using the Berny algorithm with GEDIIS, and verified by IRC calculations with forward and reverse step sizes of 40. All optimizations were performed under tight constraints, with no symmetry imposed. Several dimeric TS structures in various

protonation states were initially investigated by DFT using the Berny algorithm for local TS optimization in the gas phase. These structures were constructed manually based on optimized reactants and products, or by modifying previously published semicarbazide dimers.¹⁴⁶ Dimers without ruptured Zn-S and Zn-N bonds were also considered, but precluded based on energetic grounds.

CuL¹

Initial calculations were performed using M06, B3LYP and B97-D.^{125,126,140-142,147} Based on energetic minima results, B97-D was chosen for use as functional for subsequent calculations. Optimizations were performed in the gas phase using density functional theory (DFT) employing the B97-D exchange correlation functional, and the 6-311G(d,p) basis set for all atoms as implemented in the Gaussian09 suite of programs for electronic structure¹⁴⁵ and ChemCraft was used for graphics visualization.¹⁴⁴ All optimizations were performed under tight constraints, with no symmetry imposed. All input coordinates are available in in the Appendix.

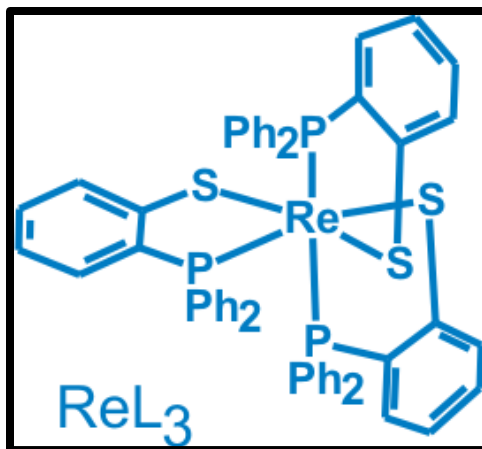
CHAPTER III:
LIGAND-CENTERED
ELECTROCATALYTIC HYDROGEN
EVOLUTION AND HYDROGEN
OXIDATION

3.1. Introduction

Hydrogen serves as a promising alternative carbon-free fuel and is an essential building block for industrial and agricultural processes. Currently, 95% of industrial H₂ derives from fossil-fuel cracking, which is environmentally unsustainable due to perpetual increases in atmospheric CO₂ levels and continual lowering of global carbon reserves.^{5,15,16} Estimates suggest a hydrogen based economy would require as much as 150 million tons of H₂ annually, further demonstrating the need for efficient electrolytic and/or photochemical catalysts that generate H₂ from carbon-free sources.⁶ As such, the development of both heterogeneous and homogeneous catalysts for hydrogen evolution reactions (HER) from water/acid for H₂ production and hydrogen oxidation reaction (HOR) catalyst for H₂ utilization have received significant attention.⁷⁻¹⁴ The energy stored within the H₂ molecule can be recovered in a fuel cell through the catalyzed oxidation of H₂ to protons (HOR); which is the reverse of a HER. The utility of H₂ as an energy storage/recovery agent has been exploited since the earliest forms of life through reactivity at the transition metal-sulfur cores of hydrogenase with H₂ evolution favored in [FeFe]-hydrogenase and H₂-oxidation preferential at [NiFe]-hydrogenase.²⁶⁻²⁸ In spite of the efficiency of these enzymes, their translation to industrial applications has been proven difficult, underscoring the need for artificial HER and HOR electrocatalysts. Platinum is the current “gold standard” because it operates at low overpotential with high turnover frequencies; however, its scarcity and high cost severely limit wide spread use.^{26-28,109} Thus, a considerable effort has been directed toward earth-abundant, first-row transition metal catalysts, including the remarkable bio-inspired pendant-base bis(diamine) nickel complexes of Dubois and Bullock.^{8,14} Furthermore, Eisenberg and Holland reported a series of metal-dithiolene complexes with the highest TOFs and

lowest overpotential of synthetic transition metal-sulfur electrocatalysts under homogeneous conditions.^{7,11,12} In addition, cobalt complexes of glyoxime ligands have been shown to be efficiently evolve H₂ at low overpotential over a wide range acid/base conditions in both aqueous and non-aqueous solvents,^{148,149} although indicate the activity may result from nanoparticles formed during catalyst degradation.¹⁵⁰ Each of these and related systems follows a metal-hydride pathway and it is widely regarded that transition metals capable of forming metal-hydride intermediates are essential to the HER mechanism. Naturally, most HER electrocatalysts reported to date closely follow a mechanism including ligand protonation, metal reduction, and proton to hydride migration with subsequent chemical/ electrochemical steps leading to H₂ release.⁸

While the metal-hydride approach has resulted in significant advances, catalyst candidates are limited to economically viable first-row transition metals complexes capable of stabilizing hydrides. Moreover, despite numerous years of effort, materials based on this paradigm have not yet yielded practical systems for wide-scale application.¹³ The development of new catalytic systems that function via a fundamentally different mechanism may prove valuable to overcome this current limitation. Given our laboratory's history^{98,151-156} with non-innocent ligands, it seemed logical to investigate ligand-centered hydrogen evolution reactivity.



Scheme 1. Stick representation of ReL_3 (L = diphenylphosphinobenzenethiolate).

The synthesis and electrochemistry of ReL_3 (L = diphenylphosphinobenzenethiolate) (scheme 1), was first reported by Dilworth *et al.* in 1992.¹⁵⁷ The electrochemistry of ReL_3 displays a reversible $\text{Re}^{\text{III/II}}$ reduction at -1.50 V and two reversible, non-innocent oxidations at -0.4 ($\text{Re}^{\text{IV/III}}$) and +0.5 V ($\text{Re}^{\text{V/IV}}$) vs Fc^+/Fc (ferrocenium/ferrocene) (Figure 8).¹⁵³

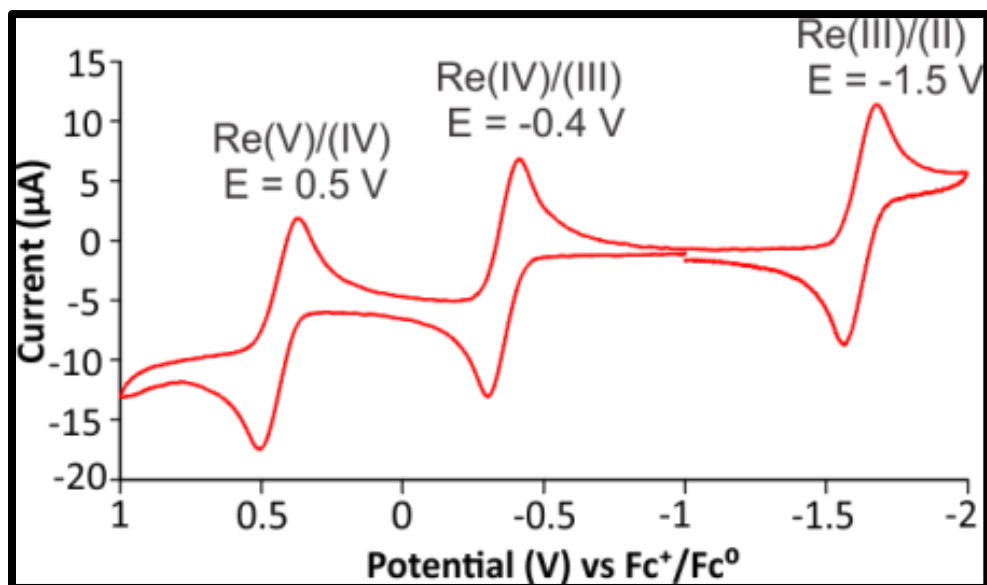


Figure 8. Cyclic Voltammogram (CV) of 0.3 mM ReL_3 in 0.1 M Bu_4NPF_6 CH_2Cl_2 solutions.

The non-innocence of the ligands is attributed to covalent metal-sulfur interactions that result in frontier molecular orbitals with significant metal-d and sulfur-p character, as also observed previously in our laboratory with the analogous ruthenium complex, RuL_3 .^{116,143,151,152,154,155,158,159} As a result, while $[\text{ReL}_3]^+$ contains a *formal* Re^{IV} , the complex has some Re^{III} -thiyl radical character and the *formal* Re^{V} of $[\text{ReL}_3]^{2+}$ has Re^{IV} -thiyl and Re^{III} -dithiyl radical character. The reactivity of this complex was previously studied for the reversible binding of ethylene.^{98,143,153,160}

Expanding upon this previous work in the Grapperhaus Lab, and given the rich literature history of HER electrocatalysis using dithiolenes, we surmised that ReL_3 could serve as an electrocatalyst for hydrogen evolution or hydrogen oxidation, dependent on the presence of acid or base and the applied potential.

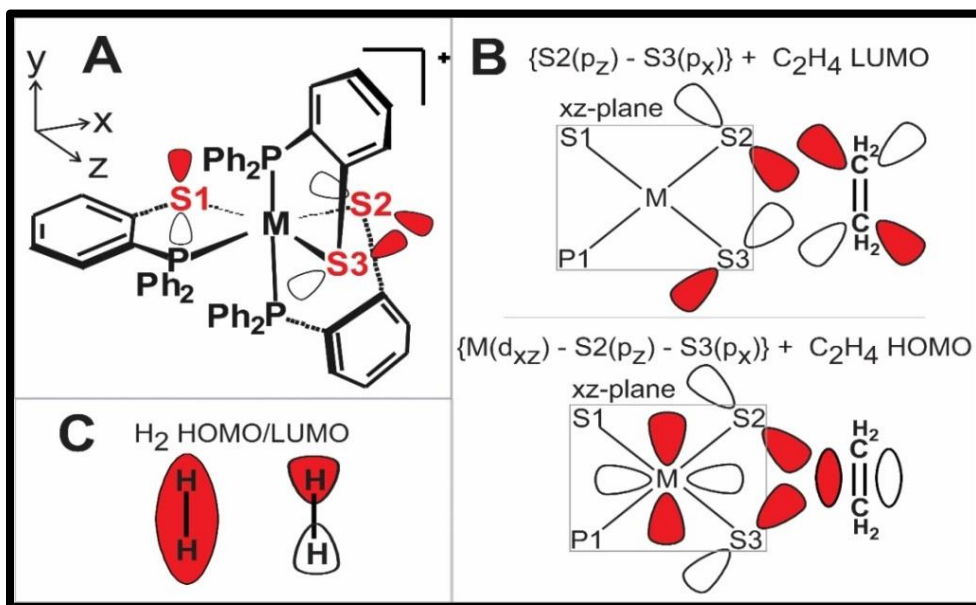


Figure 9. (A) Calculated "p-type" lone-pair orientation of $[\text{M}(\text{SP})_3]^n$ enforced by meridional PS chelates. (B) Proposed interactions of $[\text{M}(\text{SP})_3]^n$ frontier orbitals with LUMO (top) and HOMO (bottom) of C_2H_4 . (C) HOMO/LUMO symmetries of H_2 .

A combination of characteristics makes metal-thiolates an excellent HER first-sphere promoter. Employing two lone pairs, metal-thiolates will easily accept protons under even moderately acidic conditions. Dithiolenes are well-known to exhibit non-innocent redox behavior, affording ligand-centered reductions and oxidations.^{11,12,143,153,161} This ligand non-innocence offers extremely reactive thiyl radicals. As detailed in (Figure 9A) the facial arrangement of the PS chelates in $[\text{ReL}_3]^n$ enforces a symmetry preferred *interligand* addition route.^{143,153} The lone-pair p-type orbitals on S1 and S2 are coplanar, and the frontier molecular orbitals include an occupied out-of-phase combination supporting the necessary geometry needed to interact with the π^* -orbital of alkenes, and a vacant in-phase combination, which is anti-bonding with respect to the metal d-orbital, providing the proper symmetry to interact with the π orbital of alkenes, or in the case of H_2 , the σ orbital.¹⁴³ When examining the HOMO/LUMO molecular frontier orbitals of H_2 (Figure 9C) we observe the same analogous frontier orbital arrangement as that seen in the HOMO/LUMO of ethylene (Figure 9B) which suggests similar interactions with H_2 and ethylene.

3.2. Results and Discussion

3.2.1. Cyclic Voltammetry HER and HOR Studies and X-ray Crystallography

Upon addition of acetic acid to CH_2Cl_2 solutions of ReL_3 the cathodic current at -1.70 V vs Fc^+/Fc increases, indicative of electrocatalytic reduction (Figure 10). Two new peaks appear 0.18 V and -0.84 V, respectively. These values are shifted by + 0.52 and + 0.76 V relative to $[\text{ReL}_3]^{+/0}$ and $[\text{ReL}_3]^{0/-}$, respectively, suggesting protonation of a single thiolate donor.

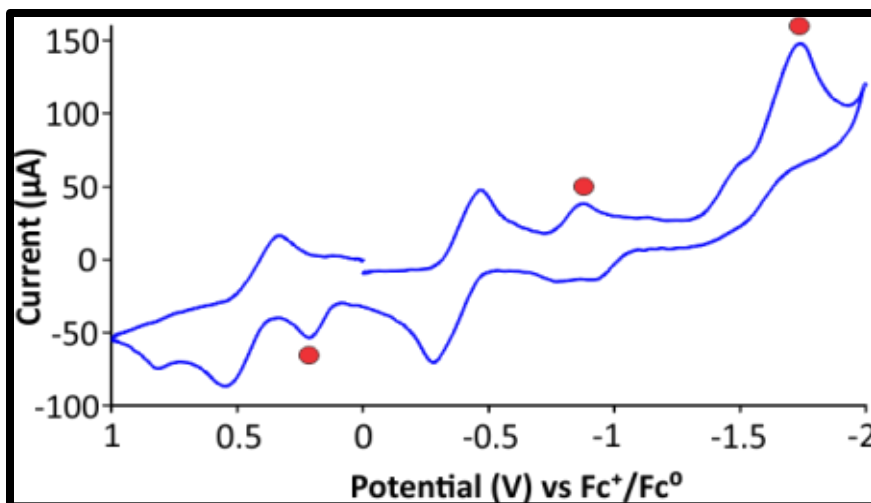


Figure 10. CV of ReL_3 with excess $\text{CH}_3\text{CO}_2\text{H}$ added in 0.1 M Bu_4NPF_6 CH_2Cl_2 solution.

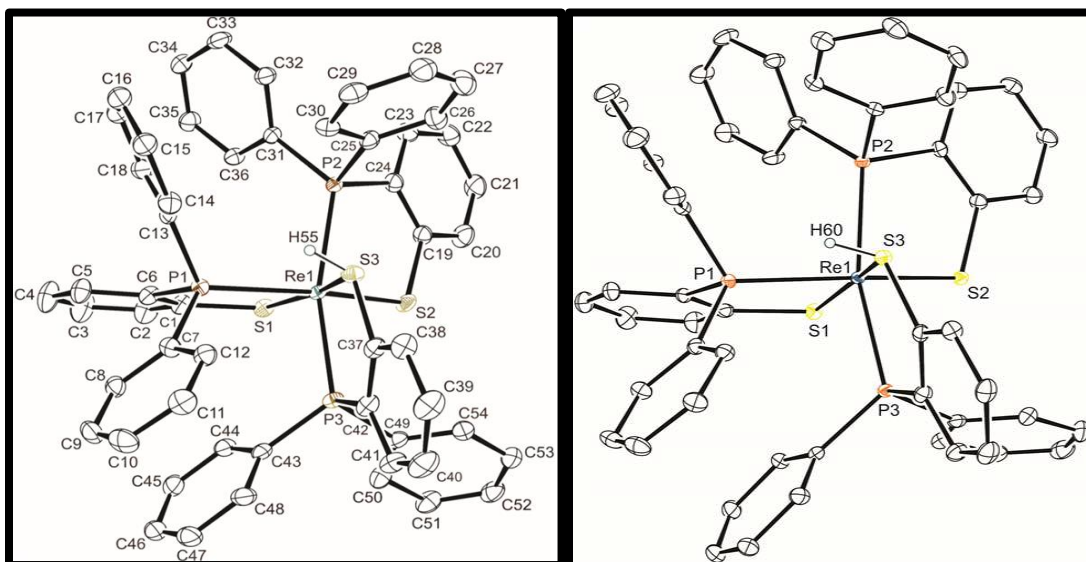


Figure 11. (Left) Labeled ORTEP¹⁶² of $[\text{Re}(\text{LH})\text{L}_2]^+$ from $[\text{Re}(\text{LH})\text{L}_2]\text{PF}_6$. (Right) Labeled ORTEP¹⁶² of $[\text{Re}(\text{LH})\text{L}_2]^+$ from $[\text{Re}(\text{LH})\text{L}_2]\text{O}_3\text{SCF}_3$.

In order to confirm the identity of the new peaks, attempts were made to isolate and crystallize the protonated intermediate, $[\text{Re}(\text{LH})\text{L}_2]^+$. High quality single crystals of $[\text{Re}(\text{LH})\text{L}_2]\text{PF}_6$, obtained as a degradation product of $[\text{ReL}_3 \cdot \text{C}_2\text{H}_4]\text{PF}_6$ in methanol, reveal S3 as thiol through the location and subsequent refinement of the proton H55 (Figure 11 left). The S3-H55 bond distance is 1.077(18) Å with a Re1-S3-H55 bond

angle of 105.8(18)°. The structure was confirmed by X-ray analysis of $[\text{Re}(\text{LH})\text{L}_2]^+$ as the triflate salt prepared upon protonation of ReL_3 with triflic acid (Figure 11 right). A comparison of metric parameters for ReL_3 , $[\text{Re}(\text{LH})\text{L}_2]^+$, and $[\text{ReL}_3\cdot\text{C}_2\text{H}_4]^{2+}$ is provided in Table 1 below.^{98,157} The metal ligand bond distances of the $[\text{Re}(\text{LH})\text{L}_2]^+$ cation in the structures of $[\text{Re}(\text{LH})\text{L}_2]\text{PF}_6$ and $[\text{Re}(\text{LH})\text{L}_2]\text{O}_3\text{SCF}_3$ are consistent. The corresponding Ru-P bond distances differ by 0.011(1) to 0.014(1) Å while the corresponding Ru-S bond distances are statistically equivalent. The S3-H bond distance of $[\text{Re}(\text{LH})\text{L}_2]\text{PF}_6$ is 0.076(26) Å longer in than $[\text{Re}(\text{LH})\text{L}_2]\text{O}_3\text{SCF}_3$, which is a small change compared to the relative error. The Re-S bond distances in ReL_3 , $[\text{Re}(\text{LH})\text{L}_2]^+$, and $[\text{ReL}_3\cdot\text{C}_2\text{H}_4]^{2+}$ reveal a common trend upon sulfur-modification. Conversion of S3 from an anionic thiolate in ReL_3 to a neutral thiol in $[\text{Re}(\text{LH})\text{L}_2]^+$ increases the Re-S3 bond by 0.018(5) Å, whereas the bond distances to the remaining thiolates contract by 0.120(5) and 0.014(5) Å for Re-S1 and Re-S2, respectively. The same compensatory effect is observed, but to a larger degree, in the ethylene adduct $[\text{ReL}_3\cdot\text{C}_2\text{H}_4]^{2+}$. Conversion of S2 and S3 from anionic thiolates to neutral thioethers increases bond distances by 0.131(6) and 0.163(6) Å, respectively. The bond distance to the sole remaining thiolate, S1, decreases by 0.268(6) Å. Addition of strong acids to solutions of $[\text{Re}(\text{LH})\text{L}_2]^+$ results in a color change from purple to yellow-brown, although we have not yet been able to isolate $[\text{ReL}_3\cdot\text{H}_2]^{2+}$ or its reduced derivatives.

Table 1. Comparison of selected bond distances and bond angles between ReL_3 , $[\text{Re}(\text{LH})\text{L}_2]\text{PF}_6$, $[\text{Re}(\text{LH})\text{L}_2]\text{O}_3\text{SCF}_3$ and, $[\text{ReL}_3\cdot\text{C}_2\text{H}_4][\text{PF}_6]_2$.^a

Bond distances (Å°)	ReL_3^a	$[\text{Re}(\text{LH})\text{L}_2]\text{PF}_6$	$[\text{Re}(\text{LH})\text{L}_2]\text{O}_3\text{SCF}_3$	$[\text{ReL}_3\cdot\text{C}_2\text{H}_4][\text{PF}_6]_2$^b
Re-P1	2.473(5)	2.4976(6)	2.4836(8)	2.420(3)
Re-P2	2.411(5)	2.4493(6)	2.4480(8)	2.457(3)
Re-P3	2.391(5)	2.4419(6)	2.4308(8)	2.467(3)

Re-S1	2.477(5)	2.3575(6)	2.3547(8)	2.209(3)
Re-S2	2.303(5)	2.2884(6)	2.2855(8)	2.434(3)
Re-S3	2.269(5)	2.2875(6)	2.2917(7)	2.432(3)
S3-H55		1.077(18)	1.001(19)	
S2-C55				1.857(10)
S3-C56				1.831(10)
Bond Angles (°)				
S(1)-Re(1)-S(3)	166.4(1)	168.17(2)	166.53(3)	169.97(9)
P(1)-Re(1)-S(2)	159.6(1)	162.63(2)	163.23(3)	174.00(9)
P(2)-Re(1)-P(3)	166.7(1)	164.48(2)	164.85(3)	162.68(9)
S(3)-Re(1)-S(2)	113.0(2)	109.95(2)	108.54(3)	84.37(10)
S(2)-C(55)-C(56)				112.3(7)
a) Data from reference 149 with relabeling of atomic positions for consistency.				
b) Data from reference 90.				

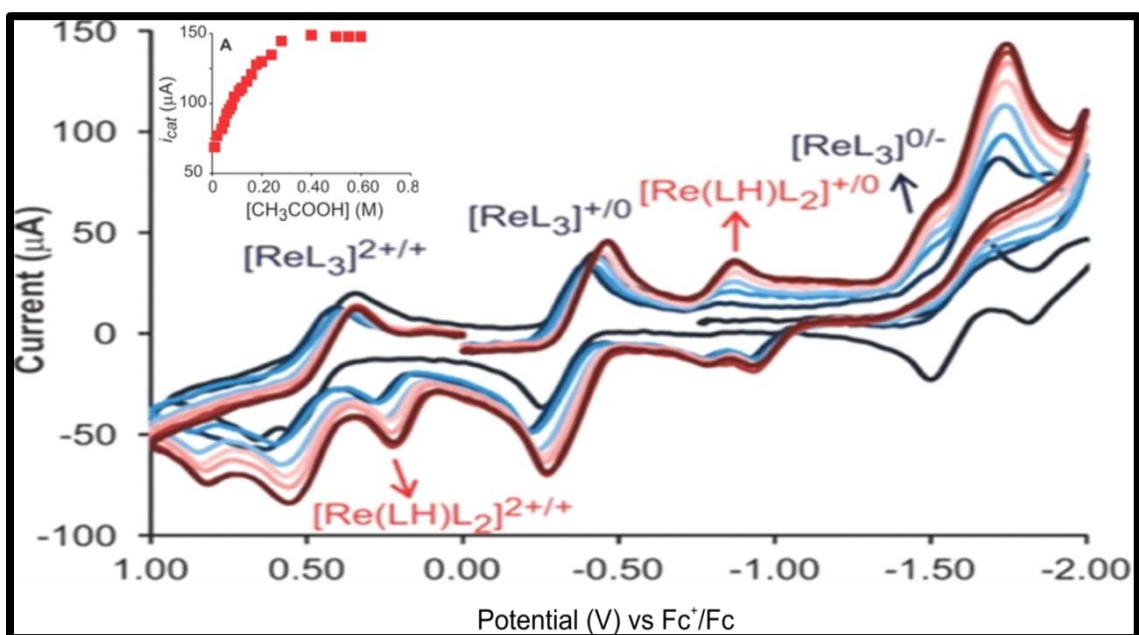


Figure 12. Cyclic Voltammograms of 0.3 mM ReL_3 in 0.1 M Bu_4NPF_6 CH_2Cl_2 solution showing H_2 evolution upon successive additions of $\text{CH}_3\text{CO}_2\text{H}$. Inset: Plot of catalytic current vs $\text{CH}_3\text{CO}_2\text{H}$ concentration, showing acid saturation above 0.4 M $\text{CH}_3\text{CO}_2\text{H}$.

CVs obtained during titration of $\text{CH}_3\text{CO}_2\text{H}$ into 0.1 M Bu_4NPF_6 CH_2Cl_2 solutions of 0.3 mM ReL_3 display a gradual growth in the intensity of the catalytic current at -1.7 V vs Fc^+/Fc (Figure 12) (see appendix for additional data). At low acid concentrations, the current displays a linear dependence on the acid concentration, indicating diffusion control to the electrode surface. At acid concentrations above 0.4 M, the current is acid-independent indicating the solution is acid saturated, and that CV response is no longer limited by diffusion (Figure 12;inset).^{121,163-165} Under these pseudo-first order conditions, the turnover frequency (TOF), which is also the observed rate constant, is $30 \pm 4 \text{ s}^{-1}$. Hydrogen evolution using sulfuric acid as the H^+ source yields a statistically equivalent TOF of $32 \pm 3 \text{ s}^{-1}$. The overpotential for hydrogen evolution is 0.708 V with either acid source, based on open circuit potential measurements (Figure 13).¹¹⁷

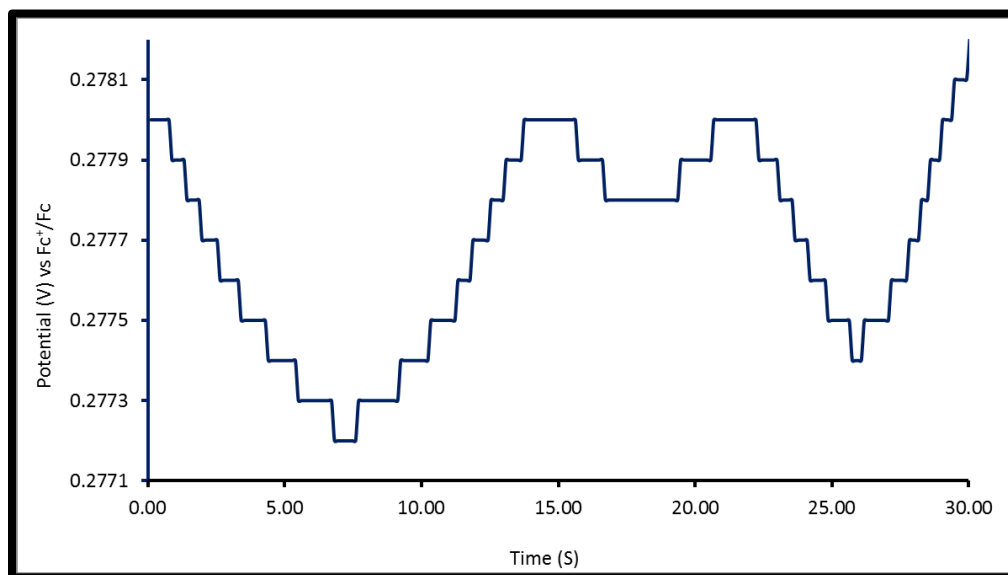


Figure 13. Open circuit potential for the reduction of protons to acetic to H_2 with 0.4 M CH_3COOH added to 0.1 M Bu_4NPF_6 CH_2Cl_2 solution.

A series of controls were performed to confirm that the electrocatalyst ReL_3 was indeed responsible for catalysis. Acetic acid (0.4 M) was added to a 0.1 M Bu_4NPF_6

CH₂Cl₂ solution without any added catalyst. CVs display that the reduction of acetic acid occurs with an onset potential of -1.9 V vs Fc⁺/Fc, giving values far below those observed upon the addition of ReL₃. A subsequent *dip-test* control was performed in order to eliminate the possibility of catalyst decomposition or deposition on the electrode surface as source of possible catalysis. Prolonged reduction of ReL₃ was performed by holding an applied potential of -2.0 V vs Fc⁺/Fc. The electrodes were then removed from the solutions rinsed with DI water and then immersed into a fresh solution containing no catalyst, upon which no current was observed, thus eliminating the possibility of decomposition or absorption onto the electrode surface.

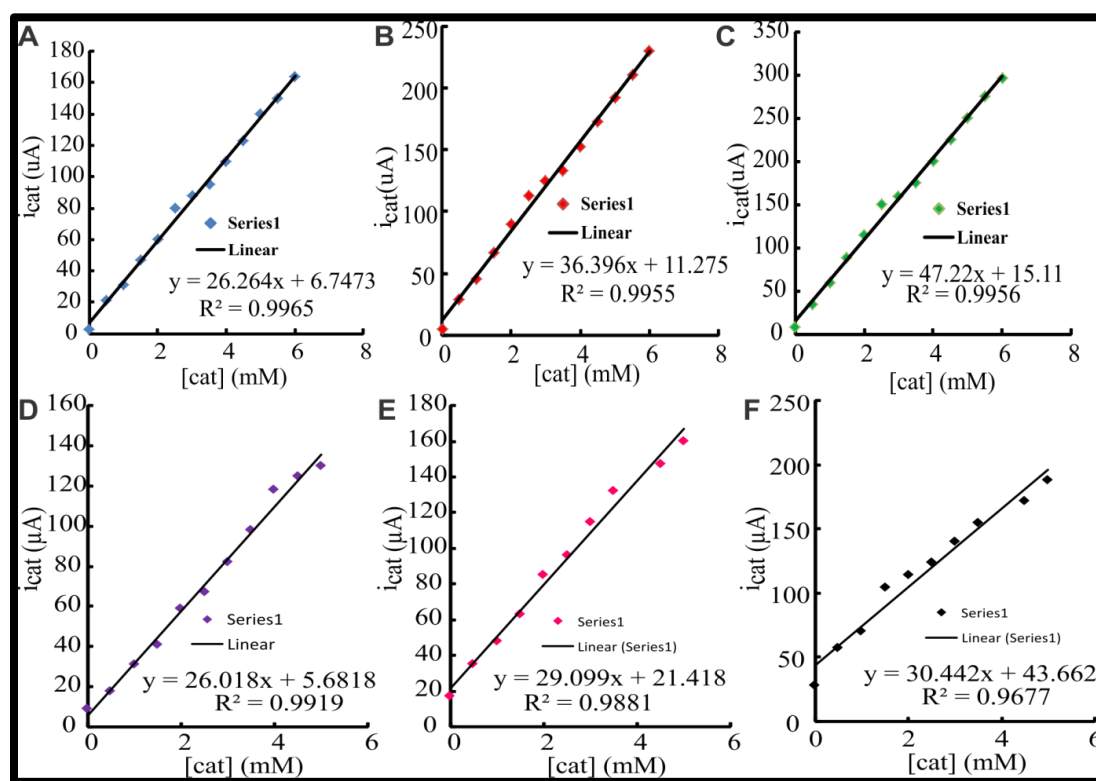


Figure 14. Peak Current vs. [ReL₃] using weak acid (CH₃CO₂H) at (A) 0.2, (B) 0.5, (C) 1 V/s, and using strong acid (H₂SO₄) at (D) 0.2 (E) 0.5, (F) 1.0 V/s.

In order to determine the order of the reaction with respect to catalyst concentration, CVs were run at scan rates of 0.2, 0.5 and 1.0 V/s at fixed [H⁺] (20 mM

for both strong and weak acids) under varied concentrations of ReL_3 . The peak currents from each CV were recorded and plotted against the concentration of the ReL_3 electrocatalyst. Plots for both strong and weak acids across all scan rates display a linear correlation between peak current and catalyst concentration, indicating a first-order dependence on the concentration of catalyst (Figure 14A-F). Overall, the rate law for H_2 evolution is third-order with a rate constant $k = 184 \text{ M}^{-2} \text{ s}^{-1}$ (see Chapter II for more information on calculation of k).

In addition to electrocatalytic hydrogen evolution, ReL_3 also catalyzes H_2 oxidation. Addition of triethylamine to ReL_3 under 1 atmosphere of H_2 increases anodic current near the formal $\text{Re}^{\text{V/IV}}$ couple (Figure 15). At concentrations above 0.8 mM, the catalytic current is base-independent and a TOF of $4 \pm 1 \text{ s}^{-1}$ was determined at an overpotential of 970 mV (see appendix for more information).^{86,117,166} Control experiments with triethylamine/ H_2 , but no ReL_3 , show no significant current.

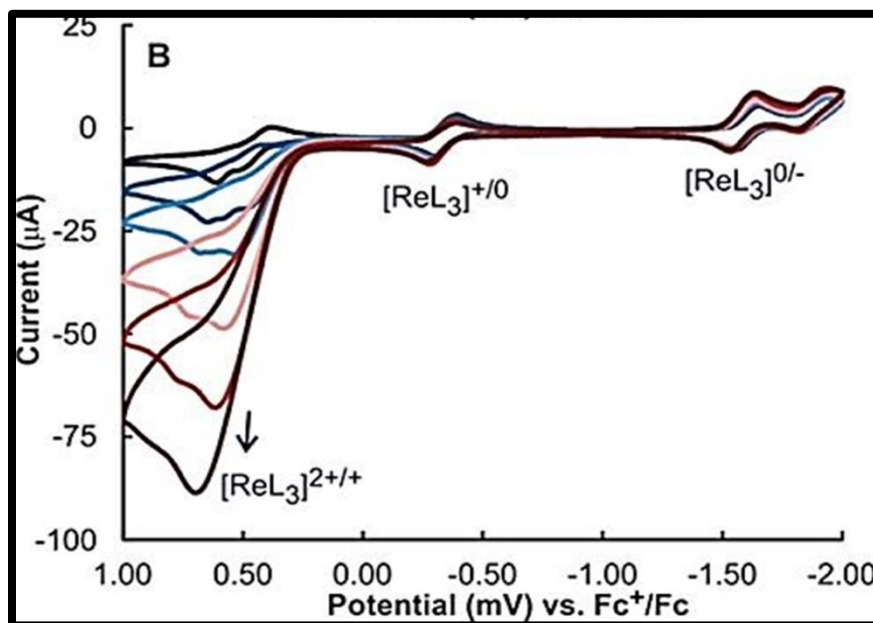


Figure 15. CV showing H_2 oxidation upon successive additions of triethylamine to 0.3 mM ReL_3 in 0.1 M Bu_4NPF_6 CH_2Cl_2 solution under 1 atm of H_2 gas.

3.2.2. Controlled Potential Coulometry and Gas Product Analysis

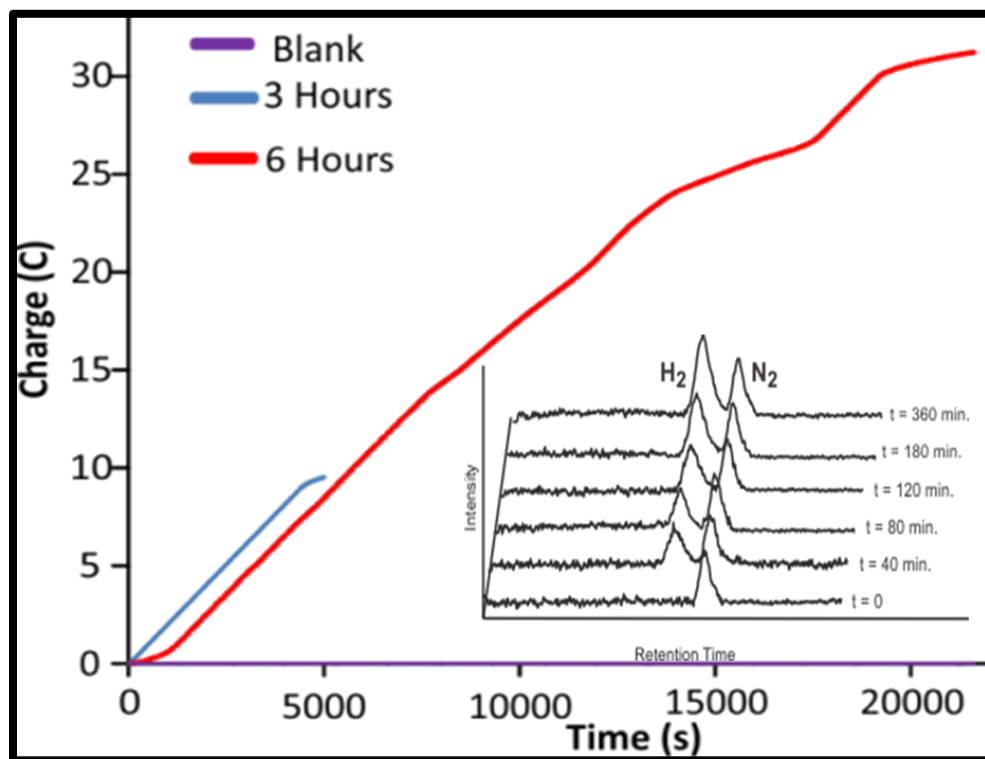


Figure 16. Plot of charge vs time recorded during the controlled potential coulometry of 0.3 mM ReL_3 for 1.5 hours (blue) and 6 hours (red) in the presence of $\text{CH}_3\text{CO}_2\text{H}$. Inset: Gas chromatography thermal conductivity (GC-TCD) readout of headspace analysis during electrolysis.

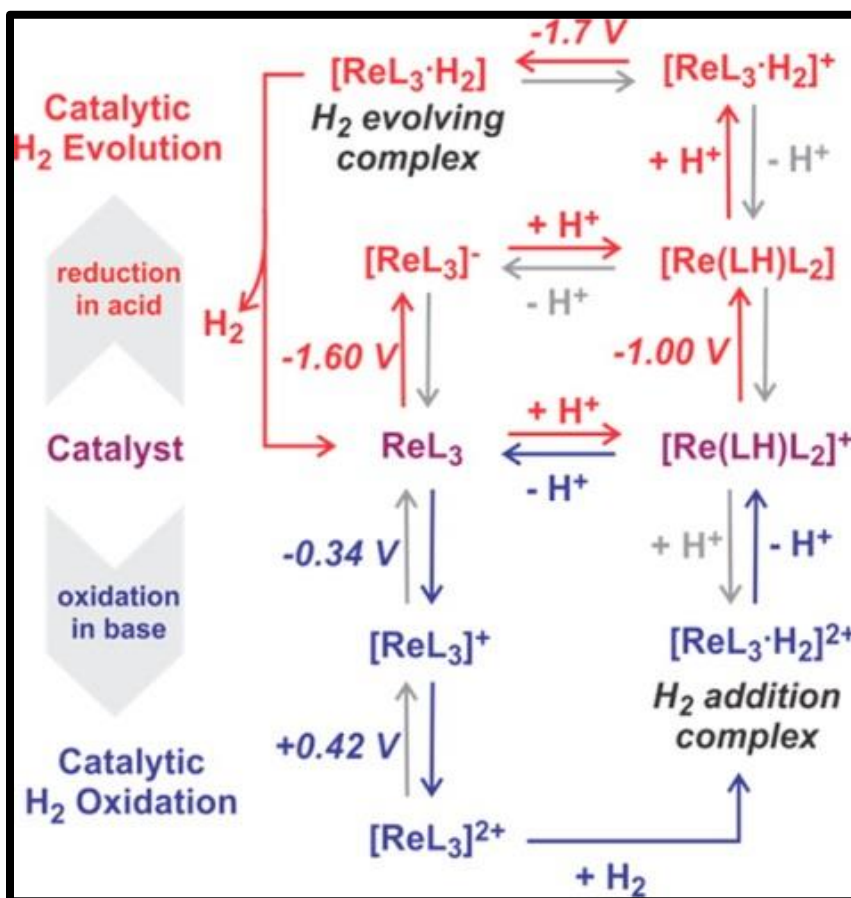
The robustness of the catalyst was evaluated by controlled potential coulometry bulk electrolysis experiments. At an applied potential of $-1.8\text{ V vs Fc}^+/\text{Fc}$, ReL_3 catalytically evolved H_2 from 0.1 M Bu_4NPF_6 CH_2Cl_2 solutions containing 0.05 M acetic acid, with turnover numbers (TON) of 13.6 and 54.0 after 1.5 and 6 h, respectively (Figure 16). Under these conditions, the TOF remains at $\sim 9\text{ h}^{-1}$ with no significant decrease in HER activity over 6 h. The gas evolved during electrolysis was confirmed as H_2 by gas chromatography analysis of headspace (Figure 16 inset). After 6 h, the headspace consisted of 22% H_2 indicating a minimum Faradaic efficiency of 73%, although the

actual value may be higher as some H₂ escaped during electrolysis (see appendix for more information).

3.2.3. Deuterated Acid Studies

The ReL₃ complex catalyzes H₂ evolution approximately 8 times faster than it catalyzes H₂ oxidation. The TOF for H₂ evolution is statistically equivalent for weak and strong acids, suggesting the two pathways share a common rate-determining step (RDS). Further information into the RDS was obtained by performing catalysis using deuterated acid substrates. The ReL₃ catalyst exhibits a large kinetic isotope effect (KIE) of 9 ± 1 for both weak and strong acids, CH₃CO₂H/ CD₃CO₂D and CF₃SO₃H/CF₃SO₃D. The similarities of the KIE values for strong and weak acids further support a common RDS, in which evolution of H₂ does not involve reaction with a proton, given that KIE values are statistically equivalent when using strong or weak acid. The large value of the KIE further suggests the rate determining step is H₂ release with significant catalyst-hydrogen bond breaking occurring at the transition state. Despite the significant number of electrocatalysts reported for HERs, relatively few studies have reported KIE data. Gray and coworkers reported an inverse KIE with values ranging from 0.54–0.57.¹⁶⁷ A similar inverse value observed by Fukuzumi was attributed to rate-determining metal hydride formation via proton coupled electron transfer.¹⁶⁸ The relatively high KIE values for ReL₃ as compared to the inverse KIE observed for metal hydrides by Gray *et al.*, clearly indicate a different mechanism for H₂ evolution. Markedly, Fukuzumi recently reported a KIE of 40 for H₂ evolution with [Ir^{III}(Cp*)(H₂O)(bpm)Ru^{II}(bpy)₂](SO₄)₂(Cp* = η⁵-pentamethylcyclopentadienyl, bpm = 2,2-bipyrimidine, bpy = 2,2'-bipyridine) attributing the unusually high KIE to large tunneling effects during catalytic H₂ evolution

reactions.¹⁶⁹ Overall, the rate law for hydrogen evolution is third-order with a rate constant $k = 184 \text{ M}^{-2} \text{ s}^{-1}$. The rate constant is approximately 200 times lower than the corresponding value for the Mo–S dimer metal thiolate, $k = 3.7 \times 10^4 \text{ M}^{-2} \text{ s}^{-1}$, reported by Dubois.⁷⁹



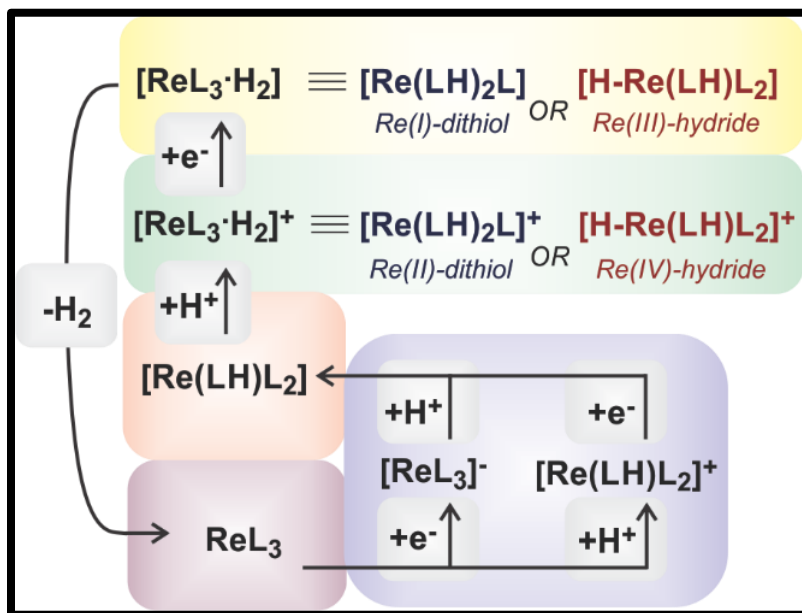
Scheme 2. Proposed Mechanism for Electrocatalytic H₂ evolution and oxidation by ReL₃.

3.2.4. Mechanism Discussion and Theoretical Insight

Based on kinetic studies and the unusually large KIE values observed with ReL₃, we initially assigned the rate-determining step for H₂ evolution as H₂ release from the H₂ evolving intermediate [ReL₃·H₂], Scheme 2. The cyclic voltammetry studies clearly demonstrate that both electrons must be delivered prior to the H₂ evolution step. We can discount a catalytic route involving a single reduction prior to H₂ release (via [ReL₃·H₂]⁺)

since this route proceeds through the monothiol complex $[\text{Re}(\text{LH})\text{L}_2]^+$, which is reduced at potentials significantly more positive than the catalytic event. As shown in Figure 12, under catalytic conditions the cyclic voltammogram contains redox events associated with $[\text{ReL}_3]^n$ and $[\text{Re}(\text{LH})\text{L}_2]^n$, in addition to the catalytic event. Potentials associated with $[\text{Re}(\text{LH})\text{L}_2]^{2+/+}$ and $[\text{Re}(\text{LH})\text{L}_2]^{+/0}$ are observed at 0.18 and -0.84 V, respectively. These values are shifted by $+0.52$ and $+0.76$ V relative to $[\text{ReL}_3]^{+/0}$ and $[\text{ReL}_3]^{0/-}$, respectively, consistent with protonation of a single thiolate donor, as previously described.^{170,171}

While reduction of $[\text{ReL}_3 \cdot \text{H}_2]^+$ is the final step of hydrogen evolution, hydrogen oxidation proceeds through sequential oxidations followed by H_2 addition. Oxidation of ReL_3 by two electrons in the presence of H_2 generates the hydrogen addition complex, $[\text{ReL}_3 \cdot \text{H}_2]^{2+}$. Stepwise deprotonation with two equivalents of triethylamine regenerates ReL_3 via $[\text{Re}(\text{LH})\text{L}_2]^+$, Scheme 2 bottom.



Scheme 3. Proposed Mechanism of H_2 Evolution by ReL_3 .

In order to elucidate the mechanism of hydrogen evolution by ReL_3 , DFT calculations were performed. The electronic and geometric properties of all complexes of the proposed mechanism in Scheme 3 were explored along with location of their transition states for H_2 evolution pathways. Complexes with an even number of electrons (ReL_3 , $[\text{Re}(\text{LH})\text{L}_2]^+$, $[\text{HRe}(\text{LH})\text{L}_2]$ and $[\text{Re}(\text{LH})_2\text{L}]$) were considered in both the singlet ($S = 0$) and triplet ($S = 1$) ground states for both closed-shell and open-shell configurations. All odd electron complexes ($[\text{ReL}_3]^-$, $[\text{Re}(\text{LH})\text{L}_2]^0$, and $[\text{Re}(\text{LH})_2\text{L}]^+$) were calculated as doublets ($S = 1/2$). Intermediates formed upon the addition of one proton were evaluated with protonation at S3, consistent with previous x-ray crystallographic studies.¹⁵⁷ Addition of the second proton was examined for both ligand-based protonation at S2 and metal-based addition as the Re-hydride.

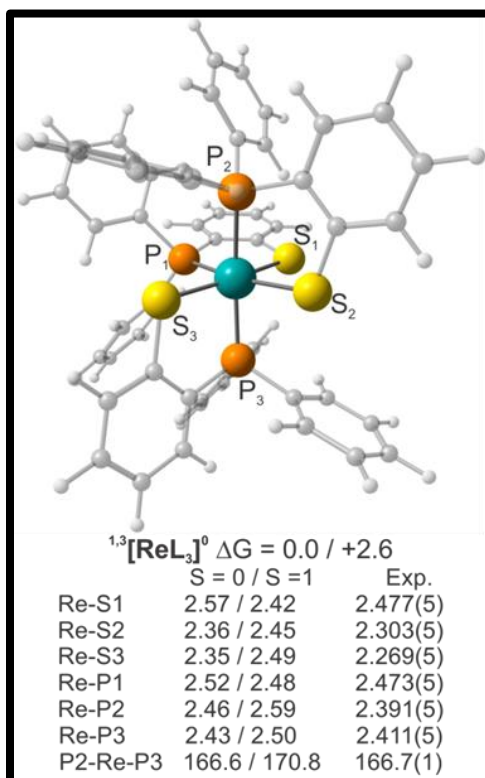


Figure 17. Bond lengths (\AA) and angles ($^\circ$) for ReL_3 from $S = 0$ and $S = 1$ DFT optimizations (M06/LANL2DZ) and the experimental (Exp.) x-ray crystal structure.¹⁵⁷ ΔG indicates relative zero-point free energy (kcal / mole) values of the $S = 0$ and $S = 1$ electronic states.

The ground state of the neutral ReL_3 complex is best described as a restricted singlet $\text{Re(III)} (d^4, S = 0)$ center bound to three thiolate ligands (Figure 17). Optimized metal-ligand bond lengths for the singlet ground state are 0.02 to 0.09 Å longer than experimental values, as typical for DFT calculations, while triplet state deviations from experimental bond lengths were larger. Furthermore, the neutral singlet species ($S = 0$) was favored over the triplet state ($S = 1$) by 2.6 kcal/mole. Due to the small difference in energy between the singlet and triplet states, attempts were made to obtain broken symmetry solution for the open-shell singlet. Calculations for the open-shell singlet were performed using the singlet geometry in combination with triplet orbitals as initial guesses. Examination of optimization steps show a decrease in the $\langle S^2 \rangle$ value moving from 2.0152 and collapsing to a final value of 0.00. This result confirms the nature of the ReL_3 complex as a closed-shell restricted singlet.

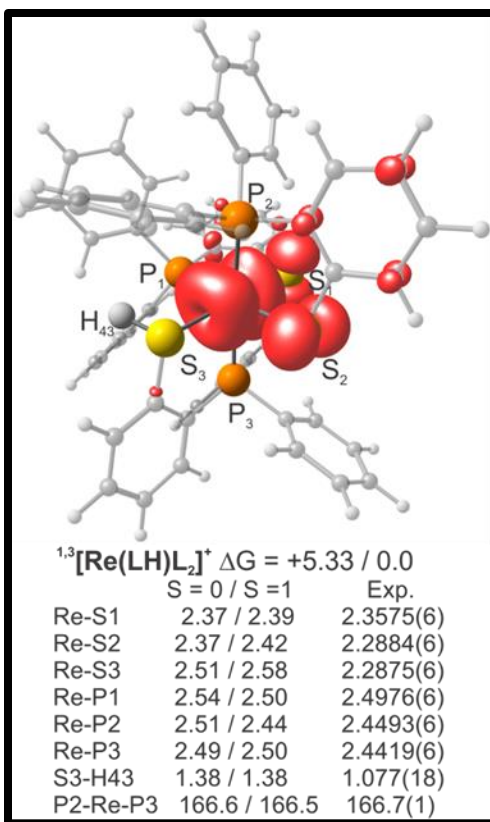


Figure 18. Bond lengths (Å) and angles (°) for $[\text{Re}(\text{LH})\text{L}_2]^+$ from S = 0 and S = 1 DFT optimizations (B3LYP/LANL2DZ) and the experimental (Exp.) x-ray crystal structure.⁹ ΔG indicates relative zero-point free energy (kcal / mole) values of the S = 0 and S = 1 electronic states.

The initial steps of the catalytic mechanism involve the transfer of one proton and one electron to ReL_3 to yield the neutral $[\text{Re}(\text{LH})\text{L}_2]$ intermediate. Prior studies indicate that either proton or electron transfer can occur first.⁹ Initial protonation at S3 yields the previously isolated and characterized $[\text{Re}(\text{LH})\text{L}_2]^+$. The $[\text{Re}(\text{LH})\text{L}_2]^+$ intermediate is best described as a Re(III) (S = 1) open-shell triplet coordinated by two non-innocent thiolate donors and one thiol donor (Figure 18). Single point energy calculations were performed as both closed-shell singlet and triplet in addition to obtaining the broken symmetry solution. Comparison of the triplet state geometric parameters reveal good agreement with the x-ray crystal structures of $[\text{Re}(\text{LH})\text{L}_2]^+$. The free energy of the triplet is also

preferred energetically, lying 5.33 kcal/mole lower than the closed-shell singlet and 3.55 kcal/mole lower than the open-shell singlet. Further examination of the $\langle S^2 \rangle$ values confirms an open-shell configuration of the triplet, yielding a final value of 2.0132, with the less energetically preferred open-shell singlet with an $\langle S^2 \rangle$ value of 0.9516.

For the double intermediates, $[\text{ReL}_3]^-$, $[\text{Re}(\text{LH})\text{L}_2]^0$ and $[\text{Re}(\text{LH})_2\text{L}]^+$, examination of the atomic spin densities (SD) reveals a propagation of ligand-centered radical character around the three S donors with each protonation step. The formal Re(II) species $[\text{ReL}_3]^-$ shows 6.5 and 6.4 % SD on the S2 and S3 donors with no significant contribution from S1 (Figure 19A). This suggests S2 and S3 have a small degree of thiyl character and can be considered “non-innocent”, while S1 is best described a thiolate. Protonation of $[\text{ReL}_3]^-$ occurs preferentially at S3 yielding $[\text{Re}(\text{LH})\text{L}_2]^0$ resulting in a notable transfer of spin-density from S3 and Re onto S1 and S2. The S1 and S2 donors are now non-innocent with 8.6 and 9.1 % SD, respectively, whereas S3 is a thiol (Figure 19B). The next step of the mechanism is the formation of $[\text{Re}(\text{LH})_2\text{L}]^+$ upon addition of the second proton. Although this may potentially occur at sulfur yielding a Re(II)-dithiol or at the metal to give a Re(IV)-hydride, only the former structure could be optimized. Protonation is favored at S2 prompting a shift of SD onto S1, which now accounts for 23.1% of the unpaired SD (Figure 19C). The electronic structure of $[\text{Re}(\text{LH})_2\text{L}]^+$ is doublet ($S = 1/2$) with a formal Re(II) center coordinated by a non-innocent thiolate (S1) and two thiols (S2 and S3).

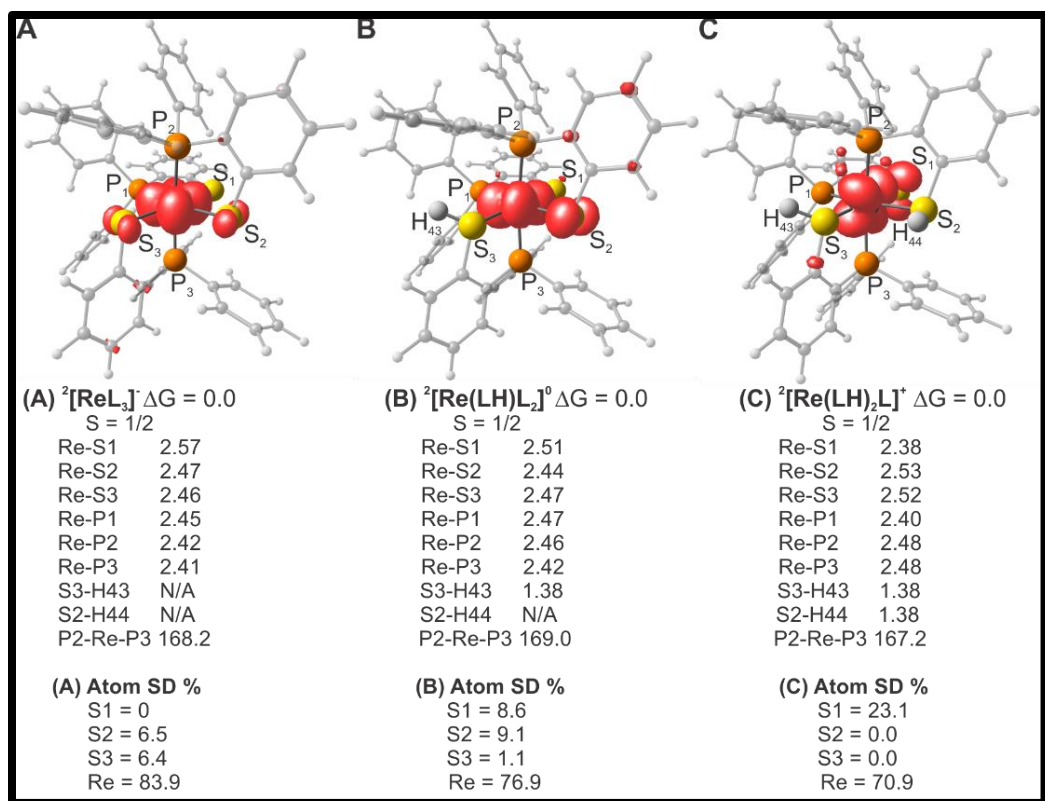


Figure 19. Bond lengths (\AA), bond angles ($^\circ$), and spin-density percentage contributions for the S = 1/2 DFT optimizations (M06/LANL2DZ) of (A) $[\text{ReL}_3]^-$, (B) $[\text{Re}(\text{LH})\text{L}_2]^0$, and (C) $[\text{Re}(\text{LH})_2\text{L}]^+$.

Propagation of spin density as a function of protonation may be seen by analyzing the geometric parameters of the doublet intermediates. The Re-S1 bond distance decreases as a function of ligand electron density, further indicating non-innocent character. The distance drops from 2.57 \AA in $[\text{ReL}_3]^-$ to 2.51 \AA in $[\text{Re}(\text{LH})\text{L}_2]^0$ after initial protonation at S3, with a further decrease to 2.38 \AA in $[\text{Re}(\text{LH})_2\text{L}]^+$ after the second protonation at S2. The Re-S2 bond distance decrease upon protonation at S3 is consistent with an increased SD, which further increases when S2 is protonated. The Re-S3 bond distance shows an increase with each protonation step.

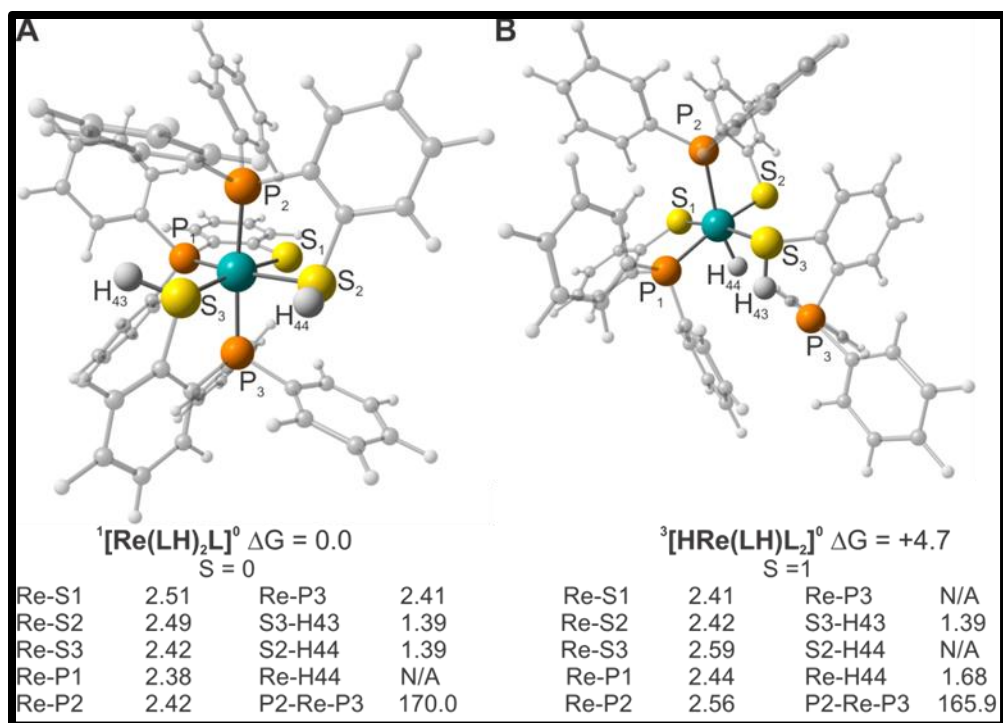


Figure 20. Bond lengths (Å) and angles (°) for optimizations (M06/LANL2DZ) of (A) $[\text{Re}(\text{LH})_2\text{L}]^0$ ($S = 0$) DFT and (B) $[\text{HRe}(\text{LH})\text{L}_2]^0$ ($S = 1$), and (c) $[\text{Re}(\text{LH})_2\text{L}]^+$. ΔG indicates relative zero-point free energy (kcal / mole) values of the $S = 0$ and $S = 1$ electronic states (see appendix for analysis of the singlet $[\text{HRe}(\text{LH})\text{L}_2]^0$ species).

The final step of the HER mechanism is the addition of a second electron to yield the hydrogen evolving complex $\text{ReL}_3 \cdot \text{H}_2$, which can be represented as either a Re(I)-dithiol or a Re(III)-hydride. The electronic and geometric parameters of the Re(I)-dithiol, $[\text{Re}(\text{LH})_2\text{L}]$, were examined in the singlet ($S = 0$), as well as the triplet ($S = 1$) states, however with only successful optimization of the singlet electronic state. The electronic and geometric parameters of the Re(III)-hydride, $[\text{HRe}(\text{LH})\text{L}_2]$, was examined as a singlet ($S = 0$) and triplet ($S = 1$) with the triplet being 2.03 kcal/mole lower in energy than the singlet (see Appendix for more information). The singlet Re(I)-dithiol ($S = 0$) configuration is favored over the triplet Re(III)-hydride ($S = 1$) by 4.7 kcal/mol (Figure 20). This energy gap is sufficiently small, and it should be noted that $[\text{HRe}(\text{LH})\text{L}_2]$

cannot completely be excluded as the H₂-evolving complex based solely on single point energy calculations.

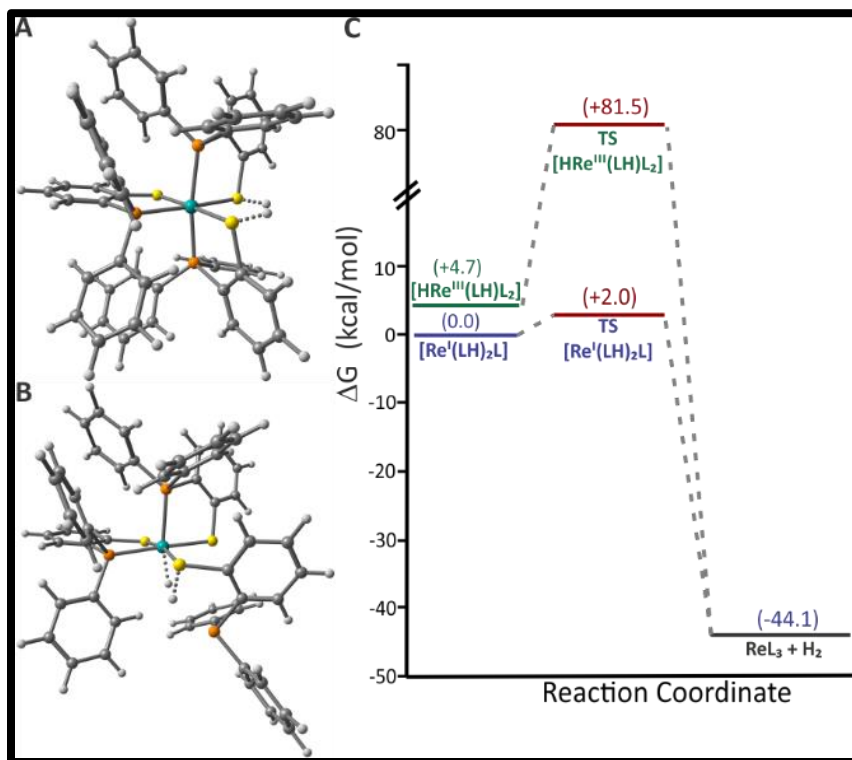


Figure 21. Transition states and energy profile for HER through Re-dithiol and Re-hydride pathways. **(A)** Representation of TS-[Re(LH)₂L] showing lengthening of two S-H bonds associated with H₂ evolution. **(B)** Representation of TS-[HRe(LH)L₂] showing H₂ evolution from Re-H and S-H. **(C)** Comparison of relative energies (ZPE corrected) for Re-dithiol and Re-hydride HER pathways using M06/LANL2DZ.

To unequivocally resolve the electronic structure of the H₂-evolving complex, transition states (TS) for reaction pathways were located for both [Re(LH)₂L] (Figure 21A) and [HRe(LH)L₂] (Figure 21B). The traditional metal-hydride [HRe(LH)L₂] pathway proceeding through TS-[HRe(LH)L₂] requires an insurmountable 81.5 kcal / mole barrier. In contrast, ligand-centered H₂ evolution along the [Re(LH)₂L] pathway proceeds through TS-[Re(LH)₂L] over a modest barrier of 2 kcal / mole (Figure 21C), represented by the imaginary frequency $i1113\text{ cm}^{-1}$. The S-H bond lengths in TS-

[Re(LH)₂L], 1.524 and 1.532 Å, are 0.125 – 0.133 Å longer than the respective equilibrium bond lengths, 1.399 and 1.399 Å in [Re(LH)₂L]. This may be attributed to a transfer of charge densities from the formal Re(I) to the thiol sulfurs moving forward along the intrinsic reaction coordinate (IRC), initiating the release of two H-atoms that couple to form hydrogen (Figure 22ABCD). The IRC analysis is consistent with a ligand-centered H₂ evolution pathway best described as homolytic cleavage of two cis-coordinated metal thiol S-H bonds.

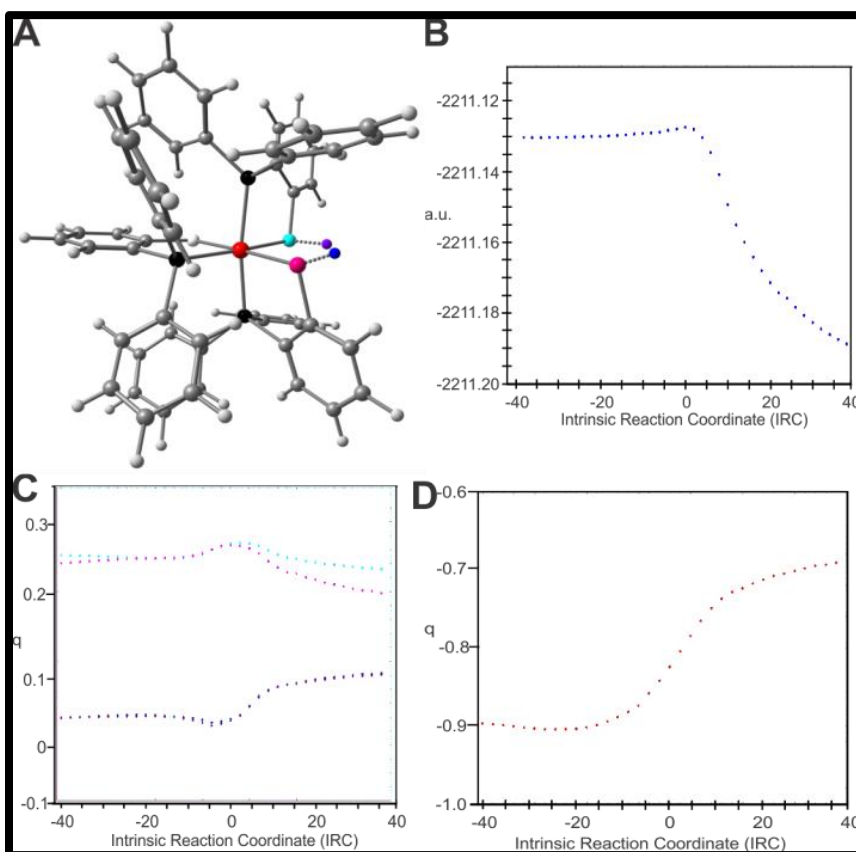


Figure 22. (A) Transition state geometry of [Re(LH)₂L₂] along the HER pathway, shown with active S-H bond dissociations and Re atom associated with the imaginary frequency, $i1113\text{ cm}^{-1}$. (B) Transition State Analysis of H₂ Evolving Complex [Re(LH)₂L]. Internal reaction coordinates (IRC) moving through the TS for [Re(LH)₂L] associated with the imaginary frequency $i1113\text{ cm}^{-1}$. (C) Charge densities of sulfur and hydrogen atoms near H₂ evolution for [Re(LH)₂L] along the HER pathway with respect to IRC, associated with the imaginary frequency $i1113\text{ cm}^{-1}$, S3 / S4 (cyan, magenta) and H5 / H105 (blue, purple). Transition State S-H bond lengths = 1.524 Å and 1.532 Å. (D) Charge densities of the Rhenium atom near H₂ evolution with respect to IRC, associated with the imaginary frequency $i1113\text{ cm}^{-1}$, Re1 (red).

3.3. Conclusion

Homogeneous electrochemical studies were performed to assess ReL_3 as an electrocatalyst for H_2 evolution and oxidation.⁹ Electrochemical studies show that ReL_3 reduces acid in CH_2Cl_2 to H_2 with an overpotential of 0.708 V and a turnover frequency of $32 \pm 3 \text{ s}^{-1}$ via a unimolecular mechanism. Additionally, ReL_3 oxidizes H_2 in the presence of base at an overpotential of 0.970 V with a turnover frequency of $4 \pm 1 \text{ s}^{-1}$. To our knowledge this is one of four published electrocatalysts which can perform both the HER and HOR reaction. Furthermore, it was the first ligand-centered HER/HOR electrocatalyst reported. The HER mechanism is supported by DFT, including location of the transition state and intrinsic reaction coordinate analysis, identifying the H_2 evolving complex as a Re-dithiol that generates H_2 through a radical coupling mechanism. The process involves homolytic S-H bond cleavage with no formation of metal-hydride intermediates. The results represent the first example of a ligand-centered HER mechanism to be validated through a rigorous combination of digital simulations of voltammetric data, DFT optimizations and spin-density analyses of all catalytically relevant metal complexes, location of the transition state and analysis of intrinsic reaction coordinates by computational methods.

While unprecedented in homogeneous mononuclear systems, Yan *et al.* recently reported heterogeneous H_2 evolution from MoS_2 proposing exposed unsaturated S edge atoms as reaction sites.¹⁷² The unique reactivity of ReL_3 could be attributed to a sterically crowded, kinetically inert, and coordinatively saturated metal center that prevents facile formation of metal hydride, which is proposed for other active metal-sulfur catalysts. While this would normally be expected to render a complex inactive, the noninnocent ligands in ReL_3 are known to react with small molecule substrates in a ligand-centered

pathway. This could explain the unusual KIE and bifunctional (H_2 evolution and H_2 oxidation) activity of ReL_3 . Nonetheless, this work represents a valuable jumping off point into the field of strictly ligand-centered catalysis, and the lessons learned will undoubtedly be pivotal in the future design of other small molecule activation catalysts.

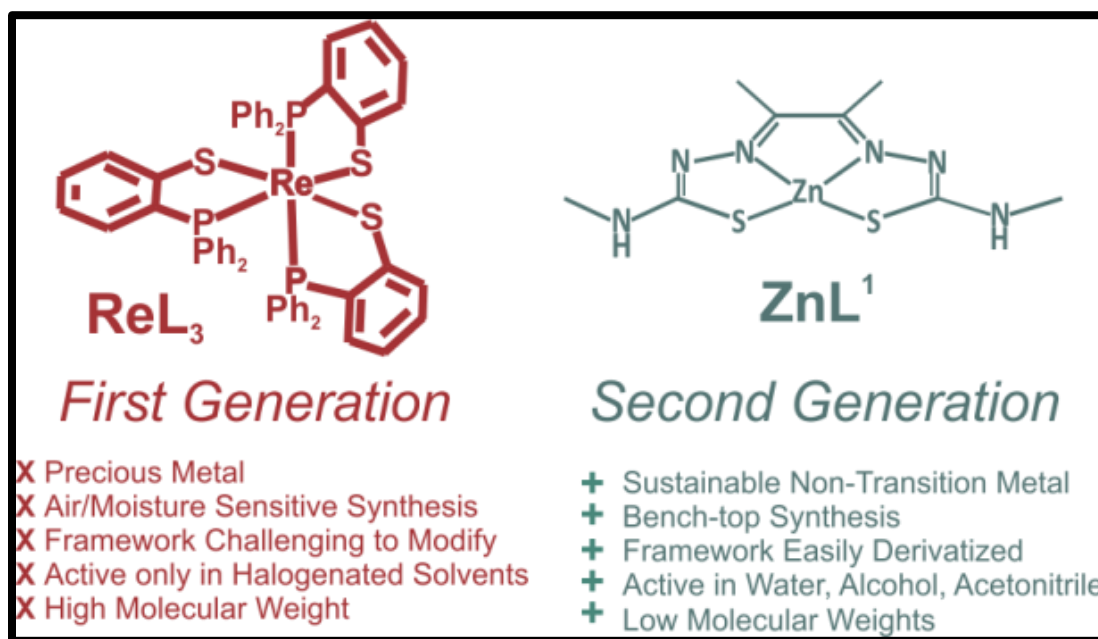
3.4. Acknowledgement

The work described in chapter 3 was supported by the National Science Foundation research grant (CHE-1361728) and a grant from the Kentucky Science and Engineering Foundation as per grant agreement no. KSEF-148-502-15-350 with the Kentucky Science and Technology Corporation. The authors are thankful to Cardinal Research Cluster at the University of Louisville for providing the computational facilities.

CHAPTER IV:
SUSTAINABLE METAL
ALTERNATIVES FOR LIGAND-
CENTERED H₂ EVOLUTION AND
HYDROGEN OXIDATION

4.1. Introduction

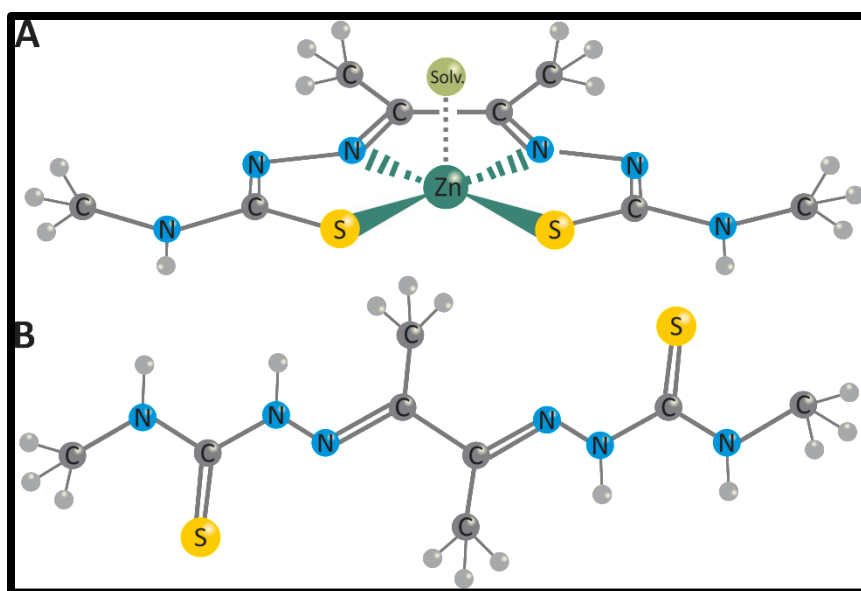
The ReL_3 system described in Chapter Three opens the door to novel pathways and alternative strategies for catalytic HER development. However, the system suffers from significant limitations including: 1) incorporation of a non-sustainable, precious metal; 2) the ligand synthesis requires multiple steps that are air, moisture, and/or light sensitive performed under inert conditions; 3) catalysis is limited to halogenated organic solvents; 4) modification of the ligand structure requires an individualized approach for each new derivative; and 5) large complex size/ 3^{rd} row transition metal complicates computational studies of the mechanism.



Scheme 4. Comparison of first and second generation Ligand-Centered HER Electrocatalysts.

To overcome the limitations of ReL_3 , we developed new catalysts based on the non-innocent bis-thiosemicarbazone ligand H_2L^1 (L^1 =diacetyl-bis(N-4-methyl-3-thiosemicarbazide), Scheme 4. This chapter will focus on two electrocatalysts based on

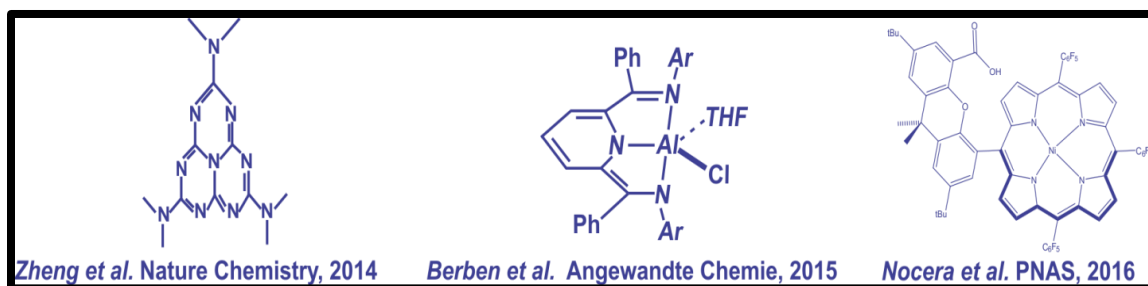
this ligand class, encompassing the metal free ligand, H_2L^1 and the transition metal free, ZnL^1 Scheme 5. H_2L^1 represents the first homogeneous metal-free HER catalyst, ZnL^1 is the most active transition metal free HER catalyst.⁷⁶ Further, these systems overcome the limitations noted above as they: 1) incorporate sustainable first-row metals; 2) the ligand syntheses require no specialized skills and can be performed on the benchtop in water and/or alcohol using inexpensive synthons; 3) catalysis occurs in water/alcohol or acetonitrile; 4) the framework is easily derivatized and very stable to hydrolysis; 5) the structures are small with metals that are well calibrated from the computational perspective.



Scheme 5. Representation of ZnL^1 and H_2L^1 .

Other ligand-centered processes for HER/HOR are emerging in the literature, Scheme 6. Initial reports focused on heterogeneous systems including a metal-free HER catalyst based on N-doped graphene with graphitic-carbon nitride¹⁰⁰ and metal-free and

zinc-phthalocyanines.^{101,105,106} Notable heterogeneous HOR electrocatalysts include a metal-free frustrated Lewis pair¹⁰⁷ that is proposed to operate through a hydride intermediate similar to homogeneous Ni and Fe HOR catalysts. More recently, an aluminum-bis(imino)pyridine complex was reported as a homogeneous, non-transition metal HER electrocatalyst with a TOF of 3.3 hr⁻¹.⁹⁹ Activity was attributed to a radical process involving homolytic C-H bond cleavage. A similar mechanism was proposed for a nickel “hangman”-porphyrin complex via a Ni phorlin intermediate, although no TOF was reported.¹⁷³ Recently, a heterobimetallic W-Ni complex employing a redox-active ligand was reported as a HER catalyst in acidic aqueous solutions with a cis-thiolate core proposed as the active site.¹⁷⁴ The recent development of ligand-centered HER/HOR catalysts underscores the need for alternate approaches to the traditional metal-hydride systems. The remainder of this chapter will cover the electrochemical, computational, and mechanistic study of H₂L¹ and ZnL¹ as electrocatalysts for hydrogen evolution or hydrogen oxidation.



Scheme 6. Selected ligand-centered HER/HOR electrocatalysts, taken from references 71, 99 and 100.^{71,99,100}

4.2. Results and Discussion

4.2.1. ZnL^I Cyclic Voltammetry Characterization

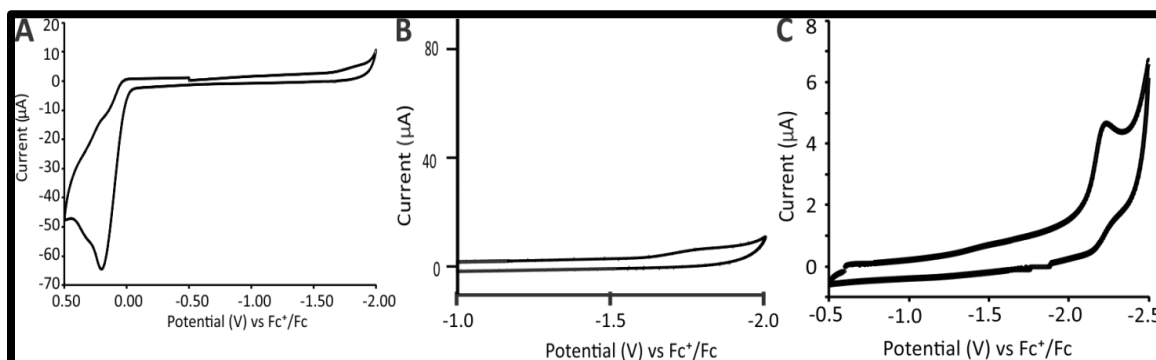


Figure 23. (A) Cyclic voltammogram of ZnL^I in 0.1 M Bu₄NPF₆ methanol solution (B) Blow up of cathodic region of cyclic voltammogram of ZnL^I in 0.1 M Bu₄NPF₆ methanol solution. (C) Cyclic voltammogram of ZnL^I in 0.1 M Bu₄NPF₆ acetonitrile solution.

ZnL^I was synthesized according to literature procedure reported by Holland *et al.*^{111,112} The ZnL^I complex is stable open to air and is soluble in a variety of solvents including, methanol, ethanol, acetonitrile, and dimethylformamide. Zn^{II} complexes of tetradentate ligands that are constrained in pseudo-square planar conformations can potentially bind a fifth donor atom in the axial coordination site, as indicated in Scheme 5,¹⁷⁵ foreshadowing the ability of the ZnL^I to dimerize, making it an excellent candidate for multi-step electrocatalysis.

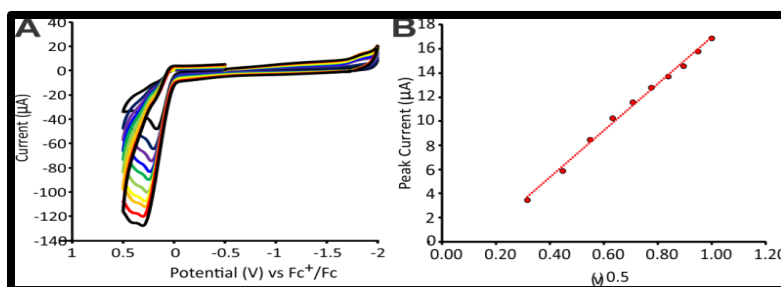


Figure 24. (A) Cyclic voltammogram of ZnL^I in 0.1 M Bu₄NPF₆ methanol solution scanned at 0.1 (black), 0.2 (dark blue), 0.3 (purple), 0.4 (blue), 0.5 (green), 0.6 (light green), 0.7 (yellow),

0.8 (orange), 0.9 (red) and, 1.0 (black) V/s. **(B)** Cottrell plot of the peak current plotted against the square root of the scan rate.

CVs of ZnL^1 were initially run in methanol and acetonitrile. In 0.1 M Bu_4NPF_6 methanol solution an irreversible oxidation observed with onset potentials near and 0.3 V vs Fc^+/Fc (Figure 23A). In methanol sweeping in the cathodic direction was limited by solvent reduction of methanol, resulting in no observed reductions (Figure 23B). However cathodic sweeps in acetonitrile show an irreversible reduction at -2.3 V vs Fc^+/Fc (Figure 23C). Subsequent CV studies without substrate were run from 0.1 to 1.0 V/s (Figure 24A) Cottrell plots were constructed by plotting the peak current from each against the square root of the scan rate in order to yield a linear relationship with a slope of 1.94×10^{-5} (Figure 24B). This was then used in conjunction with the Randles-Sevcik equation in order to calculate a diffusion coefficient of $1.15 \times 10^{-7} \text{ cm}^2/\text{s}$.

4.2.2. ZnL^1 Cyclic Voltammetry Hydrogen Evolution and Hydrogen Oxidation Studies

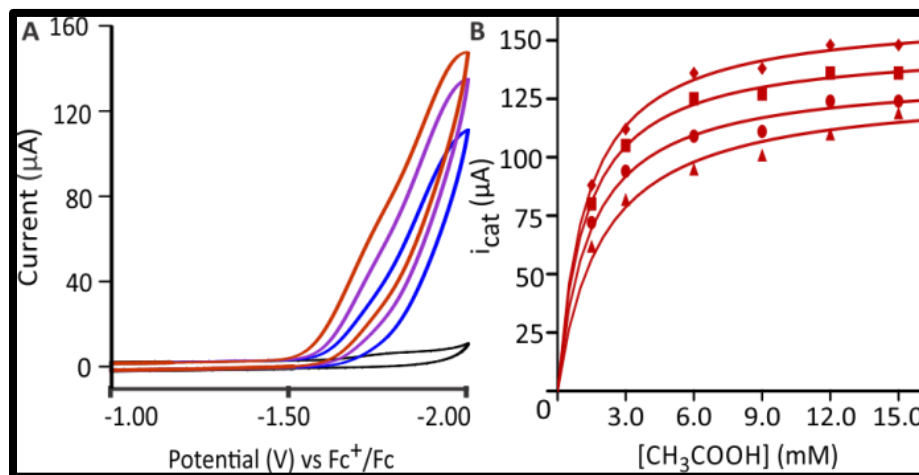


Figure 25. **(A)** Cyclic voltammograms of 3 mM ZnL^1 in methanol with no added acid (black), 6 mM CH_3COOH (blue), 9 mM CH_3COOH (purple), and 12 mM CH_3COOH (red). Data collected at a scan rate of 0.5 V/s in the presence of 0.1 M Bu_4NPF_6 as supporting electrolyte. **(B)** Plot of

i_{cat} vs $[\text{CH}_3\text{COOH}]$ for 3 mM ZnL^1 (red) at scan rates of 0.2 (\blacktriangle), 0.3 (\bullet), 0.4 (\blacksquare), and 0.5 (\blacklozenge) V/s.

Solutions of ZnL^1 in methanol display catalytic hydrogen evolution upon reduction in the presence of acetic acid. The cathodic current intensity at -1.7 V increases with increasing acid concentration indicative of an electrocatalytic process (Figure 25A). The current plateaus at 12.0 mM acetic acid, indicating acid saturation and signifying that CV response is no longer limited by diffusion of the substrate to the electrode surface (Figure 25B) ^{121,163-165}, with a maximum TOF of 1170 s^{-1} at overpotential of 756 mV (see appendix for more information).^{121,176,177} The new reduction event observed during catalysis at -1.5 V in methanol signifies that the HER undergoes an initial protonation prior to reduction, effectively pushing the first reduction to more anodic potentials than that observed in the absence of acid.

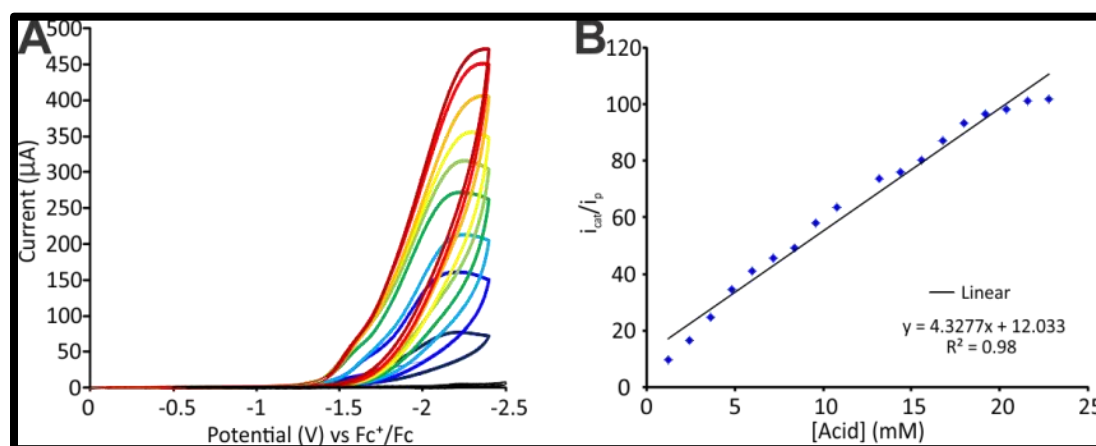


Figure 26. (A) Cyclic voltammograms of 3 mM ZnL^1 in ACN with no added acid (black), 2.4 mM CH_3COOH (dark blue), 4.8 mM CH_3COOH (blue), 7.2 mM CH_3COOH (light blue), 9.6 mM CH_3COOH (green), 12.0 mM CH_3COOH (light green), 14.4 mM CH_3COOH (yellow), 16.8 mM CH_3COOH (orange), 19.2 mM CH_3COOH (red), and 21.6 mM CH_3COOH (dark red). Data collected at a scan rate of 0.5 V/s in the presence of 0.1 M Bu_4NPF_6 as supporting electrolyte. (B) Plot of i_{cat} vs $[\text{CH}_3\text{COOH}]$ for 3 mM ZnL^1 (red) at scan rates of 0.2 (\blacklozenge) V/s.

In acetonitrile, addition of acetic acid results in catalytic current at -2.3 V (Figure 26A), which is within the range of reduction potentials previously reported for similar thiosemicarbazones.¹⁷⁸ The catalytic current becomes independent of acid concentration at 23 mM (Figure 26B), yielding a higher TOF value of 11700 s⁻¹ than that observed in methanol, but with a larger overpotential of 1.07 V (see appendix for more information). The lower overpotential in methanol is consistent with outer-coordination sphere proton shuttling,¹⁷⁹ which facilitates ligand protonation prior to electrochemical reduction, as previously suggested for thiosemicarbazone complexes.¹⁸⁰

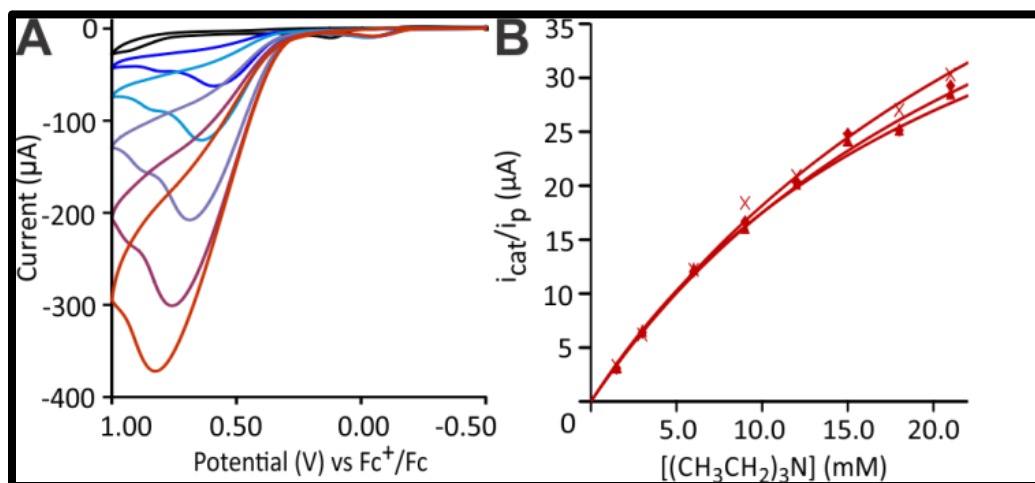


Figure 27. (A) Cyclic voltammograms of 0.3 mM ZnL in methanol under 1 atm. H₂ with no added base (black), 3 mM (CH₃CH₂)₃N (dark blue), 6 mM (CH₃CH₂)₃N (light blue), 12 mM (CH₃CH₂)₃N (light purple), 21 mM (CH₃CH₂)₃N (dark purple), and 30 mM (CH₃CH₂)₃N (red). Data collected at a scan rate of 0.5 V/s in the presence of 0.1 M Bu₄NPF₆ as supporting electrolyte. (B) Plot of i_{cat}/i_p vs $[(CH_3CH_2)_3N]$ for 0.3 mM ZnL under 1 atm. H₂ (red) at scan rates of 0.2 (▲), 0.5 (◆), and 1.0 (×) V/s.

As well as electrocatalytic HER, ZnL¹ also catalyzes HOR. Introduction of triethylamine to methanol solutions of ZnL¹ under 1 atm of H₂ results in an increase in anodic current near the irreversible oxidation wave of ZnL¹. (Figures 27A). The catalytic current intensity shows saturation behavior (Figure 27B) with near saturation at a base

concentration of 30 mM, indicating that catalysis is no longer limited by diffusion of the substrate to the electrode surface, yielding a TOF of 72 s^{-1} with an overpotential of 0.31 V (see appendix for more information). The HER and HOR TOF values of ZnL^1 is substantially higher than those of other proposed ligand-centered catalysts, suggesting that H_2L^1 itself may also demonstrate catalytic activity.

In order to determine the reaction order with respect to the catalyst for the HER, CVs were run at a fixed acid concentration of 12 mM with increasing concentration of ZnL^1 (Figure 28A). The peak current was measured at each catalyst concentration. Rather than yielding a linear first-order relationship, a second-order dependence was observed. A plot of the peak current versus the squared catalyst concentration yielded a linear dependence confirming the second-order dependence on ZnL^1 , although above concentrations of 2.0 mM the plot deviates from a second-order to first-order dependence (Figure 28B).

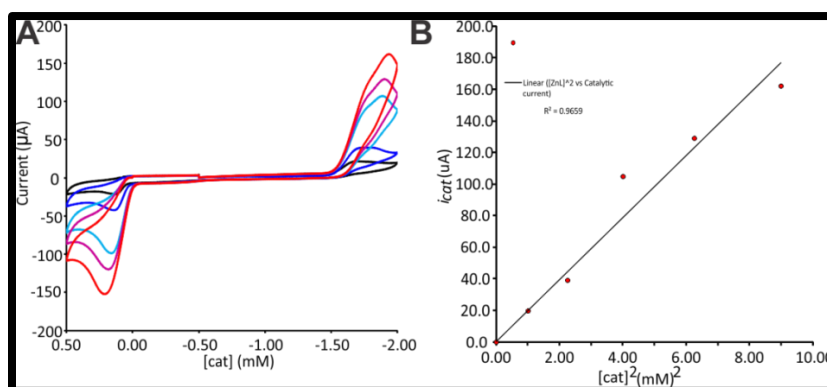


Figure 28. (A) Cyclic Voltammograms of 1.0 mM (black), 1.5 mM (blue), 2.0 mM (light blue), 2.5 mM (magenta), 3.0 mM (red) ZnL^1 with 12 mM CH_3COOH in 0.1 M Bu_4NPF_6 methanol solution. (B) Plot of peak current versus $[\text{ZnL}^1]^2$.

4.2.3. H₂L¹ Cyclic Voltammetry Hydrogen Evolution and Hydrogen Oxidation Studies

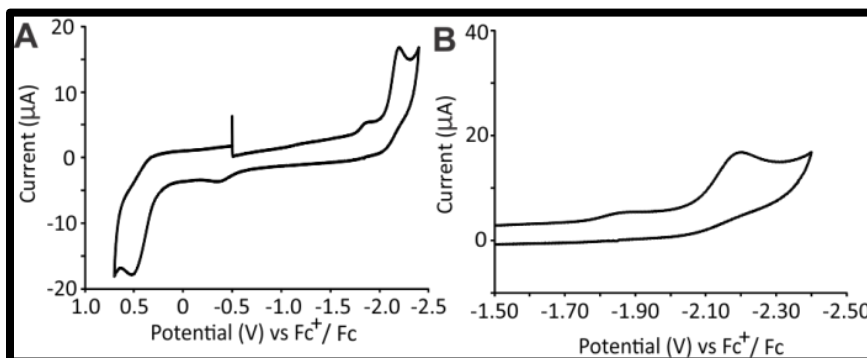


Figure 29. (A) Cyclic Voltammogram of H₂L¹ in 0.1 M Bu₄NPF₆ solution collected at 0.5 V/s. (B) Blow up showing cathodic scan only of H₂L¹.

The metal-free H₂L¹ ligand was subsequently evaluated as a proton reduction and hydrogen oxidation electrocatalyst. In the absence of acid, H₂L¹ displays an irreversible reduction at -2.1 V and an irreversible oxidation at +0.5 V vs Fc⁺/Fc in 0.1 M Bu₄NPF₆ methanol solutions (Figure 29AB). Upon addition of acetic acid, the cathodic current at -2.1 V increases steadily (Figure 30A), reaching a maximum at concentrations of 9.8 mM (Figure 30B). Under acid-saturated conditions, H₂L¹ displays a TOF of 1320 s⁻¹ with an overpotential of 1430 mV (see appendix for more information). To our knowledge, this is the only reported metal free, homogeneous, electrocatalyst for HER.

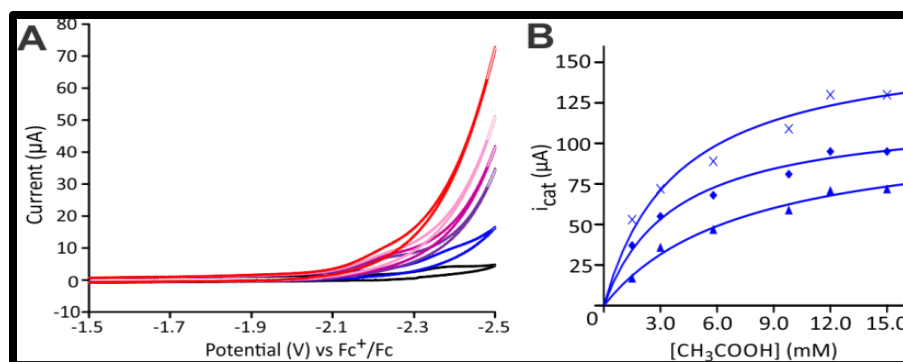


Figure 30. (A) Cyclic voltammograms of 3 mM H_2L^1 with no added acid (black), 3 mM CH_3COOH (blue), 5.8 mM CH_3COOH (purple), 7 mM CH_3COOH (light purple), 8.2 mM CH_3COOH (pink) and, 9.8 mM CH_3COOH (red). Data collected at a scan rate of 0.5 V/s in the presence of 0.1 M Bu_4NPF_6 as supporting electrolyte. (B) Plot of i_{cat} vs $[\text{CH}_3\text{COOH}]$ for 3 mM H_2L^1 (blue) at scan rates of 0.2 (\blacktriangle), 0.5 (\blacklozenge), and 1.0 (\times) V/s.

Given the bi-functional nature of the Zn based system we decided to investigate H_2L^1 as an electrocatalyst for hydrogen oxidation. Introduction of triethylamine to methanol solutions of H_2L^1 under 1 atmosphere of H_2 results in an increase in anodic current near the irreversible oxidation wave of H_2L^1 (Figures 31A). The catalytic current intensity shows saturation behavior (Figure 31B) with near saturation at a base concentration of 21 mM, indicating that catalysis is no longer limited by diffusion of the substrate to the electrode surface, yielding a TOF of 32 s^{-1} with an overpotential of 0.33 V (see appendix for more information). Again, to our knowledge this is the only reported metal-free homogeneous electrocatalyst for the oxidation of H_2 .

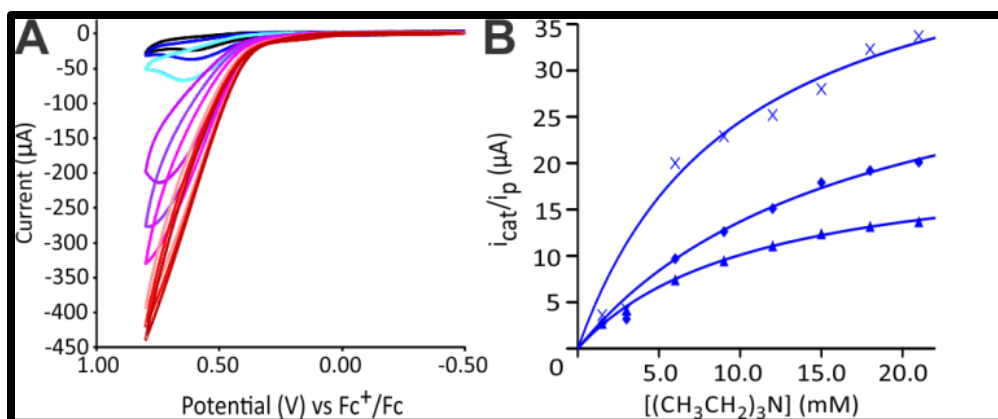


Figure 31. (A) Cyclic voltammograms of 0.3 mM H₂L in methanol under 1 atm. H₂ with no added base (black), 0.75 mM (CH₃CH₂)₃N (blue), 1.5 mM (CH₃CH₂)₃N (cyan), 3 mM (CH₃CH₂)₃N (light blue), 6 mM (CH₃CH₂)₃N (light purple), 9 mM (CH₃CH₂)₃N (purple), 12 mM (CH₃CH₂)₃N (pink), 15 mM (CH₃CH₂)₃N (rose), 18 mM (CH₃CH₂)₃N (red) and, 21 mM (CH₃CH₂)₃N (dark red). (B) Plot of i_{cat}/i_p vs [(CH₃CH₂)₃N] for 0.3 mM ZnL under 1 atm. H₂ (blue) at scan rates of 0.2 (▲), 0.5 (◆), and 1.0 (×) V/s.

4.2.4. ZnL¹ Extended Stability and Gas Identification: Controlled Potential Coulometry Studies

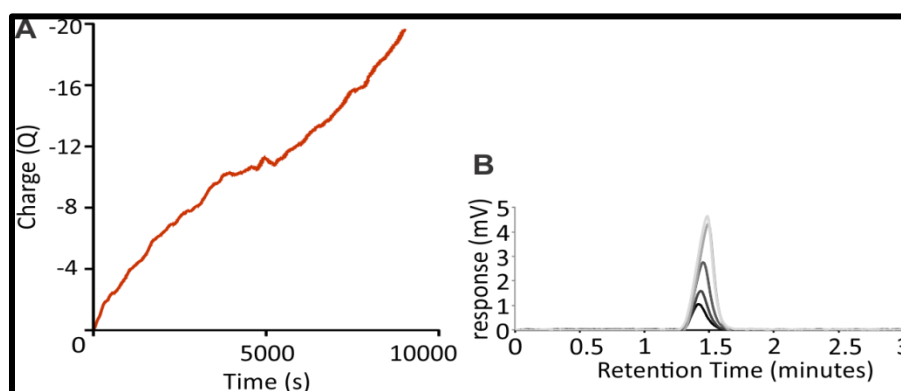


Figure 32. (A) Plot of charge vs time recorded during bulk electrolysis of 0.1 mM ZnL¹ and 12 mM CH₃COOH in methanol with 0.1M Bu₄NPF₆ as supporting electrolyte. (B) Headspace readout of GC-TCD showing H₂ as gaseous product at times 30, 60, 90, 120, and 150 minutes during electrolysis.

The stability of ZnL¹ as a HER electrocatalyst was further examined by controlled potential coulometry. At an applied potential of -1.7 V vs Fc⁺/Fc, ZnL¹ evolves H₂ from 12 mM acetic acid solutions in methanol with a turnover number of 37 after 2.5 h (Figure

32A) based on a total charge of 19.8 C. The identity of the gaseous product was confirmed as H₂ by gas chromatography thermal conductivity (Figure 32B). The integrated peak areas of headspace samples collected during electrolysis indicate a minimum Faradaic efficiency of 85% (see Chapter II for more information) throughout the electrolysis; the TOF remained consistent at 15 h⁻¹ with no signs of decreasing activity.

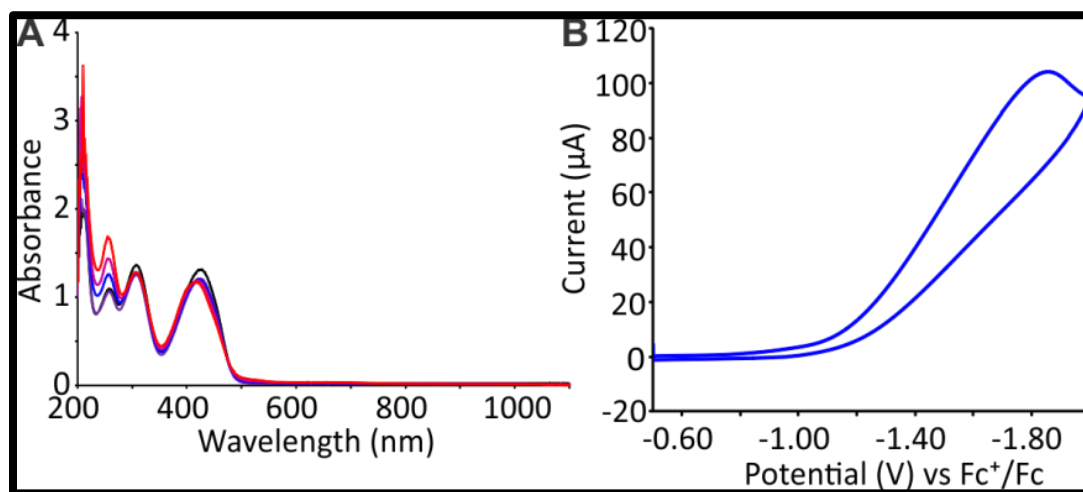


Figure 33. (A) UV spectra recorded every 15 minutes during the electrolysis of 1 mM ZnL¹ under applied potential of -1.7 V in 0.1 M Bu₄NPF₆ methanol solution. (B) CV of ZnL after electrolysis in 0.1 M Bu₄NPF₆ methanol solution with 12 mM acetic acid added. $v = 0.2$ V/s vs Fc⁺/Fc.

Spectroelectrochemical experiments were performed on 0.1 M Bu₄NPF₆ methanol solutions of ZnL¹ with an applied potential of -1.7 V in order to identify the absorption characteristics of the one-electron reduced electrocatalyst, [ZnL]⁻. UV-vis spectra were recorded before electrolysis and then measured every 15 min during electrolysis showing the growth of the absorption band near 250 nm and a decrease in the absorption band near 430 nm (Figure 33A). A cyclic voltammogram was then recorded with addition of 12

mM acetic acid (Figure 33B). An additional control was performed after prolonged reduction in order to rule out ligand decomposition onto electrode surface as a possible source of catalysis. After reduction, the working electrode was removed, washed with DI water, and then placed in fresh solution containing no catalyst, upon which no current was observed.

4.2.5. ZnL¹ Mechanism Evaluation: Digital Simulations, Isotope Effect Studies

To evaluate the HER mechanism of ZnL, we first determined the rate law and measured the H/D kinetic isotope effect (KIE). As shown earlier in Chapter 4.2, under non-saturating acid conditions i_{cat} is directly proportional to $[H^+]$ indicating a first-order dependence on acid concentration.¹⁰ Varying the $[ZnL^1]$ at fixed acid concentrations confirm first-order dependence at catalyst concentrations above 2 mM (Figure 28B). Using the deuterated acid CD₃CO₂D, the ZnL¹ catalyst displays a small KIE of 1.2, which is distinct from the inverse KIEs reported for several metal-hydride HER catalysts and from the large KIEs associated with electrocatalysts thought to be proceeding through tunneling.

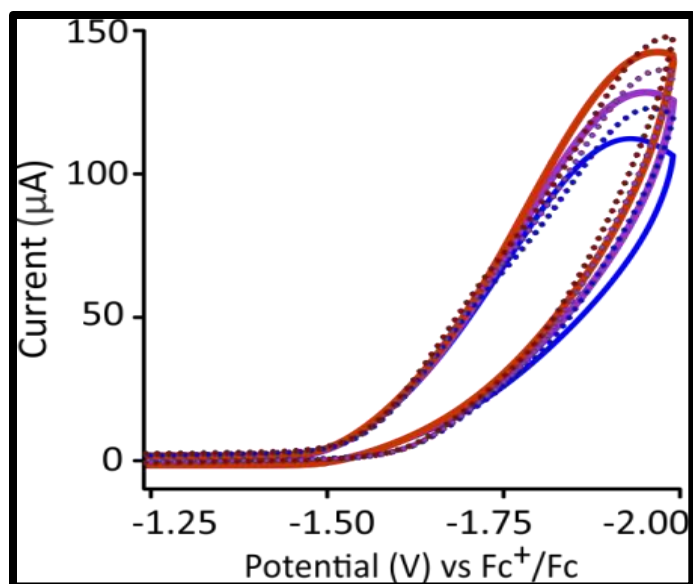


Figure 34. Comparisons of experimental (solid) and simulated (dotted) cyclic voltammograms for 3 mM ZnL^1 and 12 mM CH_3COOH in methanol with 0.1M Bu_4NPF_6 as supporting electrolyte at scan rates of 0.3 (blue), 0.4 (purple), and 0.5 (red) V/s.

Digital simulations of the cyclic voltammograms (Figure 34) reveal parallel routes to proton reduction involving homocoupling of two, neutral $\text{Zn}(\text{HL}\bullet)$ radicals and heterocoupling of a neutral $\text{Zn}(\text{HL}\bullet)$ radical with the cationic radical $[\text{Zn}(\text{H}_2\text{L}\bullet)]^+$. The proposed mechanism (Figure 35) begins with protonation of ZnL^1 , $K = 2.4 \times 10^5$, followed by reduction to $\text{Zn}(\text{HL}\bullet)$, $E^\circ = -1.81 \text{ V vs Fc}^+/\text{Fc}$. In the homocoupling pathway, two $\text{Zn}(\text{HL}\bullet)$ rapidly combine, $k_f = 3 \times 10^9 \text{ M}^{-1} \text{ s}^{-1}$, to evolve H_2 and regenerate 2 equivalents of ZnL^1 . In the alternate pathway, 1 equivalent of $\text{Zn}(\text{HL}\bullet)$ is further protonated, $K = 8.8$, prior to heterocoupling. Combination of $[\text{Zn}(\text{H}_2\text{L}\bullet)]^+$ with the second equivalent of $\text{Zn}(\text{HL}\bullet)$, $k_f = 2 \times 10^{10} \text{ M}^{-1} \text{ s}^{-1}$, yields H_2 completing the catalytic cycle. The simulated kinetic and thermodynamic parameters reveal that both routes to H_2 evolution are operational across a range of experimental conditions (see Appendix for more information).

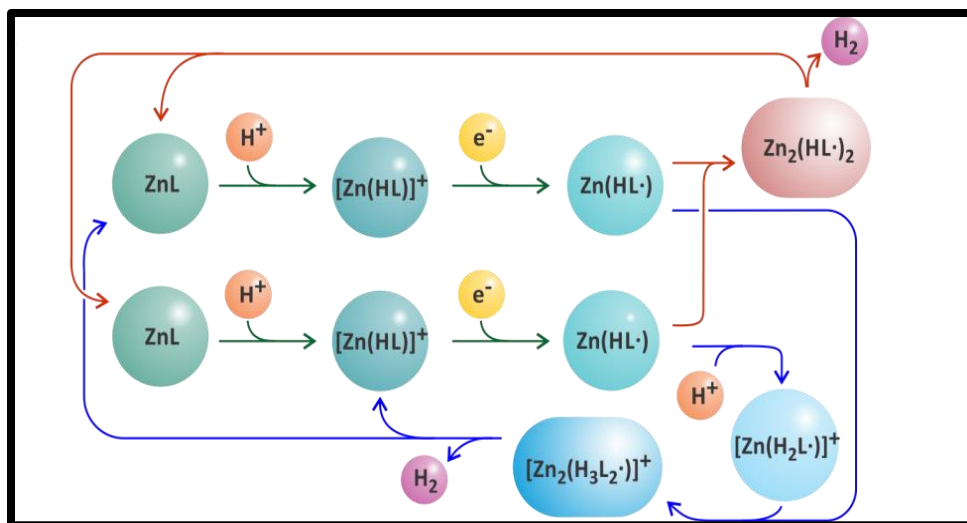


Figure 35. Concurrent catalytic pathways for hydrogen evolution through homocoupling of neutral $\text{Zn}(\text{HL}\cdot)$ radicals (red arrows) and heterocoupling of a neutral $\text{Zn}(\text{HL}\cdot)$ and cationic $[\text{Zn}(\text{H}_2\text{L}\cdot)]^+$ radicals (blue arrows).

4.2.6. ZnL^1 Density Functional Theory Study

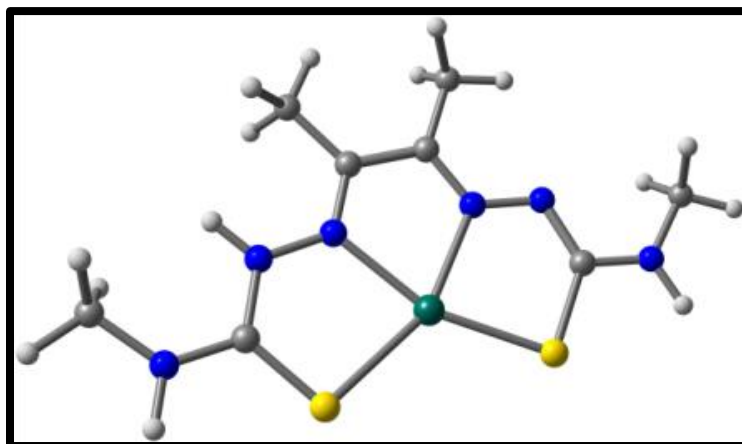


Figure 36. Optimized Structure of $[\text{ZnLH}]^+$ with protonation on the hydrazino nitrogen, B97-D/6-311G(d)

Density functional theory calculations using the B97-D functional and the 6-311G(d) basis set support the proposed catalytic cycle and elucidate the hydrazino nitrogen as the site of protonation. Each of the metal complexes in Figure 35 was successfully optimized.

Energies reveal that protonation at the hydrazino nitrogen (Figure 36) is favored by at least 13.0 kcal/mol relative to other potential basic sites within ZnL^1 (Figure 37).

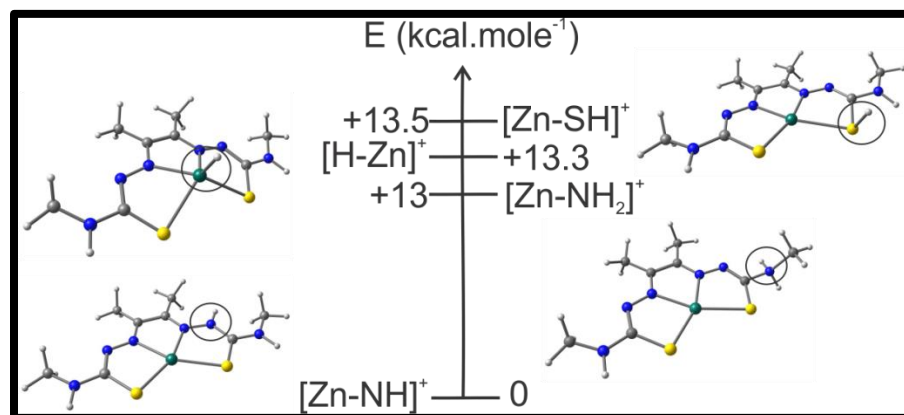


Figure 37. DFT optimized structures showing energetic stability of protonated species, $[\text{ZnL}^1\text{H}]^+$.

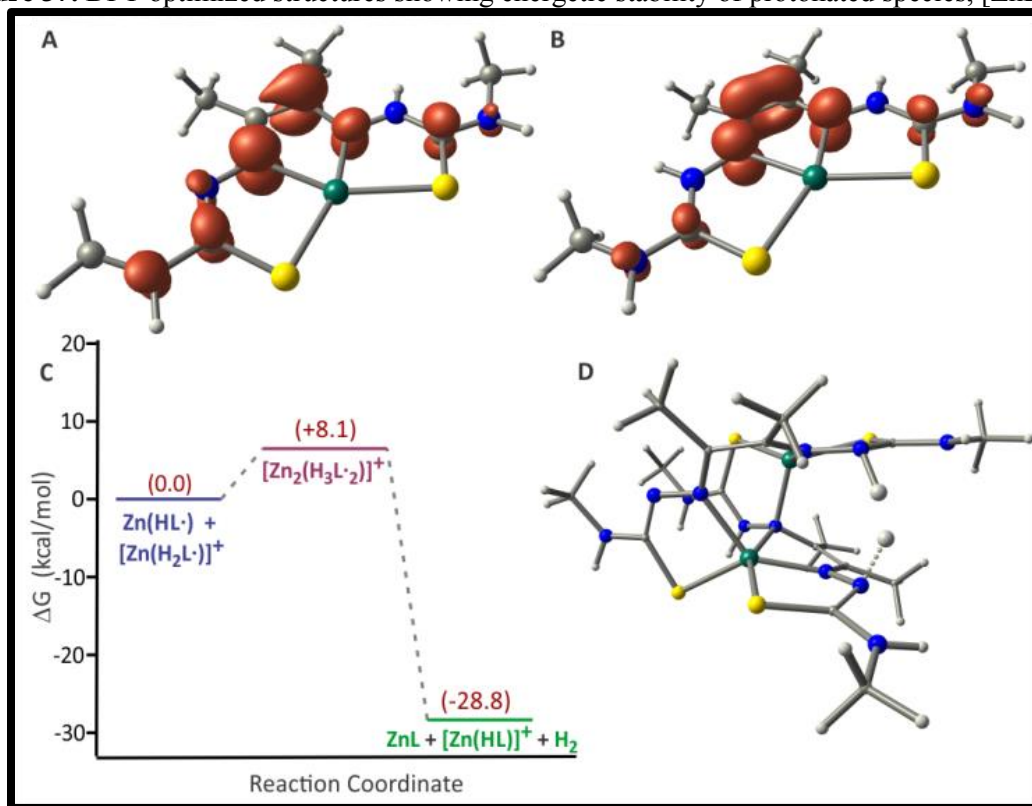
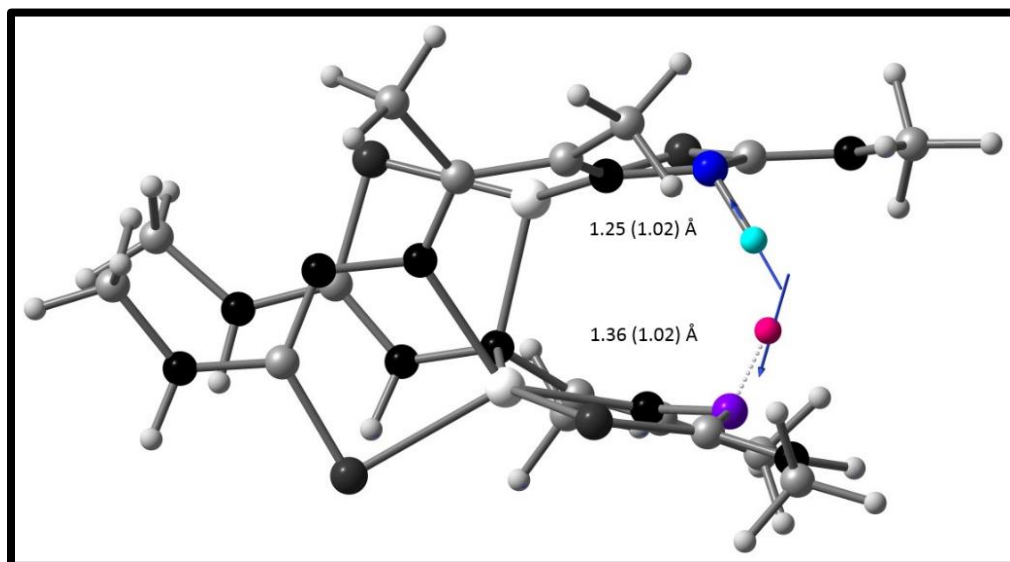


Figure 38. Energy profile along with spin densities of species involved in catalyzed H_2 evolution. Spin-density profiles for (A) $\text{Zn}(\text{HL}\cdot)$ and (B) $[\text{Zn}(\text{H}_2\text{L}\cdot)]^+$. (C) Relative energies (ZPE corrected) for H_2 evolution through the heterocoupling of $\text{Zn}(\text{HL}\cdot)$ and $[\text{Zn}(\text{H}_2\text{L}\cdot)]^+$ using the B97-D/6-311G(d) level of theory. (D) Structure of the singlet $[\text{Zn}_2(\text{H}_3\text{L}\cdot_2)]^+$ transition state through the heterocoupling pathway. Analysis of the eigenvector associated with the imaginary

frequency $i1572\text{ cm}^{-1}$, and the charge densities of atoms for H_2 evolution with respect to intrinsic reaction coordinate.

Evolution of H_2 through homocoupling of two $\text{Zn}(\text{HL}\cdot)$ radicals is exergonic by 42.6 kcal/mol, while the parallel pathway involving heterocoupling of $\text{Zn}(\text{HL}\cdot)$ and $[\text{Zn}(\text{H}_2\text{L}\cdot)]^+$ releases 28.8 kcal/mol. Analyses of the $\text{Zn}(\text{HL}\cdot)$ and $[\text{Zn}(\text{H}_2\text{L}\cdot)]^+$ spin density profiles (Figure 38A,B) show radical character delocalized on both protonated ligand frameworks. H_2 is evolved by radical heterocoupling, overcoming an 8.1 kcal/mol barrier (Figure 38C,D). The absence of spin density on Zn for all species involved in the HER is in unequivocal support of ligand based reduction.



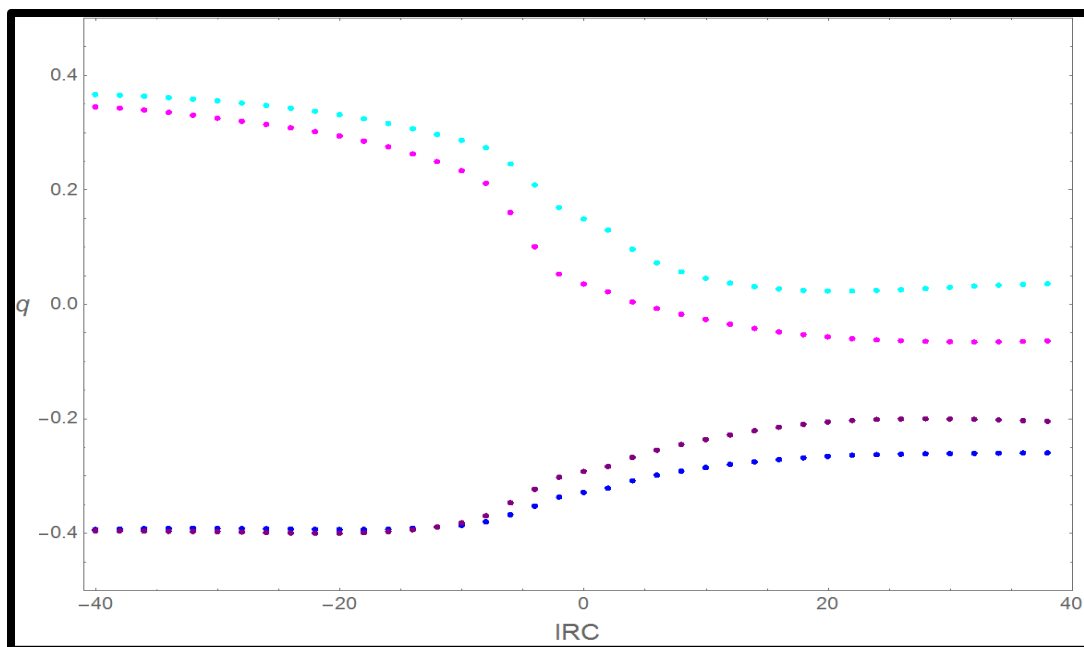


Figure 39. (Upper) Transition state geometry of $[\text{Zn}_2\text{H}_3\text{L}\bullet_2]^+$ along the HER pathway, shown with active N-H bond lengths associated with the imaginary frequency $i1572\text{ cm}^{-1}$, and equilibrium bond lengths in parentheses. **(Lower)** Charge densities of atoms near H_2 evolution with respect to IRC; N-H of $[\text{Zn}(\text{HL}\bullet)]^+$ (blue, and cyan), and N-H of $\text{Zn}(\text{H}_2\text{L}\bullet)$ (magenta, purple).

The transition state (TS) can be described as a dimer with H dissociations from each monomer fragment, along their respective N-H coordinates to form H_2 (39 Upper). This is consistent with N-H bond lengths in the TS of 1.25 \AA for $\text{Zn}(\text{HL}\bullet)$ and 1.36 \AA for $[\text{Zn}(\text{H}_2\text{L}\bullet)]^+$ compared to respective equilibrium N-H distances, both of 1.02 \AA . The longer N-H bond in the TS associated with $[\text{Zn}(\text{H}_2\text{L}\bullet)]^+$ may also be attributed to an increased charge density along the forward IRC for both N and H, compared to $\text{Zn}(\text{HL}\bullet)$ (Figure 39 Lower). The HER from $[\text{Zn}_2\text{H}_3\text{L}\bullet_2]^+$ is thus interpreted as dimeric, where the now charge-reorganized $\text{Zn}(\text{H}_2\text{L}\bullet)$ fragment promotes early electron transfer and is coupled to proton transfer from $[\text{Zn}(\text{HL}\bullet)]^+$ to form H_2 .

Table 2. Bond length comparison of calculated HER intermediates

Structures		ZnL	[ZnHL] ⁺	Zn(HL•)	[ZnH ₂ L•] ⁺
Bond Lengths (Å)	Zn-S1	2.368	2.423	2.458	2.386
	Zn-S2	2.368	2.318	2.341	2.386
	Zn-N2	2.116	2.118	2.059	2.061
	Zn-N3	2.116	2.125	2.045	2.061
	S1-C1	1.774	1.719	1.728	1.732
	C1-N5	1.356	1.343	1.373	1.349
	N5-C5	1.460	1.467	1.459	1.463
	C1-N1	1.339	1.373	1.351	1.361
	N1-N2	1.344	1.357	1.368	1.362
	N1-H15	-	1.015	1.016	1.015
	N2-C2	1.312	1.313	1.368	1.348
	C2-C3	1.478	1.470	1.427	1.436
	C3-N3	1.312	1.322	1.345	1.348
	N3-N4	1.344	1.321	1.349	1.362
	N4-C4	1.339	1.361	1.329	1.361
	C4-S2	1.774	1.767	1.792	1.732
	C4-N6	1.356	1.341	1.367	1.349
	N6-C8	1.460	1.469	1.458	1.463

Examination of the change in bond lengths and bond angles amongst ZnL, [Zn(HL)]⁺, Zn(HL•), and [Zn(H₂L•)]⁺ (Tables 2-3) assist to explain structural and electronic changes over the course of the ZnL¹ catalyzed HER mechanism. Initial protonation of ZnL¹ to give [Zn(HL)]⁺ results in a slight puckering of the ligand framework around the Zn center shown by the lengthening of the Zn-S1, Zn-N2, Zn-N3 bonds and a decrease in the Zn-S2 bond as well as an increase in the S1-Zn-S2, N3-Zn-S2 bond angles and decrease of the S1-Zn-N2, N2-Zn-N3 bond angles. Subsequent reduction to the neutral radical species, Zn(HL•), is accompanied by significant contraction of the Zn-N2 and Zn-N3 bonds, 2.118 Å and 2.125 Å to 2.059 Å and 2.045 Å, respectively. Furthermore, moving across the mechanism from protonation to reduction, the C2-C3 bond length always decreases in length moving from an initial

length of 1.478 Å to 1.470 Å after protonation, and then decreasing further to 1.427 Å after reduction, in agreement with the spin-density map of Zn(HL•).

Table 3. Bond angle comparison of calculated HER intermediates.

Structures	ZnL	[ZnHL] ⁺	Zn(HL•)	[ZnH ₂ L•] ⁺
Bond Angles (°)				
S1-Zn-S2	118.02	119.08	116.68	117.56
S1-Zn-N2	82.78	81.57	82.39	83.80
N2-Zn-N3	76.43	74.94	77.40	73.34
N3-Zn-S2	82.78	84.41	85.07	83.30
C1-S1-Zn	93.70	96.92	95.10	95.54
N1-N2-C2	121.88	122.99	120.43	122.41
N1-N2-Zn	122.08	119.62	119.13	118.45
C2-N2-Zn	116.04	117.39	115.19	118.59
C3-N3-Zn	116.04	117.76	117.15	118.59
C3-N3-N4	121.88	122.01	121.05	122.41
N4-N3-Zn	122.08	120.23	121.44	118.45

4.3. Conclusion

In summary, the non-transition-metal complex ZnL¹ and the metal-free ligand H₂L¹ represent a fundamentally new class of homogeneous HER and HOR electrocatalysts. Unlike traditional catalysts that employ a metal-hydride as the key intermediate, this new approach facilitates H₂ evolution through ligand-centered radical coupling. The combination of the redox active ligand H₂L¹ with the non-transition-metal Zn constrains redox activity to the ligand, in contrast to transition-metal complexes where spin-coupling between the ligand radical and unpaired electrons on the metal may reduce reactivity. The confinement of radical character to the ligand is further evidenced by the catalytic activity of H₂L¹; albeit with higher overpotential than ZnL¹. The enhanced activity with Zn is attributed in part to the Lewis acidity of Zn(II), which balances the charge of the anionic ligand, promotes protonation, and lowers the reduction potential. Further, Zn(II) provides a structural framework for the N₂S₂ chelate that pre-organizes

the radical complexes for H₂ evolution. We can envision the strategies introduced in this study being tailored in future works to improve TOF and lower overpotential and for the development of other catalysts for small molecule activation.

4.4. Acknowledgement

The work described in Chapter Four was supported in part by the National Science Foundation (CHE-1361728) and a grant from the Kentucky Science and Engineering Foundation as per grant agreement no. KSEF-148-502-15-350 with the Kentucky Science and Technology Corporation. The authors are thankful to Cardinal Research Cluster at the University of Louisville for providing the computational facilities. A.Z.H, R.M.B., and C.A.G. are inventors on a U.S. provisional patent application no. 62/348,420, filed by the University of Louisville Research Foundation, Inc., and related to this work.

CHAPTER V:
TRANSITION METAL ASSISTED
LIGAND-CENTERED H₂
EVOLUTION

5.1. Introduction

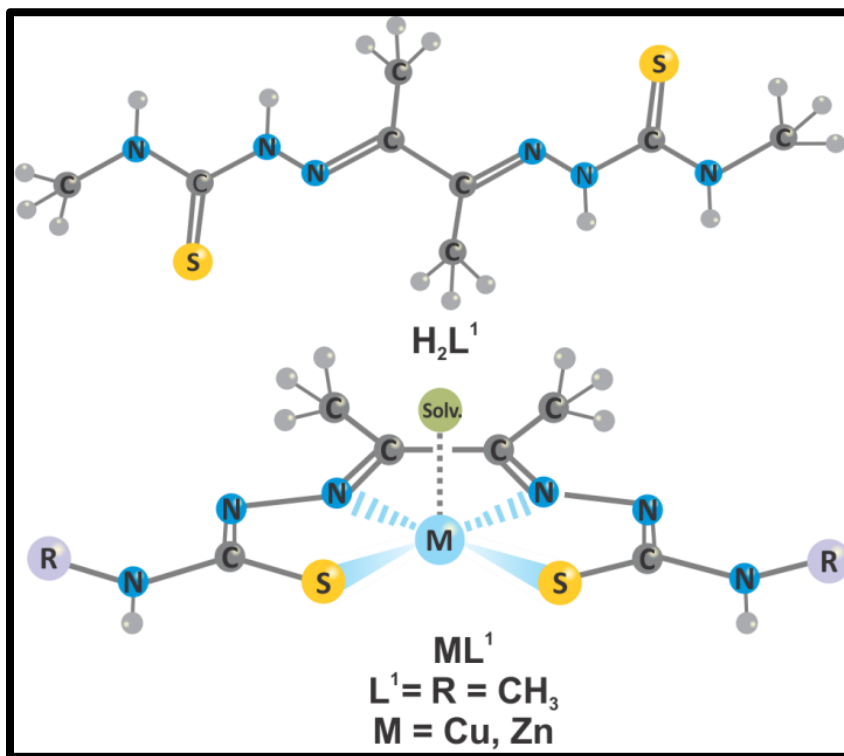
Rising international energy demands, coupled with growing concerns of repercussion from global climate change, have ignited considerable interest in the development of carbon-free and carbon neutral energy systems.^{5,15,16} Hydrogen is a promising component of these systems as a light weight, energy dense carrier. Hydrogen evolution reactions (HERs), which involve a two-electron reduction of protons, can be used to store energy in H₂, with subsequent energy release through hydrogen oxidation reactions (HORs).^{1,181,182} Consequently, there has been significant research into the development of inexpensive, abundant homogeneous and heterogeneous materials that serve as electrocatalysts for the production of H₂. Platinum is an excellent catalyst for HER and HOR,¹⁸³ yet its scarcity and high costs limit practical large scale application, leading to the pursuit of sustainable alternates that employ abundant first-row transition metals.^{80,89,90,184-191} Not surprisingly, much of these works have taken an approach to generate HER catalysts which operate via mechanisms invoking metal-hydrides. While this approach has led to substantial advances, sustainable candidates are limited to economically viable first-row transition metals complexes capable of stabilizing metal-hydrides. The recent development of HER catalysts that function via ligand-centered processes or employ redox-active ligands,¹⁹² has expanded the realm of HER electrocatalysts beyond traditional transition metal-hydrides to include non-transition metal,^{76,99} and metal-free catalysts⁷⁶ for HER invoking ligand-directed radical coupling of H-atoms^{77,193} or protonation of ligand-centered hydrides.^{71,76}

As discussed previously in Chapter Four, we reported the first examples of HER/HOR activity with the non-innocent bis(thiosemicarbazone) ligand framework.⁷⁶

The zinc complex of diacetyl-bis(N-4-methyl-3-thiosemicarbazone), ZnL^1 , catalyzes HER with a maximum TOF of 1170 s^{-1} and the HOR in the presence of triethylamine with a maximum TOF of 72 s^{-1} . The HER mechanism was established through a rigorous protocol involving kinetic studies, including digital simulations of electrochemical data, DFT computations of catalytic intermediates, and location of the transition state. Results indicate a ligand-centered process involving a binuclear transition state with evolution of H_2 via ligand hydride-proton coupling. Notably, the free ligand H_2L^1 also demonstrates similar HER activity. Very recently, Straistari *et al.* reported HER activity with a related bis(thiosemicarbazonato)Ni(II) complex with an enhanced TOF of 3080 s^{-1} , proposed to involve initial ligand-centered reduction and protonation followed by metal-centered reduction.⁸⁸ The compound studied in this chapter, CuL^1 , was previously investigated by Holland *et al.* in 2008 as a radiopharmaceutical agent for the treatment of hypoxic cells.¹⁹⁴ In their studies, electrochemical characterizations were performed in an array of conditions, including under slightly acidic reducing conditions (22 mM maximum). In that report, the authors state that they observe the production of hydrogen, however, no complete analysis of these observations was provided. In this study, we reexamine these findings while continuing our pursuit of alternate HER strategies which avoid metal-hydride intermediates, and provide a more complete report of ligand-centered HER activity observed with the bis(thiosemicarbazonato)Cu(II) complex, CuL^1 , Scheme 7.

5.2. Results and Discussion

5.2.1. CuL^1 Cyclic Voltammetry HER Studies



Scheme 7. Representation of thiosemicarbazone based electrocatalysts.

Building upon our previous work, the neutral, monomeric complex diacetyl-bis(N-4-methyl-3-thiosemicarbazonato)Cu(II), CuL^1 , was evaluated as HER electrocatalyst, Scheme 7. The synthesis and single crystal x-ray structure of CuL^1 was originally reported by Dilworth *et al.*^{195,196} The CuL^1 compound was isolated as air-stable burgundy solid from H_2L^1 and copper(II) acetate per prior methods (described in Chapter II).

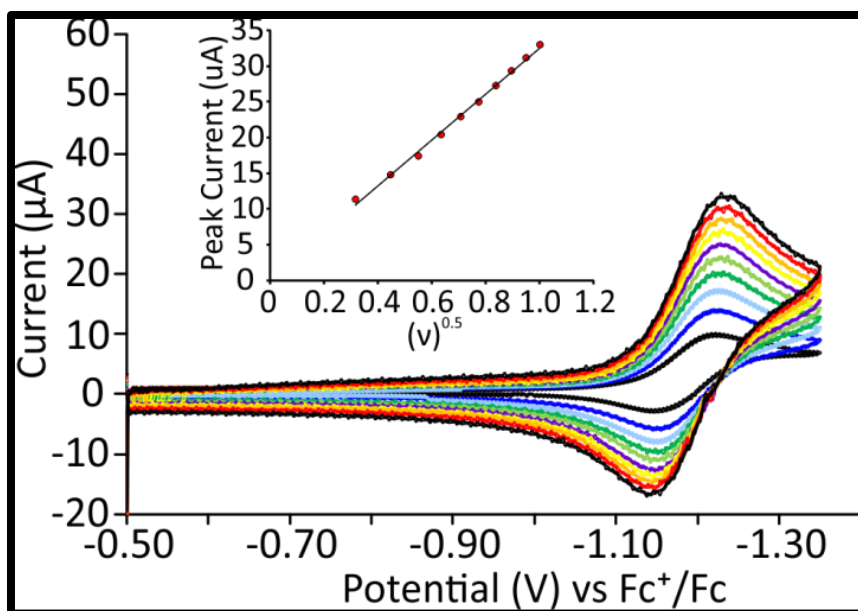


Figure 40. CVs of CuL^1 in 0.1 M Bu_4NPF_6 acetonitrile solution at scan rates of 0.1 (black), 0.2 (blue), 0.3 (light blue), 0.4 (green), 0.5 (light green), 0.6 (purple), 0.7 (yellow), 0.8 (orange), 0.9 (red) and 1.0 (black) V/s. CuL^1 . **Inset:** Cottrell plot of peak current vs square root of scan rate.

The cyclic voltammogram (CV) of CuL^1 in acetonitrile containing 0.1 M Bu_4NPF_6 as supporting electrolyte displays a reversible $\text{Cu}^{\text{II/I}}$ event at -1.20 V vs. Fc^+/Fc consistent with prior reports. Additional CV data collected at multiple scan rates from 0.1 to 1.0 V/s (Figure 40) were used to construct Cottrell plots (Figure 40, inset) establishing that the $\text{Cu}^{\text{II/I}}$ reduction is diffusion limited and demonstrating the potential of CuL^1 as a homogeneous electrocatalyst. The slope of the plot yields a diffusion coefficient of $7.9 \times 10^{-6} \text{ cm}^2/\text{s}$. The catalytic activities for hydrogen evolution were then evaluated in two solvents, acetonitrile and dimethylformamide (DMF).

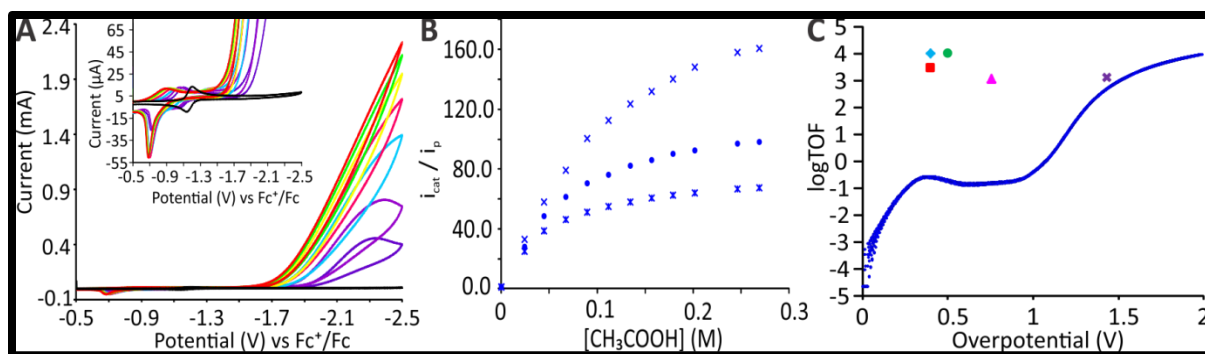


Figure 41. (A) CVs of 0.6mM CuL^1 (black) in 0.1M Bu_4NPF_6 acetonitrile with 0.0244 (purple), 0.0448 (light purple), 0.0896 (light blue), 0.134 (pink), 0.179 (yellow), 0.244 (light green) and 0.269 (red) M CH_3COOH , **Inset.** Blow up of CV showing shift of $\text{Cu}^{\text{II/I}}$ reduction event. (B) Plot of i_{cat}/i_p vs $[\text{CH}_3\text{COOH}]$ for 0.60 mM CuL^1 (blue) at scan rates of 0.20 (X), 0.50 (●) and 1.00 (*) V/s (C) Catalytic Tafel Plot of CuL^1 (blue) with comparison of performance for hydrogen evolution with those of others reported in literature. Blue \diamond : $\text{Co}^{\text{II}}(\text{dmgH})_2\text{py}$; green \bullet : $[\text{Ni}(\text{P}_2^{\text{PhN}^{\text{Ph}}})_2]^{2+}$; red \blacksquare : NiL^2 ; magenta \blacktriangle : ZnL^1 ; purple X: H_2L^1 .¹⁹⁷

Addition of acetic acid to 0.6 mM acetonitrile solutions of CuL^1 shifts the $\text{Cu}^{\text{II/I}}$ potential from -1.20 V to -0.95 V and introduces a catalytic cathodic current at -1.70 V vs Fc^+/Fc (Figure 41A). The +0.25 V shift is consistent with a single protonation event prior to the initial electrochemical reduction (Figure 41A, inset).⁷⁷ The catalytic current intensity at -1.70 V displays linear dependence on the concentration of acid, indicating diffusion control to the electrode and confirming a first-order dependence on acid concentration.¹⁰ At concentrations greater than 0.269 M, catalytic current saturates at a maximum value of 2.25 mA (Figure 41B). The i_p of $\text{Cu}^{\text{II/I}}$ reduction event, 14.0 μA , and the i_{cat} max of 2.25 mA correspond with a maximum i_{cat}/i_p value of 161, affording a TOF of 9,900 s^{-1} .¹²⁰⁻¹²³

Catalytic activity was also assessed in DMF. CVs of 0.6 mM CuL^1 in 0.1 M Bu_4NPF_6 DMF solutions exhibit an increase in current at -1.9 V vs Fc^+/Fc upon increasing additions of acetic acid (Figure 42A). At concentrations of acid greater than

0.292 M, the current saturates reaching a maximum i_{cat} of 1.49 mA (Figure 42B). Acid addition results in the same shift of the $\text{Cu}^{\text{II/I}}$ potential from -1.20 V to -0.95 V, as observed in acetonitrile, which is consistent with previous reports suggesting a single protonation event prior to reduction.¹⁹⁴ Catalytic current becomes independent of scan rate above 1.0 V/s. Under these conditions when i_{cat} is 1490 μA and i_p is 29 μA , the TOF is estimated to be 5140 s^{-1} , significantly lower than values observed when performed in acetonitrile.

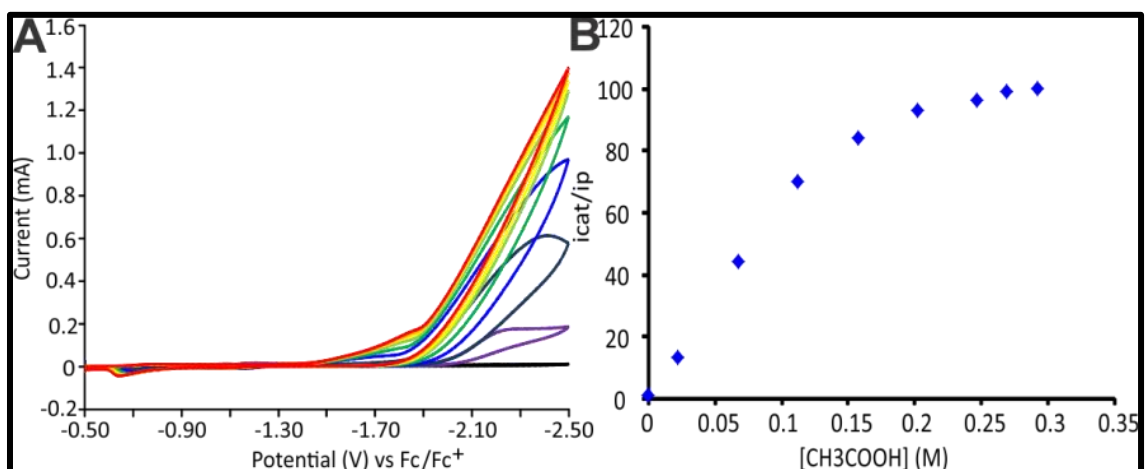


Figure 42. (A) CVs of 0.6mM CuL^1 (black) in 0.1M Bu_4NPF_6 DMF with 0.0244 (light purple), 0.0448 (purple), 0.0896 (blue), 0.157 (green), 0.202 (light green), 0.246 (yellow), 0.269 (orange). And 0.292 (red) M CH_3COOH . (B) Plot of i_{cat}/i_p vs $[\text{CH}_3\text{COOH}]$ concentration.

Control CVs containing only acetic acid were run in acetonitrile and DMF. Addition of 67.2 mM acetic acid to of 0.1 M Bu_4NPF_6 acetonitrile solutions resulted in an observable current of 300 μA . However after 2 CV cycles the current drops to a stable value near 100 μA . Upon addition of 0.6 mM CuL^1 , the current increases to 900 μA (see appendix). In DMF addition of 22.4 mM acetic acid results in almost no current increase, giving current values of roughly 5 μA . Addition of 0.6 mM CuL^1 to this solution resulted in an

increase, giving a value of 200 μA (see appendix) Higher concentrations of acetic acid were also performed as controls. Addition of 0.292 M acetic acid to 0.1 M Bu_4NPF_6 DMF solutions results in a current value of 50 μA . Upon addition of 0.6 mM CuL^1 results in an increase of current to 650 μA (see appendix).

The Tafel plot of the log TOF versus overpotential for CuL^1 (Figure 41C) represents the TOF activity as a function of the applied overpotential.¹⁹⁷ CuL^1 displays the highest maximum logTOF values reported to date of any homogeneous ligand-centered electrocatalyst, reaching a maximum of 3.99. The CuL^1 electrocatalyst maintains a logTOF value greater than one, with applied overpotentials greater than 1.2 V. Overpotentials less than 1.2 V result in significantly decreased TOF values, correlating with negative or near zero logTOF values. The local maxima observed near 0.4 V is indicative of the pre-catalytic $\text{Cu}^{\text{II/I}}$ reduction, which has an anodic shift of 0.25 V during catalysis.

The maximum logTOF for CuL^1 of 3.99 requires a large overpotential of 2.0 V. Comparatively, state of the art metal-hydride HER electrocatalysts, such as nickel-bis(diphosphine) and cobaloxime exhibit logTOF values of 4.00 at overpotentials of 0.50 and 0.40 V, respectively.¹⁹⁷ Our previously reported ligand-centered electrocatalysts ZnL^1 and H_2L^1 have lower maximum logTOF values than CuL^1 , but they achieve logTOF values of 3.06 and 3.12 at lower overpotentials of 0.75 and 1.4 V, respectively.⁷⁶ Artero's related NiL^2 electrocatalyst achieves a maximum logTOF of 3.50 at an overpotential of 0.4 V, similar to the state of the art metal-hydride HER catalysts.⁸⁸

5.2.2. CuL¹ Extended Stability: Controlled Potential Coulometry and Gas Identification

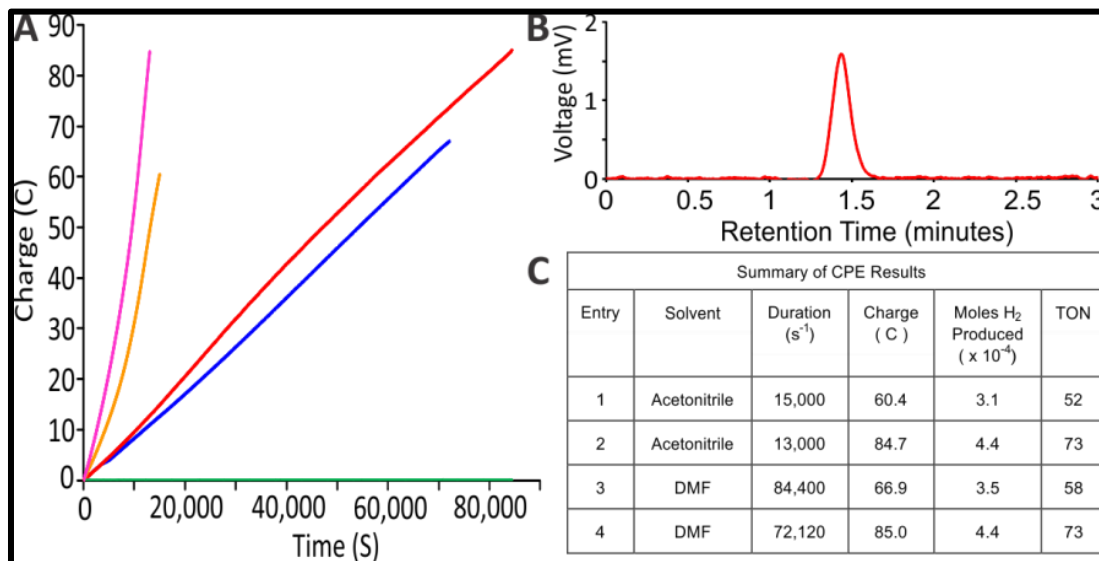


Figure 43. (A) Bulk electrolysis showing plot of charge versus time of 0.6mM CuL¹ in 0.1 M Bu₄NPF₆ acetonitrile (pink and orange) and in 0.1 M Bu₄NPF₆ DMF (red and blue) with 0.292M CH₃COOH added. Blank acetonitrile (green). (B) GC-TCD headspace readout of H₂ from electrolysis. (C) Summary of CPE results.

A series of controlled potential electrolysis (CPE) experiments were performed using 0.6 mM CuL¹ and 0.292 M acetic acid, held at -1.7 V vs Fc⁺/Fc (the potential of half maximum catalytic current), in both DMF and acetonitrile (Figure 43A). Electrolysis in 0.1 M Bu₄NPF₆ DMF solutions was as allowed to run for 84,400 seconds (23.4 hours) resulting in a total charge passed of 85 C, corresponding to 4.4 x 10⁻⁴ moles of H₂ produced with a turnover number (TON) of 73.3. Gas analysis of the headspace was analyzed using gas chromatography thermal conductivity (GC-TCD) (Figure 43B), confirming H₂ as the gaseous product. The growth of charge during the electrolysis remained linear over the course of the experiments and showed no signs of degradation or decrease in activity over 23 hours. A second CPE in DMF over 72,120 seconds (20 hours) yielded similar results giving a slightly lower charge of 66.96 C, producing 3.5 x

10^{-4} moles of H_2 corresponding with a TON of 58.3. CPE's performed in 0.1 M Bu_4NPF_6 passed similar charge, giving values of 60.43 and 84.74 C corresponding to TON values of 51.7 and 73.3 over electrolysis times of 15,000 and 13,000 respectively. In contrast to CPE's performed in DMF, the growth of the charge with respect to time is much steeper, possibly indicating that the HER reaction proceeds faster in acetonitrile, which is consistent with CV studies which indicate that the HER TOF in acetonitrile is approximately twice as fast than when performed in DMF. After 15,000 of electrolysis in acetonitrile solutions, the auxiliary compartment began to become discolored, changing from the clear solution which initially is just 0.1 M Bu_4NPF_6 , to a cloudy brown color, suggesting diffusion of some species across the frit from the working compartment. Around the same time when this happens, the charge begins to plateau reaching a maximum value. All CPE trials in acetonitrile resulted in diffusion across the frit, thus only shorter electrolysis's were able to be performed.

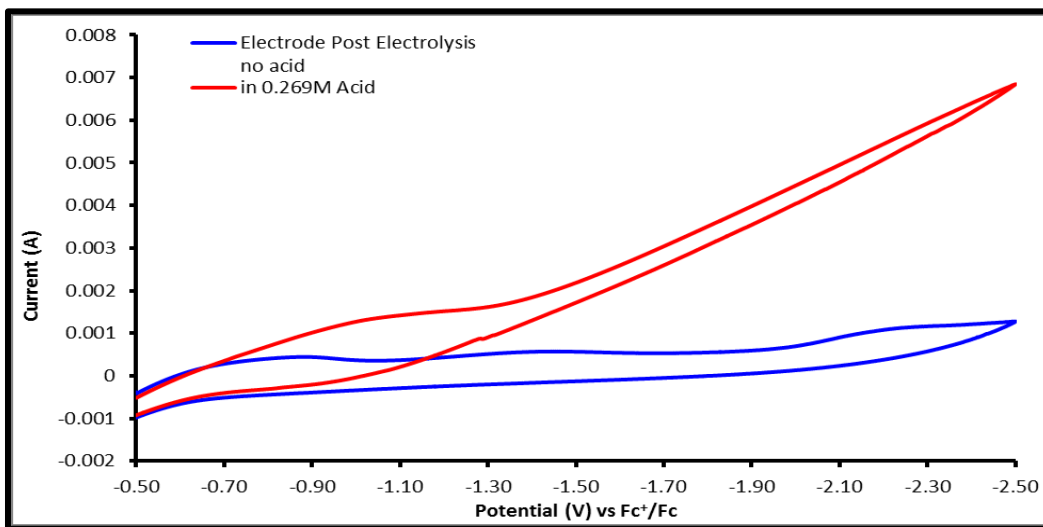


Figure 44. Dip test post electrolysis in acetonitrile: After electrolysis working electrode was rinsed with water and immersed in a fresh solution of 0.1 M Bu_4NPF_6 acetonitrile

solution and a CV was recorded (blue). 0.269 M acetic acid was then added and a CV was obtained (red)

After electrolysis, dip-tests were performed on the working glassy carbon electrode to identify any potential electrode adsorbed species. In both DMF and acetonitrile, the electrode was removed and washed with D.I water and then immersed into a fresh 0.1 M Bu_4NPF_6 DMF/acetonitrile solution and a CV was run. In both cases the electrode displays a reduction event near -0.9 V, the same potential at which $[\text{CuL}^1\text{H}]^+$ is observed during CV studies, suggesting that the adsorbed species may be $[\text{CuL}^1\text{H}]^+$. Upon addition of acetic acid to these new solutions current increases and catalysis is observed (Figure 44). Recently, Dempsey and co-workers reported that protonation of the unreduced cobalt dithiolene HER catalyst results in an electrode adsorbed intermediate which regenerates the homogeneous cobalt complex upon reduction.¹⁹⁸ Using the methods of Dempsey and co-workers we then performed a “soak test”, in which the working electrode was left to sit in a 0.1 M Bu_4NPF_6 acetonitrile solution with 0.6 mM CuL^1 and 0.292 M acetic acid. The electrode was left immersed in the solution overnight. The electrode was then removed and put into a fresh solution of 0.1 M Bu_4NPF_6 acetonitrile solution with no added acid or catalyst. A CV was run, and no redox events were observed, suggesting that electrode adsorption occurs only under reducing conditions, contrary to what is observed by Dempsey and co-workers. The electrode adsorbed films that resulted post electrolysis in DMF and acetonitrile were then scraped off of the electrode and collected for analysis by x-ray photoelectron spectroscopy, in order to gain insight into its composition. We are currently awaiting these results.

5.2.3. Mechanistic Insights

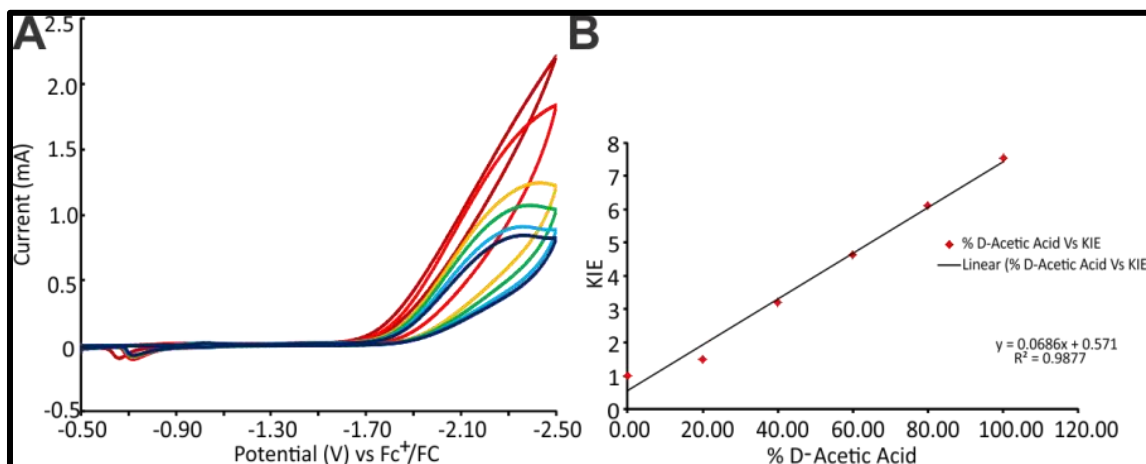


Figure 45. (A) CVs of 0.6 mM CuL¹ in 0.1 M Bu₄NPF₆ acetonitrile solution with 0.269 M acetic acid, from 0-100% D-acetic acid use. (B) Plot of %D-Acetic acid use vs KIE.

To further evaluate the HER mechanism of CuL¹, we examined the H/D kinetic isotope effect (KIE). Using deuterated acetic acid CD₃CO₂D, the CuL¹ catalyst displays a large KIE of 7.54, suggesting that the rate-determining step involves the breaking/making of labeled acid substrate. In order to gain more insight into the nature of this transition, CVs were run in 0.1 M Bu₄NPF₆ acetonitrile solution with 0.269 M acetic acid added. The percent fraction of CD₃CO₂D was increased from 0 to 100% in increments of 20%. (Figure 45A). The ratio of the observed reaction rates relative to the rates obtained when not using CD₃CO₂D were interpreted in order to obtain KIE values. These were then plotted against their respective percent CD₃CO₂D concentrations yielding a linear fit, with KIE values ranging from 1 at 0% CD₃CO₂D, to 7.54 when using 100% CD₃CO₂D (Figure 45B). The linear response of the KIE with respect to the percent CD₃CO₂D used suggests a RDS with a concerted bond making/breaking process, in which both hydrogen atoms are equivalent. The high KIE value observed when using

100% $\text{CD}_3\text{CO}_2\text{D}$ are distinct from the inverse KIEs reported for some HER catalysts proceeding through metal-hydrides,¹⁶⁷ but similar to that observed for a ligand-centered Re-thiolate HER catalyst.⁷⁷ It has been reported previously that KIE values exceeding seven, may implicate some semblance of quantum tunneling.^{168,169,199,200}

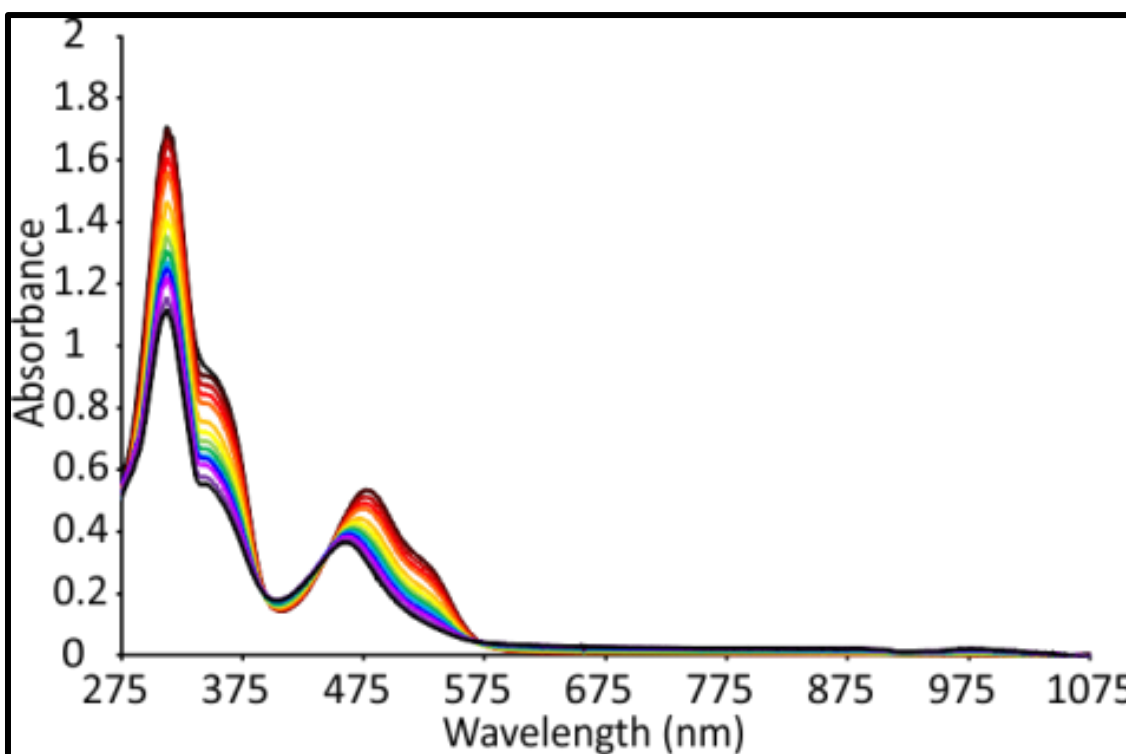


Figure 46. UV-Visible spectrum of CuL^1 titrated with acetic acid; 0.022 (dark red), 0.044 (red), 0.056 (light red), 0.067 (orange), 0.089 (light orange), 0.112 (yellow), 0.134 (light green), 0.157 (green), 0.202 (sky blue), 0.244 (blue), 0.269 (magenta), 0.292 (light blue), 0.337 (purple), and 0.382 (black) M.

In order to confirm that protonation of CuL^1 occurs before electrochemical reduction, UV-Visible spectroscopy acid titrations were performed. 0.6 mM CuL^1 was dissolved into deoxygenated DMF and the UV spectrum was recorded showing an absorbance bands at 310, 375, 475 and 520 nm. The solution was then titrated with acetic acid increasing in concentration from 0.022 M to 0.382 M. Upon increasing additions, the

absorbance bands at 310, 375, 475, and 520 decrease in intensity concurrent with an increase in intensity of new bands at 405 and 460 nm, yielding isosbestic points near 380 and 450 nm, consistent with the formation of the protonated intermediate, $[\text{CuL}^1\text{H}]^+$ (Figure 46).

^1H NMR further confirms the hydrazino nitrogen as the site of protonation. In the glove box, 6×10^{-6} moles of CuL^1 was dissolved in DMSO-d_6 , to which one equivalent of cobaltocene was added and stirred for 15 minutes in order to achieve the reduced anionic copper(I) complex $[\text{CuL}^1]^-$. Upon addition and stirring with cobaltocene, the solution changed color from red to light purple. An aliquot was syringed out and injected into an NMR tube for analysis. The spectrum of $[\text{CuL}^1]^-$ displays the expected peaks values with chemical shifts at 2.726, 2.886, and 7.948 ppm, integrated 3:3:1, consistent with methyl backbone CH_3 , $\text{NH}(\text{CH}_3)$, and NH , respectively. Upon addition of one equivalent of HBF_4 , the solution changes color from light purple to orange. An aliquot was taken and analyzed by ^1H NMR. All the previously identified peaks observed in $[\text{CuL}^1]^-$ are present, along with a new peak at 8.266 ppm, which integrates to 1. We assign this as the protonation of the hydrazino nitrogen. If protonation were to occur on the copper center to generate a copper hydride, a negative chemical shift would have been observed in the ^1H NMR spectrum; however, this region of the spectrum is void of any peaks.

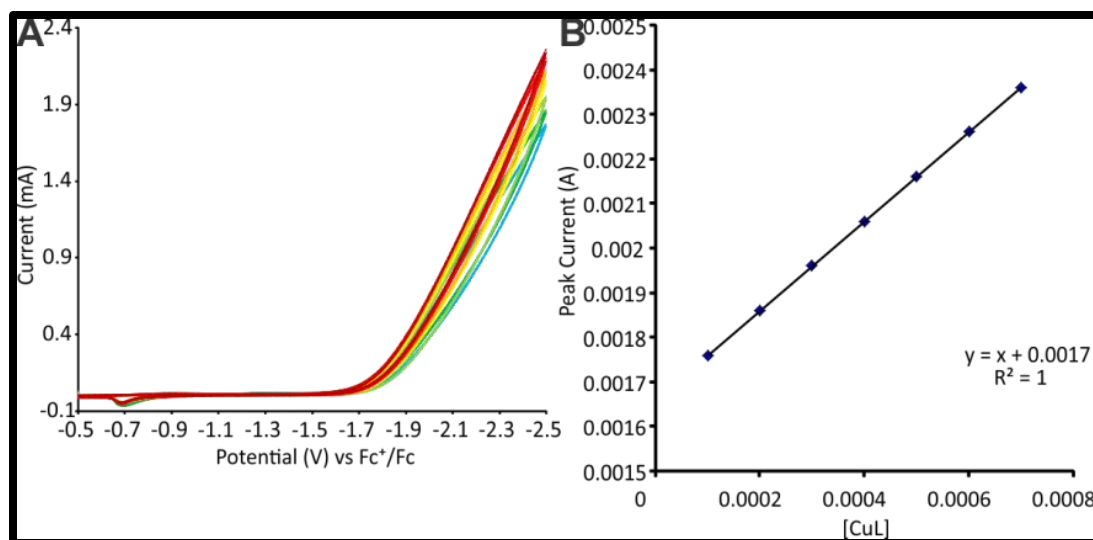


Figure 47. (A) Cyclic Voltammograms run in 0.1 M Bu₄NPF₆ acetonitrile solution with 0.269 M acetic acid added run with 0.1 (light blue), 0.2 (green), 0.3 (light green), 0.4 (yellow), 0.5 (orange), 0.6 (red), and 0.7 (dark red) mM CuL¹. (B) Plot of peak current versus catalyst concentration showing linear dependence and 1st order relationship.

Further insight into the mechanism was gained by examining the order of the reaction with respect to the concentration of the catalyst. The concentration of CuL¹ was varied from low to high at fixed acid concentrations, and peak currents from CVs were measured at each catalyst concentration. A plot of catalyst concentration versus peak current resulted in a linear relationship, confirming a first-order dependence on the concentration of the catalyst (Figures 43A and 43B).

5.2.4. CuL¹ Density Functional Theory Study

Density functional theory (DFT) calculations using the B97-D functional¹⁴⁷ and the 6-311g(d,p) basis set support the proposed mechanism in Figure 45 and help to elucidate the favored protonation and reduction sites. For [CuL¹H]⁺ (S = 1/2), the Cu, S, and each N were evaluated as possible H⁺ locations. For each structure, the geometry and frequencies were optimized and energy minimizations were performed. The hydrazino

protonated $[\text{CuL}^1\text{H}]^+$ species is energetically preferred, lying 10 kcal/mol lower than the metal-hydride (Figure 46A and Figure 47). Protonation at S is less favored by 12 kcal/mol. Attempts to optimize structures with protonation of the pendant amine nitrogen or coordinated imine nitrogen resulted in migration of the hydrogen onto the hydrazino nitrogen.

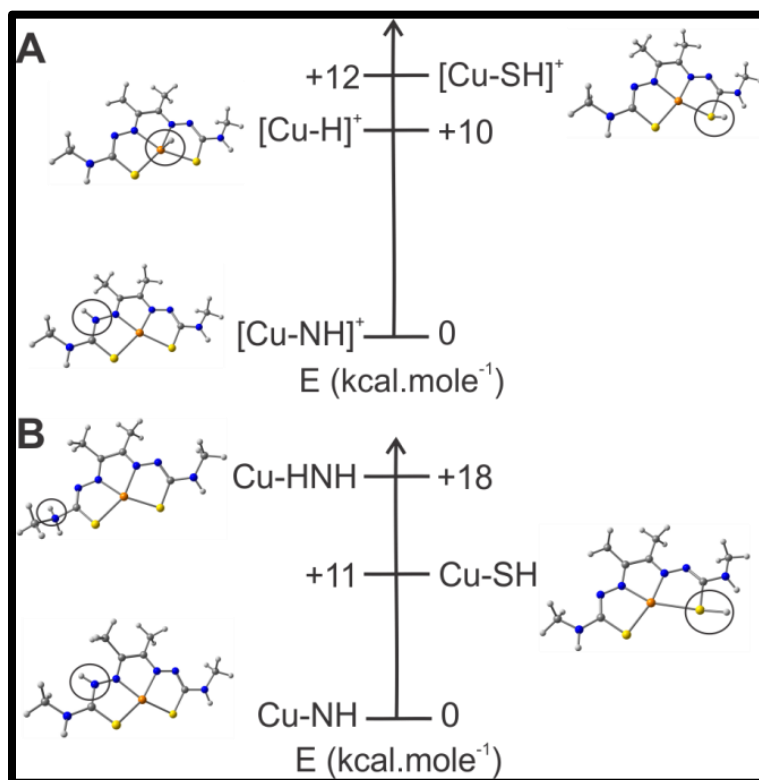


Figure 48. (A) Energetic stability of protonated species, $[\text{CuL}^1\text{H}]^+$. (B) Energetic Stability of protonated and reduced species, CuL^1H .

We also examined the site of protonation in the one-electron reduced protonated species, CuL^1H ($S = 0$) (Figure 46B and Figure 48). Computed free energies for structures with protonation at Cu, S, and each N, clearly indicate that protonation on the hydrazino N is favored, lying 11 kcal/mol lower than protonation at S. Protonation at the

pendant amine is less favored by 18 kcal/mole. Attempts to optimize CuL^1H with protonation at the coordinated nitrogen again resulted in migration of hydrogen onto the hydrazino nitrogen. Calculations performed using B3LYP gave similar results. This is in contrast to recent calculations on NiL^2H , which indicated the coordinated nitrogen is the site of protonation.⁸⁸

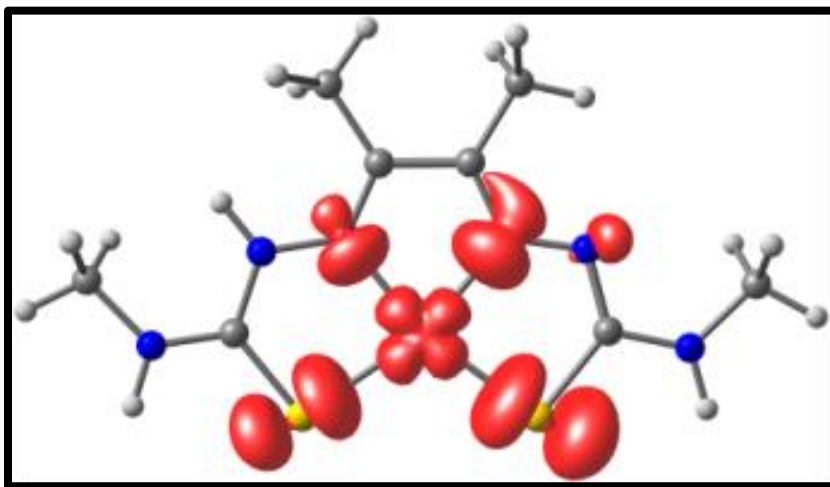


Figure 49. Spin-density map of $[\text{CuL}^1\text{H}]^+$.

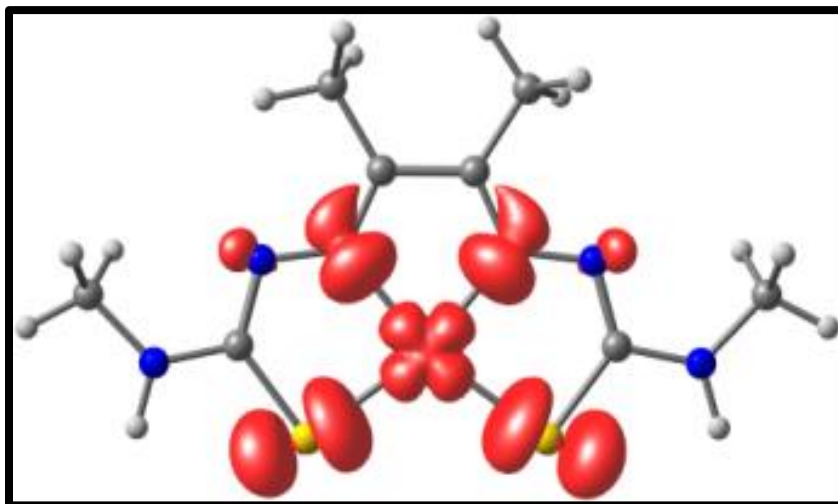
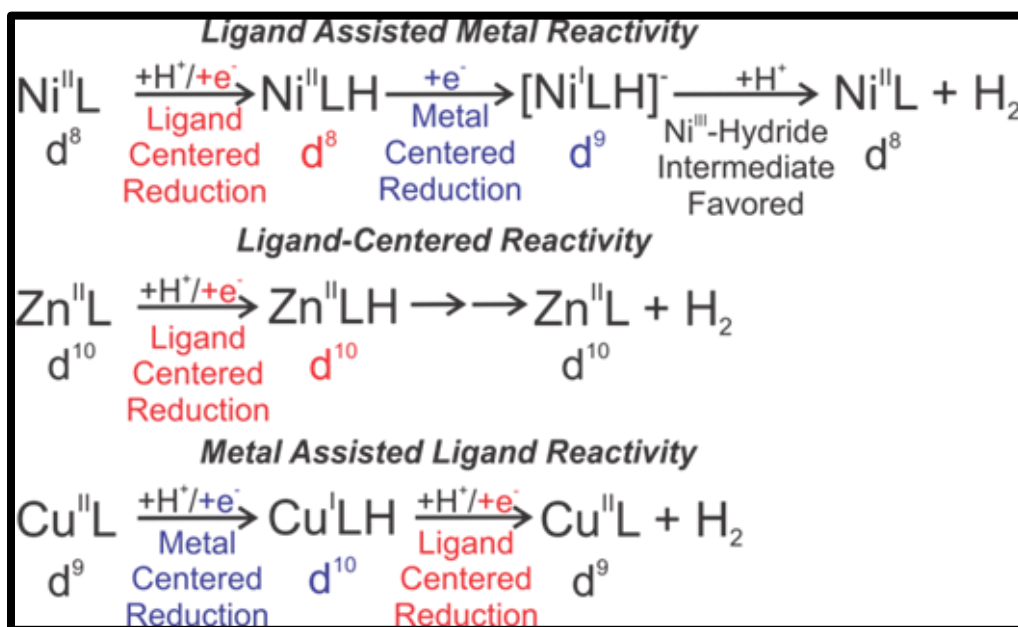


Figure 50. Spin-density map of CuL^1 ($S=1/2$).

5.2.5. Overview of CuL^I and Comparison with ZnL^I, H₂L^I and Other HER Electrocatalysts.

Thiosemicarbazone ligands and their metal complexes are relatively new to the field of electrochemical proton reduction, but are emerging as an important class of HER catalysts. The current work represents the 5th thiosemicarbazone motif to be reported as an active HER catalyst since the first report at the end of 2015.^{76,88,201} These complexes present intriguing reactivity as the thiosemicarbazone ligand can participate in electron transfer events, either with or without a transition metal—rendering it “*non-innocent*”. However, a long held question, which often arises in the field of redox-active ligand chemistry, is whether the radical character of the ligand can be used to promote reaction chemistry at the ligand.²⁰²



Scheme 8. Comparison of thiosemicarbazone HER electrocatalysts.

Thiosemicarbazone HER catalysts have shed light onto this question. The impact of the ligand non-innocence is dependent on the metal ion, Scheme 8, which can result in ligand-assisted metal reactivity, purely ligand-centered activity, or metal-assisted ligand reactivity. The NiL^2 catalyst demonstrates ligand-assisted metal reactivity that is proposed to involve initial ligand-centered reduction and protonation followed by metal-centered reduction.⁸⁸ The initial ligand reactivity allows the second reduction to occur at the d^8 Ni(II) generating a nucleophilic d^9 Ni(I). Straistari *et al.* posit that given the nature of the second reduction as metal-based, the site of the second protonation is likely on the Ni, generating a Ni^{III} -hydride as the catalytically active species for H_2 evolution. In this context, NiL^2 can be viewed in the traditional sense of ligand non-innocence, in which the ligand serves as an auxiliary redox site to facilitate two-electron chemistry at the metal site.

The HER chemistry of ZnL^1 demonstrates a strictly ligand-centered mechanism with all chemical and electrochemical reactivity being localized on the ligand, with the metal providing structural support. As in the case of NiL^2 , initial protonation and reduction is ligand-centered, however, the d^{10} Zn(II) metal center is incapable of undergoing reduction and HER proceeds via a purely ligand-centered, bimolecular process.⁷⁶

For CuL^1 , the d^9 electron configuration of Cu(II) favors metal-assisted ligand reactivity. CuL^1 undergoes an initial protonation at the energetically preferred hydrazino nitrogen, followed by a metal based reduction. The resulting CuL^1H , d^{10} Cu(I), is isoelectronic with ZnL^1 . As such, CuL^1H favors ligand-based protonation and reduction similar to ZnL^1 , as opposed to metal-hydride formation as proposed for $[\text{NiL}^2\text{H}]^-$. This

results in H₂ evolution at the protonated hydrazino nitrogen to regenerate CuL^I. In this context, CuL^I can be viewed as atypical ligand non-innocence, where the metal serves as the auxiliary redox site to facilitate two-electron chemistry at the ligand.

The metal-assisted ligand reactivity of CuL^I for H₂ evolution involves an initial protonation before electrochemical reduction to produce [CuL^IH]⁺. This species is then reduced by one electron to generate the neutral intermediate, CuL^IH. This intermediate can then be reduced in order to generate the anion, [CuL^IH]⁻, which then reacts with a free proton in solution to evolve H₂. However, due to adsorption onto the electrode surface during prolonged electrolysis when held at cathodic potentials, we cannot discount the possibility that the catalytically active species for H₂ evolution is this adsorbed film. We are currently investigating this in order to determine if all observed catalysis is due to the electrode adsorbed film, or if adsorption generates some alternate species, which also catalyses HER in a heterogeneous fashion, in addition to the observed homogeneous catalysis via CuL^I. Nonetheless, the identification of this third type of reaction mechanism employing redox-active ligands represents an important step in the development of further redox-active based catalysts for HER and the activation of small molecules.

5.3. Conclusions

In summary, the CuL^I electrocatalyst demonstrates that Cu^{II} metals, when paired with robust redox-active ligands can demonstrate high activity as HER catalysts. This further confirms that organic redox-active ligands have the ability to store and transfer electrons in the ligand and work in unison with late transition metals in order to carry out catalysis. To the best of our knowledge, the CuL^I electrocatalyst exhibits the highest reported TOF

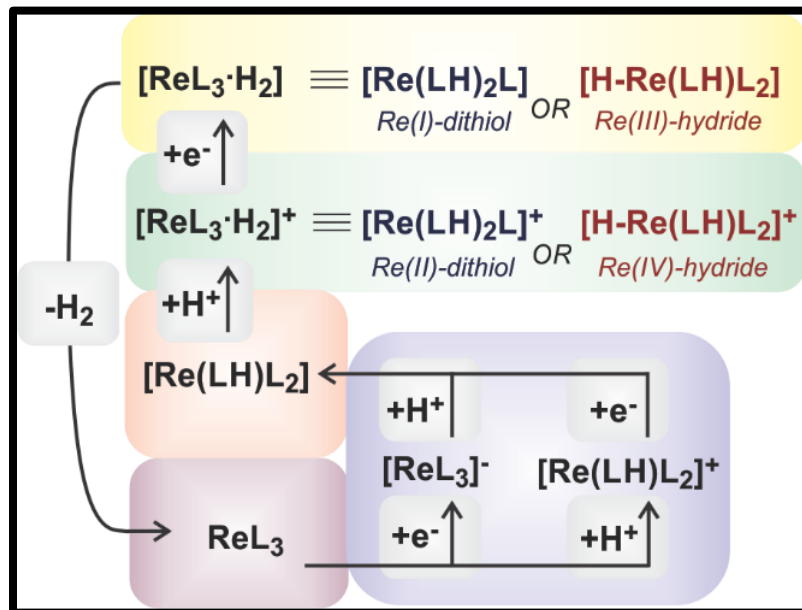
of any ligand-centered homogeneous HER catalysts to date, however, its high activity coincides with substantially large overpotentials. This signifies the need for the development of new thiosemicarbazone ligands that employ more electron-donating auxiliary R group's which should greatly increase proton binding affinity, as well as drastically lower overpotentials. Thiosemicarbazones and thiosemicarbazonato frameworks display significant potential for hydrogen evolution, and demonstrate that incorporation of redox-active ligands into HER systems could potentially lead to a new class of HER electrocatalysts.

5.4. Acknowledgement

This research shown in Chapter Five was funded in part by the National Science Foundation (CHE-1361728) and a grant from the Kentucky Science and Engineering Foundation as per grant agreement no. KSEF 148-502-15-350 with the Kentucky Science and Technology Corporation. The authors are thankful to Cardinal Research Cluster at the University of Louisville for providing the computational facilities. A provisional patent has been filed on the work described in chapter 5.

CHAPTER VI: CONCLUSIONS

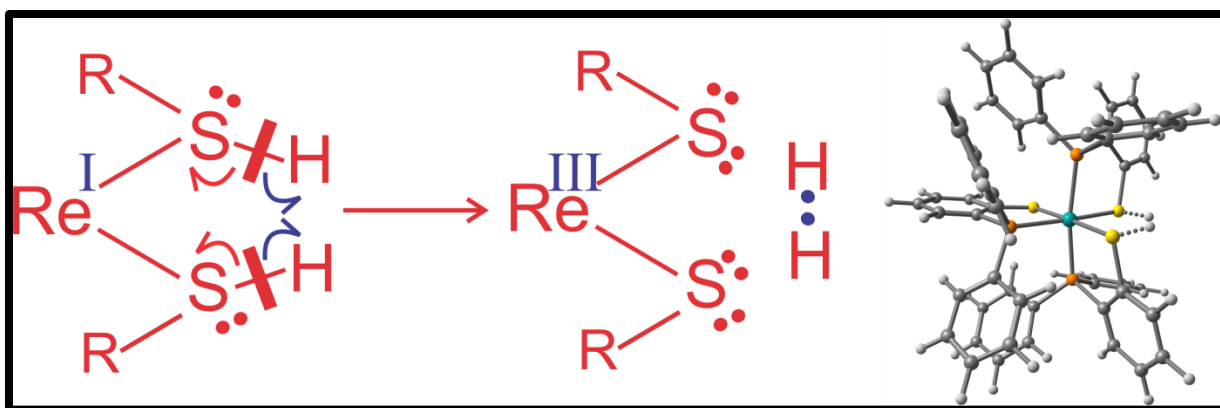
6.1. Ligand-Centered Electrochemical Hydrogen Evolution and Hydrogen Oxidation



Scheme 9. ReL_3 HER mechanism

Homogeneous electrochemical studies were performed to assess ReL_3 as an electrocatalyst for H_2 evolution and oxidation.⁹ Homogeneous studies show that ReL_3 reduces acid in CH_2Cl_2 to H_2 with an overpotential of 0.708 V and a turnover frequency of $32 \pm 3 \text{ s}^{-1}$ via a unimolecular mechanism. Additionally, ReL_3 oxidizes H_2 in the presence of base at an overpotential of 0.970 V with a turnover frequency of $4 \pm 1 \text{ s}^{-1}$. To our knowledge, this is one of four published electrocatalysts which can perform both the HER and HOR reaction.^{76,77,203} Furthermore, it was the first ligand-centered HER/HOR electrocatalyst reported. The HER mechanism, Scheme 9, is consistent with experimental results and further supported by density functional theory. Further, computational studies, including location of the transition state and intrinsic reaction coordinate analysis, identified the H_2 evolving complex as a Re-dithiol that generates H_2 through a radical

coupling mechanism. The process involves homolytic S-H bond cleavage with no formation of metal-hydride intermediates, Scheme 10. The results represent the *first example* of a ligand-centered HER mechanism to be validated through a rigorous combination of study.



Scheme 10. Representation of homolytic S-H bond cleavage leading to H₂ evolution via radical coupling and calculated transition state for H₂ evolution.

While unprecedented in homogeneous mononuclear systems, there have been numerous reports of heterogeneous H₂ production electrocatalysis that are believed to proceed without the formation of metal-hydrides.^{100,101,172,204-206} The unique reactivity observed with ReL₃ could be attributed to a sterically crowded, kinetically inert, and coordinatively saturated metal center that prevents facile formation of metal hydride, rather favoring dithiol formation and H₂ evolution via homolytic S-H bond cleavage. This type of reactivity is not unusual for these complexes, as the non-innocent ligands in ReL₃ are known to react with small molecule substrates in a ligand-centered process.^{98,152,153} This could explain the unusual KIE and bifunctional (H₂ evolution and H₂ oxidation) activity of ReL₃. Nonetheless, this work represents a valuable jumping off point into the

field of strictly ligand-centered catalysis, and the lessons learned will undoubtedly be pivotal in the future design of other small molecule activation catalysts.

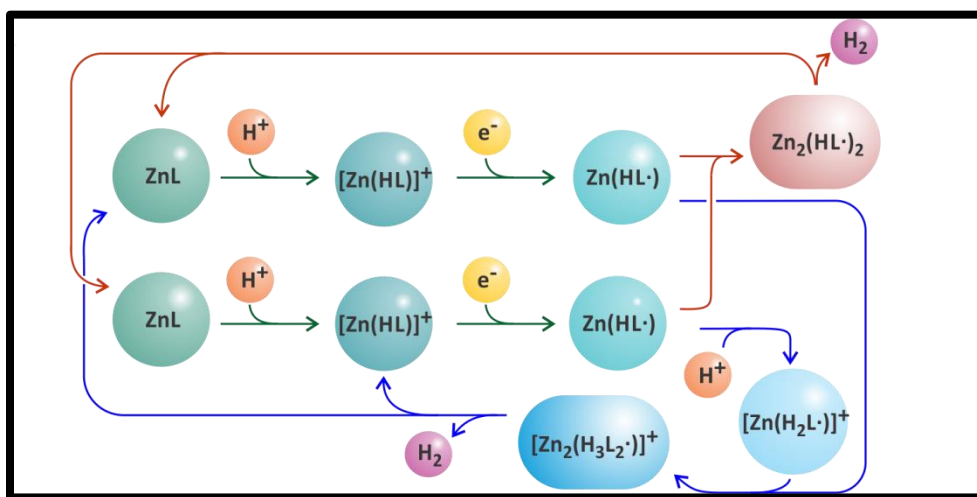
A significant disadvantage of the ReL_3 catalyst is the inclusion of the precious metal Re. As noted previously, our mechanistic studies indicate the metal is not directly involved in the HER/HOR, rather serving as an auxiliary source of electrons. This suggests similar first-row transition metal (Ni) or even non-transition metal (Zn) complexes employing the diphenylphosphinebenzenethiolate ligand may catalyze HER/HOR. Currently efforts in our lab are underway to investigate the NiL_2 and the ZnL_2 complexes for electrocatalytic small molecule activation.

6.2. Sustainable Metal Alternatives for Ligand-Centered H_2 Evolution Oxidation

The ReL_3 system opens the door to novel pathways and alternative strategies for catalytic HER development. However, the system suffers from significant limitations including: 1) incorporation of a non-sustainable precious metal; 2) the ligand synthesis requires multiple steps that are air, moisture, and/or light sensitive performed under inert conditions; 3) catalysis is limited to halogenated organic solvents; 4) modification of the ligand structure requires an individualized approach for each new derivative; and 5) large complex size/^{3rd} row transition metal complicates computational studies of the mechanism.

In lieu of this, we developed new catalysts based on the non-innocent bis-thiosemicarbazone ligand H_2L^1 (L^1 =diacetyl-bis(N-4-methyl-3-thiosemicarbazide). H_2L^1 represents the first homogeneous metal-free HER catalyst, ZnL^1 is the most active transition metal free HER catalyst.⁷⁶ Further, these systems overcome the limitations

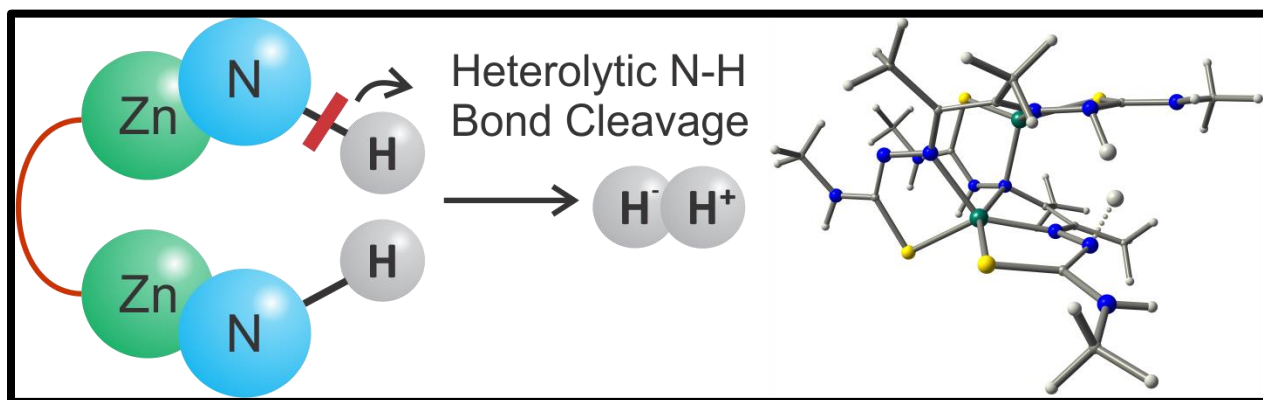
noted above as they: 1) incorporate sustainable first-row metals; 2) the ligand syntheses require no specialized skills and can be performed on the benchtop in water and/or alcohol using inexpensive synthons; 3) catalysis occurs in water/alcohol or acetonitrile; 4) the framework is easily derivatized and very stable to hydrolysis; 5) the structures are small with metals that are well calibrated from a computational perspective.



Scheme 11. Proposed mechanism for H₂ evolution by ZnL¹.

As previously discussed, the ligand diacetyl-bis(N-4-methyl-3-thiosemicarbazone) (H₂L¹) and its Zn complex (ZnL¹) display the highest reported TOFs of any homogeneous ligand-centered H₂ evolution catalyst, 1320 s⁻¹ and 1170 s⁻¹ respectively, while the zinc complex also displays one of the highest reported TOF values for H₂ oxidation, 72 s⁻¹, of any homogeneous catalyst. Controlled potential coulometry experiments show a Faradaic efficiency of 85% and a turnover number of 36.7. The reaction proceeds through a bi-molecular mechanism, supported by digital simulations of voltammetric data and DFT, and culminates in H₂ release through parallel routes, Scheme 11. In both pathways, catalysis proceeds via ligand-centered proton-transfer and electron-

transfer events while avoiding traditional metal-hydride intermediates. The calculated transition state reveals a binuclear core comprised of two protonated and reduced equivalents of ZnL^1 . Analysis of the intrinsic reaction coordinates indicates heterolytic cleavage of one hydrazino N-H bond to release H^- , which deprotonates the neighboring hydrazino N-H to evolve H_2 , Scheme 12, and regenerate the mononuclear ZnL^1 complexes. The results represent the second example from our research team of a validated ligand-centered HER mechanism. To our knowledge, the HER mechanisms presented in this dissertation for ReL_3 and ZnL^1 are the only two ligand-centered processes in the literature examined by a combined experimental simulations and computational investigations.



Scheme 12. Mechanism for H_2 evolution for ZnL^1 showing evolution through heterolytic N-H bond cleavage resulting in deprotonation of neighboring hydrogen and (right) the calculated transition state for H_2 evolution.

Other ligand-centered processes for HER/HOR are emerging. Initial work focused on heterogeneous systems including a metal-free HER catalyst based on N-doped graphene with graphitic-carbon nitride¹⁰⁰ and metal-free and zinc-phthalocyanines.^{101,105,106} Notable heterogeneous HOR electrocatalysts include a metal-

free frustrated Lewis pair¹⁰⁷ that is proposed to operate through a hydride intermediate similar to homogeneous Ni and Fe HOR catalysts. As previously discussed, an aluminum-bis(imino)pyridine complex was reported as a homogeneous, non-transition metal HER electrocatalyst with a TOF of 3.3 hr⁻¹.⁹⁹ Activity was attributed to a radical process involving homolytic C-H bond cleavage. A similar mechanism was proposed for a nickel “hangman”-porphyrin complex via a Ni phorlin intermediate, although no TOF was reported.¹⁷³ Recently, a heterobimetallic W-Ni complex employing a redox-active ligand was reported as a HER catalyst in acidic aqueous solutions with a cis-thiolate core proposed as the active site.¹⁷⁴

The recent development of ligand-centered HER/HOR catalysts underscores the need for alternate approaches to the traditional metal-hydride systems. From our own studies, it is clear the redox non-innocence and propensity of the framework to tautomerize hydrogen atoms makes the thiosemicarbazone ligand class an ideal choice for further examination of ligand-center HER/HOR electrocatalysis.

6.3. Transition Metal Assisted Ligand-Centered H₂ Evolution

Building off of the work using the non-innocent bis-thiosemicarbazone ligand H₂L¹ (L¹=diacetyl-bis(N-4-methyl-3-thiosemicarbazide), we then investigated its copper complex, CuL¹ as an electrocatalyst for hydrogen evolution. CuL¹ displays a turnover frequency (TOF) of 10,000 s⁻¹, the highest reported TOF values of any homogeneous ligand-centered H₂ evolution electrocatalyst. Gas analysis from controlled potential coulometry confirms CuL¹ as an electrocatalyst to produce H₂, with Faradaic efficiency of 86%. The H₂ evolution reaction (HER) was probed using deuterated acid, demonstrating a kinetic isotope effect of 7.54. The mechanism is proposed to involve

ligand centered protonation, metal-centered reduction and ligand-centered reduction in which hydrogen is evolved via solution proton and nitrogen-hydride coupling. The d^9 electron configuration of Cu(II) in CuL^1 favors metal-assisted ligand reactivity. CuL^1 undergoes an initial protonation at the energetically preferred hydrazino nitrogen, followed by a metal based reduction. The resulting CuL^1H , d^{10} Cu(I), is isoelectronic with the previously described ZnL^1 . As such, CuL^1H favors ligand-based protonation and reduction similar to ZnL^1 . This results in H_2 evolution at the protonated hydrazino nitrogen to regenerate CuL^1 . In this context, CuL^1 can be viewed as atypical ligand non-innocence, where the metal serves as the auxiliary redox site to facilitate two-electron chemistry at the ligand. The proposed homogeneous mechanism is further supported by density functional theory (DFT) calculations. However, due to the presence of an adsorbed film on the electrode post electrolysis, we cannot discount a heterogeneous electrode adsorbed film as the active species for hydrogen evolution.

We are currently trying to identify if adsorption generates some alternate species which also catalyses HER in a heterogeneous fashion, or if the observed catalysis is due solely to homogeneous activity from CuL^1 . Nonetheless, the identification of this third type of reaction mechanism employing redox-active ligands represents a key step in the development of further redox-active based catalysts for HER and the activation of small molecules. CuL^1 demonstrates that Cu^{II} metals, when paired with robust redox-active ligands can demonstrate high activity as HER electrocatalysts, and further confirms that organic redox-active ligands have the ability to store and transfer electrons in the ligand and work in unison with late transition metals in order to carry out catalysis.

To the best of our knowledge, the CuL¹ electrocatalyst exhibits the highest reported TOF of any ligand-centered homogeneous HER catalysts to date. However, their high activities coincide with substantially large overpotentials. This signifies the need for the development of new thiosemicarbazone ligands that employ more electron-donating auxiliary R groups which should greatly increase proton binding affinity, as well as drastically lower overpotentials. Still, thiosemicarbazones and thiosemicarbazonato frameworks display significant potential for hydrogen evolution, and demonstrate that incorporation of redox-active ligands into HER systems could potentially lead to a new class of HER electrocatalysts.

REFERENCES

1. D. G. Nocera, *Acc. Chem. Res.*, 2012, **45**, 767-776.
2. M. I. Hoffert, K. Caldeira, A. K. Jain, E. F. Haites, L. D. D. Harvey, S. D. Potter, M. E. Schlesinger, S. H. Schneider, R. G. Watts, T. M. L. Wigley and D. J. Wuebbles, *Nature*, 1998, **395**, 881-884.
3. D. A. LaVan and J. N. Cha, *Proc. Natl. Acad. Sci.*, 2006, **103**, 5251-5255.
4. S. Shafiee and E. Topal, *Energy Policy*, 2009, **37**, 181-189.
5. N. S. Lewis and D. G. Nocera, *Proc. Natl. Acad. Sci.*, 2006, **103**, 15729-15735.
6. J. A. Turner, *Science*, 2004, **305**, 972-974.
7. A. Das, Z. Han, W. W. Brennessel, P. L. Holland and R. Eisenberg, *ACS Catal.*, 2015, **5**, 1397-1406.
8. M. R. Dubois and D. L. Dubois, *Acc. Chem. Res.*, 2009, **42**, 1974-1982.
9. A. Z. Haddad, D. Kumar, K. O. Sampson, A. M. Matzner, M. S. Mashuta and C. A. Grapperhaus, *J. Am. Chem. Soc.*, 2015, **137**, 9238-9241.
10. X. L. Hu, B. S. Brunschwig and J. C. Peters, *J. Am. Chem. Soc.*, 2007, **129**, 8988-8998.
11. W. R. McNamara, Z. J. Han, P. J. Alperin, W. W. Brennessel, P. L. Holland and R. Eisenberg, *J. Am. Chem. Soc.*, 2011, **133**, 15368-15371.
12. W. R. McNamara, Z. J. Han, C. J. Yin, W. W. Brennessel, P. L. Holland and R. Eisenberg, *Proc. Natl. Acad. Sci. U. S. A.*, 2012, **109**, 15594-15599.
13. S. E. Smith, J. Y. Yang, D. L. DuBois and R. M. Bullock, *Angew. Chem. Int. Ed.*, 2012, **51**, 3152-3155.
14. S. Wiese, U. J. Kilgore, D. L. DuBois and R. M. Bullock, *ACS Catal.*, 2012, **2**, 720-727.
15. T. R. Cook, D. K. Dogutan, S. Y. Reece, Y. Surendranath, T. S. Teets and D. G. Nocera, *Chem. Rev.*, 2010, **110**, 6474-6502.
16. H. B. Gray, *Nat. Chem.*, 2009, **1**, 7-7.
17. R. Chaubey, S. Sahu, O. O. James and S. Maity, *Renewable and Sustainable Energy Reviews*, 2013, **23**, 443-462.
18. P. M. Vignais, B. Billoud and J. Meyer, *FEMS Microbiology Reviews*, 2001, **25**, 455-501.
19. P. M. Vignais and B. Billoud, *Chem. Rev.*, 2007, **107**, 4206-4272.
20. M. Stephenson and L. H. Stickland, *The properties of the enzyme*, 1931, **25**, 205-214.
21. D. E. Green and L. H. Stickland, *The reversibility of the hydrogenase system of *Bact. coli**, 1934, **28**, 898-900.
22. H. Ogata, S. Hirota, A. Nakahara, H. Komori, N. Shibata, T. Kato, K. Kano and Y. Higuchi, *Structure*, 2005, **13**, 1635-1642.
23. Y. Nicolet, C. Piras, P. Legrand, C. E. Hatchikian and J. C. Fontecilla-Camps, *Structure*, 1999, **7**, 13-23.
24. P. Tamagnini, R. Axelsson, P. Lindberg, F. Oxelfelt, R. Wünschiers and P. Lindblad, *Microbiology and Molecular Biology Reviews*, 2002, **66**, 1-20.

25. P. Tamagnini, E. Leitão, P. Oliveira, D. Ferreira, F. Pinto, D. J. Harris, T. Heidorn and P. Lindblad, *FEMS Microbiology Reviews*, 2007, **31**, 692-720.
26. M. Y. Darensbourg, E. J. Lyon, X. Zhao and I. P. Georgakaki, *Proceedings of the National Academy of Sciences of the United States of America*, 2003, **100**, 3683-3688.
27. J. C. Fontecilla-Camps, A. Volbeda, C. Cavazza and Y. Nicolet, *Chem. Rev.*, 2007, **107**, 4273-4303.
28. S. Shima, O. Pilak, S. Vogt, M. Schick, M. S. Stagni, W. Meyer-Klaucke, E. Warkentin, R. K. Thauer and U. Ermler, *Science*, 2008, **321**, 572-575.
29. J. C. Fontecilla-Camps, A. Volbeda, C. Cavazza and Y. Nicolet, *Chem. Rev.*, 2007, **107**, 4273-4303.
30. J. C. Fontecilla-Camps, P. Amara, C. Cavazza, Y. Nicolet and A. Volbeda, *Nature*, 2009, **460**, 814-822.
31. R. P. Happe, W. Roseboom, A. J. Pierik, S. P. J. Albracht and K. A. Bagley, *Nature*, 1997, **385**, 126-126.
32. A. J. Pierik, M. Hulstein, W. R. Hagen and S. P. J. Albracht, *Eur. J. Biochem.*, 1998, **258**, 572-578.
33. A. Volbeda, E. Garcin, C. Piras, A. L. de Lacey, V. M. Fernandez, E. C. Hatchikian, M. Frey and J. C. Fontecilla-Camps, *J. Am. Chem. Soc.*, 1996, **118**, 12989-12996.
34. E. J. Lyon, S. Shima, R. Boecher, R. K. Thauer, F.-W. Grevels, E. Bill, W. Roseboom and S. P. J. Albracht, *J. Am. Chem. Soc.*, 2004, **126**, 14239-14248.
35. S. Shima, E. J. Lyon, M. Sordel-Klippert, M. Kauß, J. Kahnt, R. K. Thauer, K. Steinbach, X. Xie, L. Verdier and C. Griesinger, *Angew. Chem. Int. Ed.*, 2004, **43**, 2547-2551.
36. E. J. Lyon, S. Shima, G. Buurman, S. Chowdhuri, A. Batschauer, K. Steinbach and R. K. Thauer, *Eur. J. Biochem.*, 2004, **271**, 195-204.
37. S. Shima, E. J. Lyon, R. K. Thauer, B. Mienert and E. Bill, *J. Am. Chem. Soc.*, 2005, **127**, 10430-10435.
38. K. A. Vincent, A. Parkin and F. A. Armstrong, *Chem. Rev.*, 2007, **107**, 4366-4413.
39. C. Tard and C. J. Pickett, *Chem. Rev.*, 2009, **109**, 2245-2274.
40. A. Adamska, A. Silakov, C. Lambertz, O. Rüdiger, T. Happe, E. Reijerse and W. Lubitz, *Angew. Chem. Int. Ed.*, 2012, **51**, 11458-11462.
41. D. W. Mulder, M. W. Ratzloff, E. M. Shepard, A. S. Byer, S. M. Noone, J. W. Peters, J. B. Broderick and P. W. King, *J. Am. Chem. Soc.*, 2013, **135**, 6921-6929.
42. A. Volbeda, M.-H. Charon, C. Piras, E. C. Hatchikian, M. Frey and J. C. Fontecilla-Camps, *Nature*, 1995, **373**, 580-587.
43. S. Canaguier, V. Artero and M. Fontecave, *Dalton Trans*, 2008, DOI: 10.1039/B713567J, 315-325.
44. H. Reihlen, A. Gruhl and G. v. Hessling, *Justus Liebigs Annalen der Chemie*, 1929, **472**, 268-287.
45. A. Le Cloirec, S. C. Davies, D. J. Evans, D. L. Hughes, C. J. Pickett, S. P. Best and S. Borg, *Chem. Commun.*, 1999, DOI: 10.1039/A906391I, 2285-2286.
46. M. Schmidt, S. M. Contakes and T. B. Rauchfuss, *J. Am. Chem. Soc.*, 1999, **121**, 9736-9737.
47. E. J. Lyon, I. P. Georgakaki, J. H. Reibenspies and M. Y. Darensbourg, *Angew. Chem. Int. Ed.*, 1999, **38**, 3178-3180.
48. J. W. Peters, W. N. Lanzilotta, B. J. Lemon and L. C. Seefeldt, *Science*, 1998, **282**, 1853-1858.
49. J.-F. Capon, F. Gloaguen, F. Y. Pétilion, P. Schollhammer and J. Talarmin, *Coord. Chem. Rev.*, 2009, **253**, 1476-1494.

50. C. Sommer, A. Adamska-Venkatesh, K. Pawlak, J. A. Birrell, O. Rüdiger, E. J. Reijerse and W. Lubitz, *J. Am. Chem. Soc.*, 2017, **139**, 1440-1443.
51. P. A. Eckert and K. J. Kubarych, *The Journal of Physical Chemistry A*, 2017, **121**, 608-615.
52. D. W. Mulder, Y. Guo, M. W. Ratzloff and P. W. King, *J. Am. Chem. Soc.*, 2017, **139**, 83-86.
53. Y. Li and T. B. Rauchfuss, *Chem. Rev.*, 2016, **116**, 7043-7077.
54. Y.-C. Liu, K.-T. Chu, Y.-L. Huang, C.-H. Hsu, G.-H. Lee, M.-C. Tseng and M.-H. Chiang, *ACS Catal.*, 2016, **6**, 2559-2576.
55. D. Yang, Y. Li, B. Wang, X. Zhao, L. Su, S. Chen, P. Tong, Y. Luo and J. Qu, *Inorg. Chem.*, 2015, **54**, 10243-10249.
56. D. Zheng, N. Wang, M. Wang, S. Ding, C. Ma, M. Y. Darensbourg, M. B. Hall and L. Sun, *J. Am. Chem. Soc.*, 2014, **136**, 16817-16823.
57. B. Li, T. Liu, C. V. Popescu, A. Bilko and M. Y. Darensbourg, *Inorg. Chem.*, 2009, **48**, 11283-11289.
58. J. C. Lansing, J. M. Camara, D. E. Gray and T. B. Rauchfuss, *Organometallics*, 2014, **33**, 5897-5906.
59. S. Gao, J. Fan, S. Sun, X. Peng, X. Zhao and J. Hou, *Dalton Trans*, 2008, DOI: 10.1039/B717497G, 2128-2135.
60. E. S. Donovan, J. J. McCormick, G. S. Nichol and G. A. N. Felton, *Organometallics*, 2012, **31**, 8067-8070.
61. L. Schwartz, P. S. Singh, L. Eriksson, R. Lomoth and S. Ott, *Comptes Rendus Chimie*, 2008, **11**, 875-889.
62. J. P. Collman, P. S. Wagenknecht and N. S. Lewis, *J. Am. Chem. Soc.*, 1992, **114**, 5665-5673.
63. J. P. Collman, Y. Ha, P. S. Wagenknecht, M. A. Lopez and R. Guilard, *J. Am. Chem. Soc.*, 1993, **115**, 9080-9088.
64. J. L. Dempsey, J. R. Winkler and H. B. Gray, *J. Am. Chem. Soc.*, 2010, **132**, 1060-1065.
65. J. L. Dempsey, J. R. Winkler and H. B. Gray, *J. Am. Chem. Soc.*, 2010, **132**, 16774-16776.
66. C. N. Valdez, J. L. Dempsey, B. S. Brunshwig, J. R. Winkler and H. B. Gray, *Proc. Natl. Acad. Sci.*, 2012, **109**, 15589-15593.
67. C. H. Lee, D. K. Dogutan and D. G. Nocera, *J. Am. Chem. Soc.*, 2011, **133**, 8775-8777.
68. M. M. Roubelakis, D. K. Bediako, D. K. Dogutan and D. G. Nocera, *Energy Environ Sci*, 2012, **5**, 7737-7740.
69. B. H. Solis and S. Hammes-Schiffer, *Inorg. Chem.*, 2011, **50**, 11252-11262.
70. B. H. Solis and S. Hammes-Schiffer, *J. Am. Chem. Soc.*, 2011, **133**, 19036-19039.
71. B. H. Solis, A. G. Maher, D. K. Dogutan, D. G. Nocera and S. Hammes-Schiffer, *Proc. Natl. Acad. Sci.*, 2016, **113**, 485-492.
72. J. T. Muckerman and E. Fujita, *Chem. Commun.*, 2011, **47**, 12456-12458.
73. M. Razavet, V. Artero and M. Fontecave, *Inorg. Chem.*, 2005, **44**, 4786-4795.
74. C. Baffert, V. Artero and M. Fontecave, *Inorg. Chem.*, 2007, **46**, 1817-1824.
75. B. D. Stubbert, J. C. Peters and H. B. Gray, *J. Am. Chem. Soc.*, 2011, **133**, 18070-18073.
76. A. Z. Haddad, B. D. Garabato, P. M. Kozlowski, R. M. Buchanan and C. A. Grapperhaus, *J. Am. Chem. Soc.*, 2016, **138**, 7844-7847.
77. A. Z. Haddad, D. Kumar, K. Ouch Sampson, A. M. Matzner, M. S. Mashuta and C. A. Grapperhaus, *J. Am. Chem. Soc.*, 2015, **137**, 9238-9241.
78. W. Zhang, A. Z. Haddad, B. D. Garabato, P. M. Kozlowski, R. M. Buchanan and C. A. Grapperhaus, *Inorg. Chem.*, 2017, **56**, 2177-2187.
79. A. M. Appel, D. L. DuBois and M. R. DuBois, *J. Am. Chem. Soc.*, 2005, **127**, 12717-12726.

80. N. Coutard, N. Kaeffer and V. Artero, *Chem. Commun.*, 2016, **52**, 13728-13748.
81. D. L. DuBois, *Inorg. Chem.*, 2014, **53**, 3935-3960.
82. G. M. Jacobsen, J. Y. Yang, B. Twamley, A. D. Wilson, R. M. Bullock, M. R. DuBois and D. L. DuBois, *Energy Environ Sci*, 2008, **1**, 167-174.
83. T. Liu, Q. Liao, M. O'Hagan, E. B. Hulley, D. L. DuBois and R. M. Bullock, *Organometallics*, 2015, **34**, 2747-2764.
84. A. D. Wilson, R. H. Newell, M. J. McNevin, J. T. Muckerman, M. R. DuBois and D. L. DuBois, *J. Am. Chem. Soc.*, 2006, **128**, 358-366.
85. J. M. Darmon, N. Kumar, E. B. Hulley, C. J. Weiss, S. Raugei, R. M. Bullock and M. L. Helm, *Chem. Sci.*, 2015, **6**, 2737-2745.
86. J. M. Darmon, S. Raugei, T. Liu, E. B. Hulley, C. J. Weiss, R. M. Bullock and M. L. Helm, *ACS Catal.*, 2014, **4**, 1246-1260.
87. W. A. Hoffert, J. A. S. Roberts, R. Morris Bullock and M. L. Helm, *Chem. Commun.*, 2013, **49**, 7767-7769.
88. T. Straistari, J. Fize, S. Shova, M. Réglie, V. Artero and M. Orio, *ChemCatChem*, 2016, DOI: 10.1002/cctc.201600967.
89. A. Zarkadoulas, M. J. Field, C. Papatriantafyllopoulou, J. Fize, V. Artero and C. A. Mitsopoulou, *Inorg. Chem.*, 2016, **55**, 432-444.
90. C. Tsay and J. Y. Yang, *J. Am. Chem. Soc.*, 2016, **138**, 14174-14177.
91. J. L. Dempsey, B. S. Brunschwig, J. R. Winkler and H. B. Gray, *Acc. Chem. Res.*, 2009, **42**, 1995-2004.
92. A. Bhattacharjee, E. S. Andreiadis, M. Chavarot-Kerlidou, M. Fontecave, M. J. Field and V. Artero, *Chemistry – A European Journal*, 2013, **19**, 15166-15174.
93. N. Kaeffer, A. Morozan, J. Fize, E. Martinez, L. Guetaz and V. Artero, *ACS Catal.*, 2016, **6**, 3727-3737.
94. M. Rakowski Dubois and D. L. Dubois, *Acc. Chem. Res.*, 2009, **42**, 1974-1982.
95. W. R. McNamara, Z. J. Han, C. J. Yin, W. W. Brennessel, P. L. Holland and R. Eisenberg, *Proc. Natl. Acad. Sci.*, 2012, **109**, 15594-15599.
96. W. Kaim and B. Schwederski, *Coord. Chem. Rev.*, 2010, **254**, 1580-1588.
97. W. Kaim, *Coord. Chem. Rev.*, 1987, **76**, 187-235.
98. C. A. Grapperhaus, K. Ouch and M. S. Mashuta, *J. Am. Chem. Soc.*, 2009, **131**, 64-65.
99. E. J. Thompson and L. A. Berben, *Angew. Chem. Int. Ed.*, 2015, **54**, 11642-11646.
100. Y. Zheng, Y. Jiao, Y. Zhu, L. H. Li, Y. Han, Y. Chen, A. Du, M. Jaroniec and S. Z. Qiao, *Nature Communications*, 2014, **5**.
101. N. Chebotareva and T. Nyokong, *Electrochim. Acta*, 1997, **42**, 3519-3524.
102. A. Koca, *Electrochem. Commun.*, 2009, **11**, 838-841.
103. A. Koca, Ş. Bayar, H. A. Dinçer and E. Gonca, *Electrochim. Acta*, 2009, **54**, 2684-2692.
104. A. Koca, A. Kalkan and Z. Altuntaş Bayır, *Electroanalysis*, 2010, **22**, 310-319.
105. A. Koca, A. Kalkan and Z. A. Bayır, *Electrochim. Acta*, 2011, **56**, 5513-5525.
106. Ö. A. Osmanbaş, A. Koca, M. Kandaz and F. Karaca, *Int. J. Hydrogen Energy*, 2008, **33**, 3281-3288.
107. E. J. Lawrence, R. J. Blagg, D. L. Hughes, A. E. Ashley and G. G. Wildgoose, *Chemistry – A European Journal*, 2015, **21**, 900-906.
108. J. Y. Yang, S. Chen, W. G. Dougherty, W. S. Kassel, R. M. Bullock, D. L. DuBois, S. Raugei, R. Rousseau, M. Dupuis and M. R. DuBois, *Chem. Commun.*, 2010, **46**, 8618-8620.
109. B. E. Barton, M. T. Olsen and T. B. Rauchfuss, *Curr. Opin. Biotechnol.*, 2010, **21**, 292-297.
110. E. Block, V. Eswarakrishnan, M. Gernon, G. Ofori-Okai, C. Saha, K. Tang and J. Zubietta, *J. Am. Chem. Soc.*, 1989, **111**, 658-665.

111. H. M. Betts, P. J. Barnard, S. R. Bayly, J. R. Dilworth, A. D. Gee and J. P. Holland, *Angew. Chem. Int. Ed.*, 2008, **47**, 8416-8419.
112. J. P. Holland, F. I. Aigbirhio, H. M. Betts, P. D. Bonnitcha, P. Burke, M. Christlieb, G. C. Churchill, A. R. Cowley, J. R. Dilworth, P. S. Donnelly, J. C. Green, J. M. Peach, S. R. Vasudevan and J. E. Warren, *Inorg. Chem.*, 2007, **46**, 465-485.
113. A. J. Gordon, *The Chemistry Companion*, John Wiley & Sons Inc., Canada 1972.
114. J. A. Bard, Faulkner, R. L., *Electrochemical Methods: Fundamentals and Applications*, Wiley, Somerset, New Jersey, 2nd edn., **2001**.
115. S. L. R. D.T., Heinman; J.M. Beebe, *Chemistry Experiments for Instrumental Methods*, J. Wiley & Sons, 1984.
116. C. A. Grapperhaus and S. Poturovic, *Inorg. Chem.*, 2004, **43**, 3292-3298.
117. A. M. Appel and M. L. Helm, *ACS Catal.*, 2014, **4**, 630-633.
118. D. H. Pool, M. P. Stewart, M. O'Hagan, W. J. Shaw, J. A. S. Roberts, R. M. Bullock and D. L. DuBois, *Proc. Natl. Acad. Sci.*, 2012, **109**, 15634-15639.
119. M. P. Stewart, M.-H. Ho, S. Wiese, M. L. Lindstrom, C. E. Thogerson, S. Raugei, R. M. Bullock and M. L. Helm, *J. Am. Chem. Soc.*, 2013, **135**, 6033-6046.
120. C. P. Andrieux, C. Blocman, J. M. Dumasbouchiat, F. Mhalla and Savéant, J. M., *J. Electroanal. Chem.*, 1980, **113**, 19-40.
121. V. Fourmond, P. A. Jacques, M. Fontecave and V. Artero, *Inorg. Chem.*, 2010, **49**, 10338-10347.
122. Savéant, J. M. and K. B. Su, *J. Electroanal. Chem.*, 1984, **171**, 341-349.
123. C. Costentin, G. Passard and J.-M. Savéant, *J. Am. Chem. Soc.*, 2015, **137**, 5461-5467.
124. ElchSoft, ElchSoft - Simulation Software, <http://www.elchsoft.com/digielch/DigiElch7/Default.aspx>, (accessed December 2015, 2015).
125. P. J. Stephens, F. J. Devlin, C. F. Chabalowski and M. J. Frisch, *J Phys Chem*, 1994, **98**, 11623-11627.
126. Y. Zhao and D. G. Truhlar, *Theor. Chem. Acc.*, 2008, **120**, 215-241.
127. C. Adamo and V. Barone, *J Chem Phys*, 1998, **108**, 664-675.
128. A. D. Becke, *J Chem Phys*, 2000, **112**, 4020-4026.
129. E. J. Baerends, D. E. Ellis and P. Ros, *Chem. Phys.*, 1973, **2**, 41-51.
130. B. I. Dunlap and I. V. Schweigert, *J Chem Phys*, 2011, **134**, 044122.
131. O. Vahtras, J. Almlöf and M. W. Feyereisen, *Chem. Phys. Lett.*, 1993, **213**, 514-518.
132. S. Lim and N. Park, *Appl. Phys. Lett.*, 2009, **95**, 243110.
133. G. te Velde, F. M. Bickelhaupt, E. J. Baerends, C. Fonseca Guerra, S. J. A. van Gisbergen, J. G. Snijders and T. Ziegler, *J. Comput. Chem.*, 2001, **22**, 931-967.
134. V. Weber, M. Iannuzzi, S. Giani, J. Hutter, R. Declerck and M. Waroquier, *J Chem Phys*, 2009, **131**, 014106.
135. Y. Jung, A. Sodt, P. M. W. Gill and M. Head-Gordon, *Proceedings of the National Academy of Sciences of the United States of America*, 2005, **102**, 6692-6697.
136. K. Eichkorn, O. Treutler, H. Öhm, M. Häser and R. Ahlrichs, *Chem. Phys. Lett.*, 1995, **242**, 652-660.
137. L. Füstí-Molnár and P. Pulay, *Journal of Molecular Structure: THEOCHEM*, 2003, **666-667**, 25-30.
138. S. Chris-Kriton, D. H. Peter, A. M. Arash and C. P. Mike, *J. Phys.: Condens. Matter*, 2008, **20**, 064209.
139. M. J. Frisch and e. al., *Journal*, 2009.
140. A. D. Becke, *J Chem Phys*, 1993, **98**, 5648-5652.

141. C. Lee, W. Yang and R. G. Parr, *Phys. Rev. B*, 1988, **37**, 785-789.
142. S. H. Vosko, L. Wilk and M. Nusair, *Can. J. Phys.*, 1980, **58**, 1200-1211.
143. C. A. Grapperhaus, P. M. Kozlowski, D. Kumar, H. N. Frye, K. B. Venna and S. Poturovic, *Angew. Chem. Int. Ed.*, 2007, **46**, 4085-4088.
144. G. Andrienko, ChemCraft Graphics Visualization Software, <http://www.chemcraftprog.com>, (accessed November 2015, 2015).
145. M. J. Frisch, G. W. Trucks, H. B. Schlegel, G. E. Scuseria, M. A. Robb, J. R. Cheeseman, G. Scalmani, V. Barone, B. Mennucci, G. A. Petersson, H. Nakatsuji, M. Caricato, X. Li, H. P. Hratchian, A. F. Izmaylov, J. Bloino, G. Zheng, J. L. Sonnenberg, M. Hada, M. Ehara, K. Toyota, R. Fukuda, J. Hasegawa, M. Ishida, T. Nakajima, Y. Honda, O. Kitao, H. Nakai, T. Vreven, J. A. Montgomery Jr., J. E. Peralta, F. Ogliaro, M. J. Bearpark, J. Heyd, E. N. Brothers, K. N. Kudin, V. N. Staroverov, R. Kobayashi, J. Normand, K. Raghavachari, A. P. Rendell, J. C. Burant, S. S. Iyengar, J. Tomasi, M. Cossi, N. Rega, N. J. Millam, M. Klene, J. E. Knox, J. B. Cross, V. Bakken, C. Adamo, J. Jaramillo, R. Gomperts, R. E. Stratmann, O. Yazyev, A. J. Austin, R. Cammi, C. Pomelli, J. W. Ochterski, R. L. Martin, K. Morokuma, V. G. Zakrzewski, G. A. Voth, P. Salvador, J. J. Dannenberg, S. Dapprich, A. D. Daniels, Ö. Farkas, J. B. Foresman, J. V. Ortiz, J. Cioslowski and D. J. Fox, *Journal*, 2009.
146. A. R. Cowley, J. R. Dilworth, P. S. Donnelly, E. Labisbal and A. Sousa, *J. Am. Chem. Soc.*, 2002, **124**, 5270-5271.
147. S. Grimme, *J. Comput. Chem.*, 2006, **27**, 1787-1799.
148. L. A. Berben and J. C. Peters, *Chem. Commun.*, 2010, **46**, 398-400.
149. N. Kaeffer, M. Chavarot-Kerlidou and V. Artero, *Acc. Chem. Res.*, 2015, **48**, 1286-1295.
150. N. Kaeffer, A. Morozan, J. Fize, E. Martinez, L. Guetaz and V. Artero, *ACS Catal.*, 2016, **6**, 3727-3737.
151. S. Poturovic, C. A. Grapperhaus and M. S. Mashuta, *Angew. Chem. Int. Ed.*, 2005, **44**, 1883-1887.
152. C. A. Grapperhaus, K. B. Venna and M. S. Mashuta, *Inorg. Chem.*, 2007, **46**, 8044-8050.
153. K. Ouch, M. S. Mashuta and C. A. Grapperhaus, *Inorg. Chem.*, 2011, DOI: 10.1021/ic200416y, 9904 - 9914.
154. R. Chauhan, M. S. Mashuta and C. A. Grapperhaus, *Inorg. Chem.*, 2012, **51**, 7913-7920.
155. K. Ouch, M. S. Mashuta and C. A. Grapperhaus, *Eur. J. Inorg. Chem.*, 2012, **2012**, 475-478.
156. K. O. Sampson, D. Kumar, M. S. Mashuta and C. A. Grapperhaus, *Inorg. Chim. Acta*, 2013, **408**, 1-8.
157. J. R. Dilworth, A. J. Hutson, S. Morton, M. Harman, M. B. Hursthouse, J. Zubieta, C. M. Archer and J. D. Kelly, *Polyhedron*, 1992, **11**, 2151-2155.
158. C. A. Grapperhaus, S. Poturovic and M. S. Mashuta, *Inorg. Chem.*, 2005, **44**, 8185-8187.
159. R. Chauhan, M. S. Mashuta and C. A. Grapperhaus, *Inorg. Chem. Commun.*, 2013, **37**, 186-188.
160. C. A. Grapperhaus and S. Poturovic, *Inorganic Chemistry*, 2004, **43**, 3292-3298.
161. H. I. Karunadasa, C. J. Chang and J. R. Long, *Nature*, 2010, **464**, 1329-1333.
162. L. Farrugia, *J. Appl. Crystallogr.*, 1997, **30**, 565.
163. C. P. Andrieux, C. Blocman, J. M. Dumasbouchiat, F. Mhalla and J. M. Saveant, *Journal of Electroanalytical Chemistry*, 1980, **113**, 19-40.
164. G. A. N. Felton, A. K. Vannucci, J. Z. Chen, L. T. Lockett, N. Okumura, B. J. Petro, U. I. Zakai, D. H. Evans, R. S. Glass and D. L. Lichtenberger, *J. Am. Chem. Soc.*, 2007, **129**, 12521-12530.
165. J. M. Saveant and K. B. Su, *Journal of Electroanalytical Chemistry*, 1984, **171**, 341-349.

166. J. A. S. Roberts and R. M. Bullock, *Inorg. Chem.*, 2013, **52**, 3823-3835.
167. S. C. Marinescu, J. R. Winkler and H. B. Gray, *Proc. Natl. Acad. Sci.*, 2012, **109**, 15127-15131.
168. H. Kotani, R. Hanazaki, K. Ohkubo, Y. Yamada and S. Fukuzumi, *Chem. Eur. J.*, 2011, **17**, 2777-2785.
169. S. Fukuzumi, T. Kobayashi and T. Suenobu, *J. Am. Chem. Soc.*, 2010, **132**, 1496-1497.
170. D. Sellmann, G. Mahr, F. Knoch and M. Moll, *Inorg. Chim. Acta*, 1994, **224**, 45-59.
171. F. Zhong, G. P. Lisi, D. P. Collins, J. H. Dawson and E. V. Pletneva, *Proc. Natl. Acad. Sci.*, 2014, DOI: 10.1073/pnas.1317173111, ASAP.
172. Y. Yan, B. Xia, Z. Xu and X. Wang, *ACS Catal.*, 2014, **4**, 1693-1705.
173. B. H. Solis, A. G. Maher, D. K. Dogutan, D. G. Nocera and S. Hammes-Schiffer, *Proc. Natl. Acad. Sci. U. S. A.*, 2016, **113**, 485-492.
174. A. F. Heyduk, R. A. Zarkesh and A. I. Nguyen, *Inorg. Chem.*, 2011, **50**, 9849-9863.
175. Y. R. de Miguel, N. Bampos, K. M. Nalin de Silva, J. K. M. Sanders and S. A. Richards, *Chem. Commun.*, 1998, DOI: 10.1039/A806034G, 2267-2268.
176. C. P. Andrieux, C. Blocman, J. M. Dumasbouchiat, F. Mhalla and J. M. Saveant, *J. Electroanal. Chem.*, 1980, **113**, 19-40.
177. J. M. Saveant and K. B. Su, *J. Electroanal. Chem.*, 1984, **171**, 341-349.
178. D. X. West, A. E. Liberta, S. B. Padhye, R. C. Chikate, P. B. Sonawane, A. S. Kumbhar and R. G. Yerande, *Coord. Chem. Rev.*, 1993, **123**, 49-71.
179. R. Vuilleumier and D. Borgis, *Nat. Chem.*, 2012, **4**, 432-433.
180. X. Jing, P. Wu, X. Liu, L. Yang, C. He and C. Duan, *New J. Chem.*, 2015, **39**, 1051-1059.
181. P. C. K. Vesborg, B. Seger and I. Chorkendorff, *J. Phys. Chem. Lett.*, 2015, **6**, 951-957.
182. T. S. Teets and D. G. Nocera, *Chem. Commun.*, 2011, **47**, 9268-9274.
183. J. W. S. O.T. Holton, *Platinum Met. Rev.*, 2013, **57**, 259-271.
184. J. R. McKone, S. C. Marinescu, B. S. Brunschwig, J. R. Winkler and H. B. Gray, *Chem. Sci.*, 2014, **5**, 865-878.
185. T. R. Simmons, G. Berggren, M. Bacchi, M. Fontecave and V. Artero, *Coord. Chem. Rev.*, 2014, **270-271**, 127-150.
186. V. S. Thoi, Y. Sun, J. R. Long and C. J. Chang, *Chem. Soc. Rev.*, 2013, **42**, 2388-2400.
187. D. Brazzolotto, M. Gennari, N. Queyriaux, T. R. Simmons, J. Pécaut, S. Demeshko, F. Meyer, M. Orto, V. Artero and C. Duboc, *Nat. Chem.*, 2016, **8**, 1054-1060.
188. N. Kaeffer, M. Chavarot-Kerlidou and V. Artero, *Acc. Chem. Res.*, 2015, **48**, 1286-1295.
189. H. Lei, H. Fang, Y. Han, W. Lai, X. Fu and R. Cao, *ACS Catal.*, 2015, **5**, 5145-5153.
190. M. Bacchi, E. Veinberg, M. J. Field, J. Niklas, T. Matsui, D. M. Tiede, O. G. Poluektov, M. Ikeda-Saito, M. Fontecave and V. Artero, *ChemPlusChem*, 2016, **81**, 1083-1089.
191. J. E. Armstrong, P. M. Crossland, M. A. Frank, M. J. Van Dongen and W. R. McNamara, *Dalton Trans*, 2016, **45**, 5430-5433.
192. J. W. Jurss, R. S. Khnayzer, J. A. Panetier, K. A. El Roz, E. M. Nichols, M. Head-Gordon, J. R. Long, F. N. Castellano and C. J. Chang, *Chem. Sci.*, 2015, **6**, 4954-4972.
193. J. A. Panetier, C. S. Letko, T. D. Tilley and M. Head-Gordon, *J Chem Theory Comput*, 2016, **12**, 223-230.
194. J. P. Holland, P. J. Barnard, D. Collison, J. R. Dilworth, R. Edge, J. C. Green and E. J. L. McInnes, *Chemistry – A European Journal*, 2008, **14**, 5890-5907.
195. H. M. Acta Crystallographica Section CBetts, P. J. Barnard, S. R. Bayly, J. R. Dilworth, A. D. Gee and J. P. Holland, *Angew. Chem. Int. Ed.*, 2008, **47**, 8416-8419.
196. M. Christlieb, H. S. R. Struthers, P. D. Bonnitcha, A. R. Cowley and J. R. Dilworth, *Dalton Trans*, 2007, 5043-5054.

197. V. Artero and Savéant, Jean-Michel, *Energy Environ Sci*, 2014, **7**, 3808-3814.
198. K. J. Lee, B. D. McCarthy, E. S. Rountree and J. L. Dempsey, *Inorg. Chem.*, 2017, **56**, 1988-1998.
199. J. P. Layfield and S. Hammes-Schiffer, *Chem. Rev.*, 2014, **114**, 3466-3494.
200. A. R. Zeradjanin, J.-P. Grote, G. Polymeros and K. J. J. Mayrhofer, *Electroanalysis*, 2016, **28**, 2256-2269.
201. X. Jing, P. Wu, X. Liu, L. Yang, C. He and C. Duan, *New J. Chem.*, 2015, **39**, 1051-1059.
202. P. J. Chirik, *Inorg. Chem.*, 2011, **50**, 9737-9740.
203. A. D. Wilson, R. H. Newell, M. J. McNevin, J. T. Muckerman, M. Rakowski DuBois and D. L. DuBois, *J. Am. Chem. Soc.*, 2006, **128**, 358-366.
204. E. J. Lawrence, V. S. Oganessian, D. L. Hughes, A. E. Ashley and G. G. Wildgoose, *J. Am. Chem. Soc.*, 2014, **136**, 6031-6036.
205. D. W. Stephan and G. Erker, *Angew. Chem. Int. Ed.*, 2010, **49**, 46-76.
206. F. Zhao, J. Zhang, D. Wohrle and M. Kaneko, *J. Porphyrins Phthalocyanines*, 2000, **04**, 31-36.

APPENDIX A:
CYCLIC VOLTAMMETRY
SIMULATION PARAMETER TABLES
AND DIGIELCH GUIDE

Table A4. ZnL¹ Optimized parameters of data fitting, 12 mM [acid]; $v = 0.2 - 0.5$ V/s vs Fe⁺/Fe

Charge-transfer Steps	99% Confidence	E ⁰	α	k _s
$[\text{ZnHL}]^+ + e^- = \text{Zn}(\text{HL}^\bullet)$	Optimized	-1.8110	0.3166	0.0070
	Upper Limit	-1.8113	0.3166	0.0070
	Lower Limit	-1.8107	0.3166	0.0070
$[\text{ZnH}_2\text{L}]^{2+} + e^- = [\text{Zn}(\text{H}_2\text{L}^\bullet)]^+$	Optimized	-1.5872	0.3166	0.0070
	Upper Limit	-1.5874	0.3166	0.0070
	Lower Limit	-1.5870	0.3166	0.0070
Chemical Steps	99% Confidence	K _{eq}	k _f	
$\text{ZnL} + \text{H}^+ = [\text{ZnHL}]^+$	Optimized	2.42E+05	1.28E+13	
	Upper Limit	3.42E+06	6.40E+13	
	Lower Limit	1.91E+05	1.94E+12	
$[\text{ZnHL}]^+ + \text{H}^+ = [\text{ZnH}_2\text{L}]^{2+}$	Optimized	8.80E+00	4.06E+06	
	Upper Limit	8.93E+00	6.92E+06	
	Lower Limit	8.68E+00	1.20E+06	
$\text{Zn}(\text{HL}^\bullet) + \text{Zn}(\text{HL}^\bullet) = \text{H}_2$	Optimized	4.89E+10	3.09E+09	
	Upper Limit	4.96E+10	6.51E+09	
	Lower Limit	4.80E+10	6.45E+08	
$\text{Zn}(\text{HL}^\bullet) + [\text{Zn}(\text{H}_2\text{L}^\bullet)]^+ = \text{H}_2$	Optimized	9.07E+07	2.47E+10	
	Upper Limit	9.19E+07	3.95E+10	
	Lower Limit	8.90E+07	9.94E+09	
$[\text{Zn}(\text{H}_2\text{L}^\bullet)]^+ = \text{Zn}(\text{HL}^\bullet) + \text{H}^+$	Calculated	1.87E-05	8.14E+04	
	Upper Limit	1.87E-05	1.07E+05	
	Lower Limit	1.87E-05	2.82E+04	

Table A5. ZnI¹ Optimized parameters of data fitting, 12 mM [acid]; $v = 1.0 - 5.0$ V/s vs Fc⁺/Fc

Charge-transfer Steps	99% Confidence	E ⁰	α	k _s
$[\text{ZnHL}]^+ + e^- = \text{Zn}(\text{HL}^\bullet)$	Optimized	-1.8004	0.3166	0.007
	Upper Limit	-1.8010	0.3166	0.007
	Lower Limit	-1.8000	0.3166	0.007
$[\text{ZnH}_2\text{L}]^{2+} + e^- = [\text{Zn}(\text{H}_2\text{L}^\bullet)]^+$	Optimized	-1.5264	0.3166	0.007
	Upper Limit	-1.5274	0.3166	0.007
	Lower Limit	-1.5254	0.3166	0.007
Chemical Steps	99% Confidence	K _{eq}	k _f	
$\text{ZnL} + \text{H}^+ = [\text{ZnHL}]^+$	Optimized	1364	3.20E+13	
	Upper Limit	1442.8	8.72E+15	
	Lower Limit	1285.2	8.65E+12	
$[\text{ZnHL}]^+ + \text{H}^+ = [\text{ZnH}_2\text{L}]^{2+}$	Optimized	13.438	3.06E+09	
	Upper Limit	13.6	9.83E+10	
	Lower Limit	13.276	9.22E+08	
$\text{Zn}(\text{HL}^\bullet) + \text{Zn}(\text{HL}^\bullet) = \text{H}_2$	Optimized	3.69E+11	4.57E+08	
	Upper Limit	3.69E+11	5.57E+08	
	Lower Limit	3.68E+11	3.57E+08	
$\text{Zn}(\text{HL}^\bullet) + [\text{Zn}(\text{H}_2\text{L}^\bullet)]^+ = \text{H}_2$	Optimized	4.44E+08	2.72E+11	
	Upper Limit	4.46E+08	3.84E+11	
	Lower Limit	4.42E+08	1.61E+11	
$[\text{Zn}(\text{H}_2\text{L}^\bullet)]^+ = \text{Zn}(\text{HL}^\bullet) + \text{H}^+$	Calculated	1.74E-06	2414	
	Upper Limit	1.74E-06	2414	
	Lower Limit	1.74E-06	2414	

Table A6. ZnL¹ Optimized parameters of data fitting, 6 mM [acid]; $v = 0.2 - 0.5$ V/s vs Fc⁺/Fc

Charge-transfer Steps	99%	E^0	α	k_s	
	Confidence				
$[\text{ZnHL}]^+ + e^- = \text{Zn}(\text{HL}^\bullet)$	Optimized	-1.8431	0.3166	0.007	
	Upper Limit	-1.8562	0.3166	0.007	
	Lower Limit	-1.8333	0.3166	0.007	
$[\text{ZnH}_2\text{L}]^{2+} + e^- = [\text{Zn}(\text{H}_2\text{L}^\bullet)]^+$	Optimized	-1.6958	0.3166	0.007	
	Upper Limit	-1.7939	0.3166	0.007	
	Lower Limit	-1.5977	0.3166	0.007	
Chemical Steps	99%	K_{eq}	k_f		
	Confidence				
$\text{ZnL} + \text{H}^+ = [\text{ZnHL}]^+$	Optimized	32000	5.00E+11		
	Upper Limit	6.68E+05	1.43E+12		
	Lower Limit	6.04E+03	1.04E+10		
$[\text{ZnHL}]^+ + \text{H}^+ = [\text{ZnH}_2\text{L}]^{2+}$	Optimized	19.942	2.86E+02		
	Upper Limit	95.717	2.86E+03		
	Lower Limit	0.55833	2.23E+01		
$\text{Zn}(\text{HL}^\bullet) + \text{Zn}(\text{HL}^\bullet) = \text{H}_2$	Optimized	7.28E+09	2.00E+08		
	Upper Limit	1.05E+11	1.35E+12		
	Lower Limit	9.08E+08	1.35E+06		
$\text{Zn}(\text{HL}^\bullet) + [\text{Zn}(\text{H}_2\text{L}^\bullet)]^+ = \text{H}_2$	Optimized	8.58E+07	2.00E+12		
	Upper Limit	1.28E+09	1.49E+13		
	Lower	1.11E+06	1.09E+10		

	Limit		
$[\text{Zn}(\text{H}_2\text{L}^\bullet)]^+ = \text{Zn}(\text{HL}^\bullet) + \text{H}^+$	Calculated	1.55E-04	4000
	Upper Limit	1.55E-04	4754.6
	Lower Limit	1.55E-04	3245.4

DigiElch Guide

Obtain the CV of your complex at several scan rates, starting at different potentials, going from high to low and vice-versa, as well at different concentrations. In any event you will most likely need to go back and redo the experiment at some point. Generally, a concentration of 1 mM catalyst with 0.1 M supporting electrolyte will be sufficient to obtain a good CV.

Once you have a series of CVs that you wish to model, the first thing that you must do is export the potential and current values from the Gamry Analyst software. To do this, first click on the cyclic voltammetry tab, this will give a drop down menu. Then, click on “Export to DigiElch”. Doing this will prompt you to save the data file, save as a .use file. Repeat for every individual voltammogram you wish to model. For example, if you were modeling catalytic reactions at a certain concentration of analyte, it would be a good idea to export CVs run over a range of scan rates, so that you have multiple data points to fit your model.

```

1 source program: DigiElch for Windows
2 program version: 3.0
3 file type: CV
4
5 experimental parameters:
6 Pre-Equilibrium: Enabled
7 Diffusion: Semi-Infinite 1D
8 Geometry: Planar
9 Area (cm2): 0.071
10 Ru (Ohm): 0
11 Cd1 (F): 0
12 Temp. (K): 298.2
13 Potential steps(V): 0.001
14 Estart (V): 0
15 Segment: 1
16 Eend (V): -2
17 v (V/s): 0.2
18 Segment: 2
19 Eend (V): 0
20 v (V/s): 0.2
21
22 species parameters:
23 [cat] (M/l): 0.0006
24 [H+] (M/l): 0.2688
25
26 experimental CV-data :
27 number of E (V), I (A) couples: 4002
28 1.68680999195203E-05 , 2.99403995995817E-06

```

Figure A51. Screenshot of a .use file used for import into DigiElch.

After successfully exporting your data and converting it to a .use file, it is a good idea to make sure that all parameters have been exported correctly. To do this, open the .use file using notepad++ and confirm that values of electrode area, species concentrations, potential step values, and CV segment descriptions are all correct and as intended (Figure A49). If they are not formatted correctly, the files will not import. In order to import to DigiElch, open DigiElch, click on the experiments tab, and click on the import icon at the top of the page. Doing so prompts the selection of files; select the appropriate .use files that you have previously prepared (Figure A50).

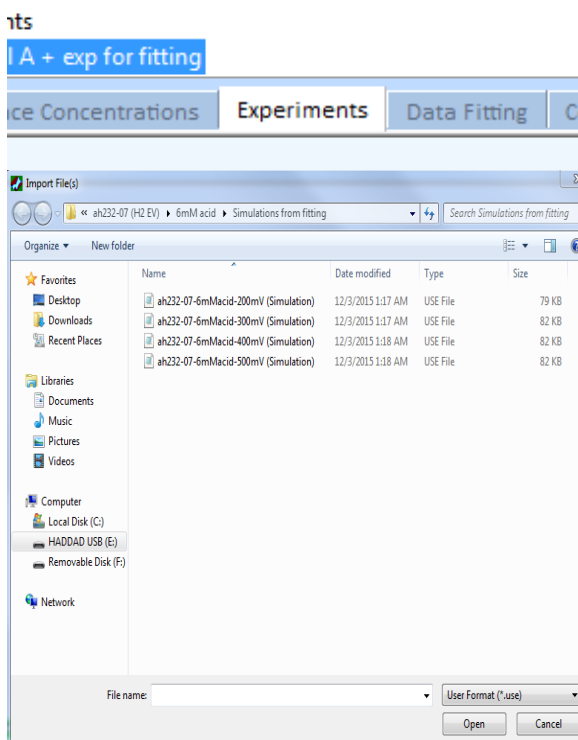
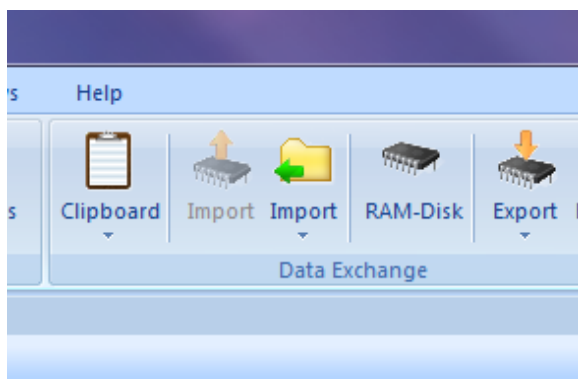


Figure A52. (Left) Screenshot showing how to import files to DigiElch using import icon. **(Right)** Sample .use files to import.

Next you will want to build a model to fit your experimental data. In DigiElch, click on the data fitting tab and click edit mechanism. This will prompt a new screen to appear reading, define mechanism and starting parameters. This window will contain three tabs: chemical reactions, surface reactions and simulation parameters. Within this there are a number of parameters to consider (Figure A51 and A52): α = the symmetry

factor and 0.5 is initial programmed approximation. This variable affects the symmetry of the electron transfer reaction, a reasonable value will be between 0.2 and 0.7. The variable, k_s = heterogeneous reaction constant, changes overall peak shape, smaller value → wider the current peak will be. E_o (V): potential at which the electron transfer reaction is observed, this is often experimentally measured. $R_u(\text{Ohm})$ = changing this variable results in the slanted response in the current response of the CV, it can be approximated by taking the first derivative of CV curve (Gamry Data Analysis). $CdI(\text{F})$ = capacitance - how much the cell needs be charged before current begins to flow through the cell and results in making the current response wider. Changing results in either increase or decrease of separation between anodic and cathodic current values (thickness of CV essentially). Usually 1×10^{-6} is a good starting place. Change by moving value up until simulation overlays well with experimental data. It is important to note that values of k_s and α can be obtained by fitting CVs of a $1 e^-$ reduction/oxidation with just your complex and supporting electrolyte from data over a large range of scan rates.

Under the chemical reactions tab there will be three boxes reading charge-transfer reactions, chemical reactions, and species (Figure A52.) All charge transfer reactions are read as reductions by DigiElch (keep in mind if trying to model oxidations). You can adjust species concentrations and diffusion coefficients for all species. Values of E^0 , α , and k_s can be entered for each charge transfer step. Clicking on the charge transfer box prompts a new window to appear (Figure A53) which allows you to specify the type of reduction 1-9 electrons, enable absorption to the electrode, or make charge-transfer events irreversible. For chemical reaction steps, you can enter and adjust the equilibrium constants and forward reaction rates. You can also make reactions irreversible by double

clicking on the chemical reaction box and specifying this by changing the = sign in the electron transfer equation to the => sign.

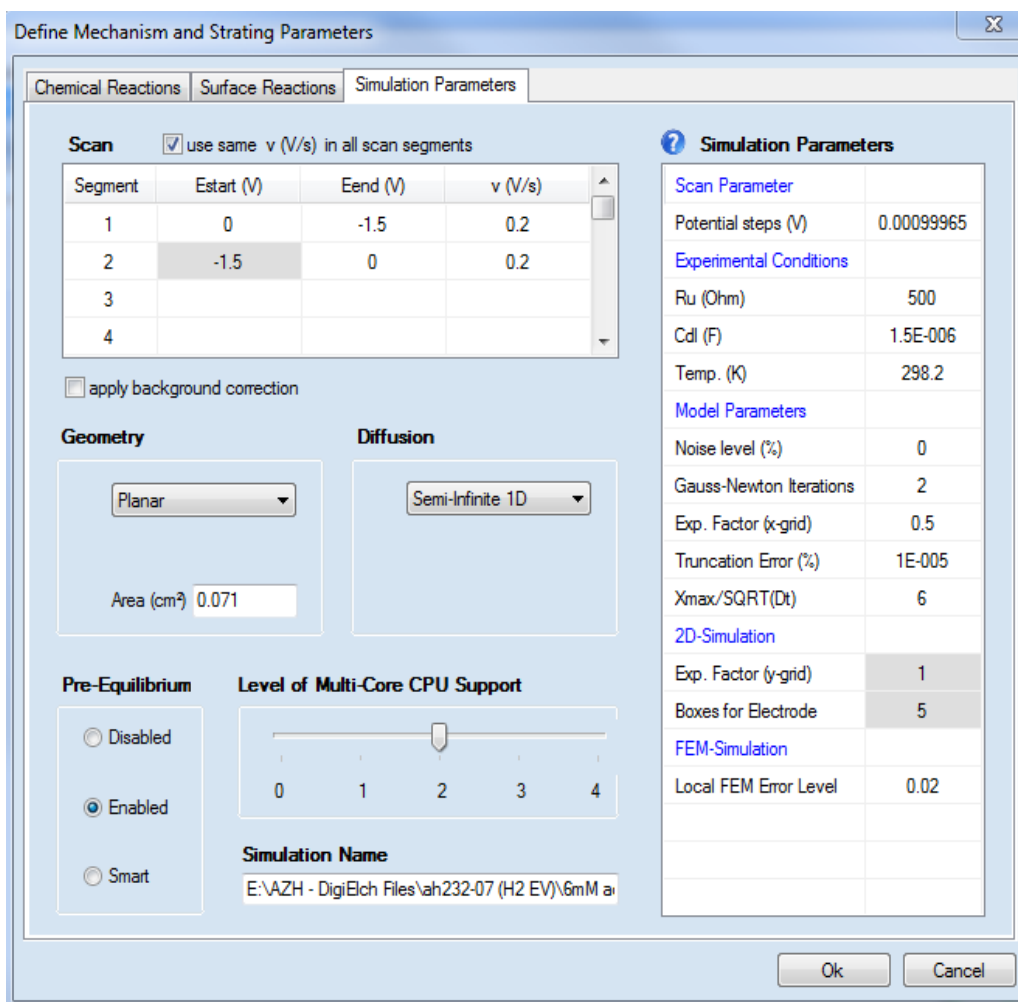


Figure A53. Screenshot of simulation parameters. Setting under Model parameters, 2D Simulation and FEM-Simulation do not need to be changed at all.

Define Mechanism and Strating Parameters

Chemical Reactions | Surface Reactions | Simulation Parameters

?	Charge-Transfer Reaction	E° (V)	<input checked="" type="radio"/> α <input type="radio"/> λ (eV)	ks (cm/s)
1	catH+ + e = catH	-1.02	0.31663	0.007
2	catH2++ + e = catH2+	-0.92472	0.92549	8.485E-005
3				
4				
5				

?	Chemical Reaction	Keq	kf	kb
1	cat + H+ = catH+	6.6561	2.1768E+015	3.2704E+014
2	catH + catH = cat + Hydrogen	1E+006	2E+006	2
3	catH + H+ = catH2+	11868	32129	2.7071
4	catH2++ => catH+ + H+	0.003434	100	0
5				

?	Species	Boundary	D (cm²/s)	Canal (mol/l)	Cnit (mol/l)
1	cat	ORB	7E-005	0.003	0.0027342
2	H+	ORB	1.2E-005	0.006	0.0055698
3	catH+	ORB	1E-005	0	0.00010137
4	catH	ORB	1E-005	0	5.8546E-022
5	Hydrogen	ORB	1E-005	0	1.2536E-034

Ok Cancel

Figure A54. Screenshot of the chemical reactions tab.

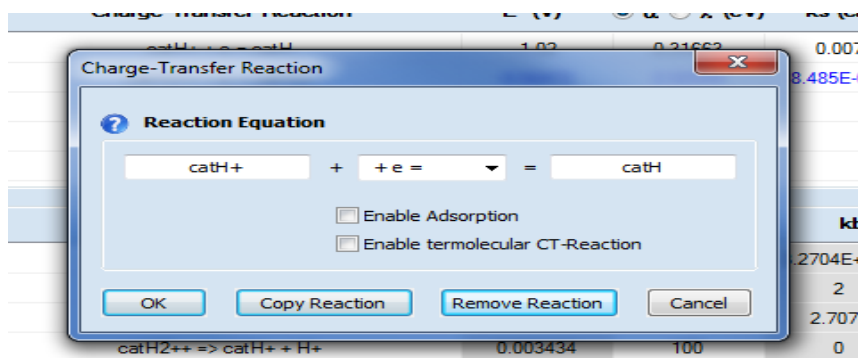


Figure A55. Screenshot of popup window obtained by double clicking on charge transfer reaction box.

After you have entered all parameters correctly, perform data fitting by clicking the fit data icon. Keep doing this and making small changes to mechanism or entered parameters until you get a good fit of experimental data. This sometimes takes weeks, so don't be discouraged if you do not succeed initially.

Once you have obtained a good fit of your experimental data, you must now export the simulated CVs. For example, if you fit your data over a scan rate range of 0.2—0.5 V/s, you will actually have 4 different simulated CVs—at each scan rate. You can scroll through by clicking the arrow reading next file. For each scan rate (performing one by one) click compare curves. The compare curve tab will be located at the top of the screen. Two new CVs will be present on this screen, one of your experimental and one of your simulated. Highlight the simulated CV and click export file. It will export and save as a .use file. Delete both curves from the compare curves section and go back to the data fitting section. Scroll to the next scan rate and repeat process by clicking compare curves. Once you have successfully exported all simulated files you can open them with

notepad++ and resave them as .csv files. This allows you to open the files in excel and then proceed to generate publication quality plots of CV data.

APPENDIX B:
EXPERIMENTAL AND SIMULATED
CYCLIC VOLTAMMOGRAMS

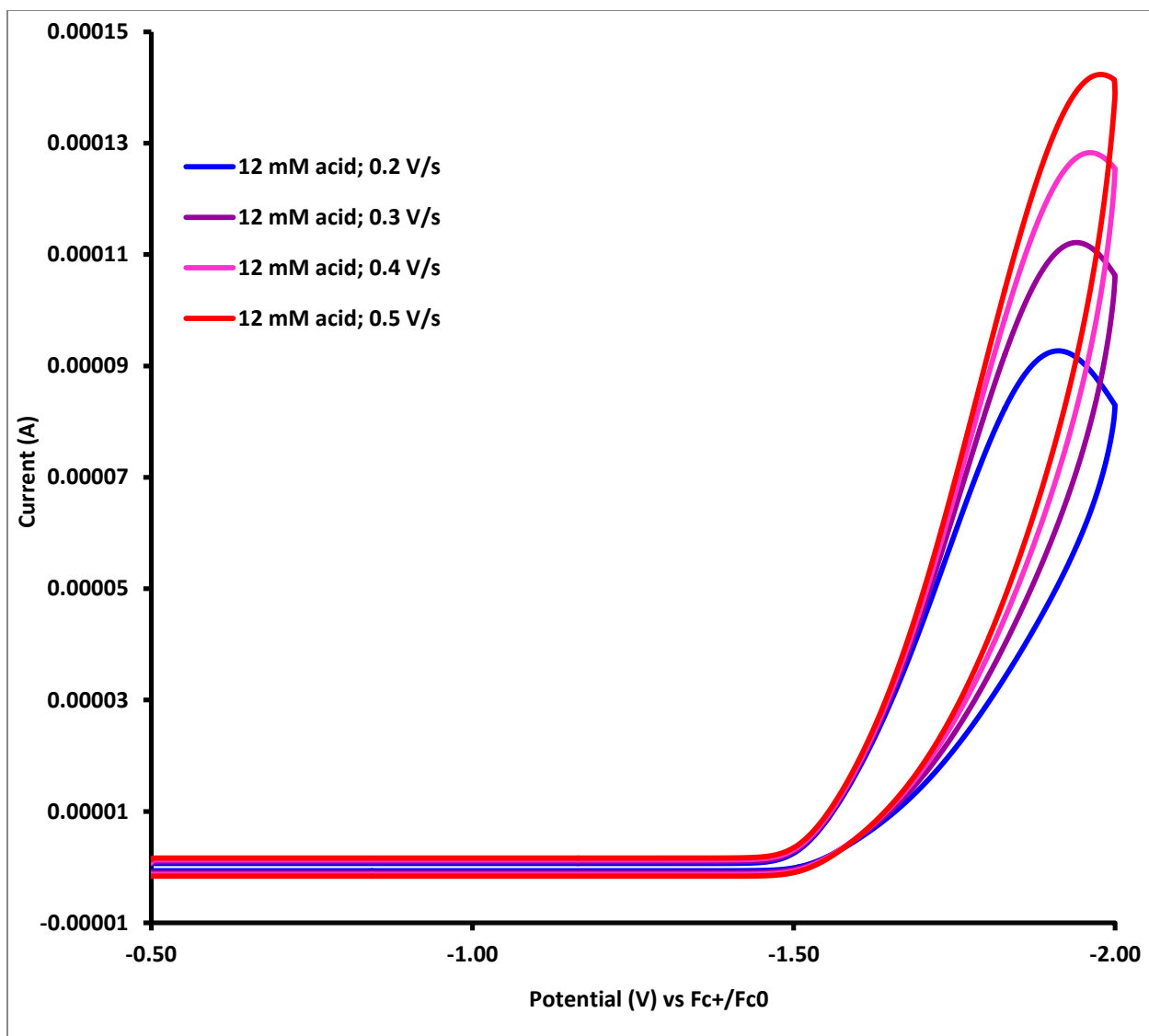


Figure B56. ZnL HER CV Simulations of experimental data; 12 mM [acid]; $v = 0.2 - 0.5$ V/s vs Fc⁺/Fc. Fit with mechanism parameters from Table A4.

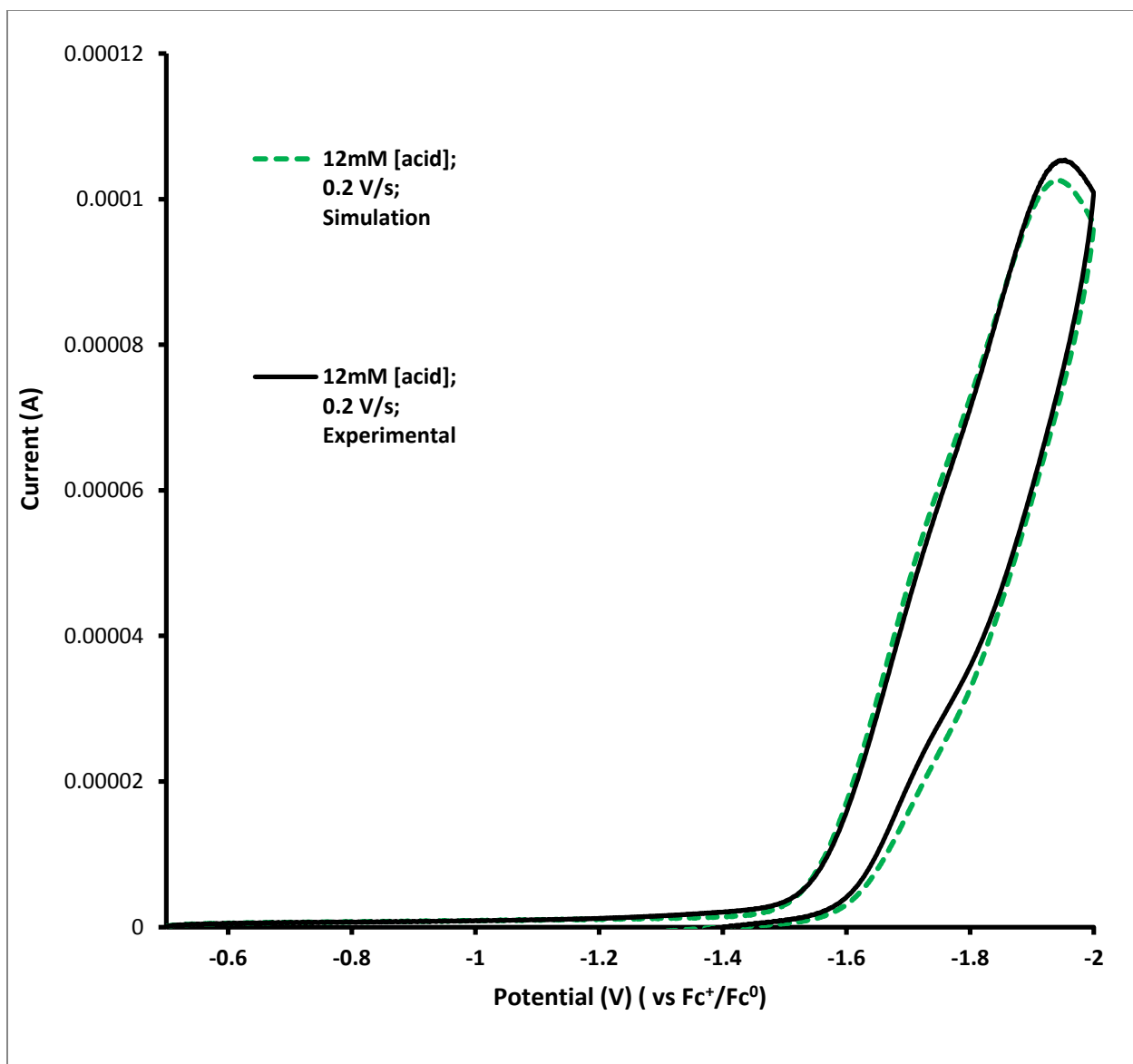


Figure B57. Comparison of experimental (black solid) and simulated (green dotted) cyclic voltammograms; ZnL¹ HER. 12 mM [acid]; $\nu = 0.2$ V/s vs Fc⁺/Fc. Fit with mechanism parameters from Table A4.

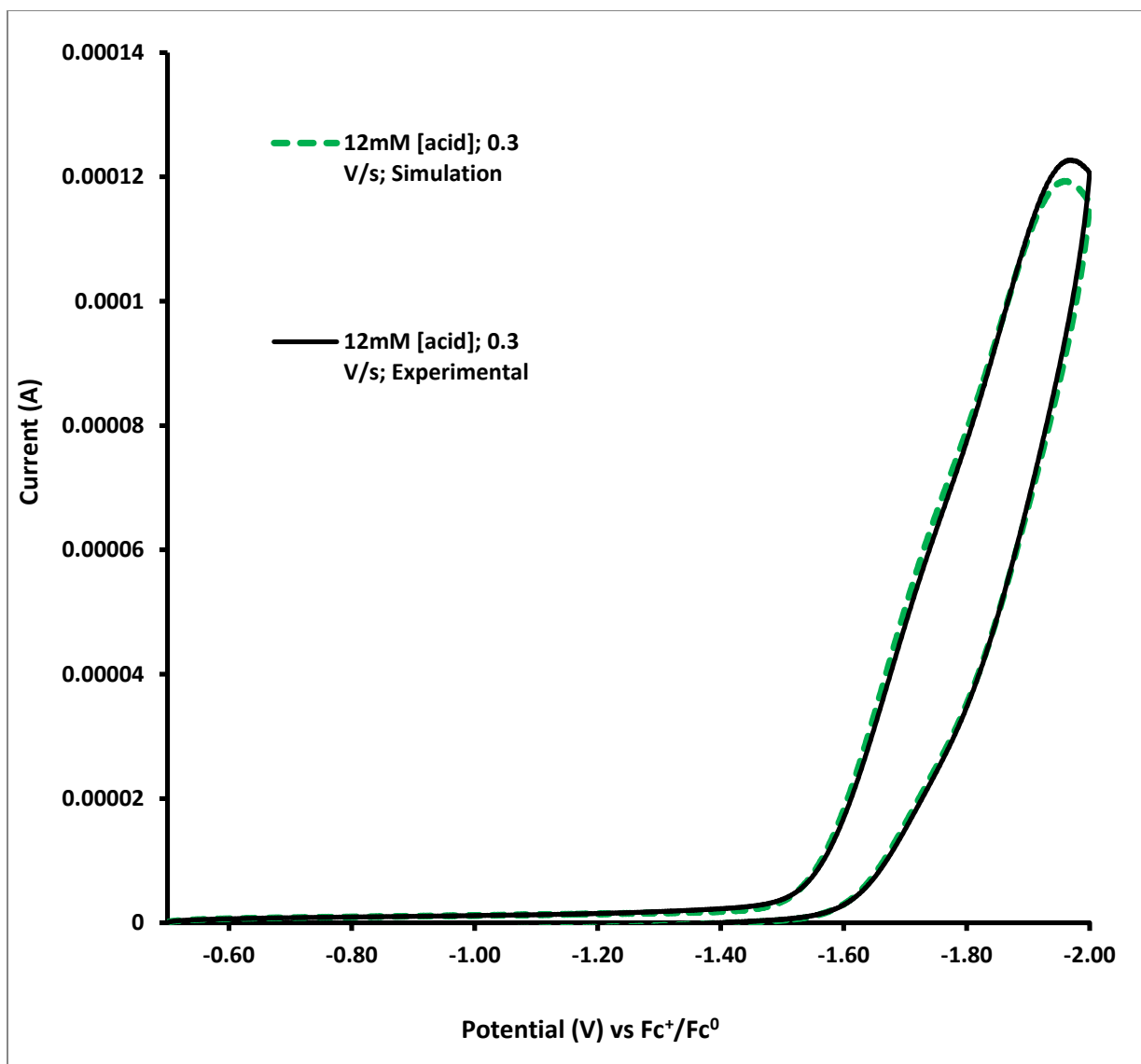


Figure B58. Comparison of experimental (black solid) and simulated (green dotted) cyclic voltammograms; ZnL¹ HER. 12 mM [acid]; $\nu = 0.3$ V/s vs Fc⁺/Fc. Fit with mechanism parameters from Table A4.

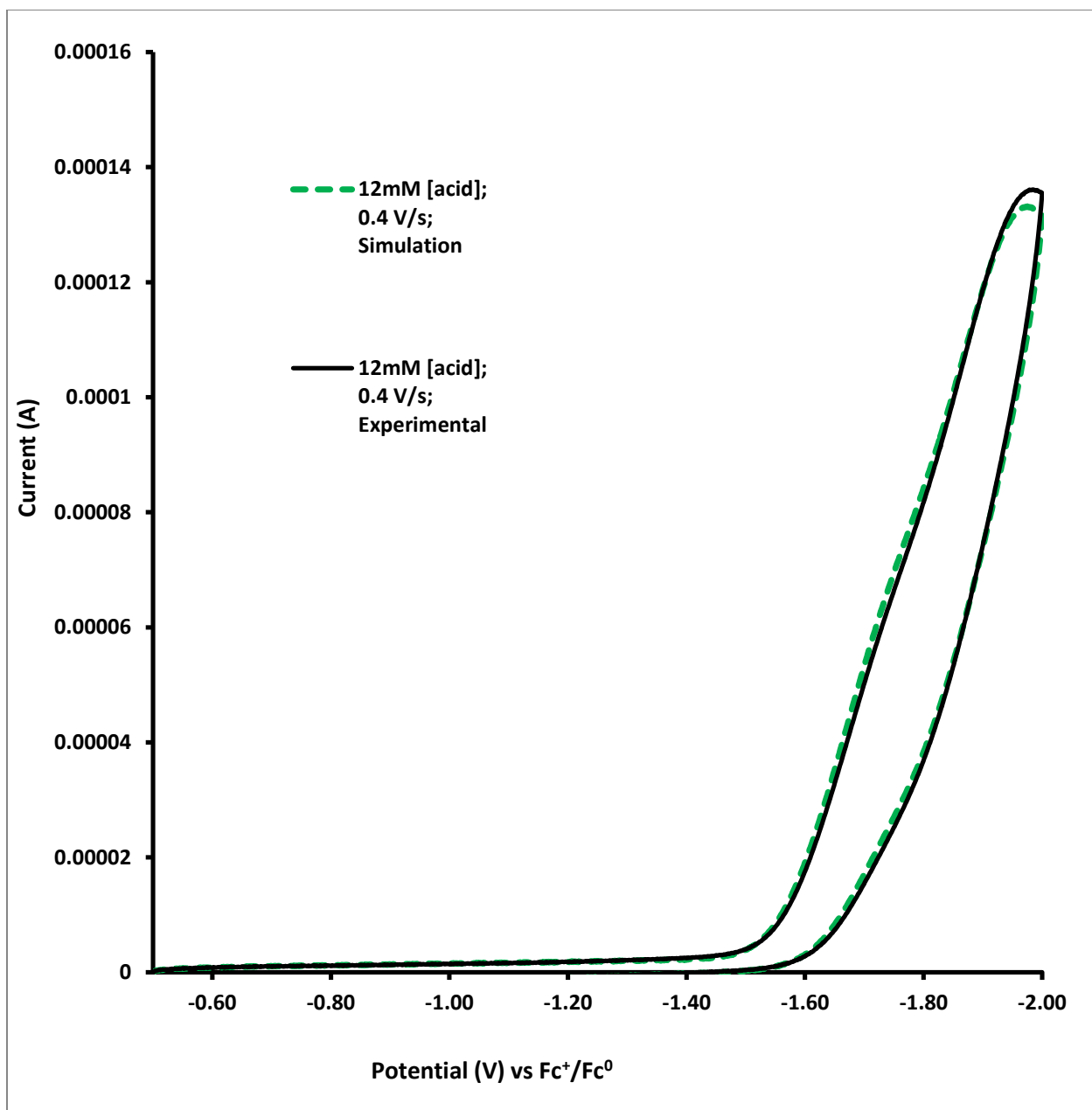


Figure B59. Comparison of experimental (black solid) and simulated (green dotted) cyclic voltammograms; ZnL^1 HER. 12 mM [acid]; $\nu = 0.4$ V/s vs Fc^+/Fc . Fit with mechanism parameters from Table A4.

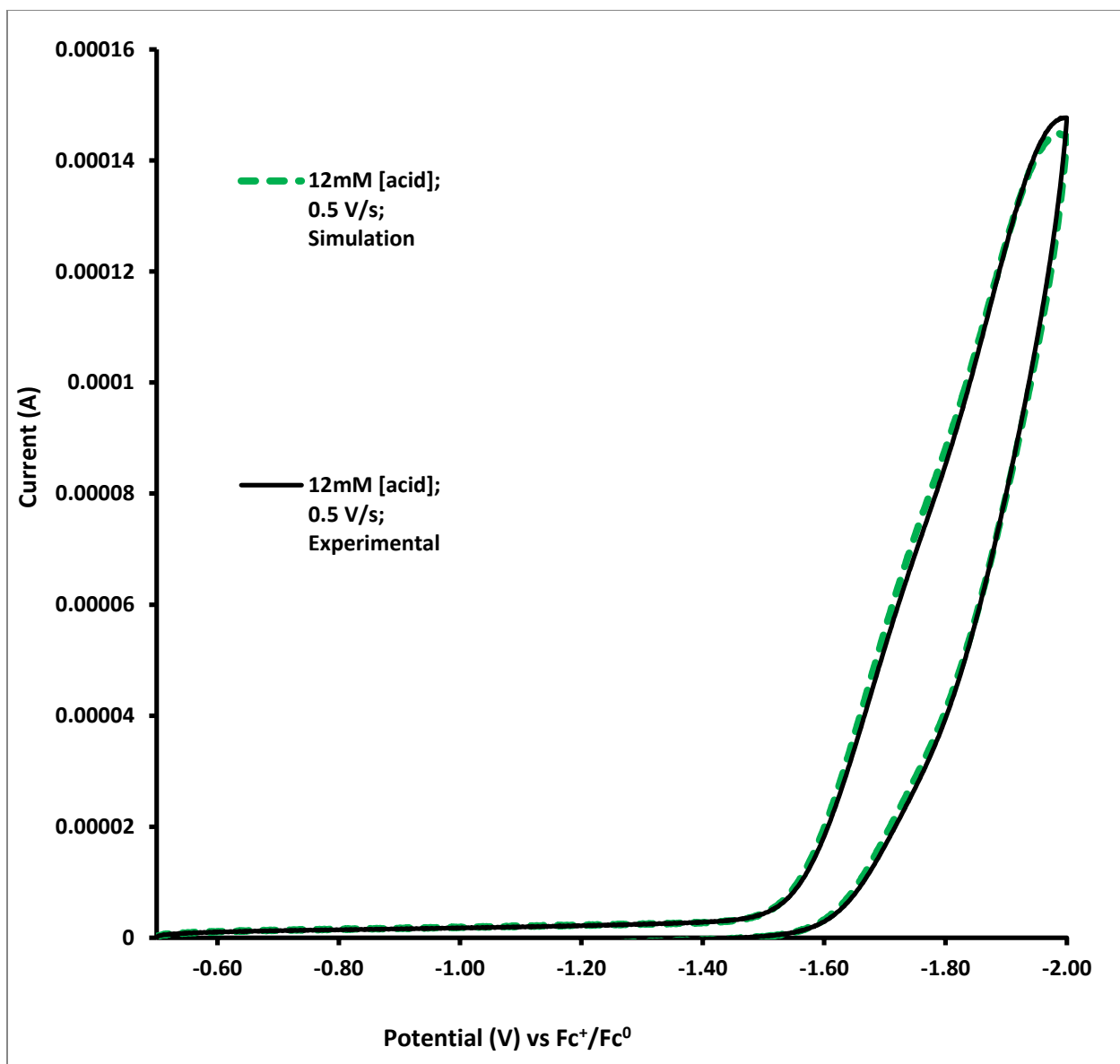


Figure B60. Comparison of experimental (black solid) and simulated (green dotted) cyclic voltammograms; ZnL^1 HER. 12 mM [acid]; $\nu = 0.5$ V/s vs Fc^+/Fc . Fit with mechanism parameters from Table A4.

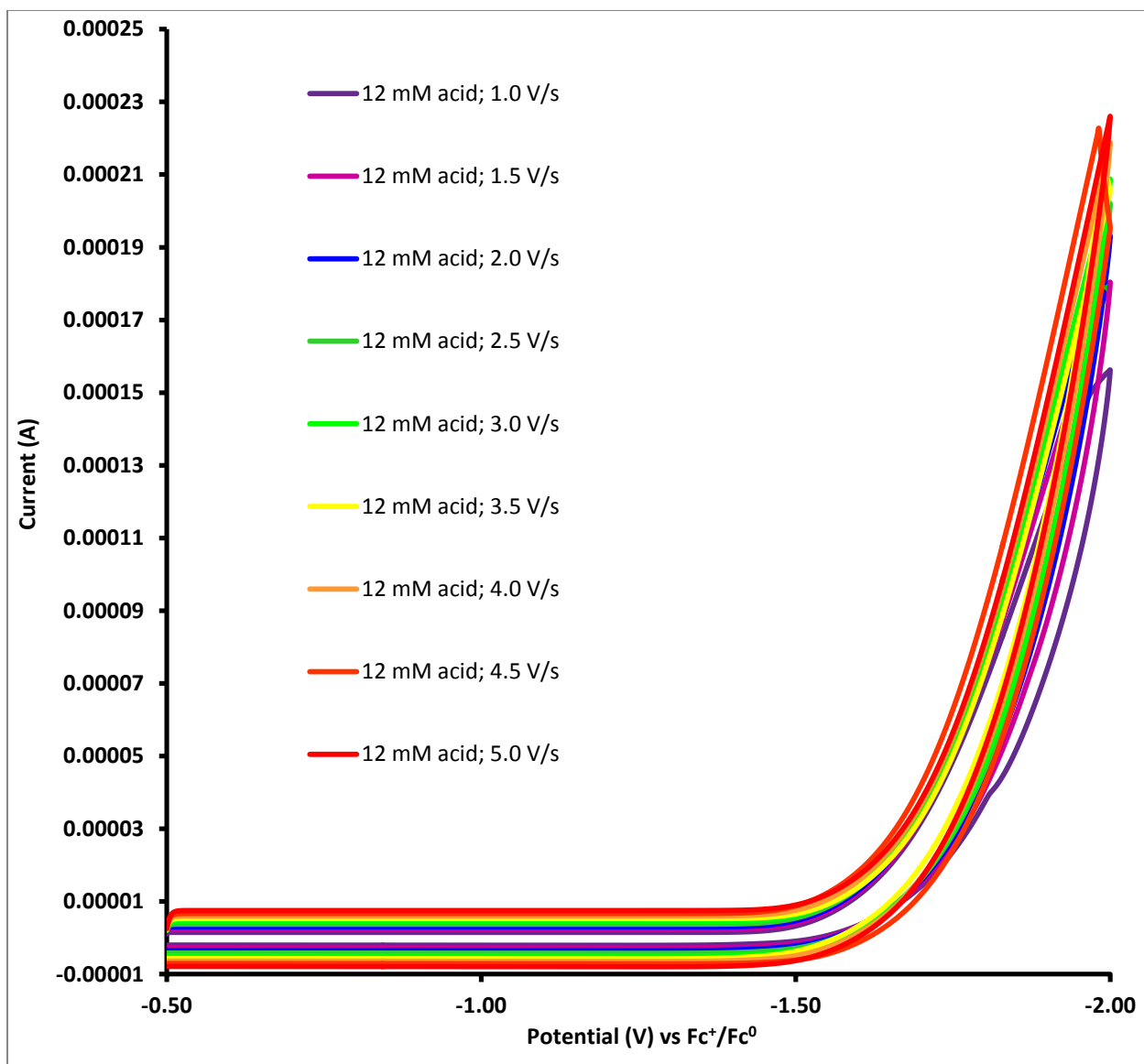


Figure B61. ZnL HER CV Simulations of experimental data; 12 mM [acid]; $v = 1.0 - 5.0$ V/s vs Fc^+/Fc . Fit with mechanism parameters from Table A5.

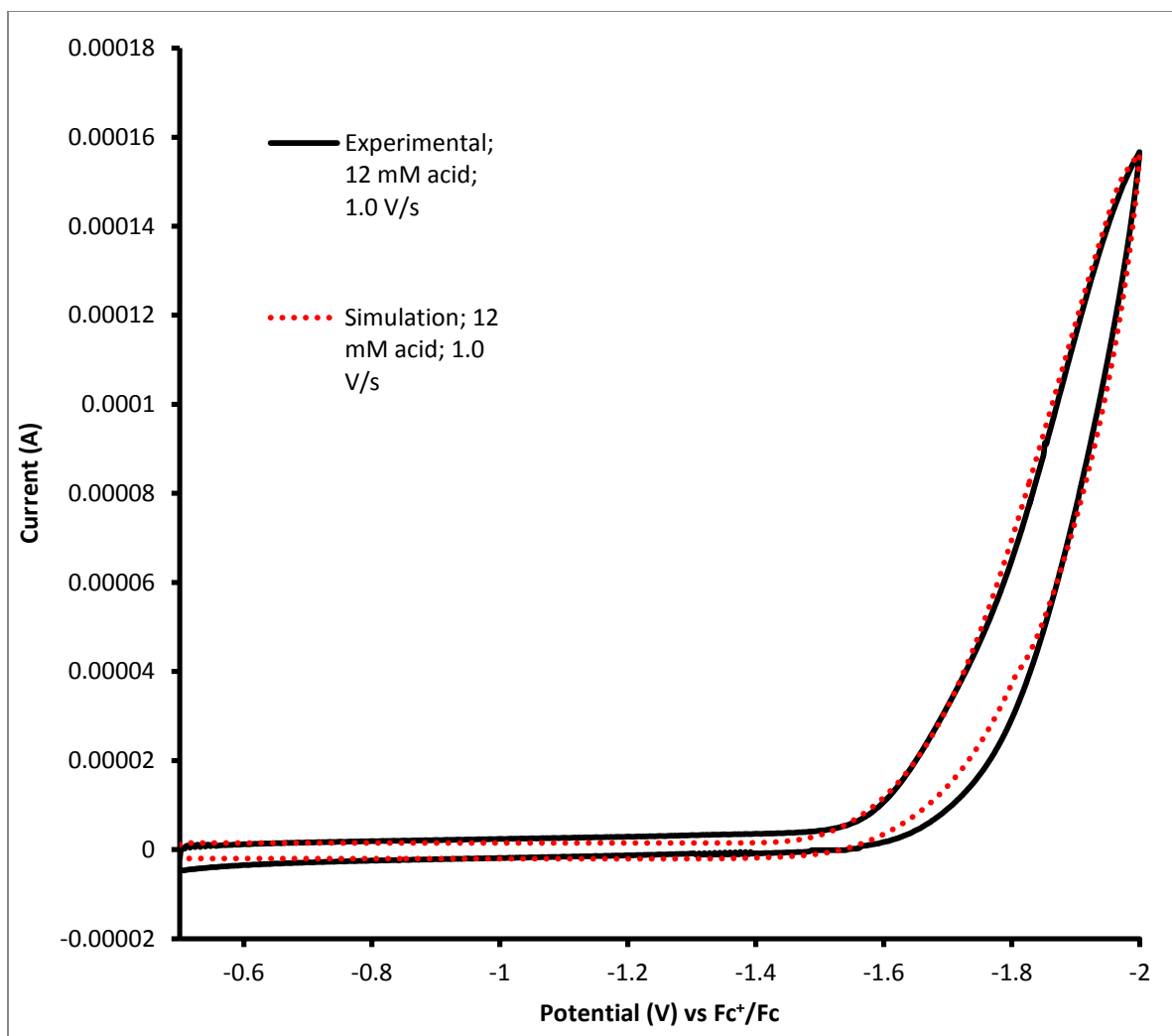


Figure B62. Comparison of experimental (black solid) and simulated (red dotted) cyclic voltammograms; ZnL¹ HER. 12 mM [acid]; $\nu = 1.0$ V/s vs Fc⁺/Fc. Fit with mechanism parameters from Table A5.

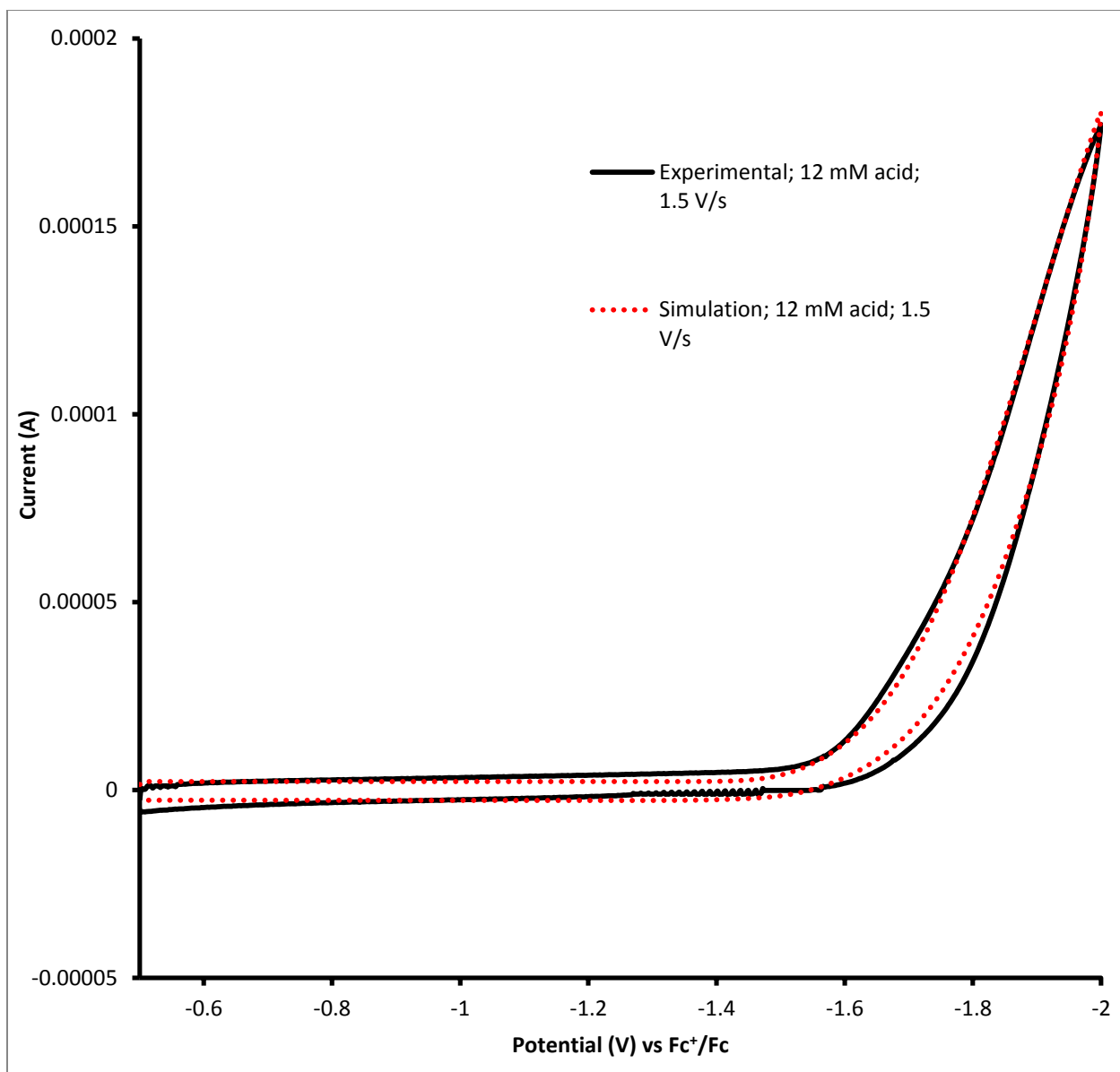


Figure B63. Comparison of experimental (black solid) and simulated (red dotted) cyclic voltammograms; ZnL¹ HER. 12 mM [acid]; $\nu = 1.5$ V/s vs Fc⁺/Fc. Fit with mechanism parameters from Table A5.

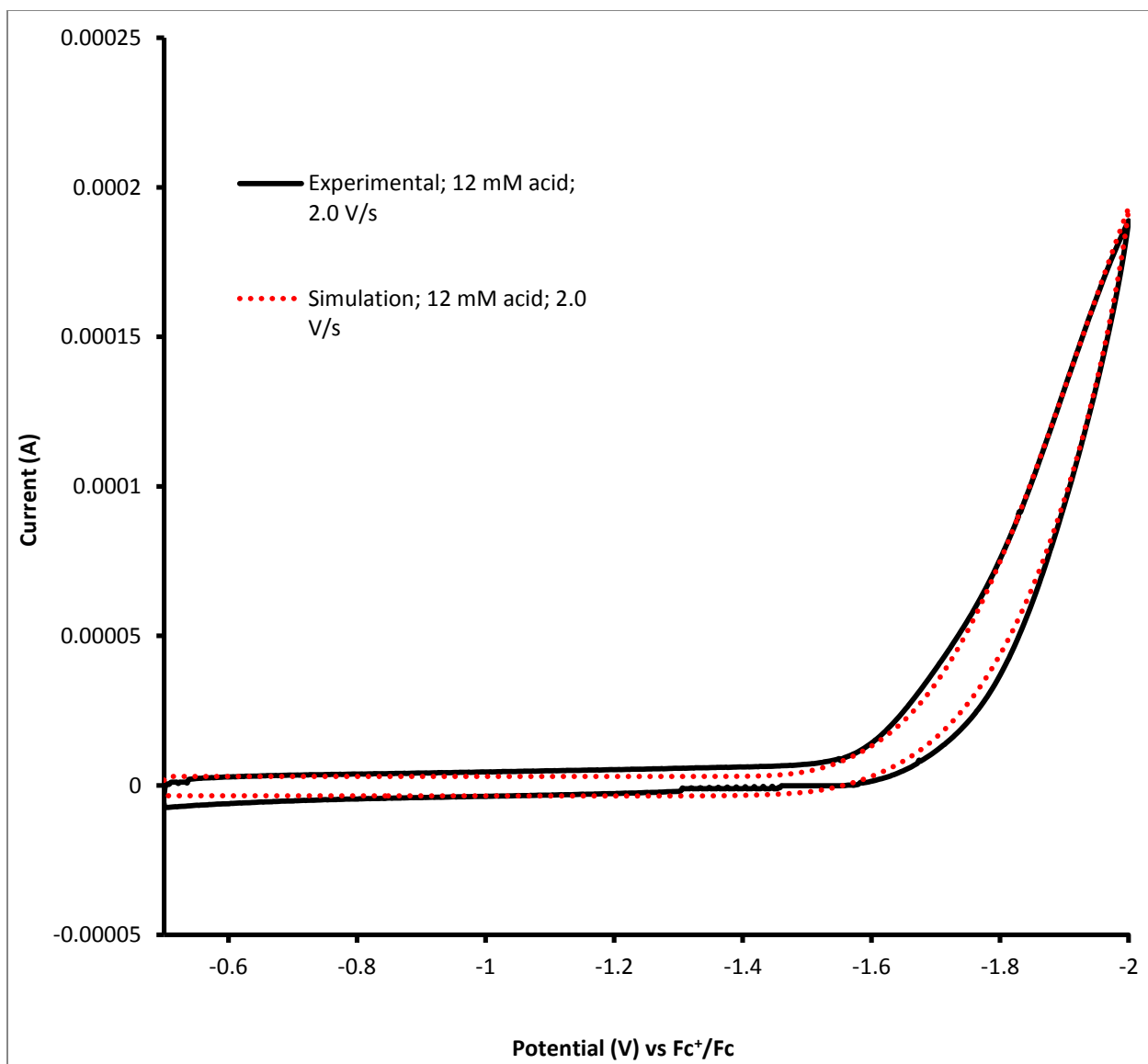


Figure B64. Comparison of experimental (black solid) and simulated (red dotted) cyclic voltammograms; ZnL^1 HER. 12 mM [acid]; $\nu = 2.0$ V/s vs Fc^+/Fc . Fit with mechanism parameters from Table A5.

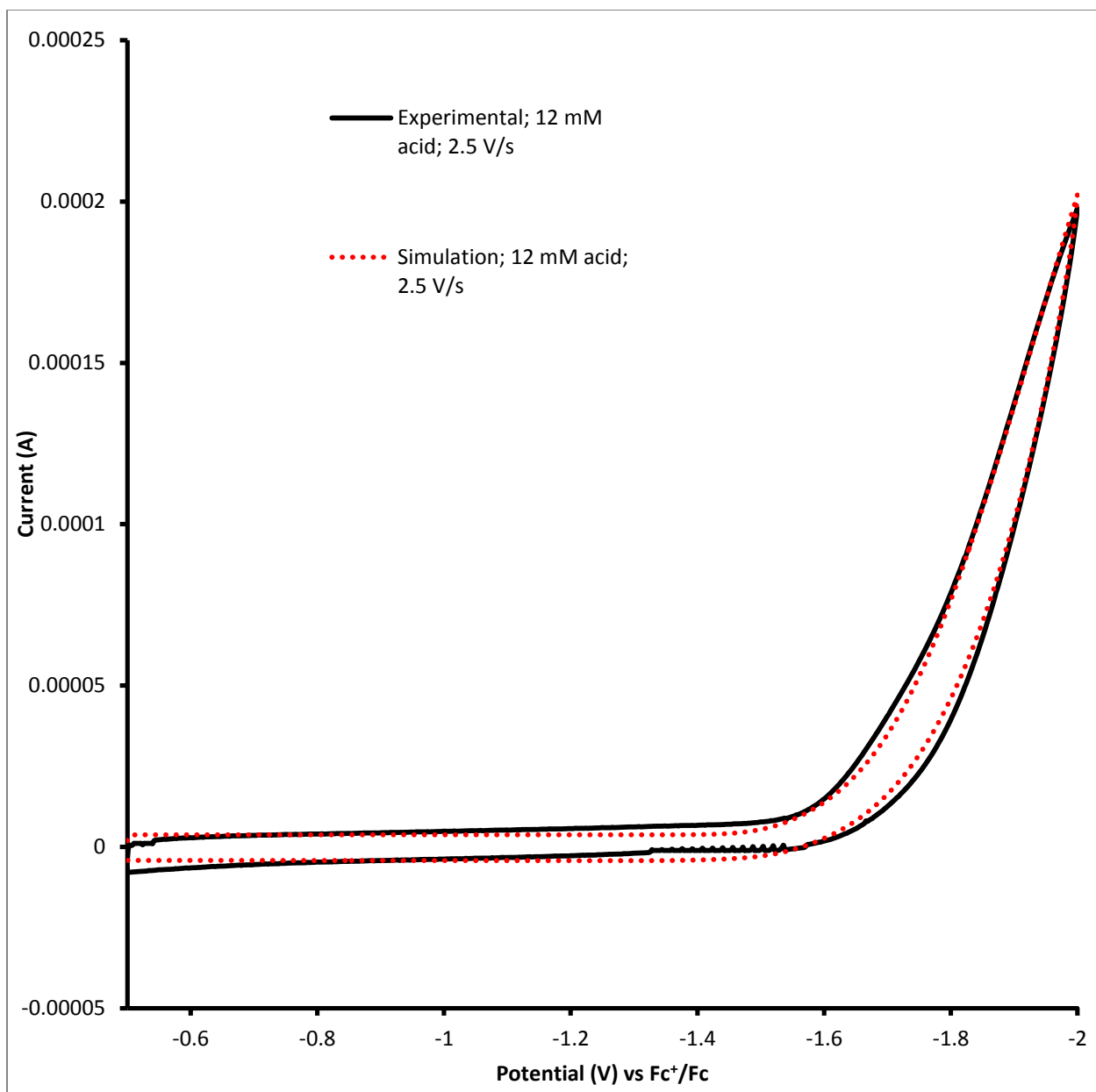


Figure B65. Comparison of experimental (black solid) and simulated (red dotted) cyclic voltammograms; ZnL¹ HER. 12 mM [acid]; $\nu = 2.5$ V/s vs Fc⁺/Fc. Fit with mechanism parameters from Table A5.

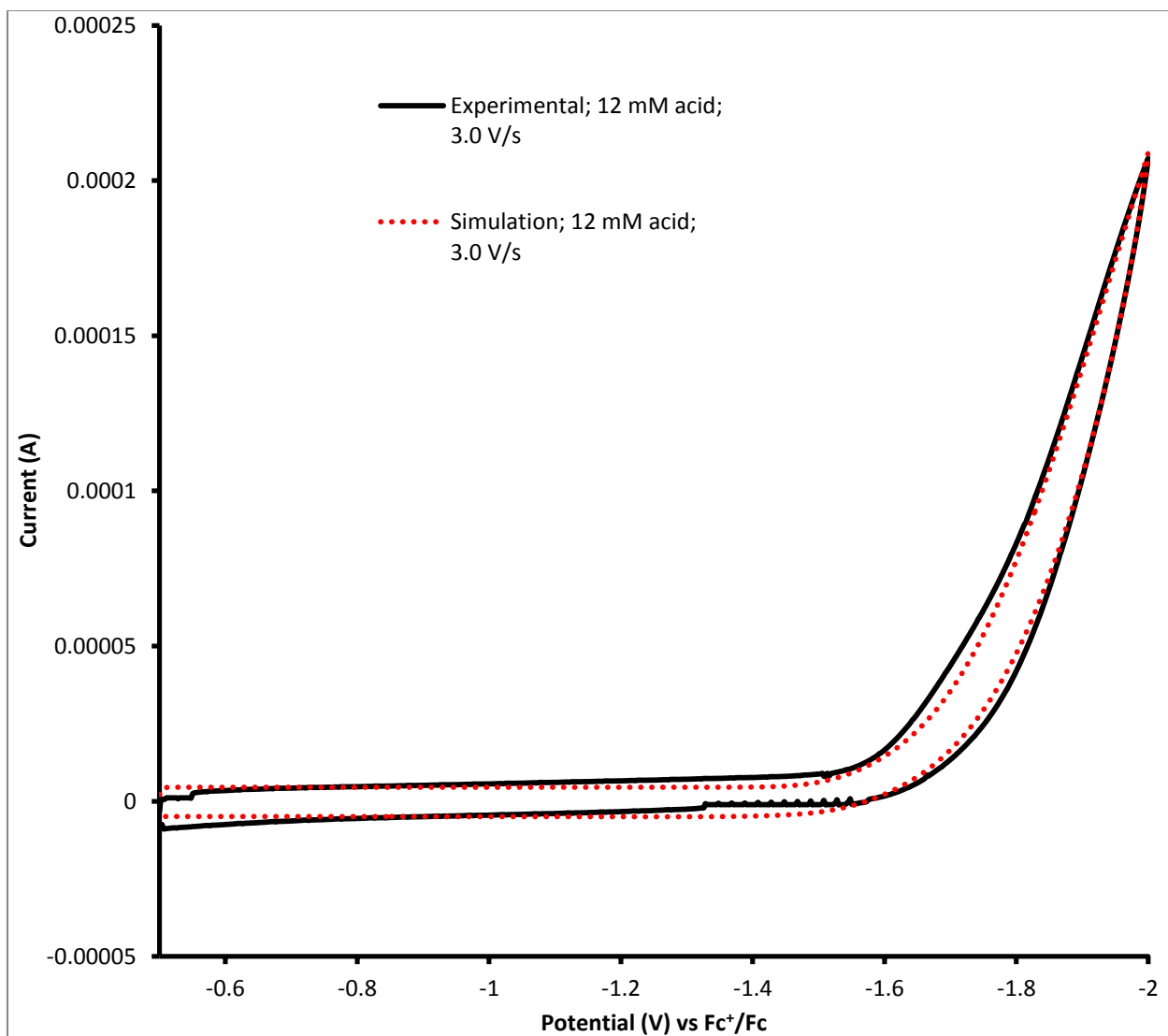


Figure B66. Comparison of experimental (black solid) and simulated (red dotted) cyclic voltammograms; ZnL¹ HER. 12 mM [acid]; $\nu = 3.0$ V/s vs Fc⁺/Fc. Fit with mechanism parameters from Table A5.

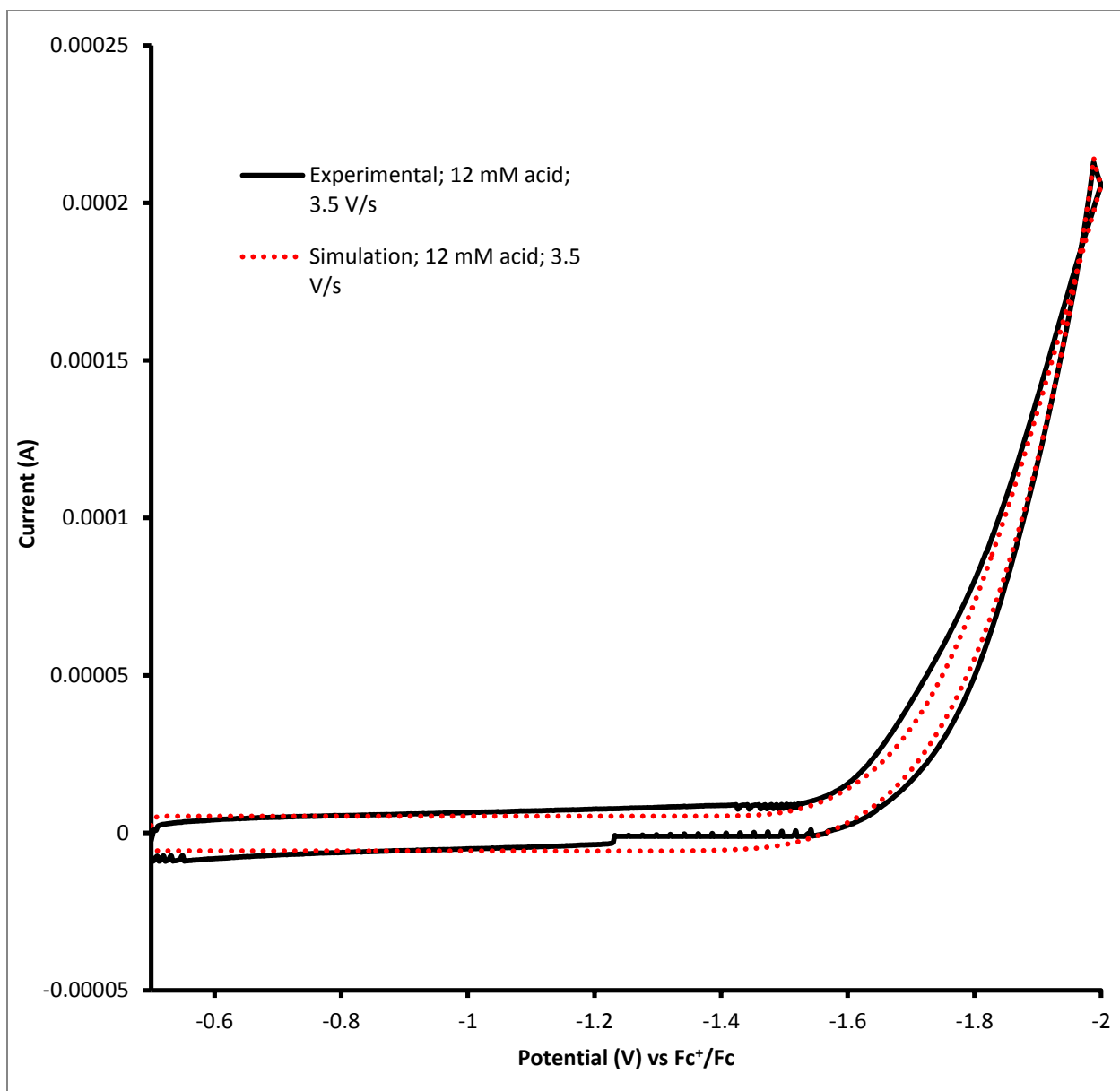


Figure B67. Comparison of experimental (black solid) and simulated (red dotted) cyclic voltammograms; ZnL¹ HER. 12 mM [acid]; $\nu = 3.5$ V/s vs Fc⁺/Fc. Fit with mechanism parameters from Table A5.

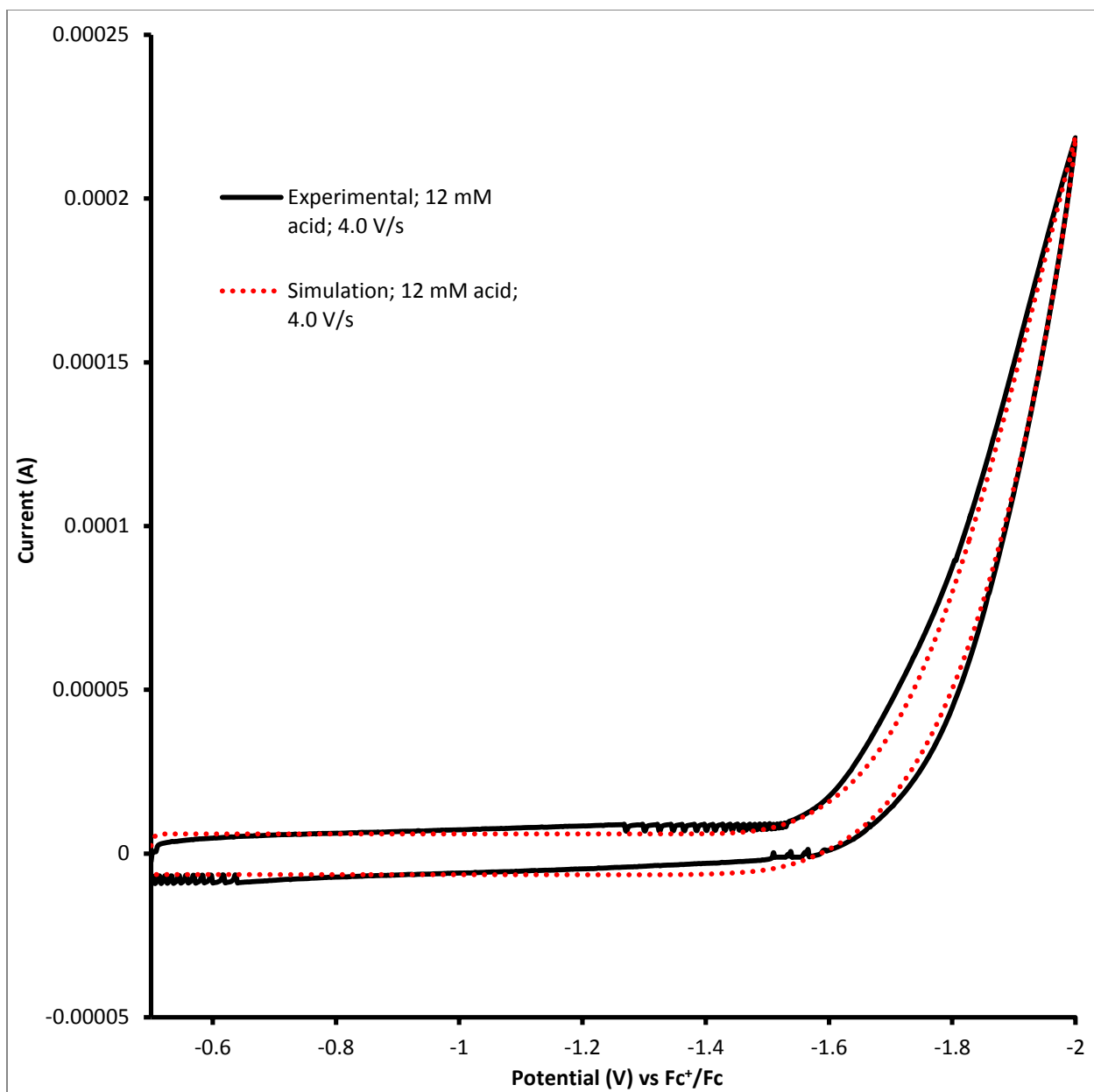


Figure B68. Comparison of experimental (black solid) and simulated (red dotted) cyclic voltammograms; ZnL^1 HER. 12 mM [acid]; $\nu = 4.0$ V/s vs Fc^+/Fc . Fit with mechanism parameters from Table A5.

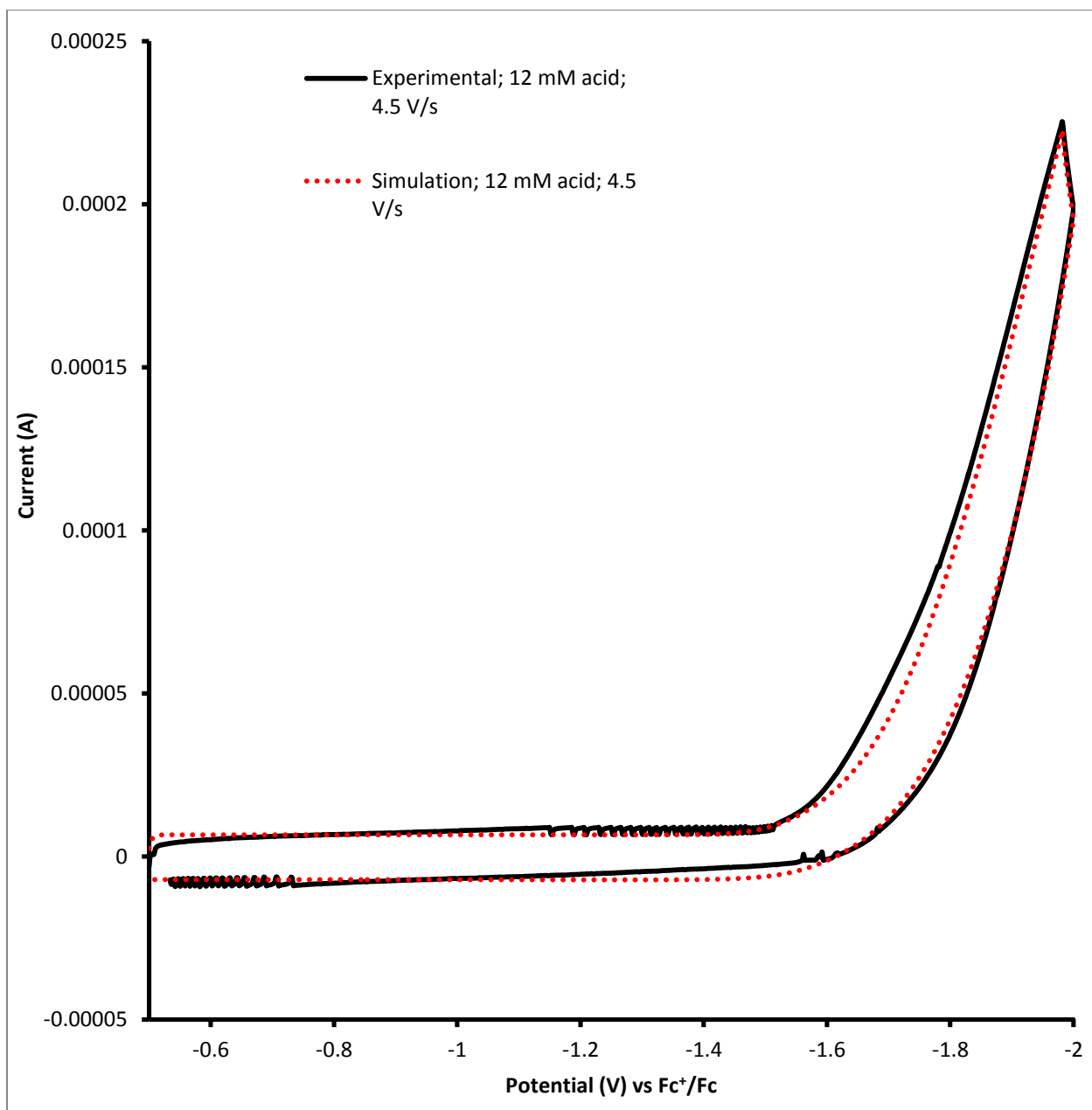


Figure B69. Comparison of experimental (black solid) and simulated (red dotted) cyclic voltammograms; ZnL¹ HER. 12 mM [acid]; $\nu = 4.5$ V/s vs Fc⁺/Fc. Fit with mechanism parameters from Table A5.

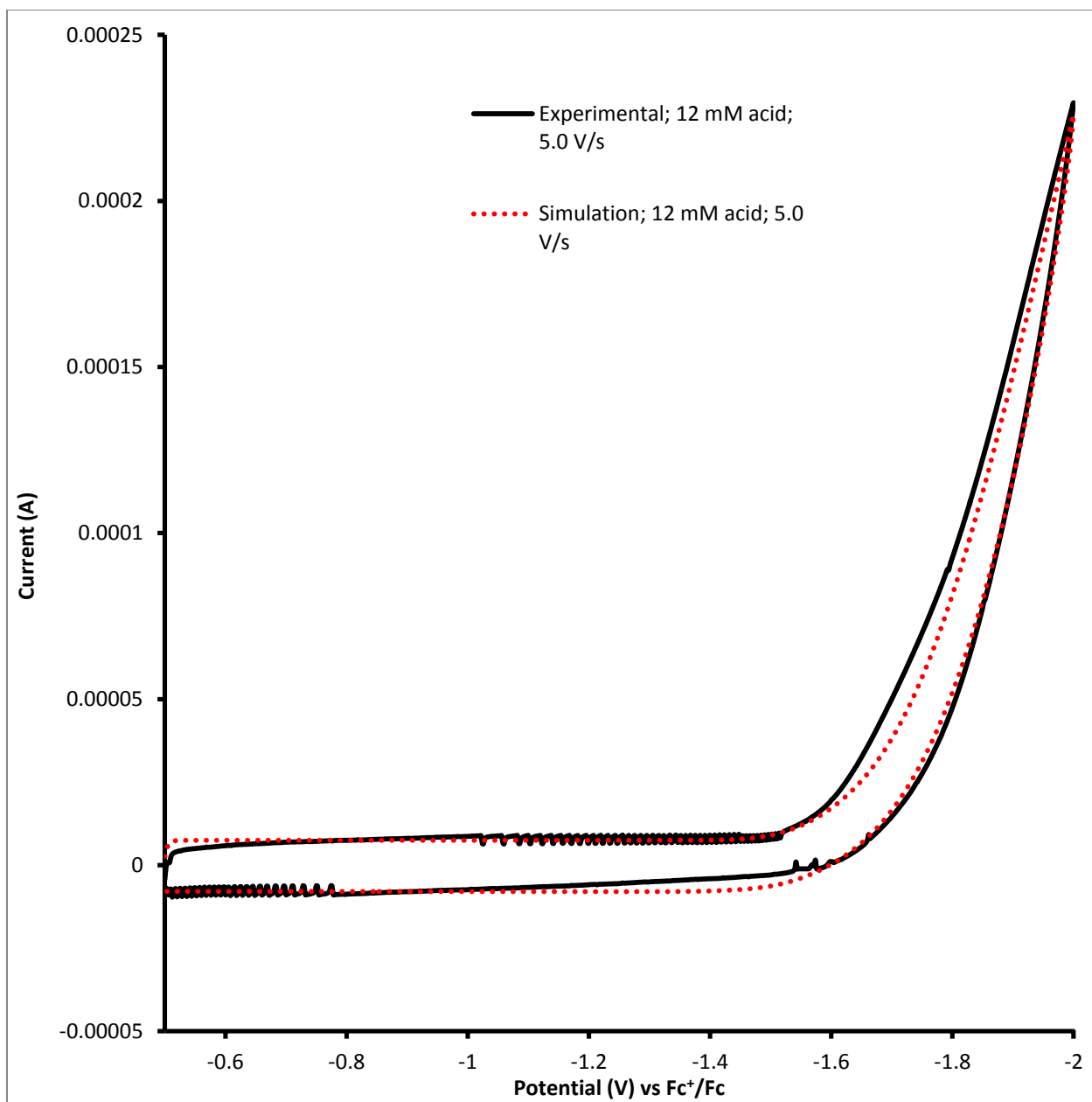


Figure B70. Comparison of experimental (black solid) and simulated (red dotted) cyclic voltammograms; ZnL¹ HER. 12 mM [acid]; $\nu = 5.0$ V/s vs Fc⁺/Fc. Fit with mechanism parameters from Table A5.

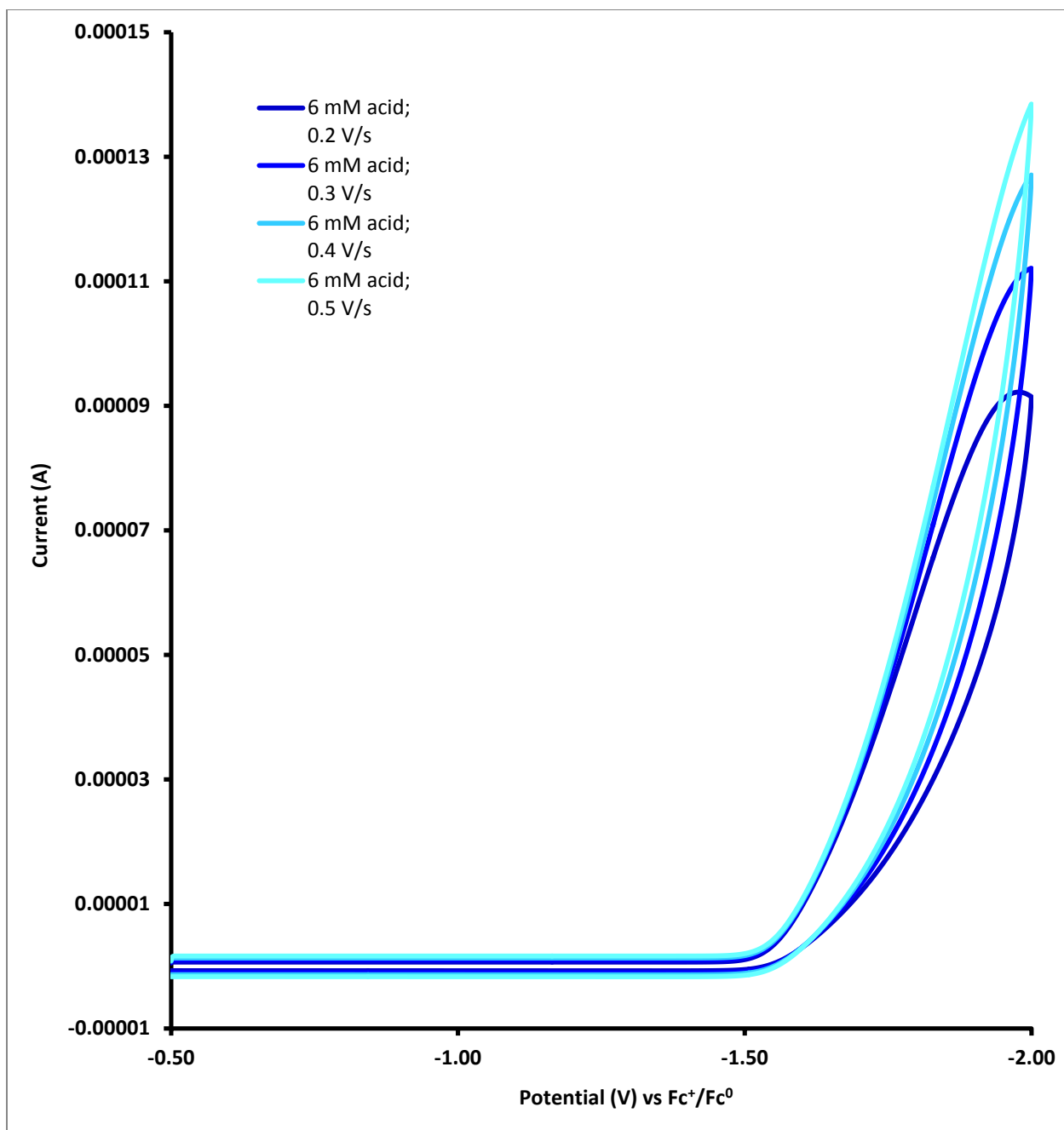


Figure B71. ZnL¹ HER. ZnL HER CV Simulations of experimental data; 6 mM [acid]; $\nu = 0.2$ — 0.5 V/s vs Fc⁺/Fc⁰. Fit with mechanism parameters from Table A6.

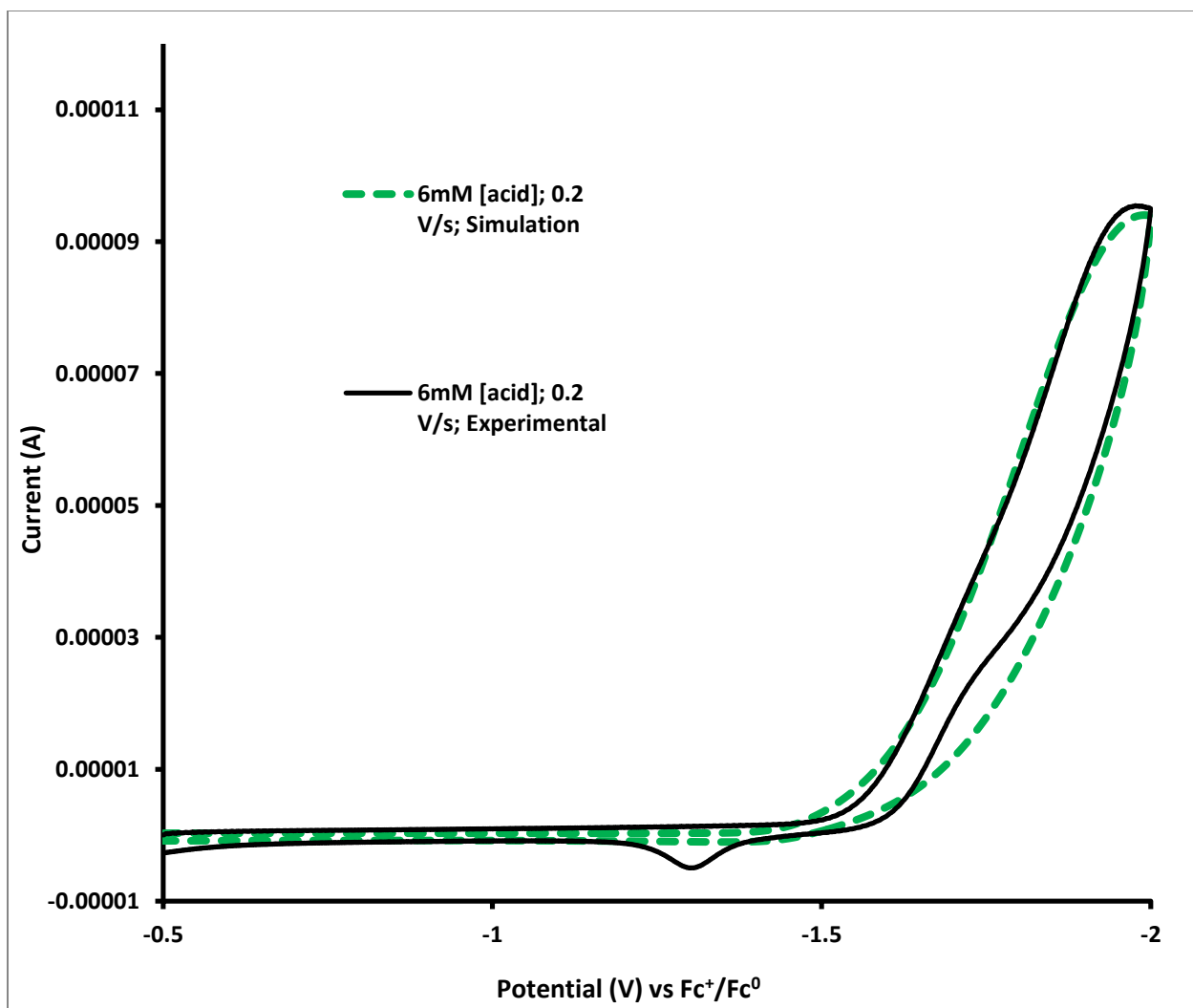


Figure B72. Comparison of experimental (black solid) and simulated (green dotted) cyclic voltammograms; ZnL¹ HER. 6 mM [acid]; $\nu = 0.2$ V/s vs Fc⁺/Fc. Fit with mechanism parameters from Table A6.

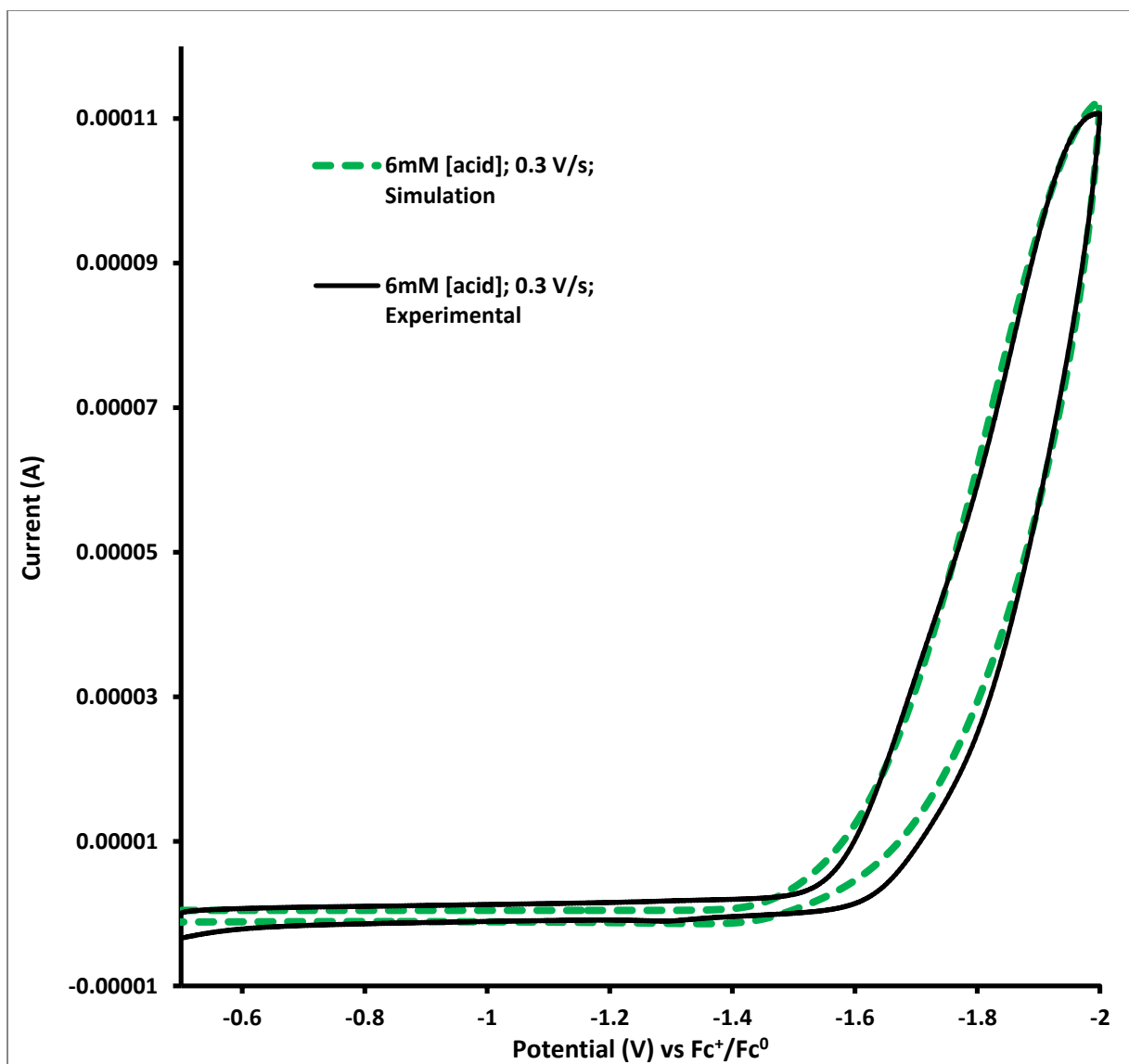


Figure B73. Comparison of experimental (black solid) and simulated (green dotted) cyclic voltammograms; ZnL^1 HER. 6 mM [acid]; $v = 0.3$ V/s vs Fc^+/Fc^0 . Fit with mechanism parameters from Table A6.

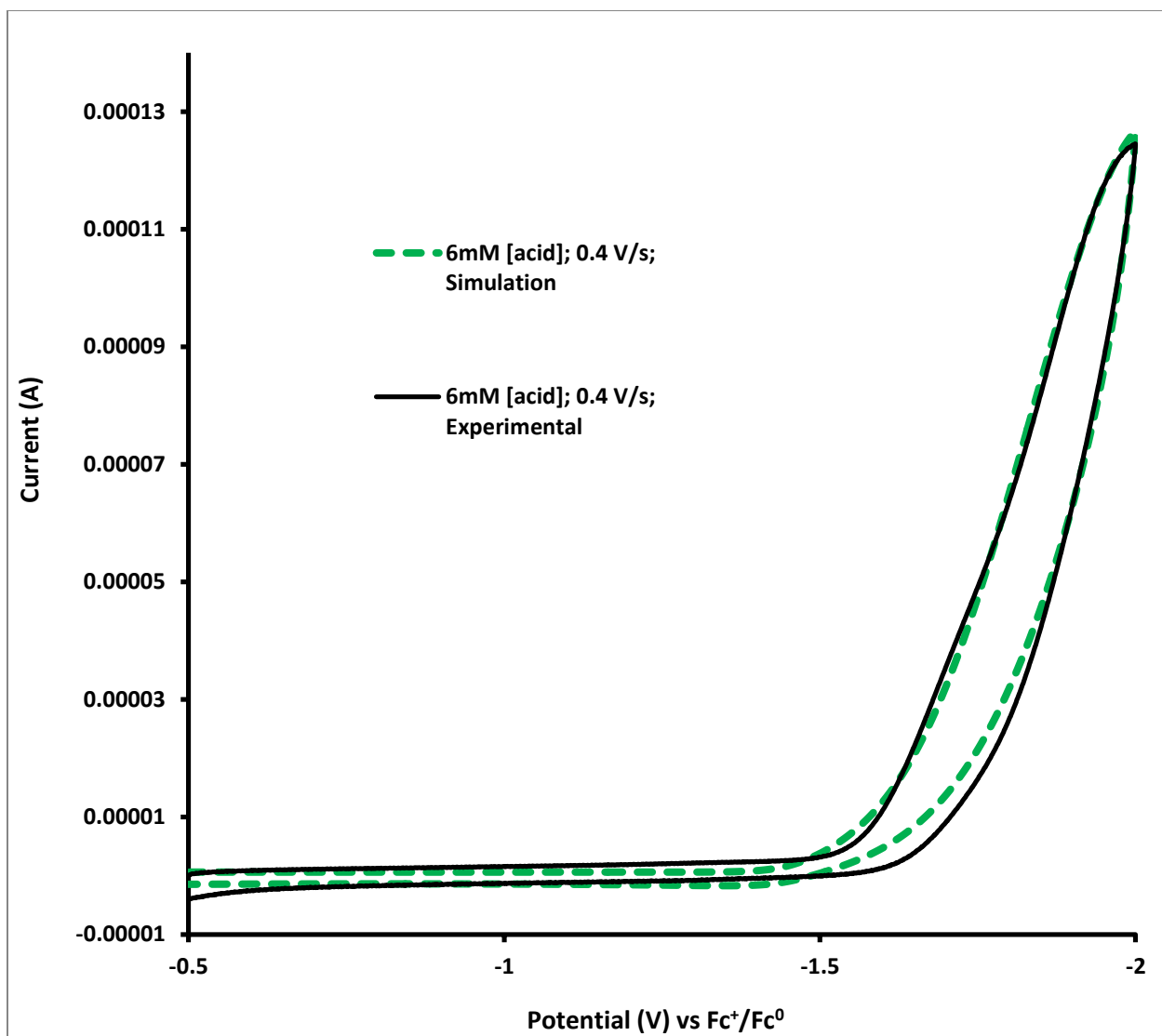


Figure B74. Comparison of experimental (black solid) and simulated (green dotted) cyclic voltammograms; ZnL^1 HER. 6 mM [acid]; $\nu = 0.4$ V/s vs Fc^+/Fc^0 . Fit with mechanism parameters from Table A6.

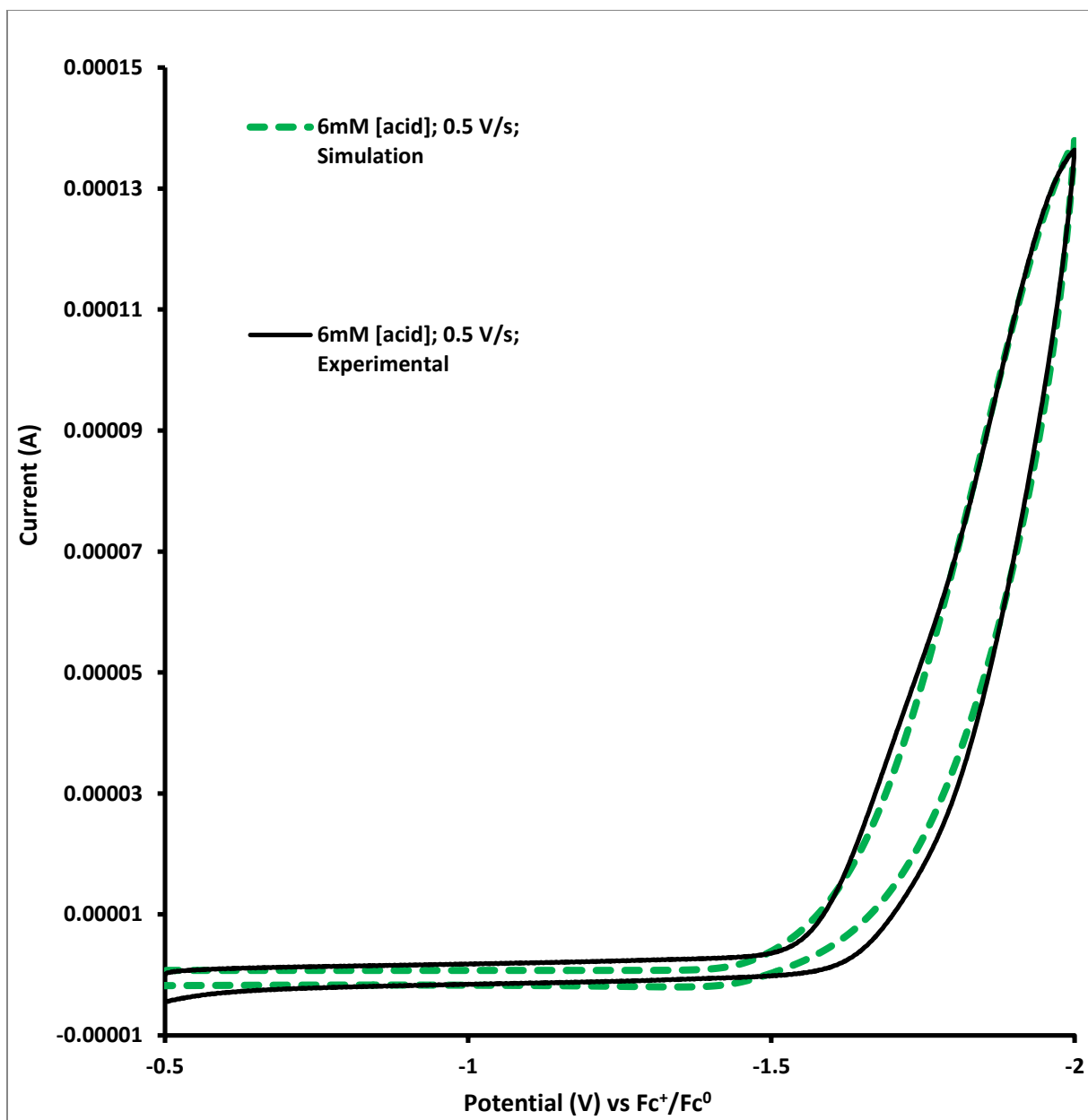


Figure B75. Comparison of experimental (black solid) and simulated (green dotted) cyclic voltammograms; ZnL¹ HER. 6 mM [acid]; $\nu = 0.5$ V/s vs Fc⁺/Fc. Fit with mechanism parameters from Table A6.

APPENDIX C:
ADDITIONAL ELECTROCHEMICAL
AND UV-VIS DATA

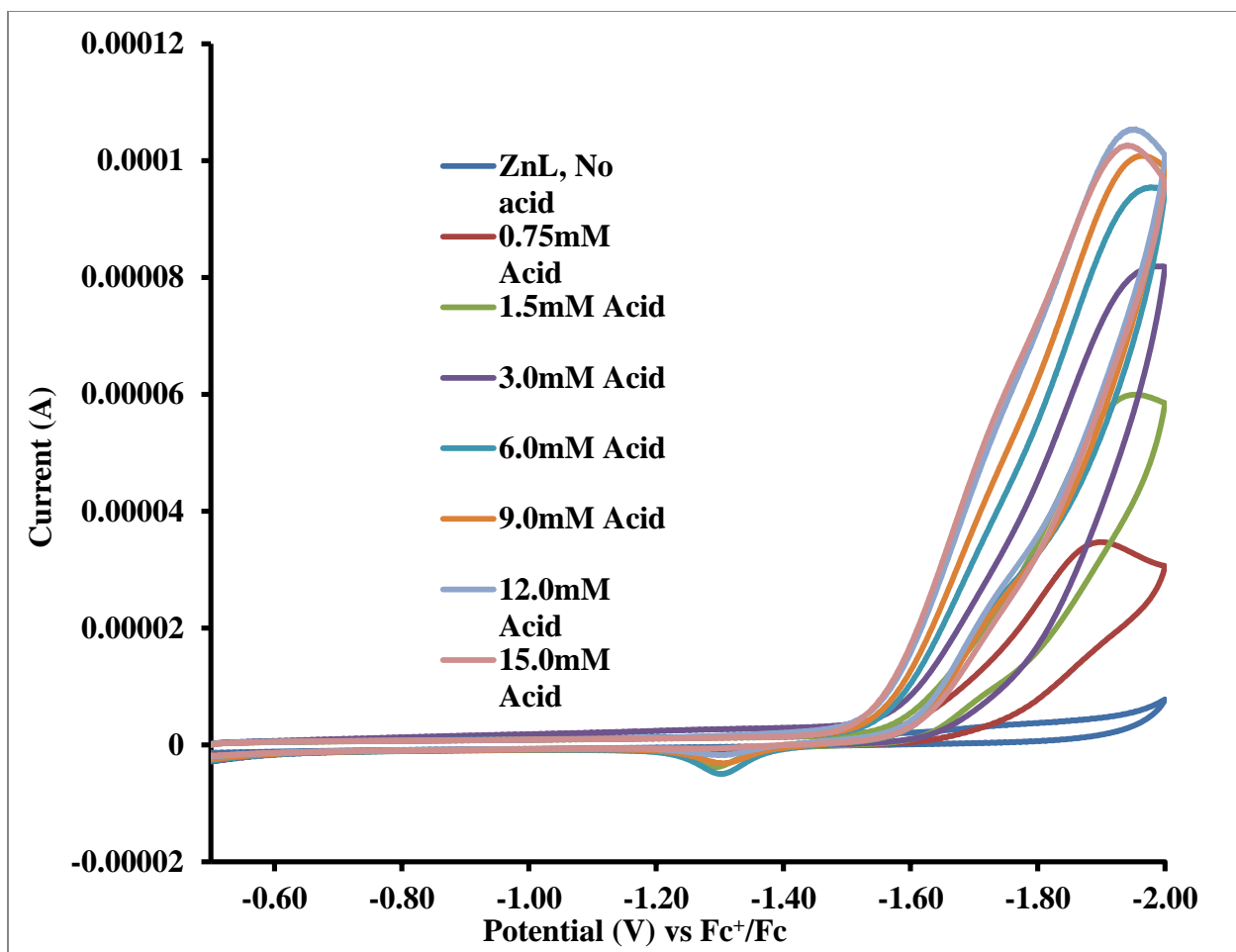


Figure C76. ZnL¹ HER cyclic voltammograms in 0.1 M Bu₄NPF₆ methanol solution with increasing concentrations of CH₃COOH added; $\nu = 0.2$ V/s.

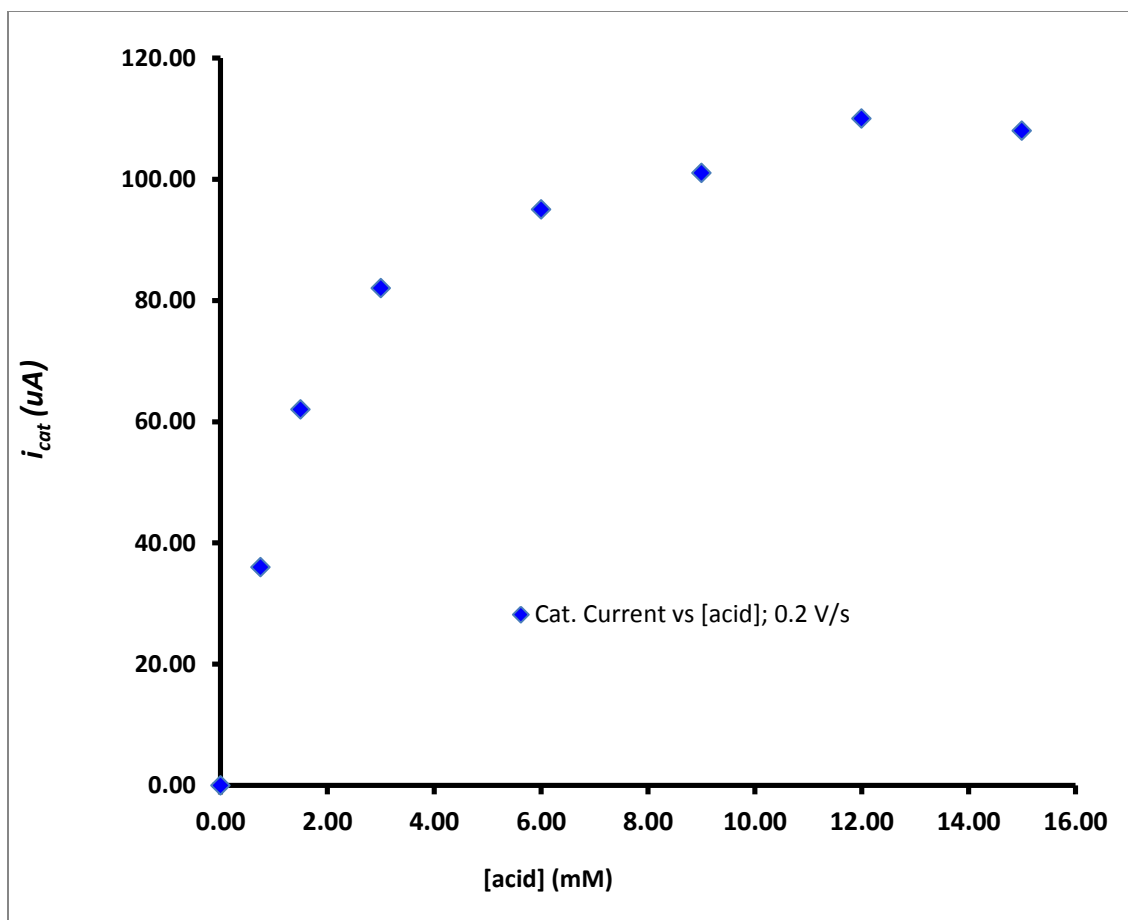


Figure C77. Plot of CH_3COOH concentration versus catalytic current for ZnL^1 in 0.1 M Bu_4NPF_6 methanol solution; $v = 0.2$ V/s.

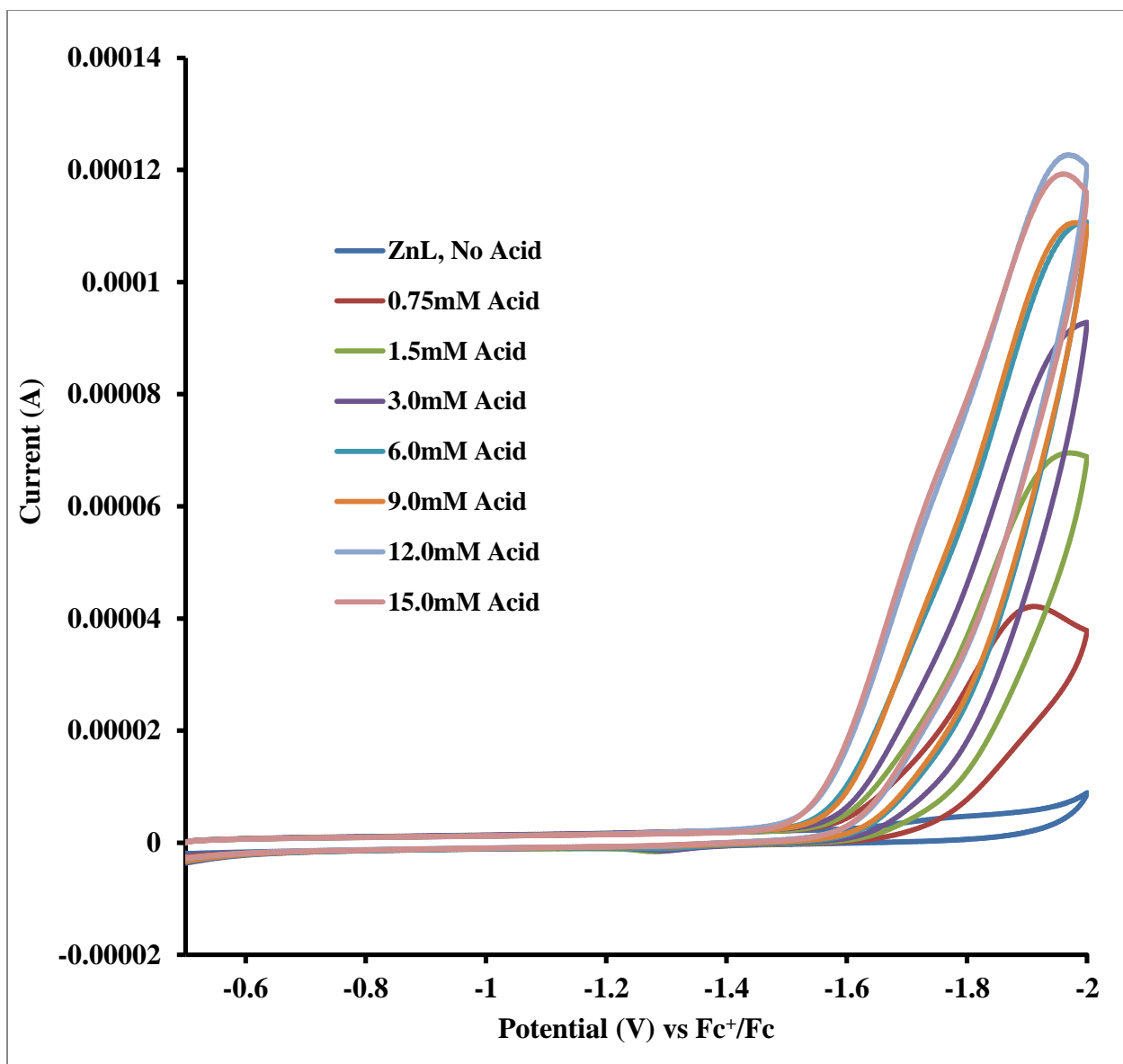


Figure C78. ZnL¹ HER cyclic voltammograms in 0.1 M Bu₄NPF₆ methanol solution with increasing concentrations of CH₃COOH added; $\nu = 0.3$ V/s.

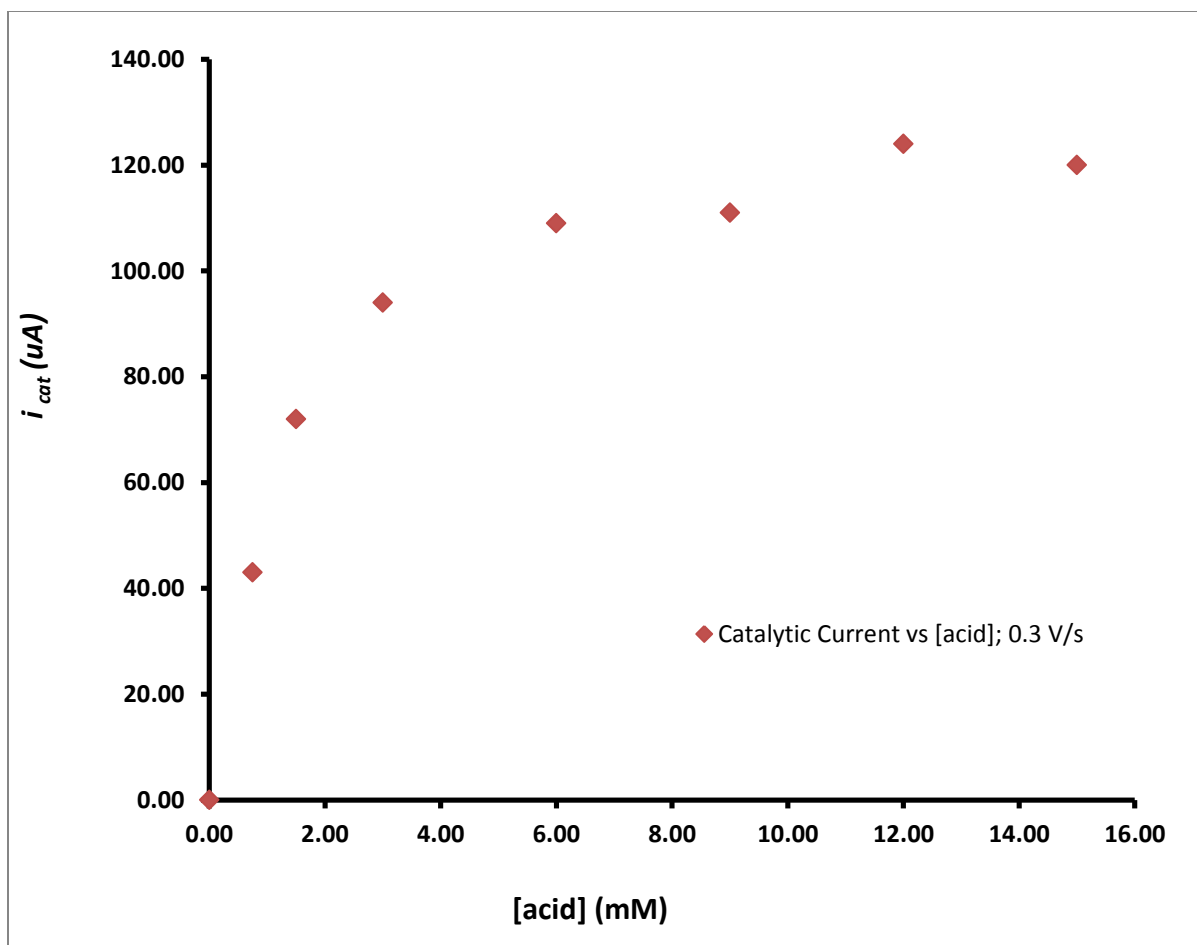


Figure C79. Plot of CH_3COOH concentration versus catalytic current for ZnL^1 in 0.1 M Bu_4NPF_6 methanol solution; $v = 0.3$ V/s.

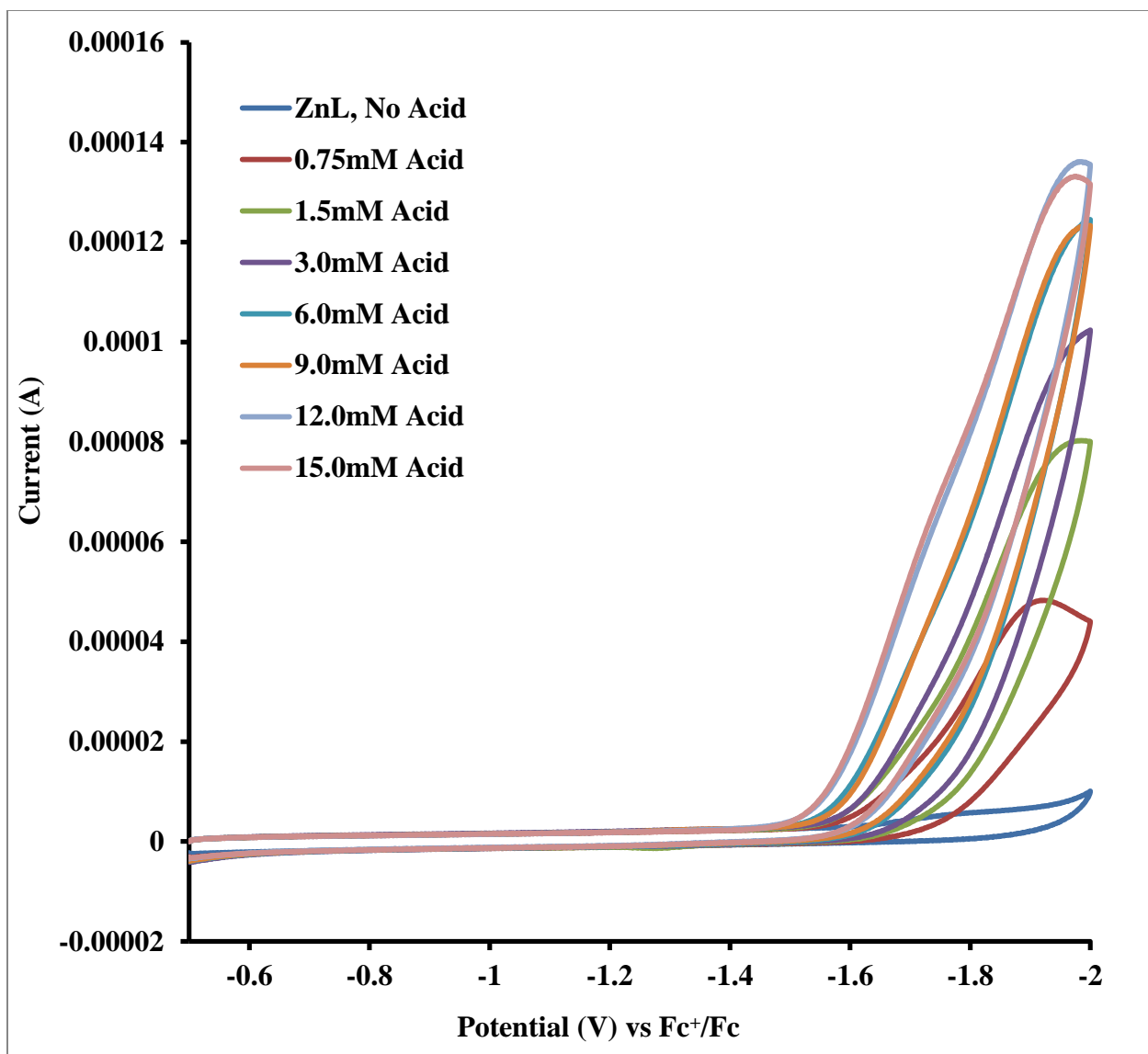


Figure C80. ZnL^1 HER cyclic voltammograms in 0.1 M Bu_4NPF_6 methanol solution with increasing concentrations of CH_3COOH added; $\nu = 0.4$ V/s.

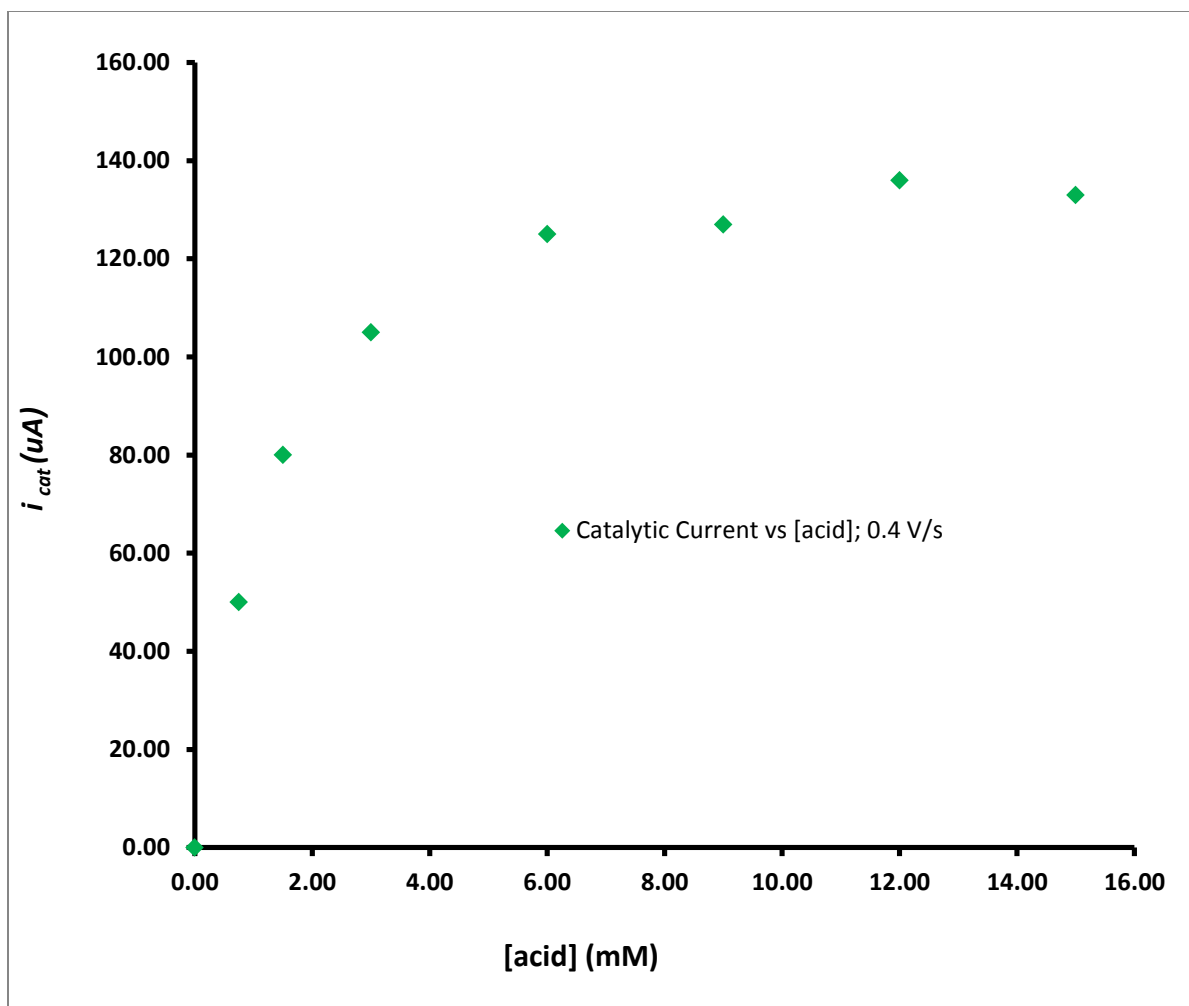


Figure C81. Plot of CH_3COOH concentration versus catalytic current for ZnL^1 in 0.1 M Bu_4NPF_6 methanol solution; $v = 0.4$ V/s.

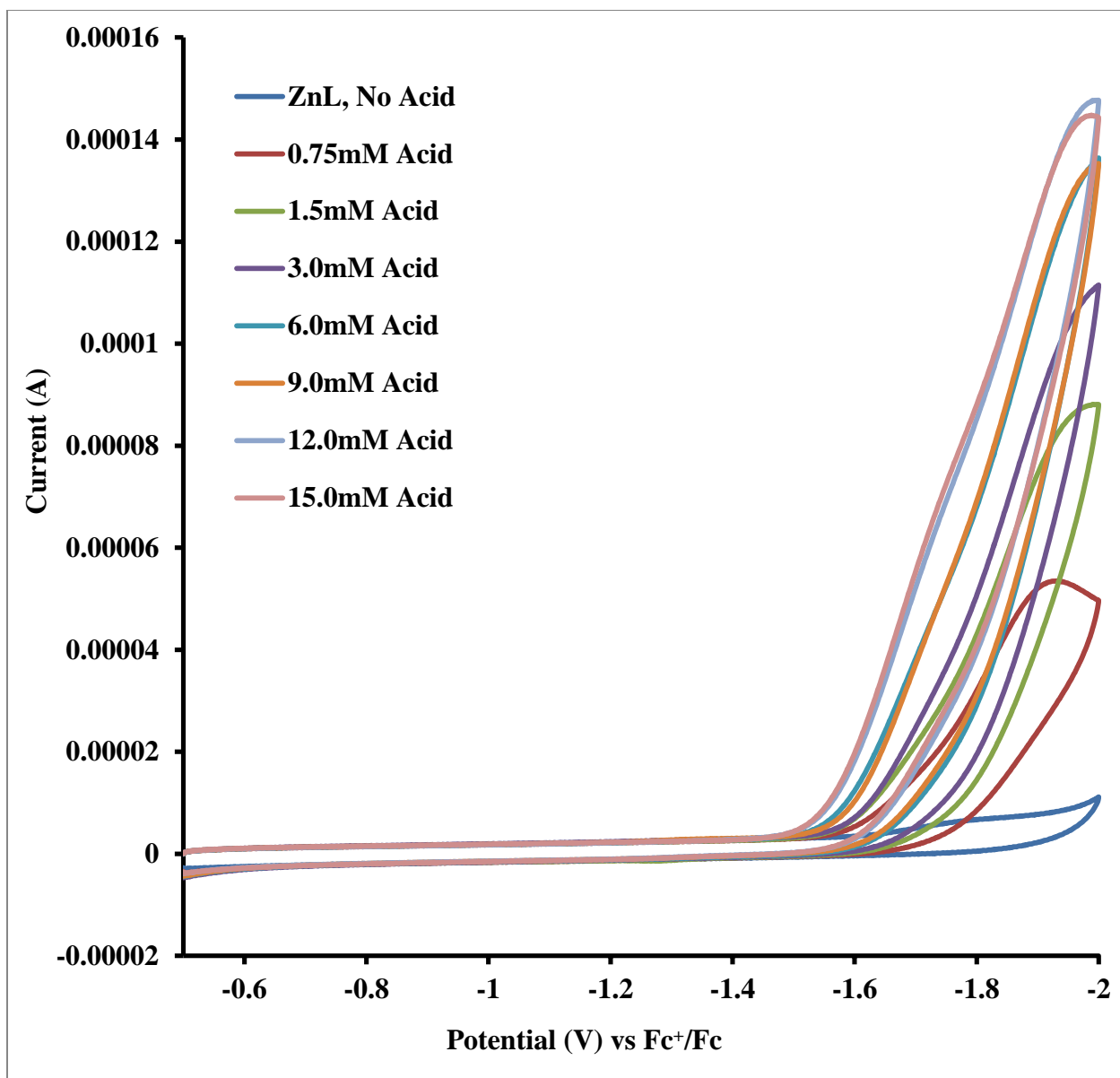


Figure C82. ZnL¹ HER cyclic voltammograms in 0.1 M Bu₄NPF₆ methanol solution with increasing concentrations of CH₃COOH added; $\nu = 0.5$ V/s.

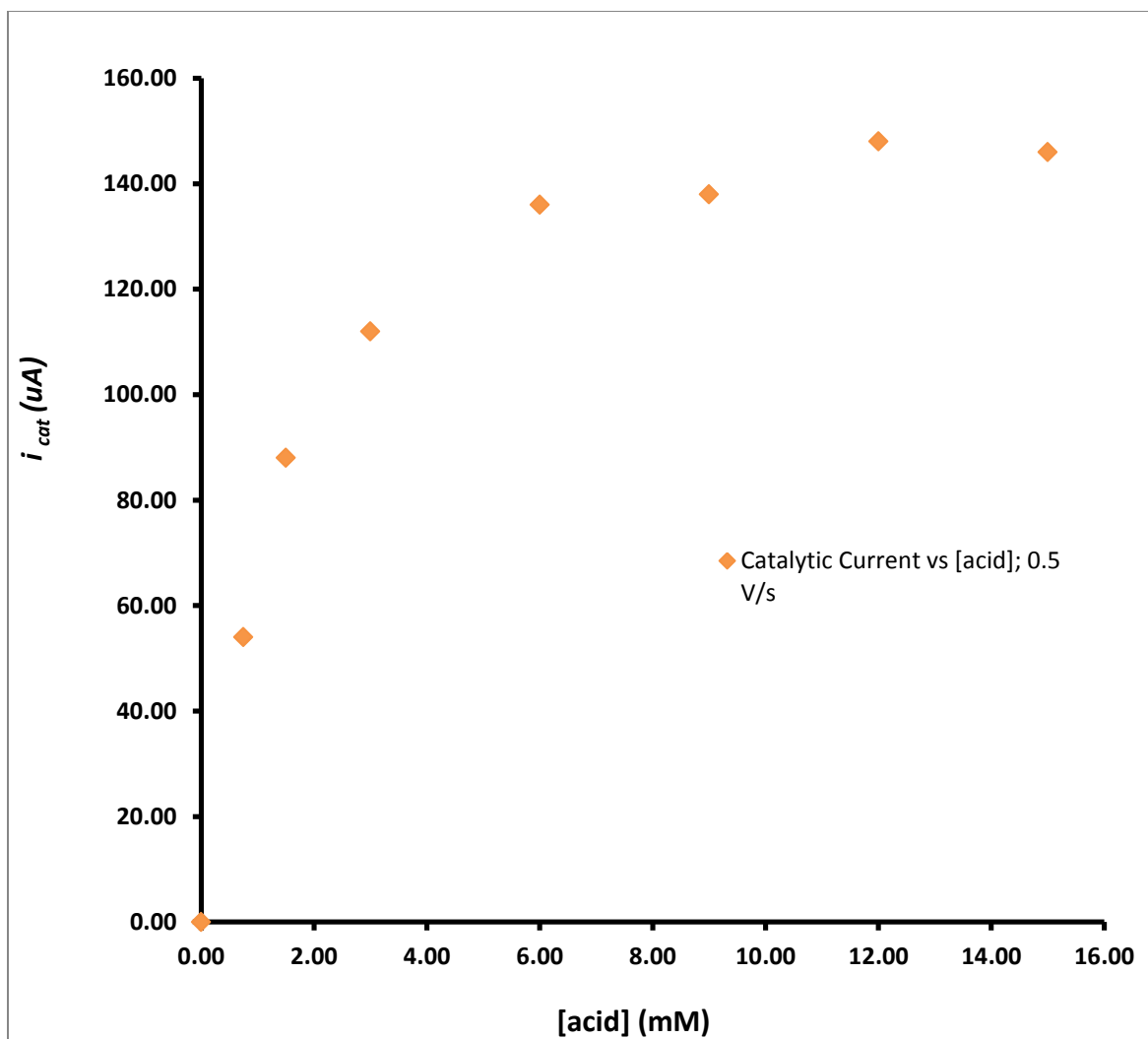


Figure C83. Plot of CH_3COOH concentration versus catalytic current for ZnL^1 in 0.1 M Bu_4NPF_6 methanol solution; $v = 0.5$ V/s.

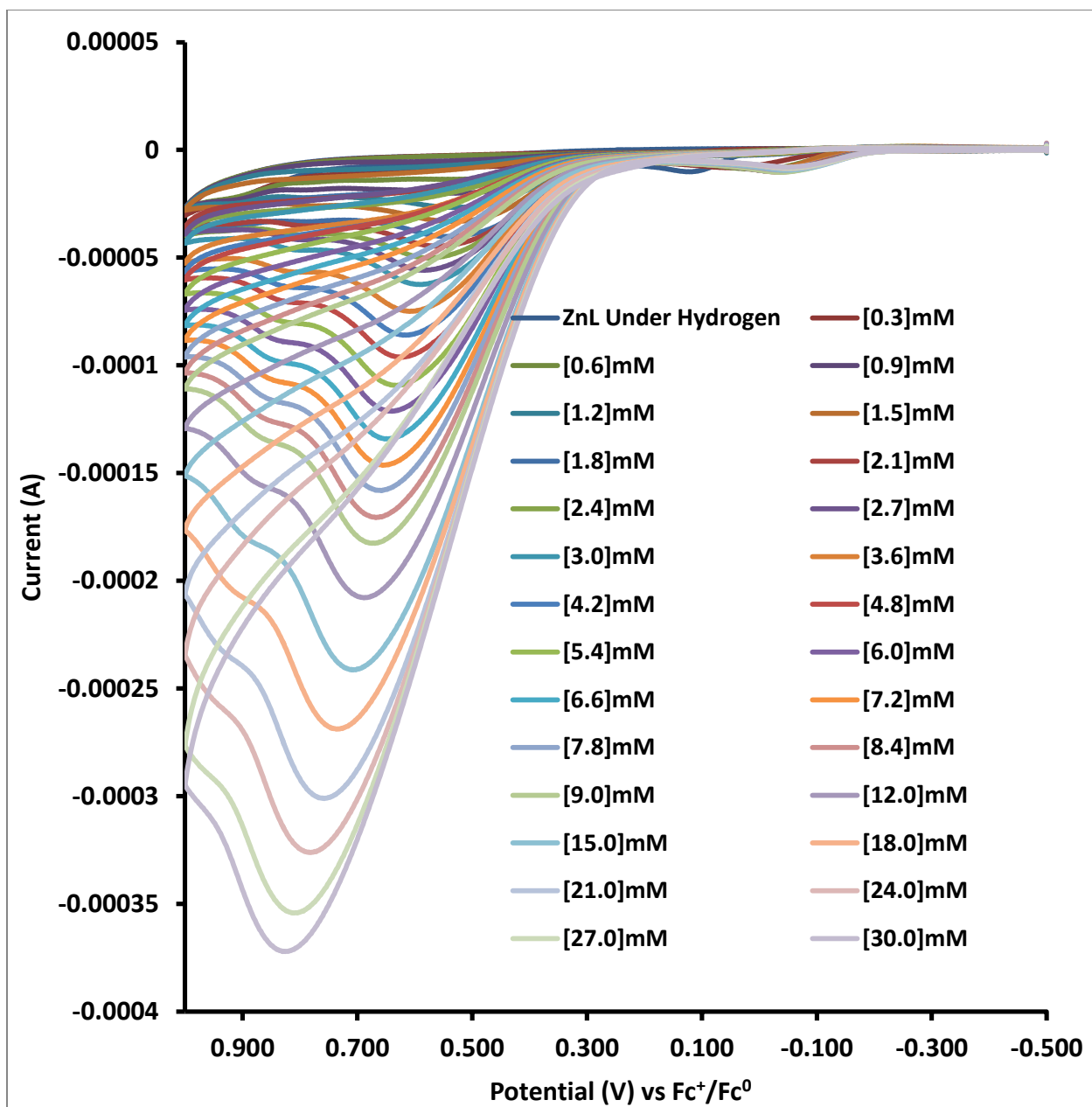


Figure C84. ZnL¹ HOR cyclic voltammograms in 0.1 M Bu₄NPF₆ methanol solution, under an H₂ atmosphere, with increasing concentrations of (CH₂CH₃)₃N added; $\nu = 0.2$ V/s.

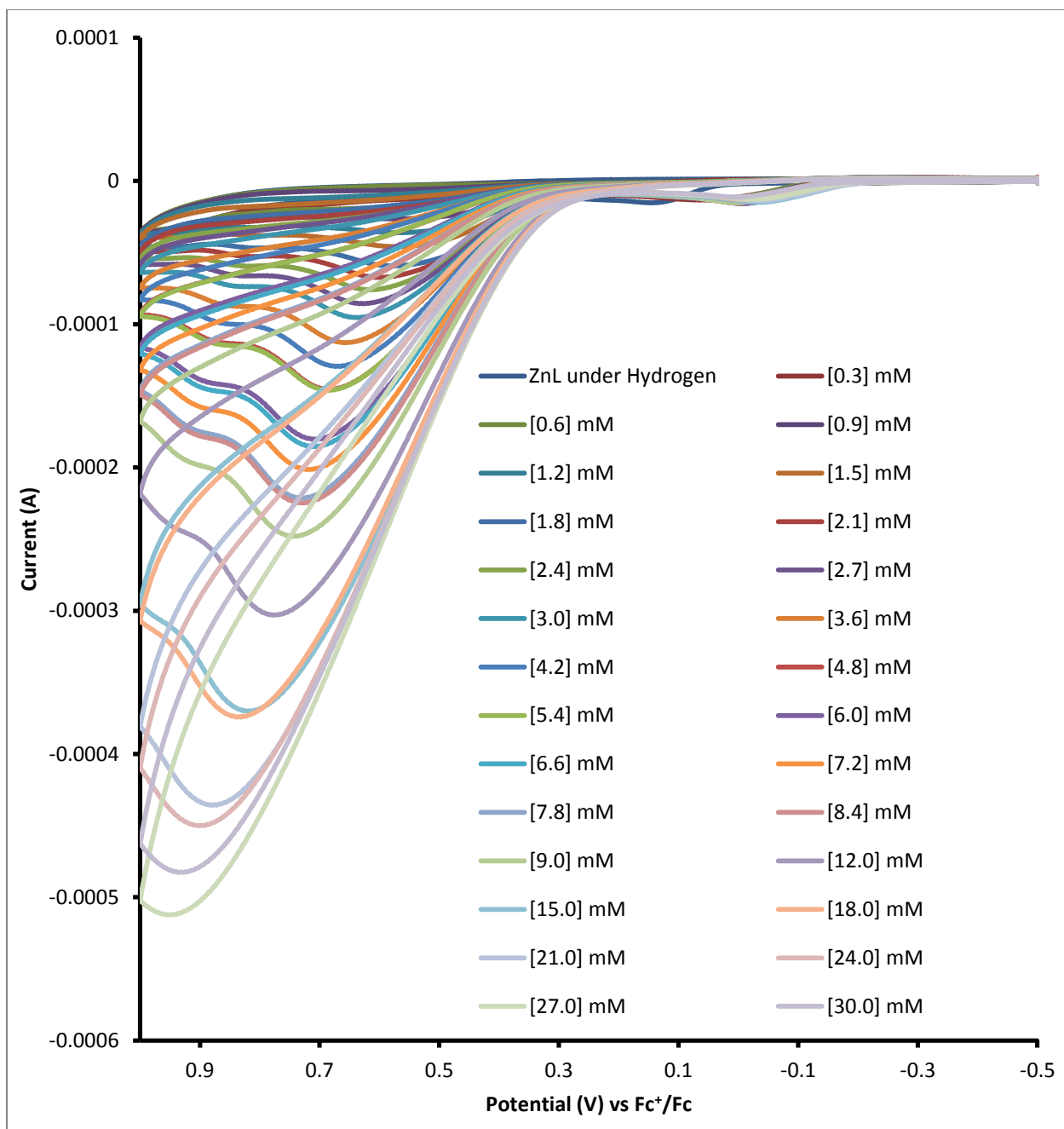


Figure C85. ZnL¹ HOR cyclic voltammograms in 0.1 M Bu₄NPF₆ methanol solution, under an H₂ atmosphere, with increasing concentrations of (CH₂CH₃)₃N added; $\nu = 0.5$ V/s.

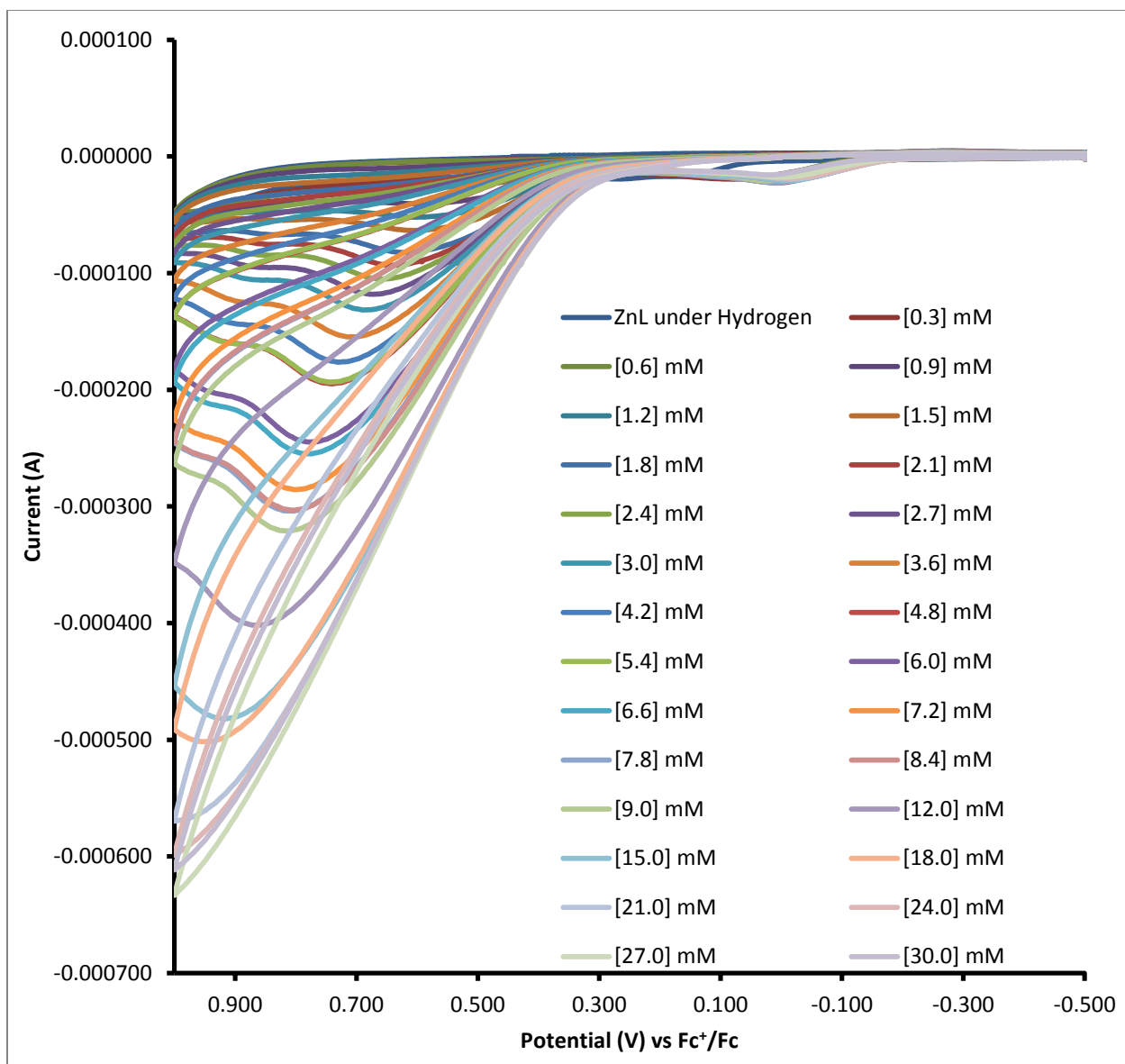


Figure C86. ZnL¹ HOR cyclic voltammograms in 0.1 M Bu₄NPF₆ methanol solution, under an H₂ atmosphere, with increasing concentrations of (CH₂CH₃)₃N added; $\nu = 1.0$ V/s.

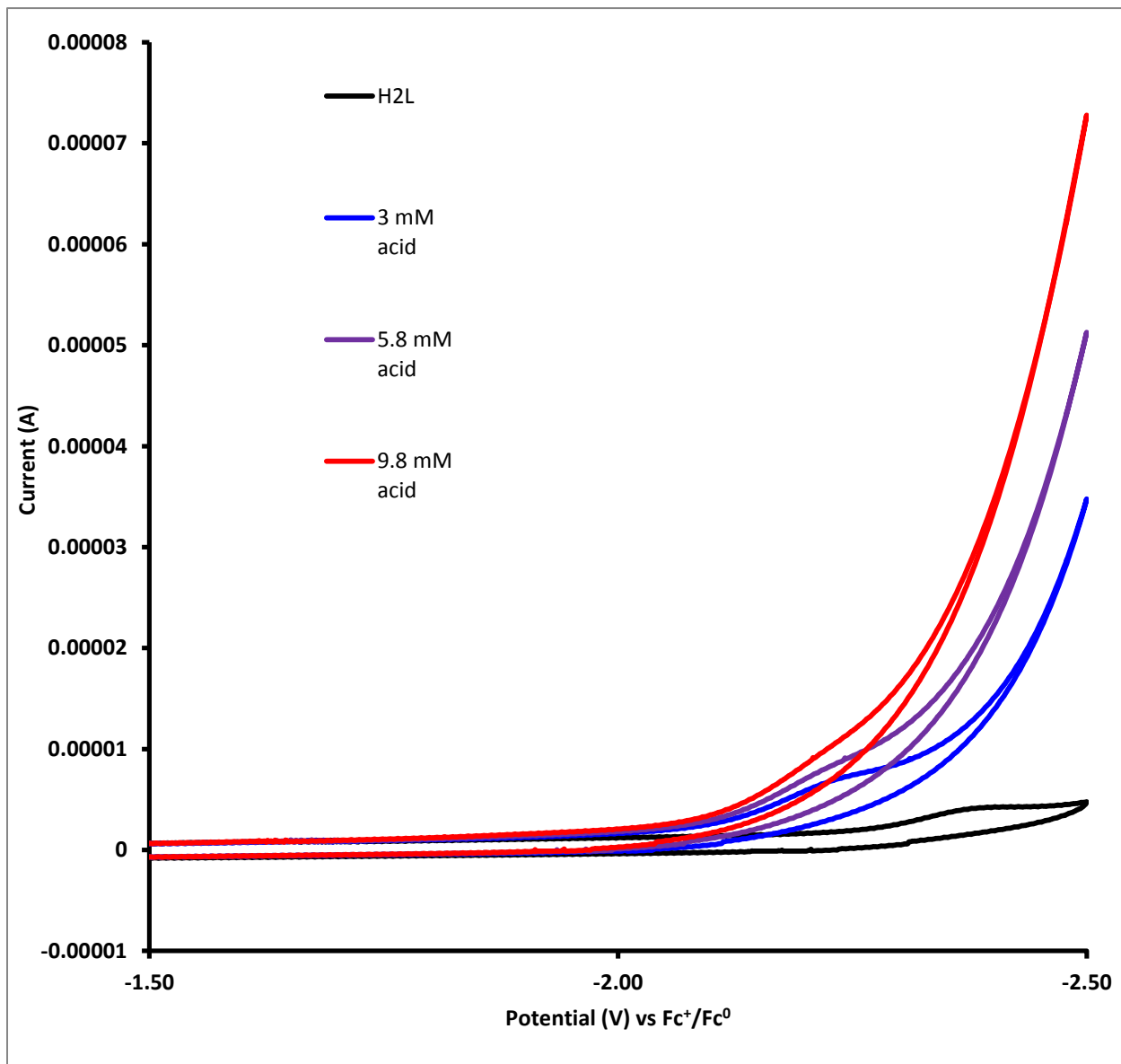


Figure C87. H₂L¹ HER cyclic voltammograms in 0.1 M Bu₄NPF₆ methanol solution with increasing concentrations of CH₃COOH added ; $\nu = 0.5$ V/s.

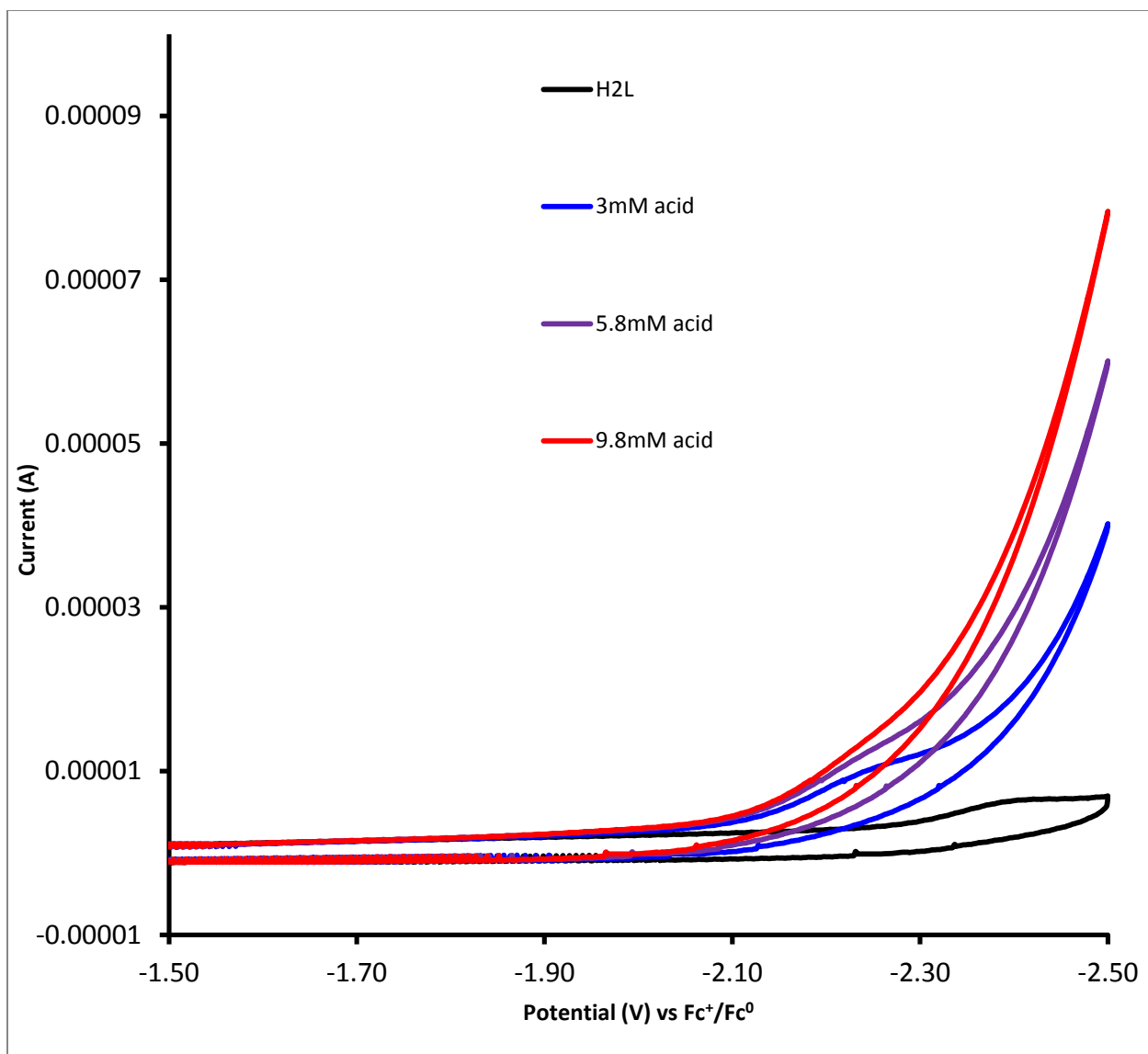


Figure C88. H₂L¹ HER cyclic voltammograms in 0.1 M Bu₄NPF₆ methanol solution with increasing concentrations of CH₃COOH added; $\nu = 1.0$ V/s.

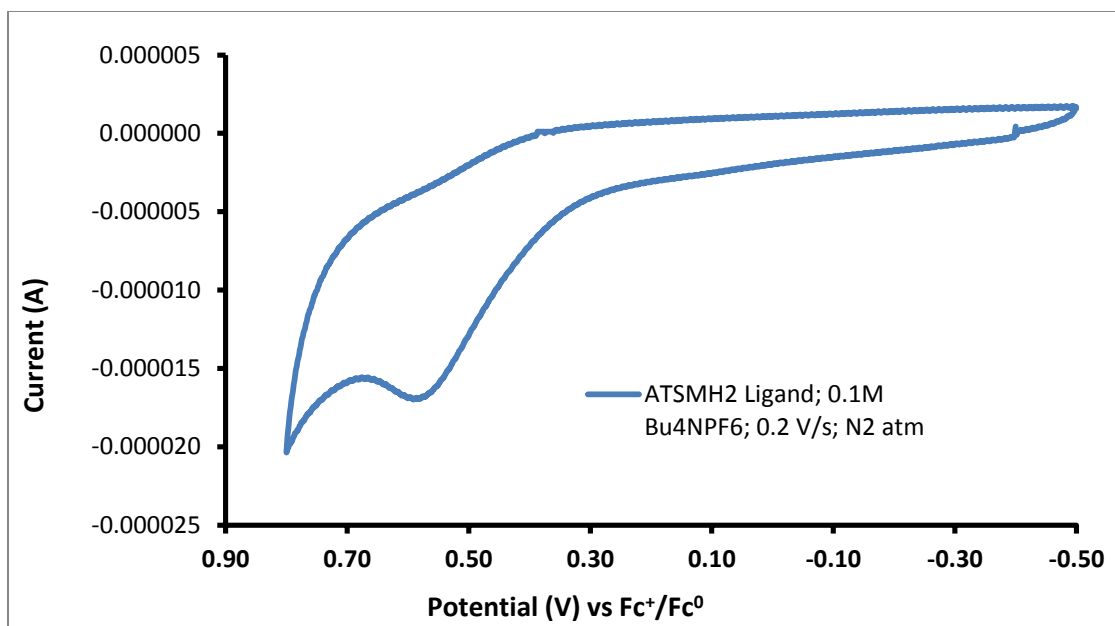


Figure C89. Cyclic Voltammogram of H_2L^1 in 0.1 M Bu_4NPF_6 methanol solution; $\nu = 0.2$ V/s.

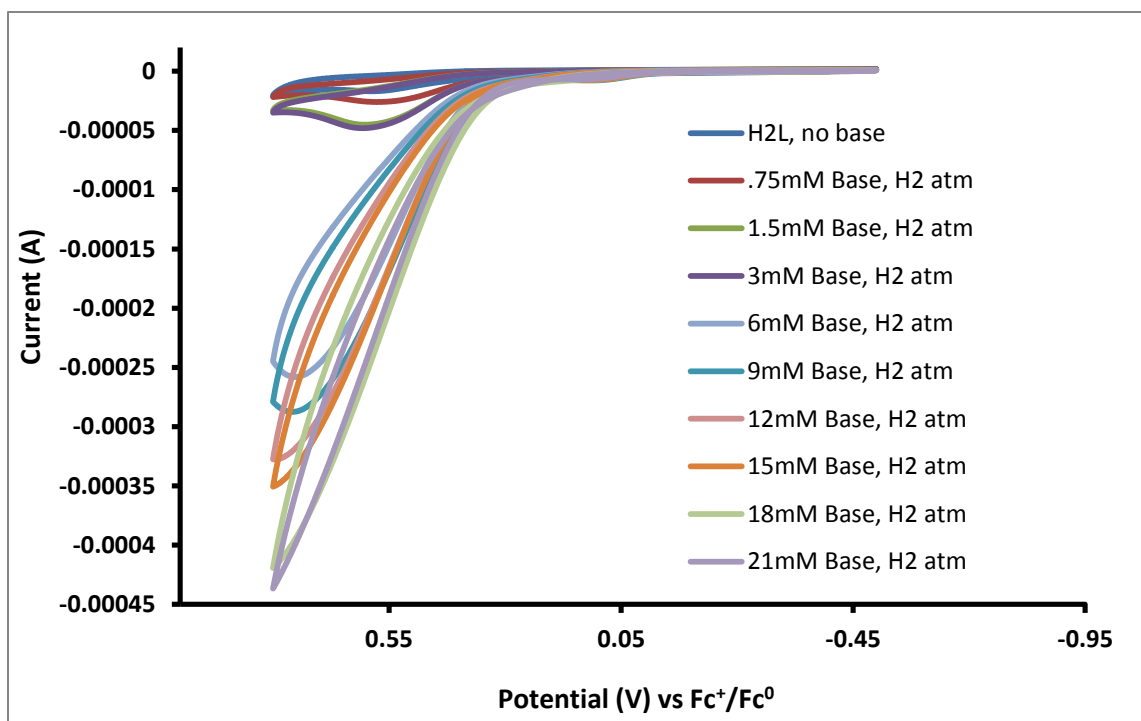


Figure C90. H_2L^1 HOR cyclic voltammograms in 0.1 M Bu_4NPF_6 methanol solution, under an H_2 atmosphere, with increasing concentrations of $(\text{CH}_2\text{CH}_3)_3\text{N}$ added; $\nu = 0.2$ V/s.

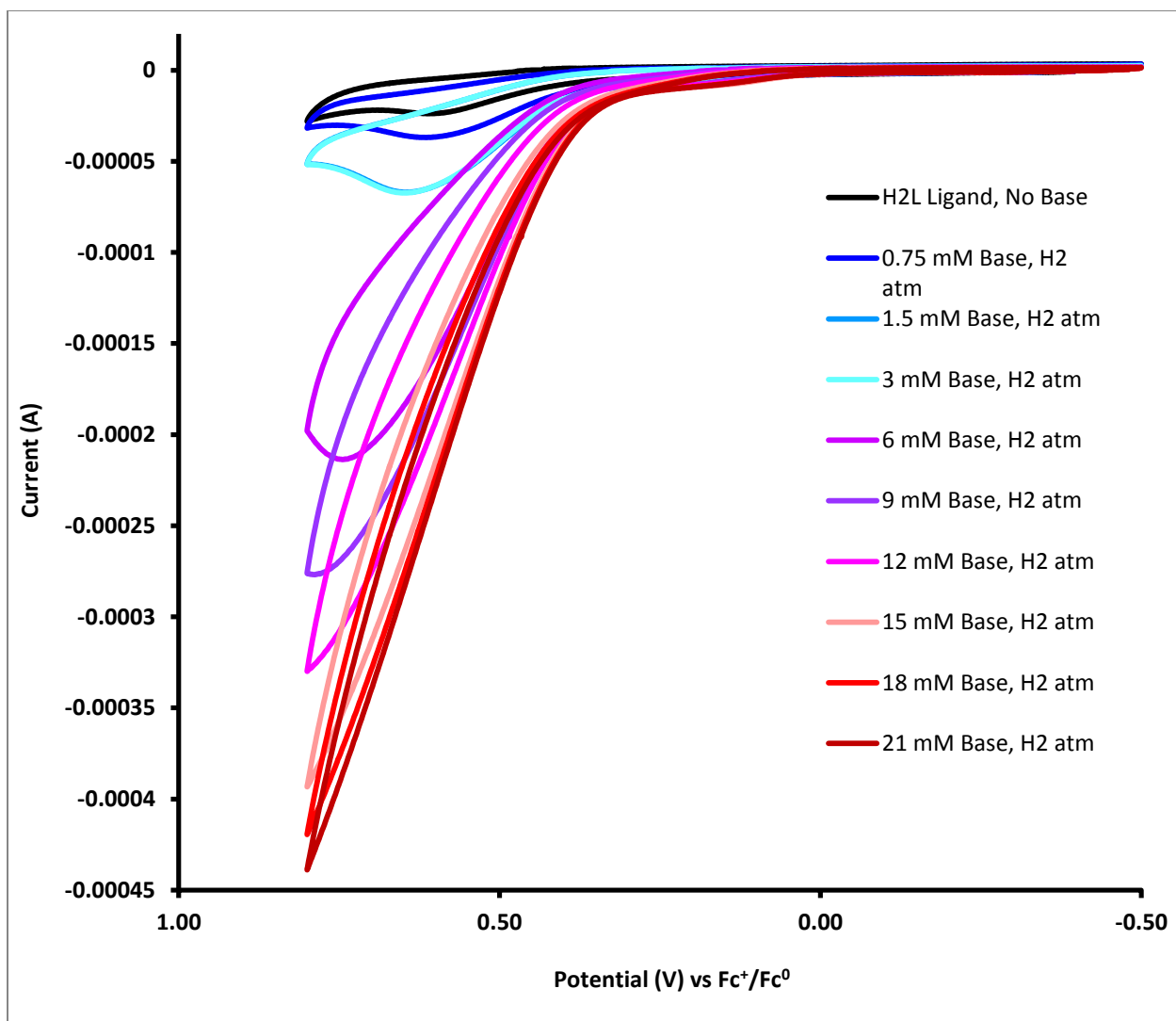


Figure C91. H₂L¹ HOR cyclic voltammograms in 0.1 M Bu₄NPF₆ methanol solution, under an H₂ atmosphere, with increasing concentrations of (CH₂CH₃)₃N added; $\nu = 0.5$ V/s.

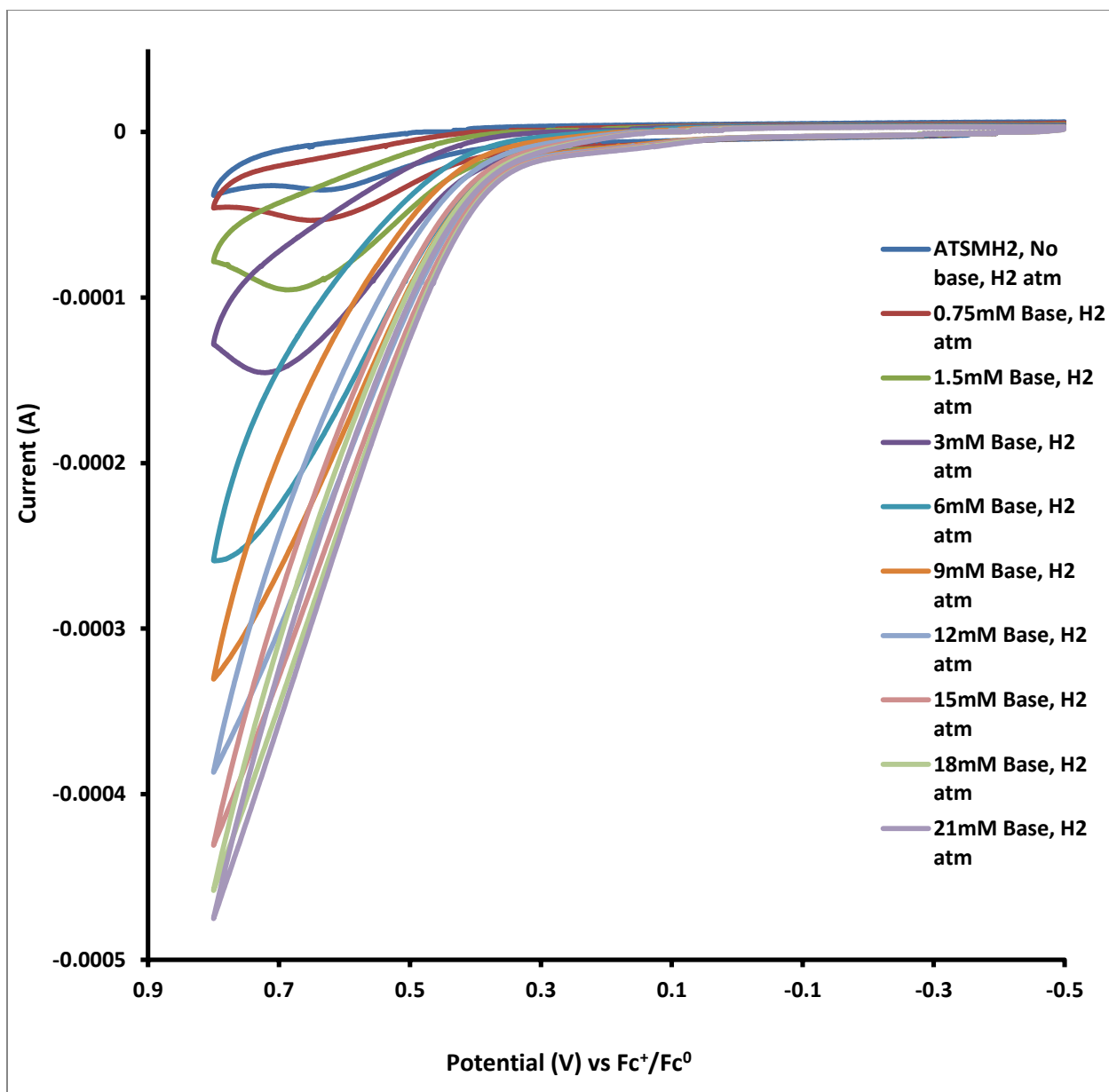


Figure C92. H₂L¹ HOR cyclic voltammograms in 0.1 M Bu₄NPF₆ methanol solution, under an H₂ atmosphere, with increasing concentrations of (CH₂CH₃)₃N added; $\nu = 1.0$ V/s.

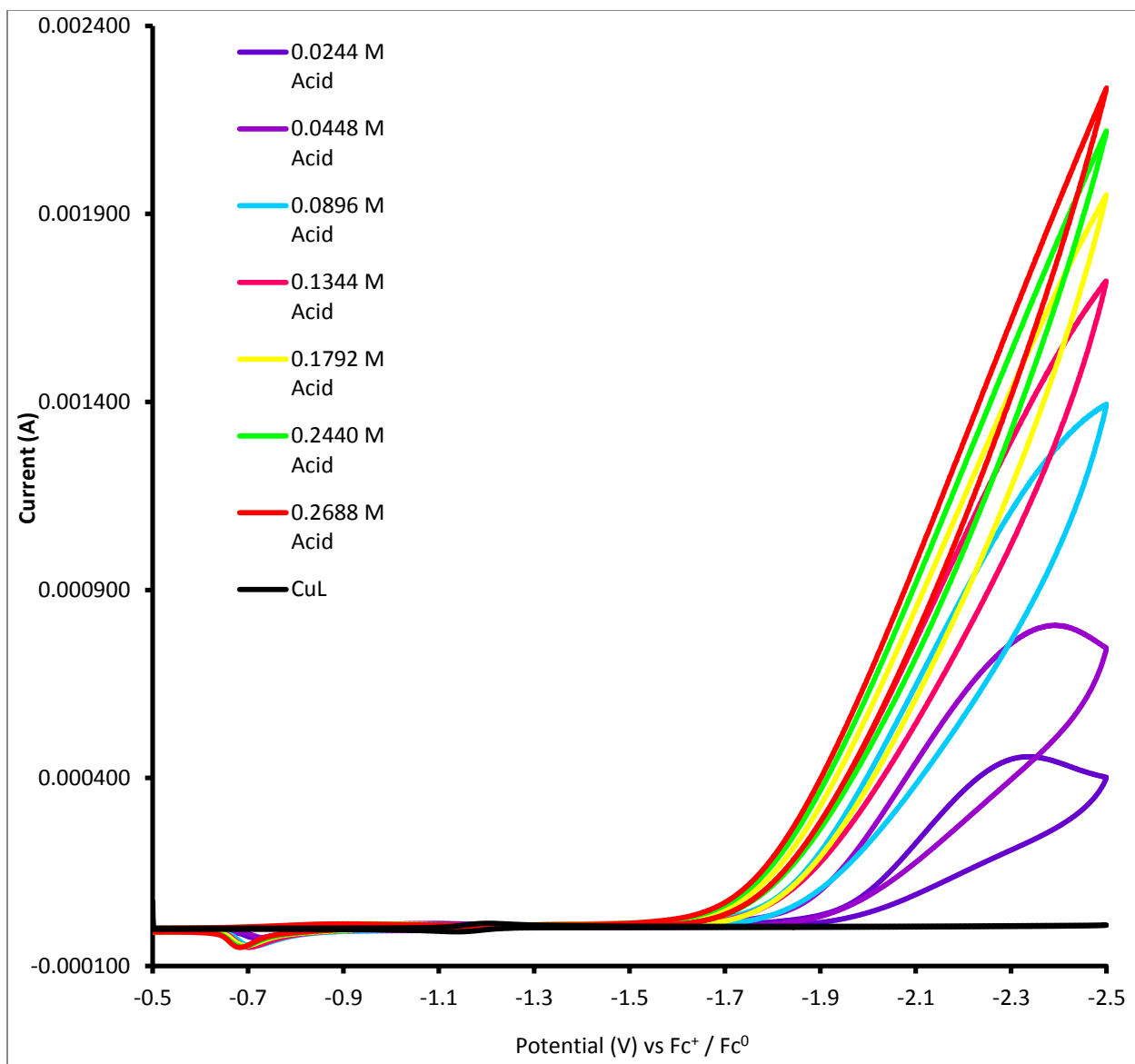


Figure C93. CuL¹ HER cyclic voltammograms in 0.1 M Bu₄NPF₆ acetonitrile solution with increasing concentrations of CH₃COOH added; $\nu = 0.2$ V/s.

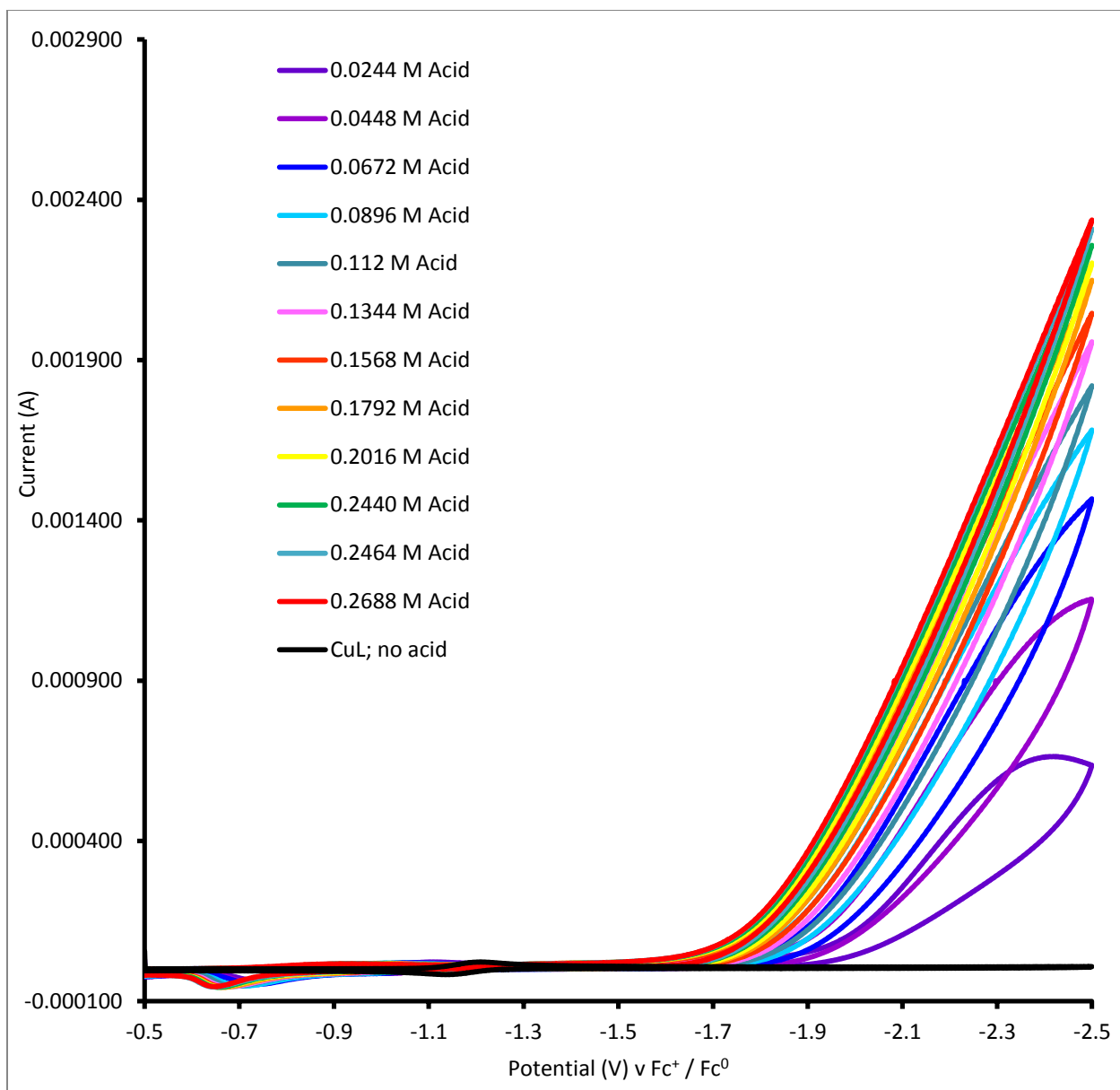


Figure C94. CuL¹ HER cyclic voltammograms in 0.1 M Bu₄NPF₆ acetonitrile solution with increasing concentrations of CH₃COOH added; $\nu = 0.5$ V/s.

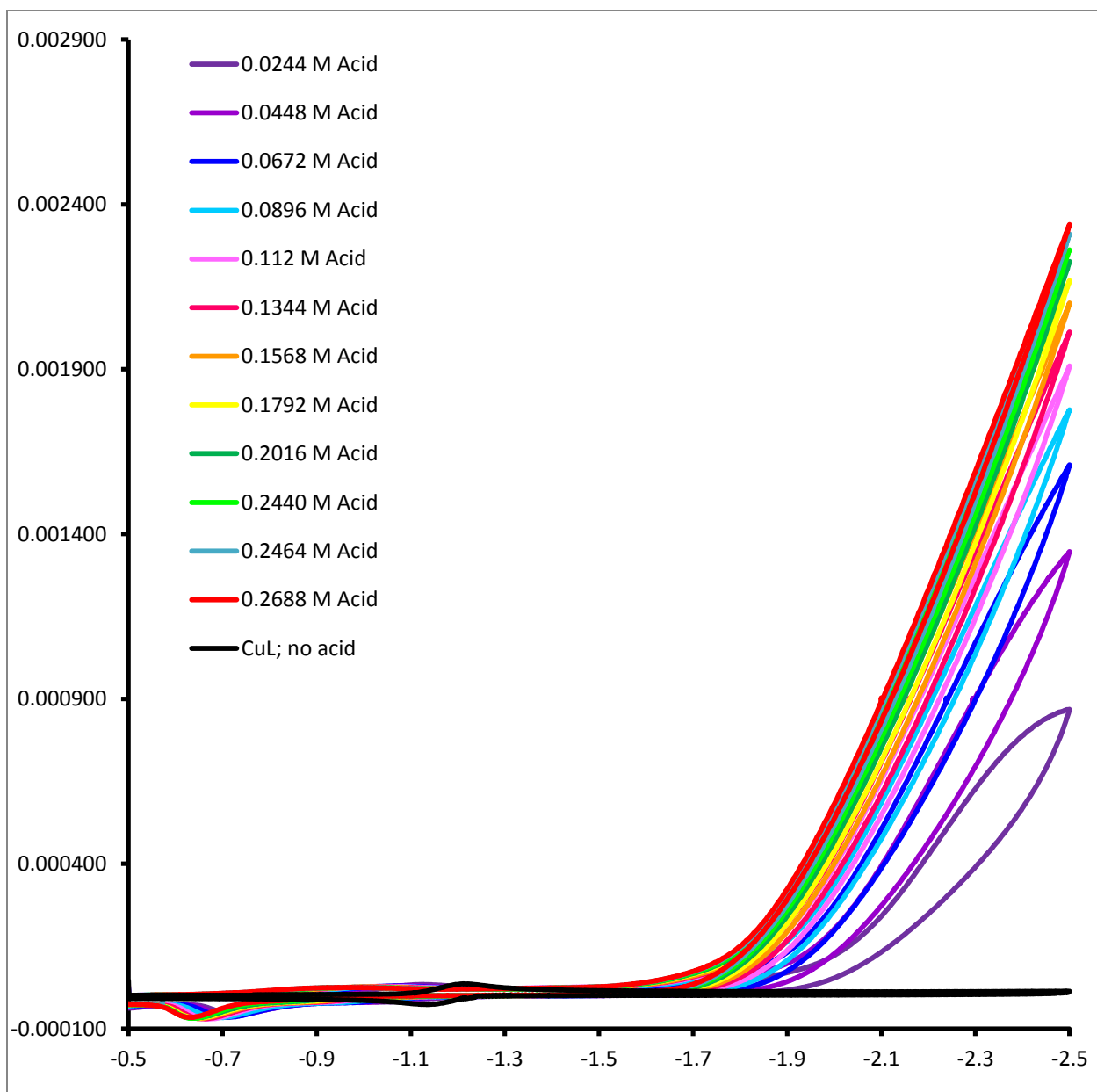


Figure C95. CuL^{I} HER cyclic voltammograms in 0.1 M Bu_4NPF_6 acetonitrile solution with increasing concentrations of CH_3COOH added; $\nu = 1.0 \text{ V/s}$.

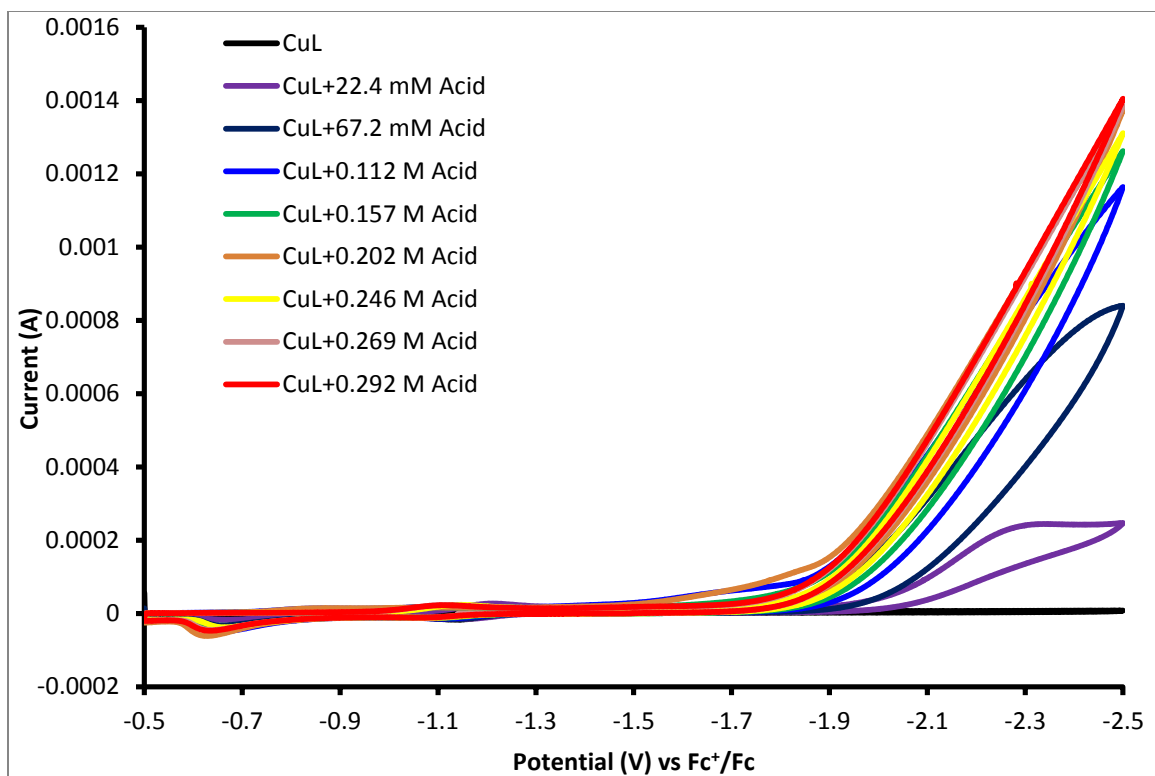


Figure C96. 0.6 mM CuL¹ in 0.1 M Bu₄NPF₆ DMF; HER CVs scanned at 0.5 V/s.

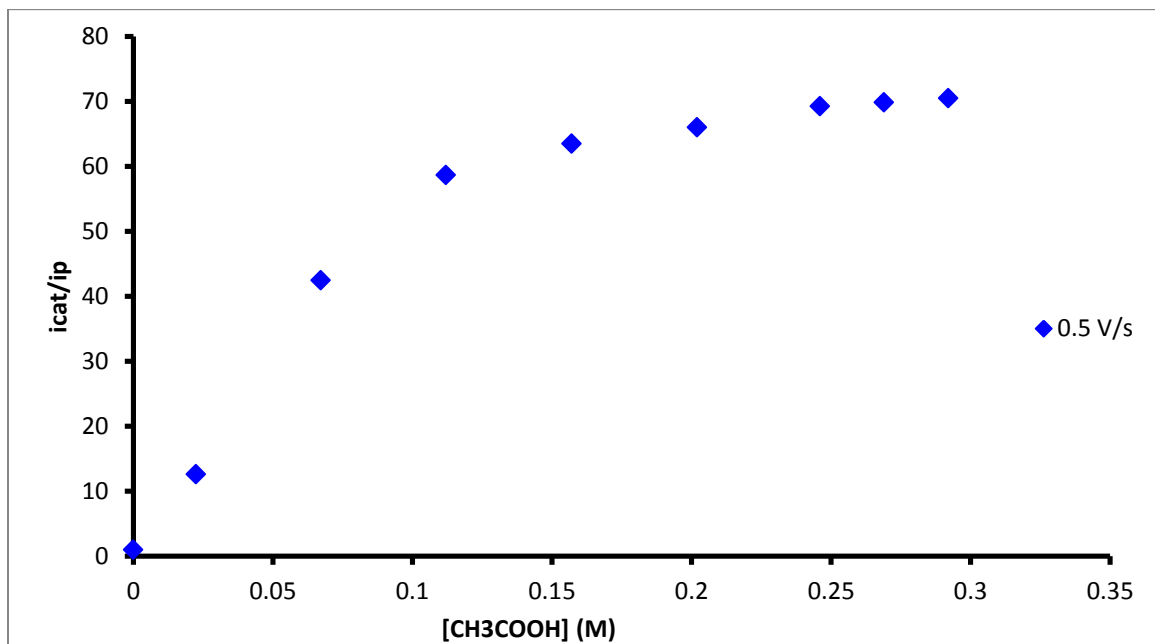


Figure C97. Plot of i_{cat}/i_p vs [CH₃COOH]; $v = 0.5$ V/s

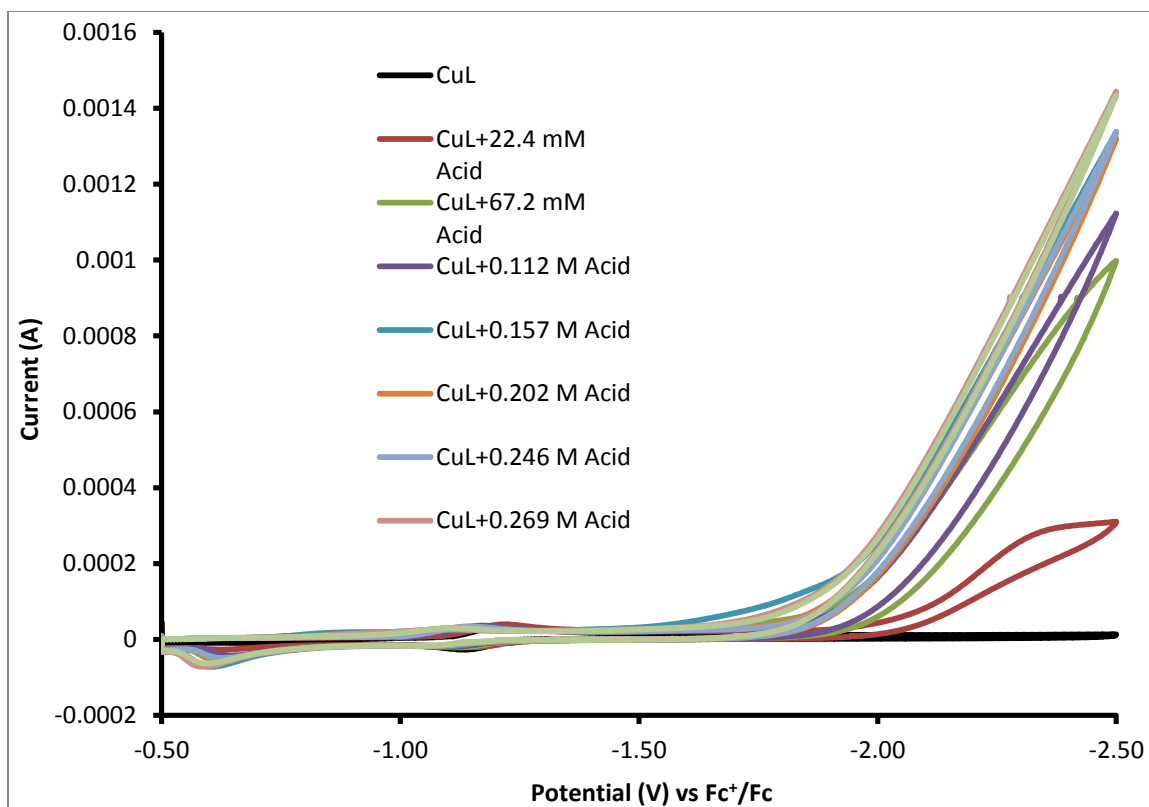


Figure C98. 0.6 mM CuL¹ in 0.1 M Bu₄NPF₆ DMF; HER CVs scanned at 1.0 V/s.

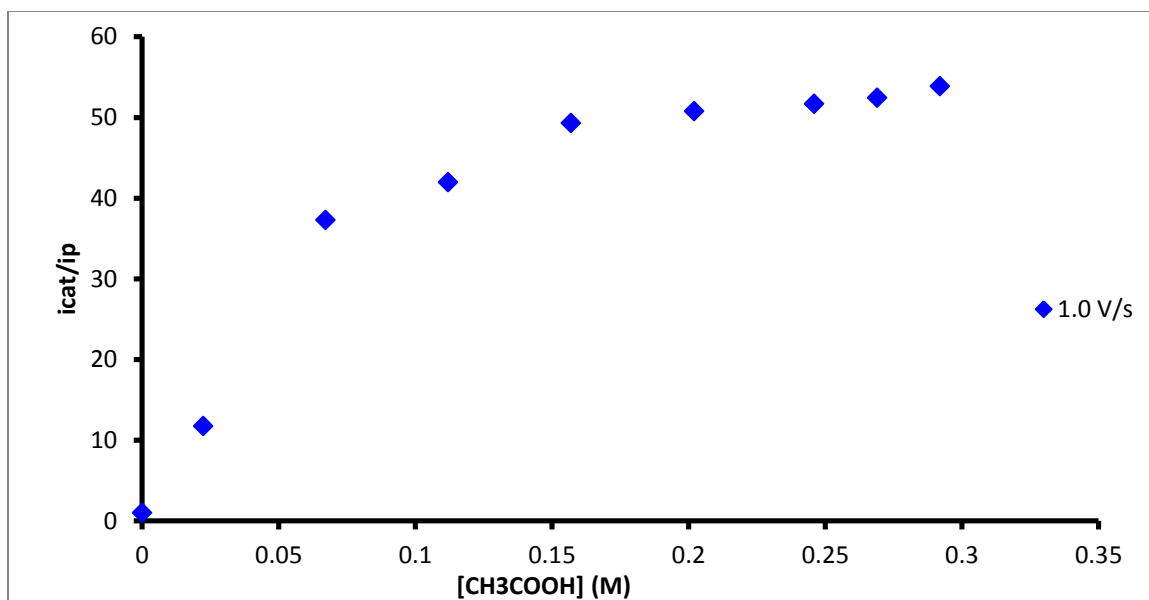


Figure C99. Plot of *i_{cat}*/*i_p* vs [CH₃COOH]; *v* = 1.0 V/s

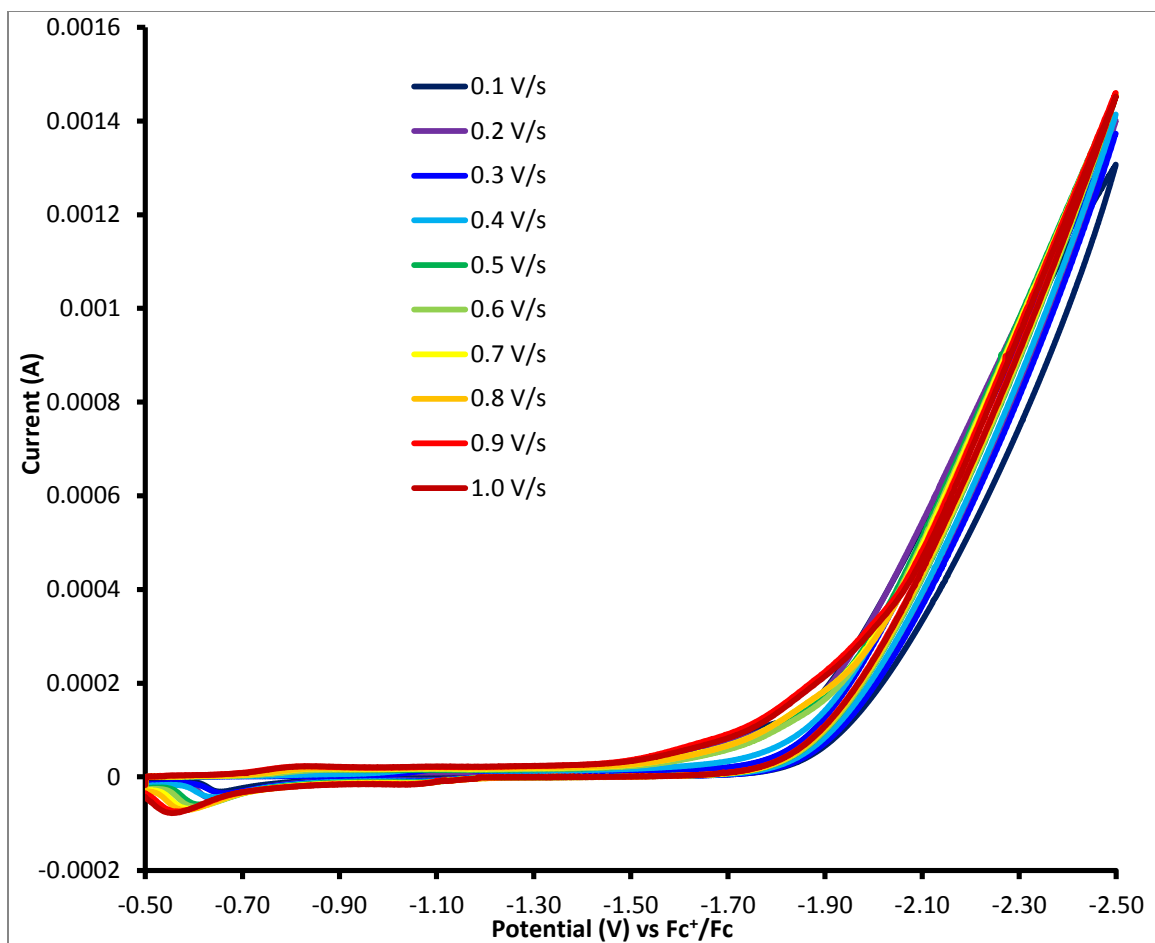


Figure C100. Scan Rate Dependence: CVs of 0.6 mM CuL¹ in 0.1 M Bu₄NPF₆ DMF solution with 0.292 M acetic acid added scanned from 0.1 – 1.0 V/s.

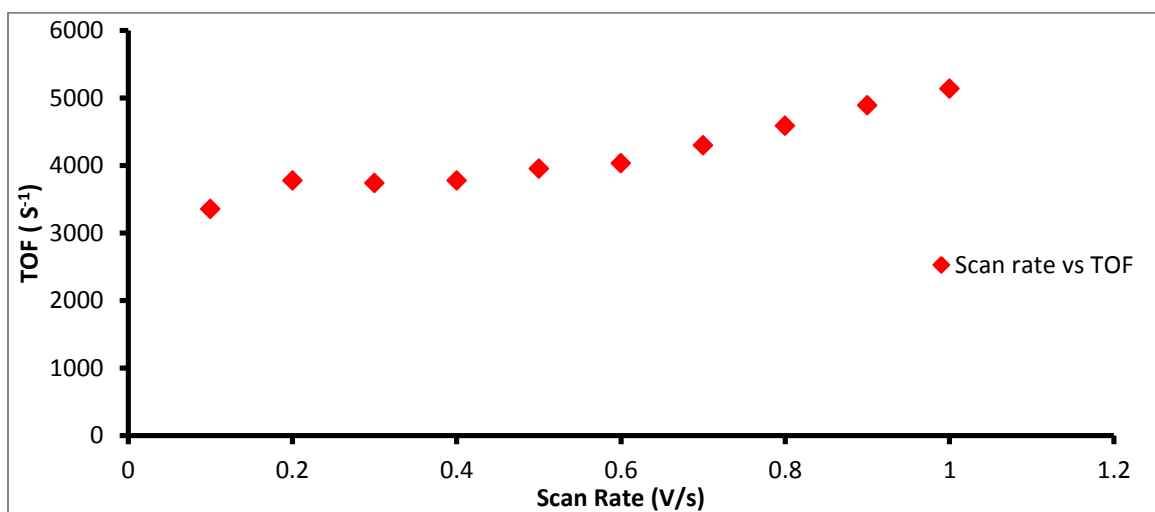


Figure C101. Plot of scan rate vs TOF for CuL¹ in DMF.

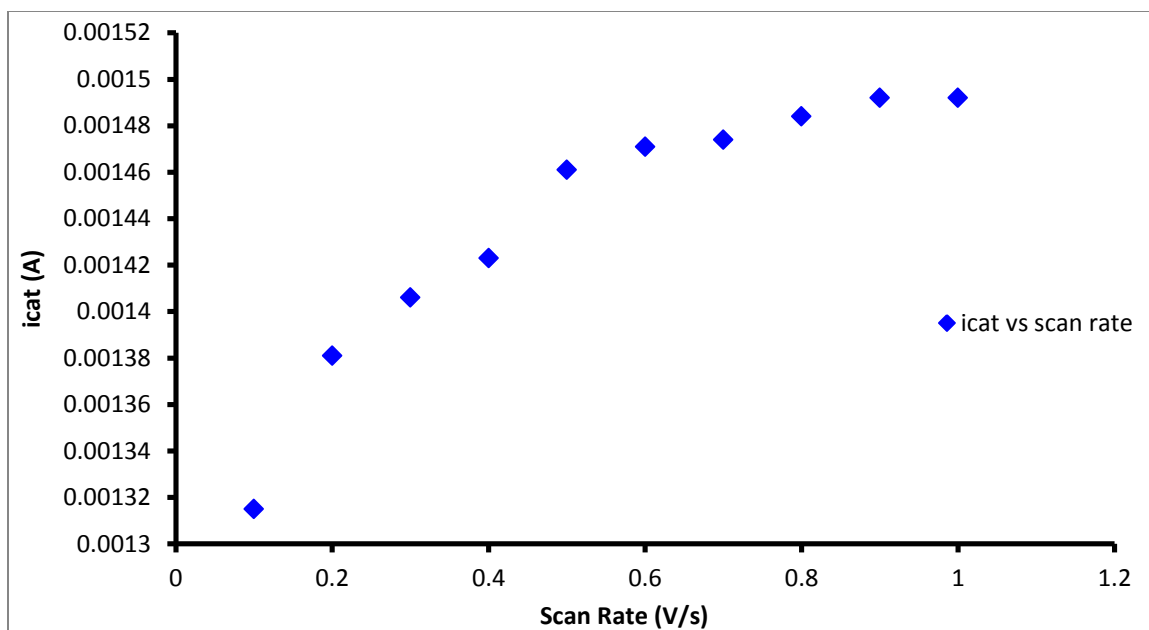


Figure C102. Plot of scan rate vs catalytic current for CuL^1 in DMF.

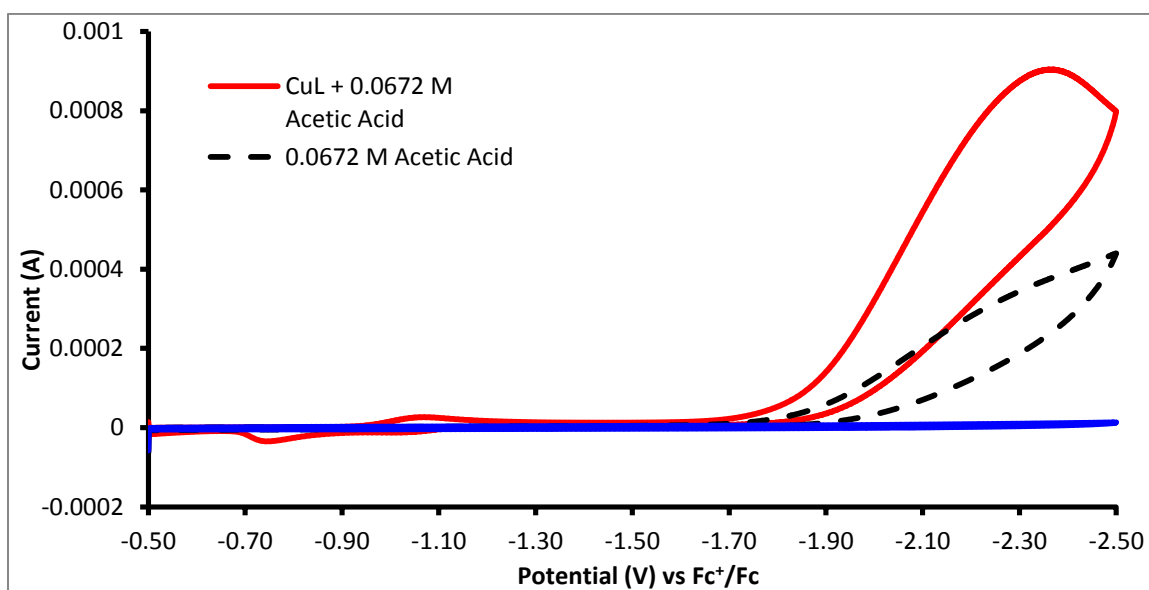


Figure C103. CVs run in 0.1 M Bu_4NPF_6 acetonitrile solutions, showing blank acetonitrile (blue), with 0.0672 M acetic acid added (black dashed), and with 0.0672 M acetic acid and 0.6 mM CuL^1 (red).

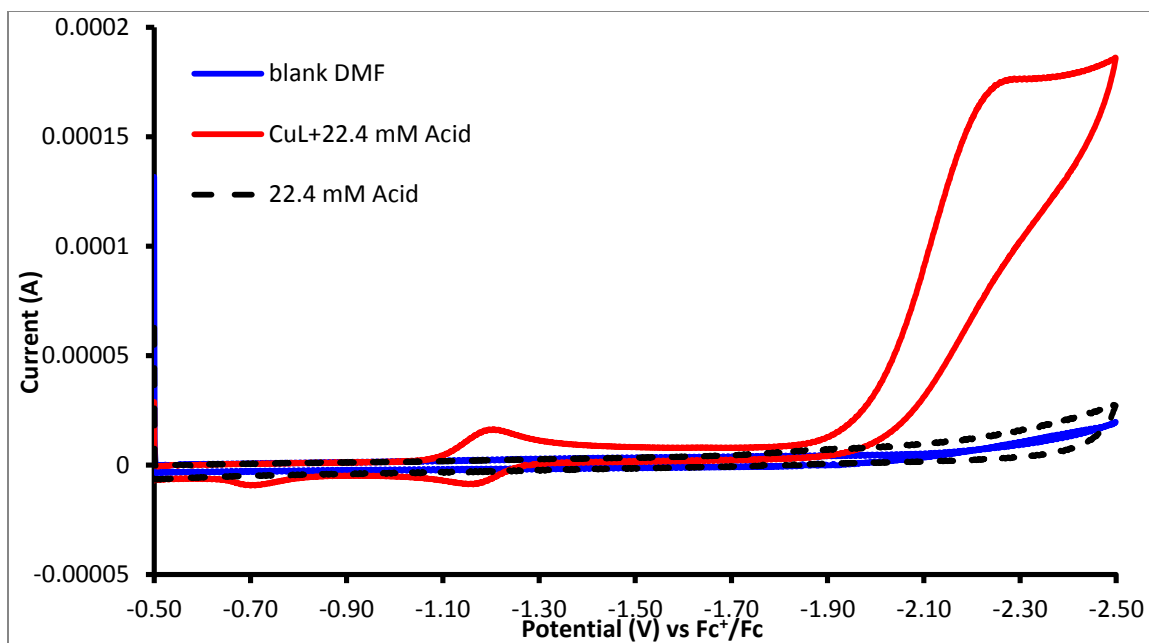


Figure 104. CVs run in 0.1 M Bu₄NPF₆ DMF solutions, showing blank DMF (blue), with 0.0224 M acetic acid added (black dashed), and with 0.0224 M acetic acid and 0.6 mM CuL¹ (red).

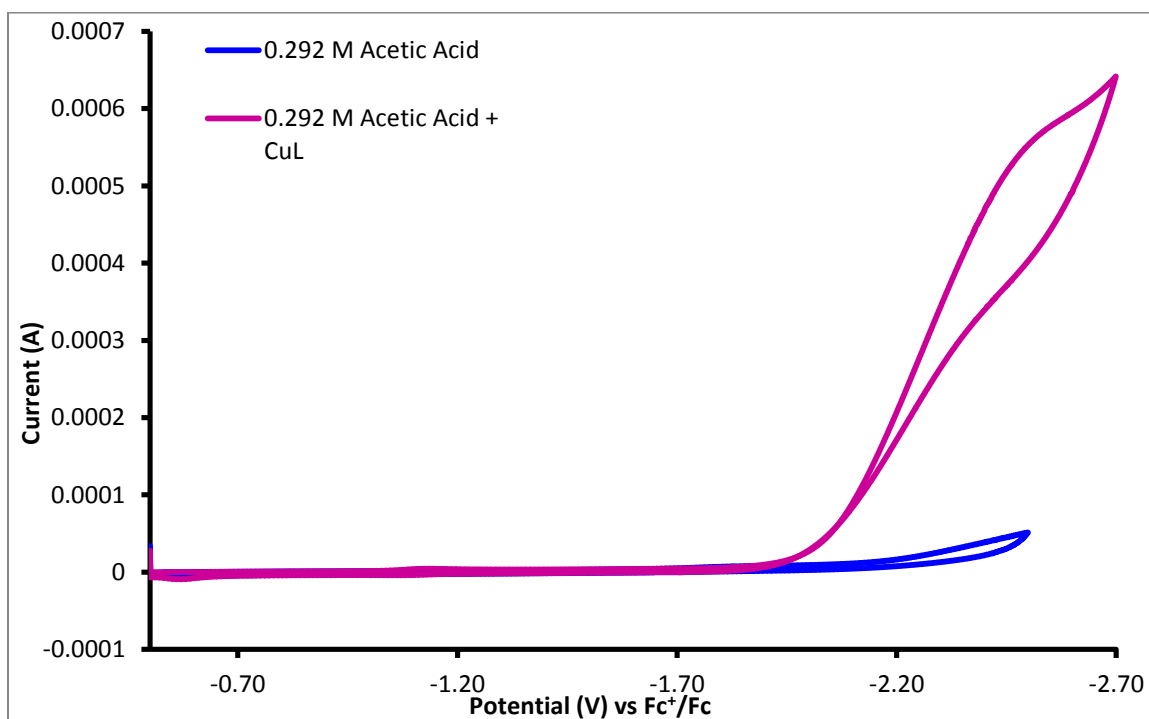


Figure C105. CVs run in 0.1 M Bu₄NPF₆ DMF solutions with 0.292 M acetic acid (blue) and upon addition of 0.6 mM CuL¹ (purple).

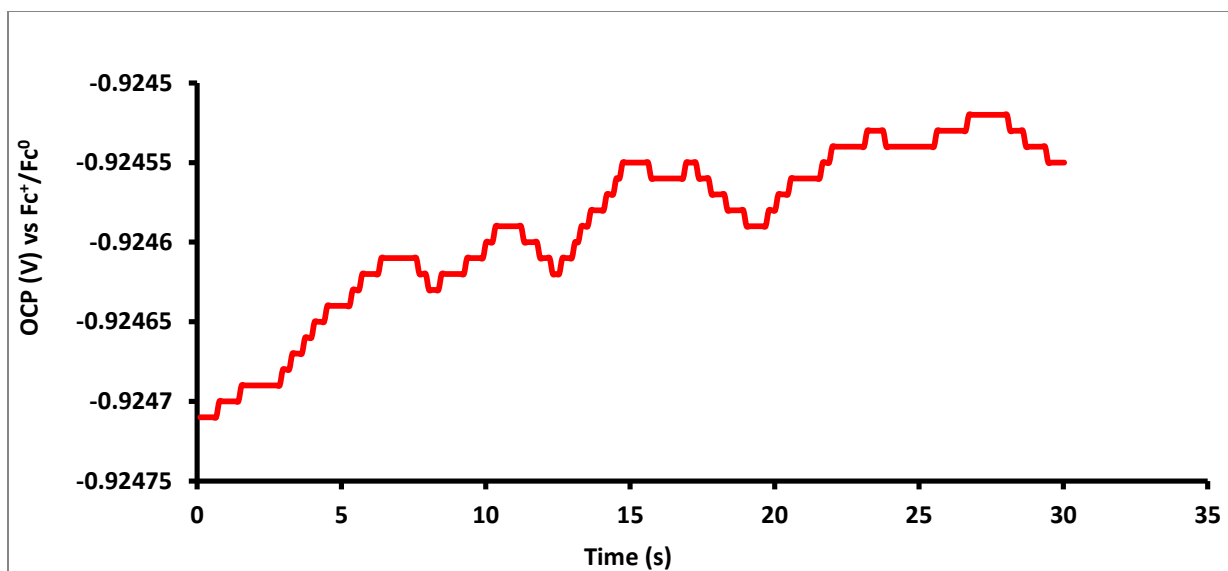


Figure C106. OCP measurement for ZnL^1 HER
 0.1M Bu_4NPF_6 methanol solution with 12 mM acetic acid added.

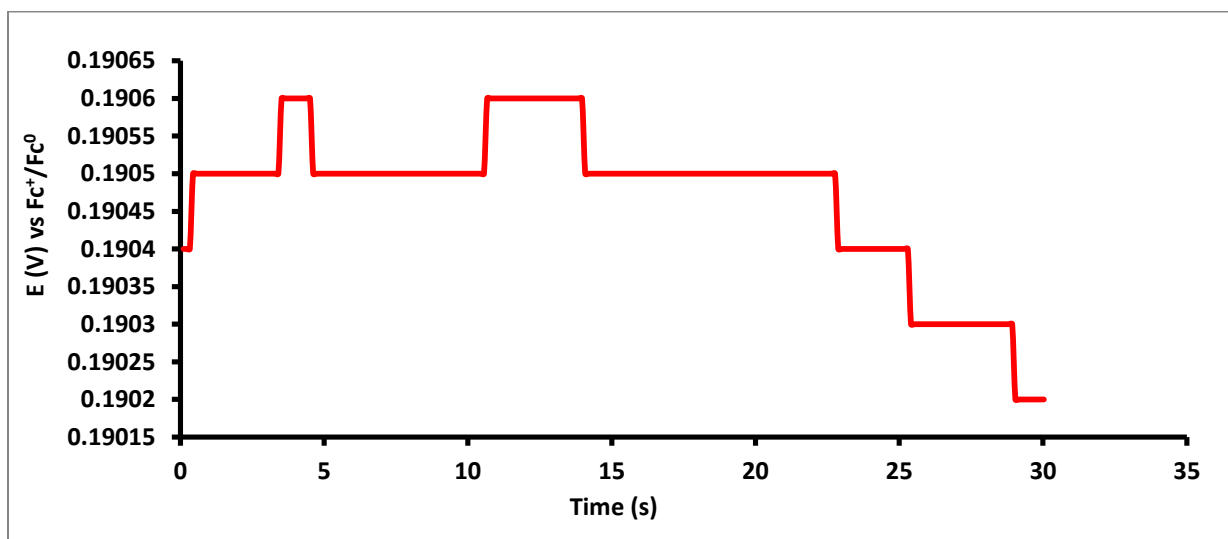


Figure C107. OCP measurement for ZnL^1 HOR
 0.1M Bu_4NPF_6 methanol solution with 30 mM triethylamine added.

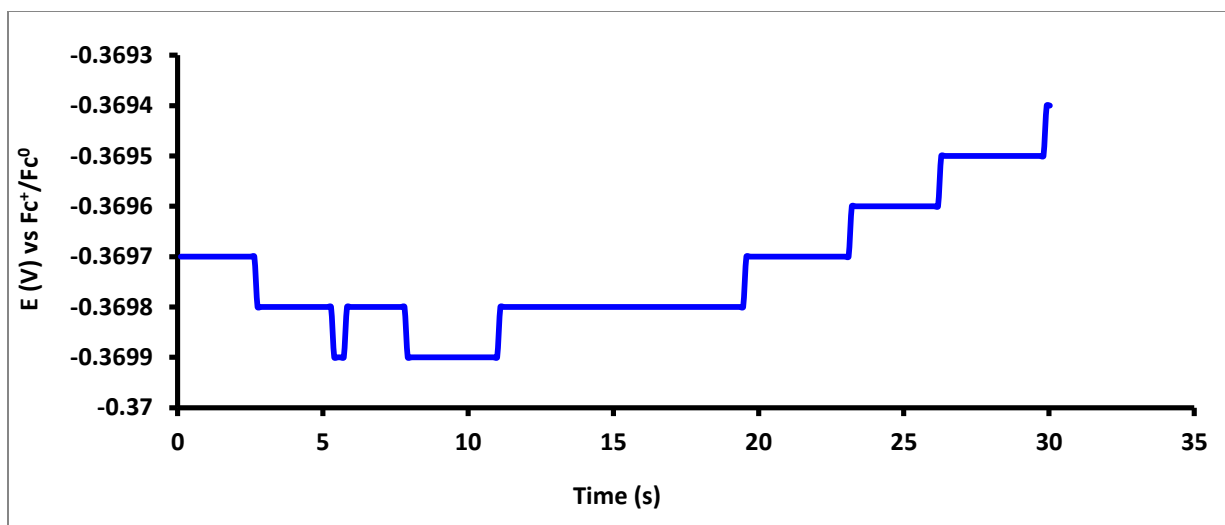


Figure C108. OCP measurement for H_2L^1 HER
 0.1M Bu_4NPF_6 methanol solution with 10 mM acetic acid added.

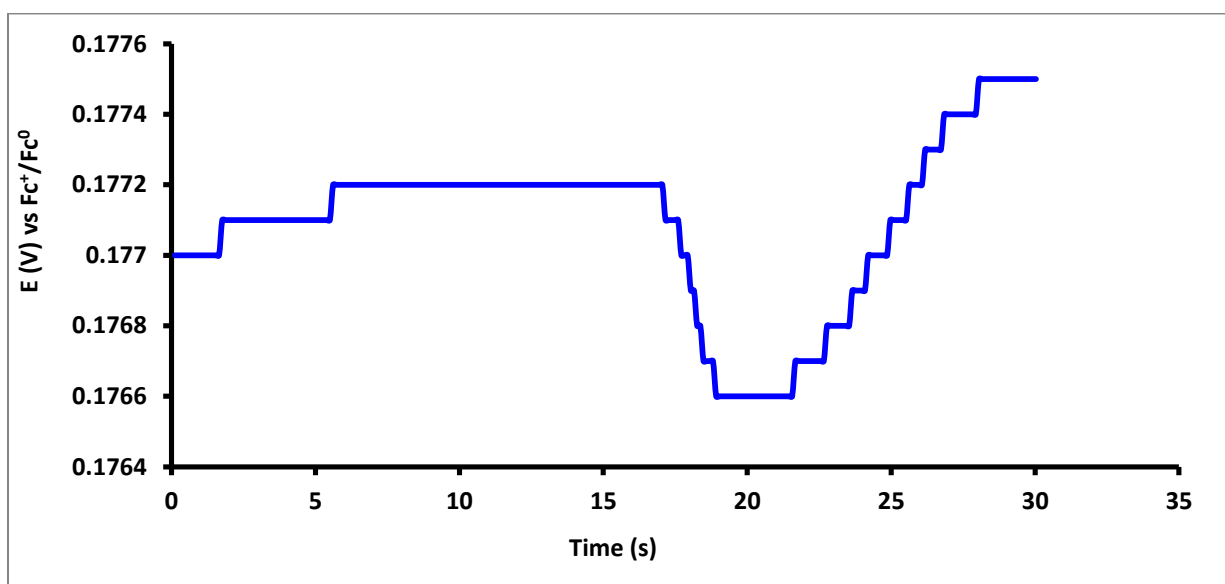


Figure C109. OCP measurement for H_2L^1 HOR
 0.1M Bu_4NPF_6 methanol solution with 10 mM acetic acid added.

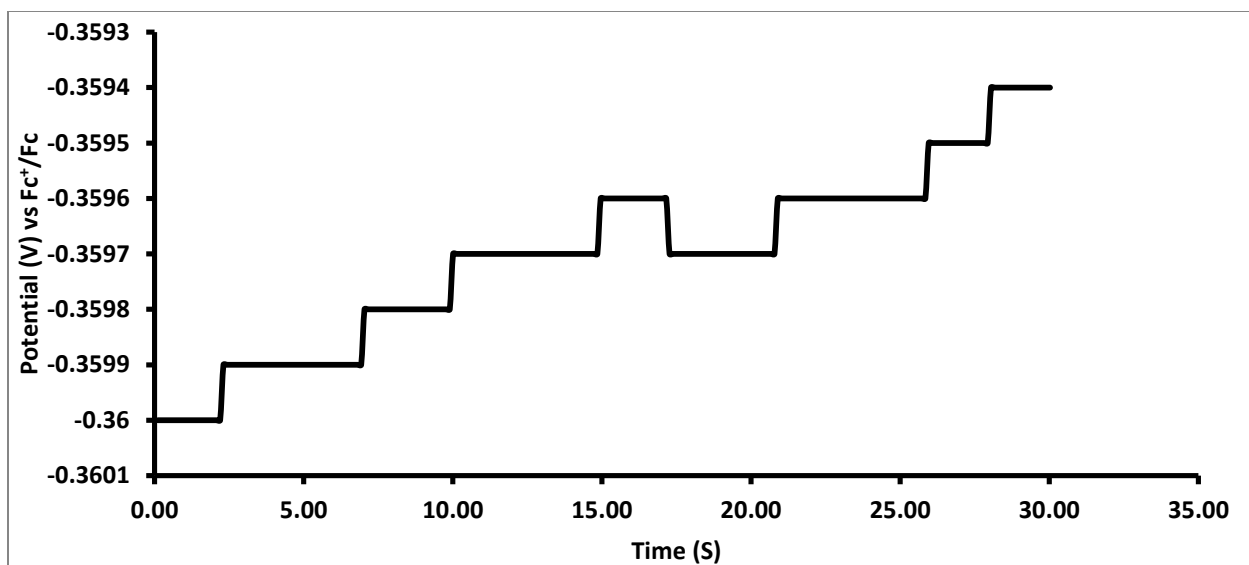


Figure C110. OCP measurement for ZnL¹ HER in Acetonitrile 0.1M Bu₄NPF₆ acetonitrile solution with 21 mM acetic acid added.

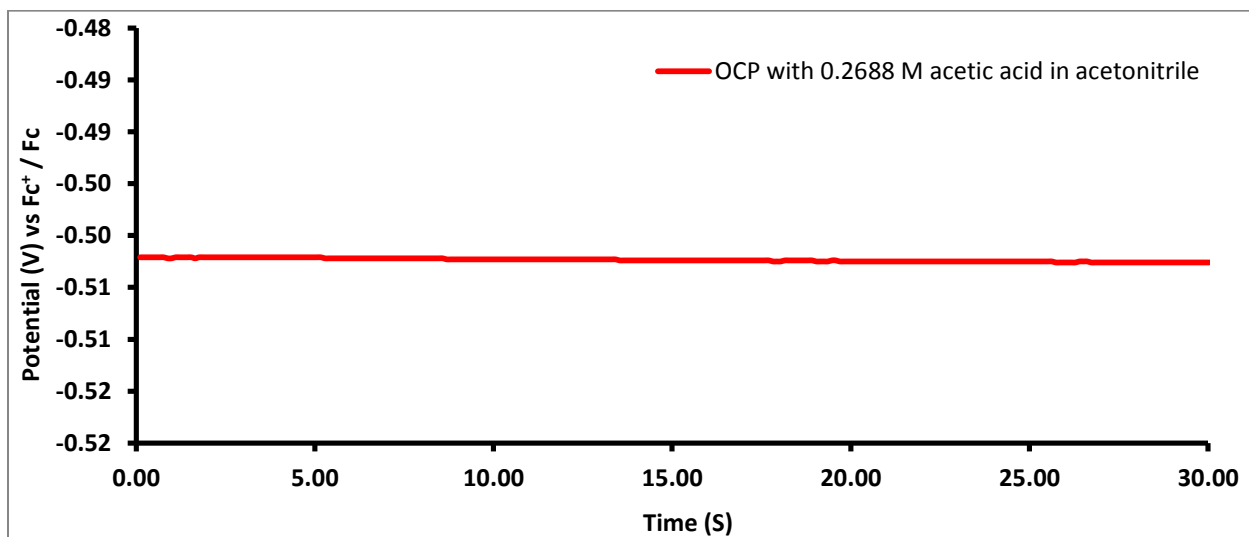


Figure C111. OCP measurement for CuL¹ HER 0.1 M Bu₄NPF₆ acetonitrile solution with 0.269 M acetic acid added

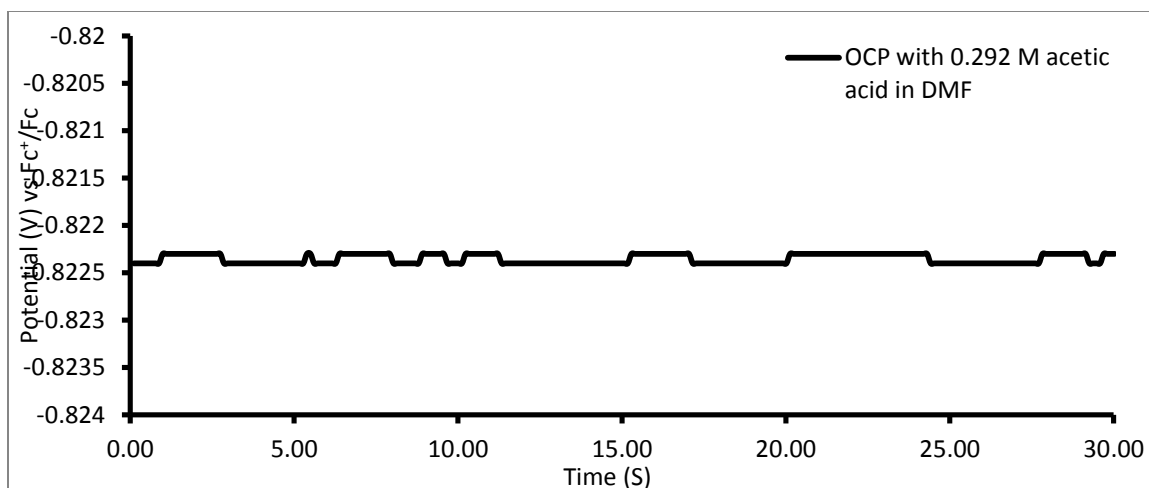


Figure C112. OCP measurement for CuL^1 HER
 0.1 M Bu_4NPF_6 DMF solution with 0.292 M acetic acid added.

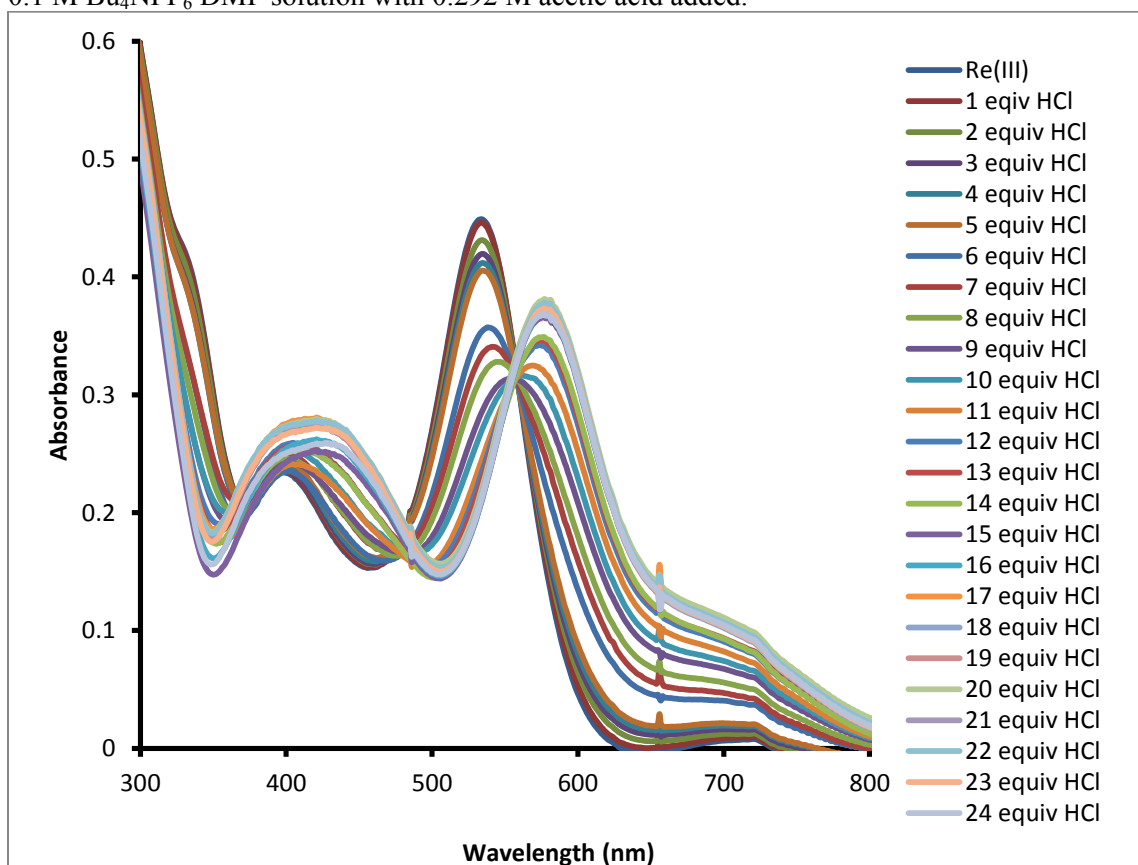
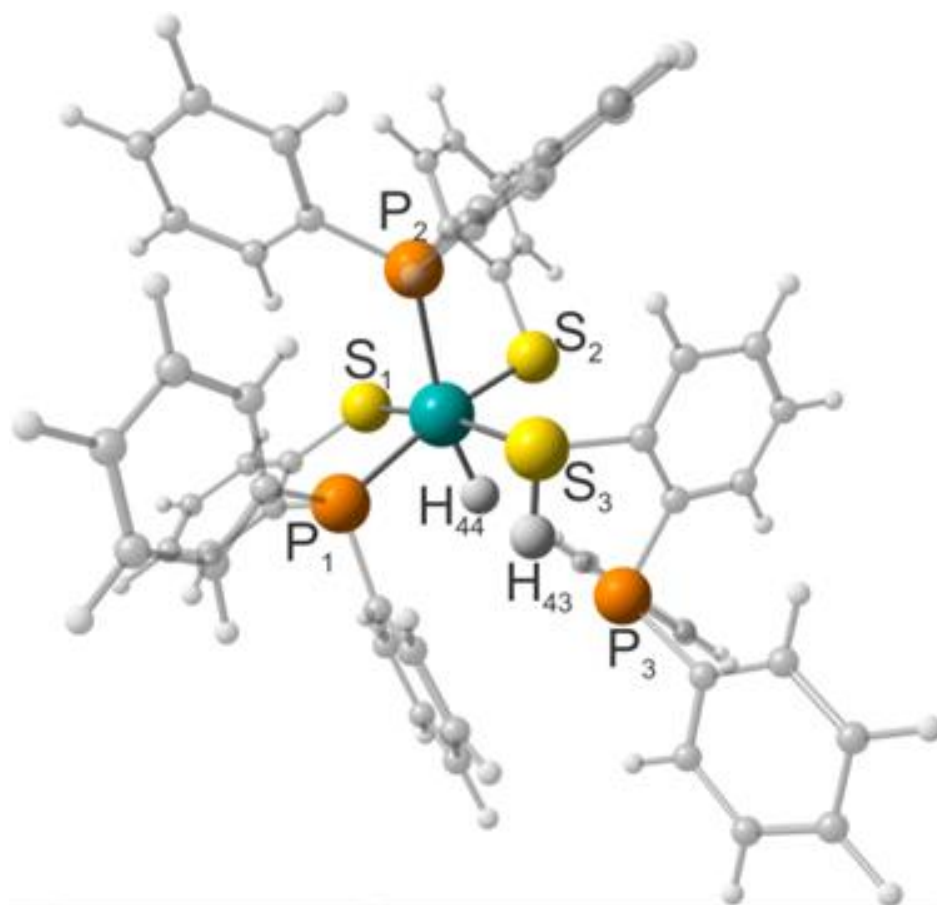


Figure C113. UV-Vis absorbance's measured during titration of ReL_3 with increasing equivalents of HCl.

APPENDIX D:
ADDITIONAL DFT STRUCTURES
AND ALL COMPUTATIONAL INPUT
COORDINATES



$^{1,3}[\text{HRe}(\text{LH})\text{L}_2]^0 \Delta G = +2.03 / 0.0$

S = 0 / S = 1

Re-S1	2.31 / 2.41
Re-S2	2.46 / 2.42
Re-S3	2.61 / 2.59
Re-P1	2.40 / 2.44
Re-P2	2.50 / 2.56
S3-H43	1.38 / 1.39
Re-H44	1.68 / 1.67
P2-Re-P3	154.7 / 165.9

Figure D114. DFT (M06 / LANL2DZ) optimized geometric parameters with bond lengths (Å) and angles (°) for $[\text{HRe}(\text{LH})\text{L}_2]^0$ with free energy energies (kcal / mole) of singlet (S = 0) and triplet (S = 1) electronic states.

Table D7. Computational input coordinates for ZnL¹ and related compounds.
ZnL¹

0 1			
Zn	0.00003000	-0.87035000	-0.00021000
S	1.99717800	-1.98187000	0.39859600
C	3.02385700	-0.57568000	0.06312600
N	2.64126500	0.68182000	-0.11295000
N	1.29611500	0.83221600	-0.13343000
C	0.74221000	2.00306700	-0.01927000
C	-0.74227000	2.00309000	0.01908300
N	-1.29622000	0.83222900	0.13305300
N	-2.64133000	0.68180300	0.11294100
C	-3.02384000	-0.57582000	-0.06295000
S	-1.99721000	-1.98199000	-0.39809000
N	4.35570700	-0.82176000	0.01195100
C	5.36070300	0.19708100	-0.24871000
C	1.51592800	3.28691200	0.08674400
C	-1.51582000	3.28710900	-0.08627000
N	-4.35572000	-0.82183000	-0.01172000
C	-5.36071000	0.19724100	0.24805300
H	4.64910400	-1.76944000	0.19775300
H	-4.64921000	-1.76953000	-0.19732000
H	6.34217200	-0.28345000	-0.24323000
H	5.33720300	0.97919000	0.51882200

H	5.19661500	0.66931400	-1.22332000
H	2.57356100	3.10001400	-0.10327000
H	1.41553600	3.72317600	1.09013800
H	1.14601100	4.03184200	-0.62751000
H	-2.57412000	3.09947900	0.09927500
H	-1.14881000	4.02987600	0.63178900
H	-1.41150000	3.72652300	-1.08785000
H	-6.34227000	-0.28309000	0.24188600
H	-5.19732000	0.66960500	1.22273300
H	-5.33643000	0.97923600	-0.51956000

[ZnHL]⁺

1 1

Zn	0.000030000	-0.870350000	-0.000210000
S	1.997178000	-1.981870000	0.398596000
C	3.023857000	-0.575680000	0.063126000
N	2.641265000	0.681820000	-0.112950000
N	1.296115000	0.832216000	-0.133430000
C	0.742210000	2.003067000	-0.019270000
C	-0.742270000	2.003090000	0.019083000
N	-1.296220000	0.832229000	0.133053000
N	-2.641330000	0.681803000	0.112941000
C	-3.023840000	-0.575820000	-0.062950000

S	-1.997210000	-1.981990000	-0.398090000
N	4.355707000	-0.821760000	0.011951000
C	5.360703000	0.197081000	-0.248710000
C	1.515928000	3.286912000	0.086744000
C	-1.515820000	3.287109000	-0.086270000
N	-4.355720000	-0.821830000	-0.011720000
C	-5.360710000	0.197241000	0.248053000
H	4.649104000	-1.769440000	0.197753000
H	-4.649210000	-1.769530000	-0.197320000
H	6.342172000	-0.283450000	-0.243230000
H	5.337203000	0.979190000	0.518822000
H	5.196615000	0.669314000	-1.223320000
H	2.573561000	3.100014000	-0.103270000
H	1.415536000	3.723176000	1.090138000
H	1.146011000	4.031842000	-0.627510000
H	-2.574120000	3.099479000	0.099275000
H	-1.148810000	4.029876000	0.631789000
H	-1.411500000	3.726523000	-1.087850000
H	-6.342270000	-0.283090000	0.241886000
H	-5.197320000	0.669605000	1.222733000
H	-5.336430000	0.979236000	-0.519560000
H	3.281842792	1.442241206	-0.219812917

Zn(HL•)

0 2

Zn	0.000030000	-0.870350000	-0.000210000
S	1.997178000	-1.981870000	0.398596000
C	3.023857000	-0.575680000	0.063126000
N	2.641265000	0.681820000	-0.112950000
N	1.296115000	0.832216000	-0.133430000
C	0.742210000	2.003067000	-0.019270000
C	-0.742270000	2.003090000	0.019083000
N	-1.296220000	0.832229000	0.133053000
N	-2.641330000	0.681803000	0.112941000
C	-3.023840000	-0.575820000	-0.062950000
S	-1.997210000	-1.981990000	-0.398090000
N	4.355707000	-0.821760000	0.011951000
C	5.360703000	0.197081000	-0.248710000
C	1.515928000	3.286912000	0.086744000
C	-1.515820000	3.287109000	-0.086270000
N	-4.355720000	-0.821830000	-0.011720000
C	-5.360710000	0.197241000	0.248053000
H	4.649104000	-1.769440000	0.197753000
H	-4.649210000	-1.769530000	-0.197320000
H	6.342172000	-0.283450000	-0.243230000
H	5.337203000	0.979190000	0.518822000

H	5.196615000	0.669314000	-1.223320000
H	2.573561000	3.100014000	-0.103270000
H	1.415536000	3.723176000	1.090138000
H	1.146011000	4.031842000	-0.627510000
H	-2.574120000	3.099479000	0.099275000
H	-1.148810000	4.029876000	0.631789000
H	-1.411500000	3.726523000	-1.087850000
H	-6.342270000	-0.283090000	0.241886000
H	-5.197320000	0.669605000	1.222733000
H	-5.336430000	0.979236000	-0.519560000
H	3.281842792	1.442241206	-0.219812917

[ZnH₂L⁺]

1 2

Zn	0.000030000	-0.870350000	-0.000210000
S	1.997178000	-1.981870000	0.398596000
C	3.023857000	-0.575680000	0.063126000
N	2.641265000	0.681820000	-0.112950000
N	1.296115000	0.832216000	-0.133430000
C	0.742210000	2.003067000	-0.019270000
C	-0.742270000	2.003090000	0.019083000
N	-1.296220000	0.832229000	0.133053000
N	-2.641330000	0.681803000	0.112941000

C	-3.023840000	-0.575820000	-0.062950000
S	-1.997210000	-1.981990000	-0.398090000
N	4.355707000	-0.821760000	0.011951000
C	5.360703000	0.197081000	-0.248710000
C	1.515928000	3.286912000	0.086744000
C	-1.515820000	3.287109000	-0.086270000
N	-4.355720000	-0.821830000	-0.011720000
C	-5.360710000	0.197241000	0.248053000
H	4.649104000	-1.769440000	0.197753000
H	-4.649210000	-1.769530000	-0.197320000
H	6.342172000	-0.283450000	-0.243230000
H	5.337203000	0.979190000	0.518822000
H	5.196615000	0.669314000	-1.223320000
H	2.573561000	3.100014000	-0.103270000
H	1.415536000	3.723176000	1.090138000
H	1.146011000	4.031842000	-0.627510000
H	-2.574120000	3.099479000	0.099275000
H	-1.148810000	4.029876000	0.631789000
H	-1.411500000	3.726523000	-1.087850000
H	-6.342270000	-0.283090000	0.241886000
H	-5.197320000	0.669605000	1.222733000
H	-5.336430000	0.979236000	-0.519560000

H	3.281842792	1.442241206	-0.219812917
H	-3.281933702	1.442187461	0.219910007

Protonation of ZnL¹ at sulfur

1 1

30	0.000030000	-0.870350000	-0.000210000
16	1.997178000	-1.981870000	0.398596000
6	3.023857000	-0.575680000	0.063126000
7	2.641265000	0.681820000	-0.112950000
7	1.296115000	0.832216000	-0.133430000
6	0.742210000	2.003067000	-0.019270000
6	-0.742270000	2.003090000	0.019083000
7	-1.296220000	0.832229000	0.133053000
7	-2.641330000	0.681803000	0.112941000
6	-3.023840000	-0.575820000	-0.062950000
16	-1.997210000	-1.981990000	-0.398090000
7	4.355707000	-0.821760000	0.011951000
6	5.360703000	0.197081000	-0.248710000
6	1.515928000	3.286912000	0.086744000
6	-1.515820000	3.287109000	-0.086270000
7	-4.355720000	-0.821830000	-0.011720000
6	-5.360710000	0.197241000	0.248053000
1	4.649104000	-1.769440000	0.197753000

1	-4.649210000	-1.769530000	-0.197320000
1	6.342172000	-0.283450000	-0.243230000
1	5.337203000	0.979190000	0.518822000
1	5.196615000	0.669314000	-1.223320000
1	2.573561000	3.100014000	-0.103270000
1	1.415536000	3.723176000	1.090138000
1	1.146011000	4.031842000	-0.627510000
1	-2.574120000	3.099479000	0.099275000
1	-1.148810000	4.029876000	0.631789000
1	-1.411500000	3.726523000	-1.087850000
1	-6.342270000	-0.283090000	0.241886000
1	-5.197320000	0.669605000	1.222733000
1	-5.336430000	0.979236000	-0.519560000
1	2.274340046	-3.233237278	0.753787688

Protonation at Amine Nitrogen

1 1			
Zn	0.000030000	-0.870350000	-0.000210000
S	1.997178000	-1.981870000	0.398596000
C	3.023857000	-0.575680000	0.063126000
N	2.641265000	0.681820000	-0.112950000
N	1.296115000	0.832216000	-0.133430000
C	0.742210000	2.003067000	-0.019270000

C	-0.742270000	2.003090000	0.019083000
N	-1.296220000	0.832229000	0.133053000
N	-2.641330000	0.681803000	0.112941000
C	-3.023840000	-0.575820000	-0.062950000
S	-1.997210000	-1.981990000	-0.398090000
N	4.355707000	-0.821760000	0.011951000
C	5.360703000	0.197081000	-0.248710000
C	1.515928000	3.286912000	0.086744000
C	-1.515820000	3.287109000	-0.086270000
N	-4.355720000	-0.821830000	-0.011720000
C	-5.360710000	0.197241000	0.248053000
H	4.649104000	-1.769440000	0.197753000
H	-4.649210000	-1.769530000	-0.197320000
H	6.342172000	-0.283450000	-0.243230000
H	5.337203000	0.979190000	0.518822000
H	5.196615000	0.669314000	-1.223320000
H	2.573561000	3.100014000	-0.103270000
H	1.415536000	3.723176000	1.090138000
H	1.146011000	4.031842000	-0.627510000
H	-2.574120000	3.099479000	0.099275000
H	-1.148810000	4.029876000	0.631789000
H	-1.411500000	3.726523000	-1.087850000
H	-6.342270000	-0.283090000	0.241886000

H	-5.197320000	0.669605000	1.222733000
H	-5.336430000	0.979236000	-0.519560000
H	4.370833470	-0.021327902	-0.587281548

Protonation on Zinc

1 1

Zn	0.000030000	-0.870350000	-0.000210000
S	1.997178000	-1.981870000	0.398596000
C	3.023857000	-0.575680000	0.063126000
N	2.641265000	0.681820000	-0.112950000
N	1.296115000	0.832216000	-0.133430000
C	0.742210000	2.003067000	-0.019270000
C	-0.742270000	2.003090000	0.019083000
N	-1.296220000	0.832229000	0.133053000
N	-2.641330000	0.681803000	0.112941000
C	-3.023840000	-0.575820000	-0.062950000
S	-1.997210000	-1.981990000	-0.398090000
N	4.355707000	-0.821760000	0.011951000
C	5.360703000	0.197081000	-0.248710000
C	1.515928000	3.286912000	0.086744000
C	-1.515820000	3.287109000	-0.086270000
N	-4.355720000	-0.821830000	-0.011720000
C	-5.360710000	0.197241000	0.248053000

H	4.649104000	-1.769440000	0.197753000
H	-4.649210000	-1.769530000	-0.197320000
H	6.342172000	-0.283450000	-0.243230000
H	5.337203000	0.979190000	0.518822000
H	5.196615000	0.669314000	-1.223320000
H	2.573561000	3.100014000	-0.103270000
H	1.415536000	3.723176000	1.090138000
H	1.146011000	4.031842000	-0.627510000
H	-2.574120000	3.099479000	0.099275000
H	-1.148810000	4.029876000	0.631789000
H	-1.411500000	3.726523000	-1.087850000
H	-6.342270000	-0.283090000	0.241886000
H	-5.197320000	0.669605000	1.222733000
H	-5.336430000	0.979236000	-0.519560000
H	0.000293000	-2.650349596	-0.001380325

Hydrogen

0 1

H	3.259348439	4.169555780	-0.124845483
H	3.259348439	4.169555780	-0.864845483

Table D8. Computational input coordinates for ReL₃ and related compounds.ReL₃

O 1

Re	0.001887000	0.522349000	-0.151905000
S	-0.053024000	0.170602000	-2.464628000
S	-0.168218000	2.947928000	-0.676510000
S	0.235228000	0.982632000	2.249003000
P	0.064739000	-1.839301000	0.025067000
P	-2.439968000	0.764165000	0.031527000
P	2.429160000	0.825934000	-0.104875000
C	-0.301468000	-1.577539000	-2.716189000
C	-0.556521000	-2.025037000	-4.018084000
H	-0.575283000	-1.302804000	-4.834265000
C	-0.803553000	-3.369352000	-4.258760000
H	-1.010875000	-3.707084000	-5.272736000
C	-0.795043000	-4.284222000	-3.206110000
H	-0.995787000	-5.337287000	-3.392194000
C	-0.526709000	-3.844709000	-1.915438000
H	-0.526242000	-4.559284000	-1.091063000
C	-0.270658000	-2.494077000	-1.656259000
C	1.613029000	-2.687870000	0.573505000
C	2.238949000	-3.691270000	-0.169394000
H	1.855648000	-3.967596000	-1.150047000
C	3.367705000	-4.339723000	0.324353000
H	3.841212000	-5.117524000	-0.272559000
C	3.893235000	-3.997206000	1.565189000

H	4.771049000	-4.513236000	1.950104000
C	3.298881000	-2.977879000	2.302993000
H	3.711237000	-2.678761000	3.266054000
C	2.176162000	-2.327649000	1.805212000
H	1.745128000	-1.514887000	2.389742000
C	-1.179490000	-2.731939000	1.074363000
C	-0.932203000	-2.986628000	2.430355000
H	0.039883000	-2.762528000	2.865459000
C	-1.899778000	-3.577639000	3.236756000
H	-1.677885000	-3.777433000	4.283962000
C	-3.134379000	-3.934001000	2.702217000
H	-3.887891000	-4.407141000	3.329047000
C	-3.389557000	-3.696825000	1.356096000
H	-4.346479000	-3.978451000	0.919431000
C	-2.425280000	-3.096296000	0.550612000
H	-2.650255000	-2.922079000	-0.500889000
C	-1.904631000	3.298883000	-1.047041000
C	-2.211759000	4.526884000	-1.627125000
H	-1.415910000	5.237700000	-1.845356000
C	-3.535280000	4.826753000	-1.928924000
H	-3.782502000	5.784282000	-2.382684000
C	-4.537204000	3.897085000	-1.663032000
H	-5.572722000	4.127569000	-1.905125000
C	-4.217527000	2.667565000	-1.099171000
H	-5.004051000	1.939035000	-0.901592000

C	-2.892279000	2.352936000	-0.784987000
C	-2.971189000	1.040659000	1.764975000
C	-3.173051000	2.327691000	2.270983000
H	-3.152166000	3.190254000	1.604393000
C	-3.406147000	2.517360000	3.630416000
H	-3.562726000	3.523518000	4.014881000
C	-3.444556000	1.428211000	4.494972000
H	-3.629630000	1.581746000	5.556491000
C	-3.251644000	0.141593000	3.997067000
H	-3.288099000	-0.721392000	4.660717000
C	-3.008874000	-0.050896000	2.642408000
H	-2.847951000	-1.058285000	2.260735000
C	-3.693431000	-0.360336000	-0.694248000
C	-4.824866000	-0.790762000	0.001785000
H	-4.993143000	-0.471241000	1.029348000
C	-5.741539000	-1.641759000	-0.610803000
H	-6.620419000	-1.971006000	-0.058855000
C	-5.535450000	-2.069420000	-1.918199000
H	-6.249257000	-2.741712000	-2.390573000
C	-4.422751000	-1.621240000	-2.627136000
H	-4.266030000	-1.935452000	-3.657435000
C	-3.511869000	-0.764223000	-2.022597000
H	-2.650858000	-0.406584000	-2.586327000
C	1.993805000	1.035542000	2.661036000
C	2.351666000	1.176395000	4.001720000

H	1.582001000	1.184349000	4.773014000
C	3.689518000	1.328199000	4.340708000
H	3.974222000	1.426527000	5.386205000
C	4.655948000	1.402548000	3.339346000
H	5.698742000	1.573337000	3.598264000
C	4.286999000	1.276995000	2.006891000
H	5.041755000	1.376832000	1.227325000
C	2.953554000	1.038507000	1.647089000
C	3.554628000	-0.421858000	-0.863119000
C	3.297504000	-0.804214000	-2.187684000
H	2.422550000	-0.416356000	-2.708412000
C	4.135443000	-1.695966000	-2.847752000
H	3.917255000	-1.971348000	-3.878076000
C	5.238018000	-2.234946000	-2.193887000
H	5.896651000	-2.930855000	-2.710072000
C	5.480417000	-1.892276000	-0.868921000
H	6.321967000	-2.331009000	-0.334982000
C	4.647080000	-0.995926000	-0.207248000
H	4.846659000	-0.778804000	0.838883000
C	2.995063000	2.420758000	-0.832613000
C	3.238245000	2.536798000	-2.204155000
H	3.237226000	1.653785000	-2.840767000
C	3.492878000	3.780314000	-2.771394000
H	3.684891000	3.853136000	-3.840184000
C	3.507567000	4.924266000	-1.980002000

H	3.707829000	5.895897000	-2.427456000
C	3.270966000	4.819435000	-0.613479000
H	3.290951000	5.707730000	0.015613000
C	3.012520000	3.577085000	-0.043616000
H	2.824596000	3.513512000	1.029318000

[ReL₃]

-1 2

Re	0.001887000	0.522349000	-0.151905000
S	-0.053024000	0.170602000	-2.464628000
S	-0.168218000	2.947928000	-0.676510000
S	0.235228000	0.982632000	2.249003000
P	0.064739000	-1.839301000	0.025067000
P	-2.439968000	0.764165000	0.031527000
P	2.429160000	0.825934000	-0.104875000
C	-0.301468000	-1.577539000	-2.716189000
C	-0.556521000	-2.025037000	-4.018084000
H	-0.575283000	-1.302804000	-4.834265000
C	-0.803553000	-3.369352000	-4.258760000
H	-1.010875000	-3.707084000	-5.272736000
C	-0.795043000	-4.284222000	-3.206110000
H	-0.995787000	-5.337287000	-3.392194000
C	-0.526709000	-3.844709000	-1.915438000
H	-0.526242000	-4.559284000	-1.091063000
C	-0.270658000	-2.494077000	-1.656259000

C	1.613029000	-2.687870000	0.573505000
C	2.238949000	-3.691270000	-0.169394000
H	1.855648000	-3.967596000	-1.150047000
C	3.367705000	-4.339723000	0.324353000
H	3.841212000	-5.117524000	-0.272559000
C	3.893235000	-3.997206000	1.565189000
H	4.771049000	-4.513236000	1.950104000
C	3.298881000	-2.977879000	2.302993000
H	3.711237000	-2.678761000	3.266054000
C	2.176162000	-2.327649000	1.805212000
H	1.745128000	-1.514887000	2.389742000
C	-1.179490000	-2.731939000	1.074363000
C	-0.932203000	-2.986628000	2.430355000
H	0.039883000	-2.762528000	2.865459000
C	-1.899778000	-3.577639000	3.236756000
H	-1.677885000	-3.777433000	4.283962000
C	-3.134379000	-3.934001000	2.702217000
H	-3.887891000	-4.407141000	3.329047000
C	-3.389557000	-3.696825000	1.356096000
H	-4.346479000	-3.978451000	0.919431000
C	-2.425280000	-3.096296000	0.550612000
H	-2.650255000	-2.922079000	-0.500889000
C	-1.904631000	3.298883000	-1.047041000
C	-2.211759000	4.526884000	-1.627125000
H	-1.415910000	5.237700000	-1.845356000

C	-3.535280000	4.826753000	-1.928924000
H	-3.782502000	5.784282000	-2.382684000
C	-4.537204000	3.897085000	-1.663032000
H	-5.572722000	4.127569000	-1.905125000
C	-4.217527000	2.667565000	-1.099171000
H	-5.004051000	1.939035000	-0.901592000
C	-2.892279000	2.352936000	-0.784987000
C	-2.971189000	1.040659000	1.764975000
C	-3.173051000	2.327691000	2.270983000
H	-3.152166000	3.190254000	1.604393000
C	-3.406147000	2.517360000	3.630416000
H	-3.562726000	3.523518000	4.014881000
C	-3.444556000	1.428211000	4.494972000
H	-3.629630000	1.581746000	5.556491000
C	-3.251644000	0.141593000	3.997067000
H	-3.288099000	-0.721392000	4.660717000
C	-3.008874000	-0.050896000	2.642408000
H	-2.847951000	-1.058285000	2.260735000
C	-3.693431000	-0.360336000	-0.694248000
C	-4.824866000	-0.790762000	0.001785000
H	-4.993143000	-0.471241000	1.029348000
C	-5.741539000	-1.641759000	-0.610803000
H	-6.620419000	-1.971006000	-0.058855000
C	-5.535450000	-2.069420000	-1.918199000
H	-6.249257000	-2.741712000	-2.390573000

C	-4.422751000	-1.621240000	-2.627136000
H	-4.266030000	-1.935452000	-3.657435000
C	-3.511869000	-0.764223000	-2.022597000
H	-2.650858000	-0.406584000	-2.586327000
C	1.993805000	1.035542000	2.661036000
C	2.351666000	1.176395000	4.001720000
H	1.582001000	1.184349000	4.773014000
C	3.689518000	1.328199000	4.340708000
H	3.974222000	1.426527000	5.386205000
C	4.655948000	1.402548000	3.339346000
H	5.698742000	1.573337000	3.598264000
C	4.286999000	1.276995000	2.006891000
H	5.041755000	1.376832000	1.227325000
C	2.953554000	1.038507000	1.647089000
C	3.554628000	-0.421858000	-0.863119000
C	3.297504000	-0.804214000	-2.187684000
H	2.422550000	-0.416356000	-2.708412000
C	4.135443000	-1.695966000	-2.847752000
H	3.917255000	-1.971348000	-3.878076000
C	5.238018000	-2.234946000	-2.193887000
H	5.896651000	-2.930855000	-2.710072000
C	5.480417000	-1.892276000	-0.868921000
H	6.321967000	-2.331009000	-0.334982000
C	4.647080000	-0.995926000	-0.207248000
H	4.846659000	-0.778804000	0.838883000

C	2.995063000	2.420758000	-0.832613000
C	3.238245000	2.536798000	-2.204155000
H	3.237226000	1.653785000	-2.840767000
C	3.492878000	3.780314000	-2.771394000
H	3.684891000	3.853136000	-3.840184000
C	3.507567000	4.924266000	-1.980002000
H	3.707829000	5.895897000	-2.427456000
C	3.270966000	4.819435000	-0.613479000
H	3.290951000	5.707730000	0.015613000
C	3.012520000	3.577085000	-0.043616000
H	2.824596000	3.513512000	1.029318000

[Re(LH)L₂]⁺

1 1

Re	0.001887000	0.522349000	-0.151905000
S	-0.053024000	0.170602000	-2.464628000
S	-0.168218000	2.947928000	-0.676510000
S	0.235228000	0.982632000	2.249003000
P	0.064739000	-1.839301000	0.025067000
P	-2.439968000	0.764165000	0.031527000
P	2.429160000	0.825934000	-0.104875000
C	-0.301468000	-1.577539000	-2.716189000
C	-0.556521000	-2.025037000	-4.018084000
H	-0.575283000	-1.302804000	-4.834265000
C	-0.803553000	-3.369352000	-4.258760000

H	-1.010875000	-3.707084000	-5.272736000
C	-0.795043000	-4.284222000	-3.206110000
H	-0.995787000	-5.337287000	-3.392194000
C	-0.526709000	-3.844709000	-1.915438000
H	-0.526242000	-4.559284000	-1.091063000
C	-0.270658000	-2.494077000	-1.656259000
C	1.613029000	-2.687870000	0.573505000
C	2.238949000	-3.691270000	-0.169394000
H	1.855648000	-3.967596000	-1.150047000
C	3.367705000	-4.339723000	0.324353000
H	3.841212000	-5.117524000	-0.272559000
C	3.893235000	-3.997206000	1.565189000
H	4.771049000	-4.513236000	1.950104000
C	3.298881000	-2.977879000	2.302993000
H	3.711237000	-2.678761000	3.266054000
C	2.176162000	-2.327649000	1.805212000
H	1.745128000	-1.514887000	2.389742000
C	-1.179490000	-2.731939000	1.074363000
C	-0.932203000	-2.986628000	2.430355000
H	0.039883000	-2.762528000	2.865459000
C	-1.899778000	-3.577639000	3.236756000
H	-1.677885000	-3.777433000	4.283962000
C	-3.134379000	-3.934001000	2.702217000
H	-3.887891000	-4.407141000	3.329047000
C	-3.389557000	-3.696825000	1.356096000

H	-4.346479000	-3.978451000	0.919431000
C	-2.425280000	-3.096296000	0.550612000
H	-2.650255000	-2.922079000	-0.500889000
C	-1.904631000	3.298883000	-1.047041000
C	-2.211759000	4.526884000	-1.627125000
H	-1.415910000	5.237700000	-1.845356000
C	-3.535280000	4.826753000	-1.928924000
H	-3.782502000	5.784282000	-2.382684000
C	-4.537204000	3.897085000	-1.663032000
H	-5.572722000	4.127569000	-1.905125000
C	-4.217527000	2.667565000	-1.099171000
H	-5.004051000	1.939035000	-0.901592000
C	-2.892279000	2.352936000	-0.784987000
C	-2.971189000	1.040659000	1.764975000
C	-3.173051000	2.327691000	2.270983000
H	-3.152166000	3.190254000	1.604393000
C	-3.406147000	2.517360000	3.630416000
H	-3.562726000	3.523518000	4.014881000
C	-3.444556000	1.428211000	4.494972000
H	-3.629630000	1.581746000	5.556491000
C	-3.251644000	0.141593000	3.997067000
H	-3.288099000	-0.721392000	4.660717000
C	-3.008874000	-0.050896000	2.642408000
H	-2.847951000	-1.058285000	2.260735000
C	-3.693431000	-0.360336000	-0.694248000

C	-4.824866000	-0.790762000	0.001785000
H	-4.993143000	-0.471241000	1.029348000
C	-5.741539000	-1.641759000	-0.610803000
H	-6.620419000	-1.971006000	-0.058855000
C	-5.535450000	-2.069420000	-1.918199000
H	-6.249257000	-2.741712000	-2.390573000
C	-4.422751000	-1.621240000	-2.627136000
H	-4.266030000	-1.935452000	-3.657435000
C	-3.511869000	-0.764223000	-2.022597000
H	-2.650858000	-0.406584000	-2.586327000
C	1.993805000	1.035542000	2.661036000
C	2.351666000	1.176395000	4.001720000
H	1.582001000	1.184349000	4.773014000
C	3.689518000	1.328199000	4.340708000
H	3.974222000	1.426527000	5.386205000
C	4.655948000	1.402548000	3.339346000
H	5.698742000	1.573337000	3.598264000
C	4.286999000	1.276995000	2.006891000
H	5.041755000	1.376832000	1.227325000
C	2.953554000	1.038507000	1.647089000
C	3.554628000	-0.421858000	-0.863119000
C	3.297504000	-0.804214000	-2.187684000
H	2.422550000	-0.416356000	-2.708412000
C	4.135443000	-1.695966000	-2.847752000
H	3.917255000	-1.971348000	-3.878076000

C	5.238018000	-2.234946000	-2.193887000
H	5.896651000	-2.930855000	-2.710072000
C	5.480417000	-1.892276000	-0.868921000
H	6.321967000	-2.331009000	-0.334982000
C	4.647080000	-0.995926000	-0.207248000
H	4.846659000	-0.778804000	0.838883000
C	2.995063000	2.420758000	-0.832613000
C	3.238245000	2.536798000	-2.204155000
H	3.237226000	1.653785000	-2.840767000
C	3.492878000	3.780314000	-2.771394000
H	3.684891000	3.853136000	-3.840184000
C	3.507567000	4.924266000	-1.980002000
H	3.707829000	5.895897000	-2.427456000
C	3.270966000	4.819435000	-0.613479000
H	3.290951000	5.707730000	0.015613000
C	3.012520000	3.577085000	-0.043616000
H	2.824596000	3.513512000	1.029318000
H	-0.076380480	0.368482252	3.100003943

[Re(LH)L₂]

0 2

Re	0.001887000	0.522349000	-0.151905000
S	-0.053024000	0.170602000	-2.464628000
S	-0.168218000	2.947928000	-0.676510000
S	0.235228000	0.982632000	2.249003000

P	0.064739000	-1.839301000	0.025067000
P	-2.439968000	0.764165000	0.031527000
P	2.429160000	0.825934000	-0.104875000
C	-0.301468000	-1.577539000	-2.716189000
C	-0.556521000	-2.025037000	-4.018084000
H	-0.575283000	-1.302804000	-4.834265000
C	-0.803553000	-3.369352000	-4.258760000
H	-1.010875000	-3.707084000	-5.272736000
C	-0.795043000	-4.284222000	-3.206110000
H	-0.995787000	-5.337287000	-3.392194000
C	-0.526709000	-3.844709000	-1.915438000
H	-0.526242000	-4.559284000	-1.091063000
C	-0.270658000	-2.494077000	-1.656259000
C	1.613029000	-2.687870000	0.573505000
C	2.238949000	-3.691270000	-0.169394000
H	1.855648000	-3.967596000	-1.150047000
C	3.367705000	-4.339723000	0.324353000
H	3.841212000	-5.117524000	-0.272559000
C	3.893235000	-3.997206000	1.565189000
H	4.771049000	-4.513236000	1.950104000
C	3.298881000	-2.977879000	2.302993000
H	3.711237000	-2.678761000	3.266054000
C	2.176162000	-2.327649000	1.805212000
H	1.745128000	-1.514887000	2.389742000
C	-1.179490000	-2.731939000	1.074363000

C	-0.932203000	-2.986628000	2.430355000
H	0.039883000	-2.762528000	2.865459000
C	-1.899778000	-3.577639000	3.236756000
H	-1.677885000	-3.777433000	4.283962000
C	-3.134379000	-3.934001000	2.702217000
H	-3.887891000	-4.407141000	3.329047000
C	-3.389557000	-3.696825000	1.356096000
H	-4.346479000	-3.978451000	0.919431000
C	-2.425280000	-3.096296000	0.550612000
H	-2.650255000	-2.922079000	-0.500889000
C	-1.904631000	3.298883000	-1.047041000
C	-2.211759000	4.526884000	-1.627125000
H	-1.415910000	5.237700000	-1.845356000
C	-3.535280000	4.826753000	-1.928924000
H	-3.782502000	5.784282000	-2.382684000
C	-4.537204000	3.897085000	-1.663032000
H	-5.572722000	4.127569000	-1.905125000
C	-4.217527000	2.667565000	-1.099171000
H	-5.004051000	1.939035000	-0.901592000
C	-2.892279000	2.352936000	-0.784987000
C	-2.971189000	1.040659000	1.764975000
C	-3.173051000	2.327691000	2.270983000
H	-3.152166000	3.190254000	1.604393000
C	-3.406147000	2.517360000	3.630416000
H	-3.562726000	3.523518000	4.014881000

C	-3.444556000	1.428211000	4.494972000
H	-3.629630000	1.581746000	5.556491000
C	-3.251644000	0.141593000	3.997067000
H	-3.288099000	-0.721392000	4.660717000
C	-3.008874000	-0.050896000	2.642408000
H	-2.847951000	-1.058285000	2.260735000
C	-3.693431000	-0.360336000	-0.694248000
C	-4.824866000	-0.790762000	0.001785000
H	-4.993143000	-0.471241000	1.029348000
C	-5.741539000	-1.641759000	-0.610803000
H	-6.620419000	-1.971006000	-0.058855000
C	-5.535450000	-2.069420000	-1.918199000
H	-6.249257000	-2.741712000	-2.390573000
C	-4.422751000	-1.621240000	-2.627136000
H	-4.266030000	-1.935452000	-3.657435000
C	-3.511869000	-0.764223000	-2.022597000
H	-2.650858000	-0.406584000	-2.586327000
C	1.993805000	1.035542000	2.661036000
C	2.351666000	1.176395000	4.001720000
H	1.582001000	1.184349000	4.773014000
C	3.689518000	1.328199000	4.340708000
H	3.974222000	1.426527000	5.386205000
C	4.655948000	1.402548000	3.339346000
H	5.698742000	1.573337000	3.598264000
C	4.286999000	1.276995000	2.006891000

H	5.041755000	1.376832000	1.227325000
C	2.953554000	1.038507000	1.647089000
C	3.554628000	-0.421858000	-0.863119000
C	3.297504000	-0.804214000	-2.187684000
H	2.422550000	-0.416356000	-2.708412000
C	4.135443000	-1.695966000	-2.847752000
H	3.917255000	-1.971348000	-3.878076000
C	5.238018000	-2.234946000	-2.193887000
H	5.896651000	-2.930855000	-2.710072000
C	5.480417000	-1.892276000	-0.868921000
H	6.321967000	-2.331009000	-0.334982000
C	4.647080000	-0.995926000	-0.207248000
H	4.846659000	-0.778804000	0.838883000
C	2.995063000	2.420758000	-0.832613000
C	3.238245000	2.536798000	-2.204155000
H	3.237226000	1.653785000	-2.840767000
C	3.492878000	3.780314000	-2.771394000
H	3.684891000	3.853136000	-3.840184000
C	3.507567000	4.924266000	-1.980002000
H	3.707829000	5.895897000	-2.427456000
C	3.270966000	4.819435000	-0.613479000
H	3.290951000	5.707730000	0.015613000
C	3.012520000	3.577085000	-0.043616000
H	2.824596000	3.513512000	1.029318000
H	-0.076380480	0.368482252	3.100003943



1 2

75	0.001887000	0.522349000	-0.151905000
16	-0.053024000	0.170602000	-2.464628000
16	-0.168218000	2.947928000	-0.676510000
16	0.235228000	0.982632000	2.249003000
1	-0.078752000	-0.110550000	2.999021000
15	0.064739000	-1.839301000	0.025067000
15	-2.439968000	0.764165000	0.031527000
15	2.429160000	0.825934000	-0.104875000
6	-0.301468000	-1.577539000	-2.716189000
6	-0.556521000	-2.025037000	-4.018084000
1	-0.575283000	-1.302804000	-4.834265000
6	-0.803553000	-3.369352000	-4.258760000
1	-1.010875000	-3.707084000	-5.272736000
6	-0.795043000	-4.284222000	-3.206110000
1	-0.995787000	-5.337287000	-3.392194000
6	-0.526709000	-3.844709000	-1.915438000
1	-0.526242000	-4.559284000	-1.091063000
6	-0.270658000	-2.494077000	-1.656259000
6	1.613029000	-2.687870000	0.573505000
6	2.238949000	-3.691270000	-0.169394000
1	1.855648000	-3.967596000	-1.150047000
6	3.367705000	-4.339723000	0.324353000
1	3.841212000	-5.117524000	-0.272559000

6	3.893235000	-3.997206000	1.565189000
1	4.771049000	-4.513236000	1.950104000
6	3.298881000	-2.977879000	2.302993000
1	3.711237000	-2.678761000	3.266054000
6	2.176162000	-2.327649000	1.805212000
1	1.745128000	-1.514887000	2.389742000
6	-1.179490000	-2.731939000	1.074363000
6	-0.932203000	-2.986628000	2.430355000
1	0.039883000	-2.762528000	2.865459000
6	-1.899778000	-3.577639000	3.236756000
1	-1.677885000	-3.777433000	4.283962000
6	-3.134379000	-3.934001000	2.702217000
1	-3.887891000	-4.407141000	3.329047000
6	-3.389557000	-3.696825000	1.356096000
1	-4.346479000	-3.978451000	0.919431000
6	-2.425280000	-3.096296000	0.550612000
1	-2.650255000	-2.922079000	-0.500889000
6	-1.904631000	3.298883000	-1.047041000
6	-2.211759000	4.526884000	-1.627125000
1	-1.415910000	5.237700000	-1.845356000
6	-3.535280000	4.826753000	-1.928924000
1	-3.782502000	5.784282000	-2.382684000
6	-4.537204000	3.897085000	-1.663032000
1	-5.572722000	4.127569000	-1.905125000
6	-4.217527000	2.667565000	-1.099171000

1	-5.004051000	1.939035000	-0.901592000
6	-2.892279000	2.352936000	-0.784987000
6	-2.971189000	1.040659000	1.764975000
6	-3.173051000	2.327691000	2.270983000
1	-3.152166000	3.190254000	1.604393000
6	-3.406147000	2.517360000	3.630416000
1	-3.562726000	3.523518000	4.014881000
6	-3.444556000	1.428211000	4.494972000
1	-3.629630000	1.581746000	5.556491000
6	-3.251644000	0.141593000	3.997067000
1	-3.288099000	-0.721392000	4.660717000
6	-3.008874000	-0.050896000	2.642408000
1	-2.847951000	-1.058285000	2.260735000
6	-3.693431000	-0.360336000	-0.694248000
6	-4.824866000	-0.790762000	0.001785000
1	-4.993143000	-0.471241000	1.029348000
6	-5.741539000	-1.641759000	-0.610803000
1	-6.620419000	-1.971006000	-0.058855000
6	-5.535450000	-2.069420000	-1.918199000
1	-6.249257000	-2.741712000	-2.390573000
6	-4.422751000	-1.621240000	-2.627136000
1	-4.266030000	-1.935452000	-3.657435000
6	-3.511869000	-0.764223000	-2.022597000
1	-2.650858000	-0.406584000	-2.586327000
6	1.993805000	1.035542000	2.661036000

6	2.351666000	1.176395000	4.001720000
1	1.582001000	1.184349000	4.773014000
6	3.689518000	1.328199000	4.340708000
1	3.974222000	1.426527000	5.386205000
6	4.655948000	1.402548000	3.339346000
1	5.698742000	1.573337000	3.598264000
6	4.286999000	1.276995000	2.006891000
1	5.041755000	1.376832000	1.227325000
6	2.953554000	1.038507000	1.647089000
6	3.554628000	-0.421858000	-0.863119000
6	3.297504000	-0.804214000	-2.187684000
1	2.422550000	-0.416356000	-2.708412000
6	4.135443000	-1.695966000	-2.847752000
1	3.917255000	-1.971348000	-3.878076000
6	5.238018000	-2.234946000	-2.193887000
1	5.896651000	-2.930855000	-2.710072000
6	5.480417000	-1.892276000	-0.868921000
1	6.321967000	-2.331009000	-0.334982000
6	4.647080000	-0.995926000	-0.207248000
1	4.846659000	-0.778804000	0.838883000
6	2.995063000	2.420758000	-0.832613000
6	3.238245000	2.536798000	-2.204155000
1	3.237226000	1.653785000	-2.840767000
6	3.492878000	3.780314000	-2.771394000
1	3.684891000	3.853136000	-3.840184000

6	3.507567000	4.924266000	-1.980002000
1	3.707829000	5.895897000	-2.427456000
6	3.270966000	4.819435000	-0.613479000
1	3.290951000	5.707730000	0.015613000
6	3.012520000	3.577085000	-0.043616000
1	2.824596000	3.513512000	1.029318000
1	-0.147353000	3.612050000	0.512809000

[HRe(LH)L₂]

0 3

75	0.613046000	-0.028143000	-0.554165000
16	1.509376000	0.802675000	-2.566135000
16	0.147988000	-2.071776000	-1.710397000
16	-0.724780000	-0.508924000	1.563418000
1	-1.712239000	0.390656000	1.246216000
15	0.560111000	2.372512000	0.087389000
15	2.648465000	-1.385303000	0.127155000
15	-3.661665000	-0.171656000	0.060986000
6	1.857257000	2.532408000	-2.349503000
6	2.547475000	3.191817000	-3.373981000
1	2.865696000	2.629250000	-4.250753000
6	2.815328000	4.549608000	-3.271696000
1	3.352904000	5.051353000	-4.074181000
6	2.400166000	5.274207000	-2.153916000
1	2.610662000	6.338755000	-2.080621000

6	1.716334000	4.627726000	-1.133806000
1	1.393934000	5.186111000	-0.253934000
6	1.443197000	3.260470000	-1.225362000
6	-1.137220000	3.029009000	0.140161000
6	-1.745276000	3.429659000	-1.053411000
1	-1.170935000	3.447951000	-1.980277000
6	-3.085609000	3.799088000	-1.061159000
1	-3.550008000	4.120690000	-1.991260000
6	-3.829211000	3.760795000	0.115215000
1	-4.876874000	4.056810000	0.107128000
6	-3.236253000	3.341001000	1.302176000
1	-3.821816000	3.293532000	2.218672000
6	-1.894222000	2.974866000	1.316673000
1	-1.436337000	2.658936000	2.255435000
6	1.378647000	2.867858000	1.640912000
6	0.988296000	3.986068000	2.384923000
1	0.118894000	4.570911000	2.085233000
6	1.708437000	4.352939000	3.517465000
1	1.398211000	5.221927000	4.094499000
6	2.822477000	3.616653000	3.910959000
1	3.380641000	3.908624000	4.798396000
6	3.225787000	2.512273000	3.165457000
1	4.103363000	1.936302000	3.456274000
6	2.506551000	2.141660000	2.035946000
1	2.840800000	1.292421000	1.438984000

6	1.697304000	-2.911634000	-1.941599000
6	1.767715000	-3.917176000	-2.911609000
1	0.880382000	-4.161338000	-3.493597000
6	2.967233000	-4.579994000	-3.141694000
1	3.014145000	-5.350792000	-3.908592000
6	4.109770000	-4.258939000	-2.410792000
1	5.047469000	-4.775736000	-2.602730000
6	4.045983000	-3.270893000	-1.434006000
1	4.930008000	-3.016204000	-0.847520000
6	2.846148000	-2.600429000	-1.197511000
6	2.397460000	-2.364631000	1.647628000
6	2.379728000	-3.761344000	1.628476000
1	2.559103000	-4.296595000	0.696858000
6	2.128201000	-4.472060000	2.799948000
1	2.119488000	-5.560114000	2.777815000
6	1.894112000	-3.795264000	3.992731000
1	1.697891000	-4.352811000	4.906492000
6	1.907641000	-2.401730000	4.017779000
1	1.721901000	-1.869684000	4.948701000
6	2.151154000	-1.688472000	2.850545000
1	2.150705000	-0.596396000	2.875573000
6	4.252438000	-0.542053000	0.338302000
6	5.082839000	-0.779982000	1.437997000
1	4.806360000	-1.522503000	2.185506000
6	6.271019000	-0.067560000	1.578731000

1	6.916764000	-0.261996000	2.433051000
6	6.632654000	0.883823000	0.630478000
1	7.559312000	1.442471000	0.746871000
6	5.812037000	1.117691000	-0.470883000
1	6.094388000	1.858407000	-1.216508000
6	4.625519000	0.411730000	-0.618470000
1	3.979571000	0.603643000	-1.476649000
6	-1.743669000	-1.946869000	1.165949000
6	-1.219526000	-3.180703000	1.540890000
1	-0.277429000	-3.232221000	2.085396000
6	-1.905864000	-4.340958000	1.209768000
1	-1.495431000	-5.307520000	1.496453000
6	-3.112180000	-4.262130000	0.519532000
1	-3.652879000	-5.168581000	0.254947000
6	-3.633373000	-3.021031000	0.175279000
1	-4.582435000	-2.964989000	-0.358777000
6	-2.966386000	-1.832084000	0.490458000
6	-5.090069000	-0.049804000	1.204254000
6	-6.035621000	0.958116000	0.967029000
1	-5.972808000	1.555234000	0.055654000
6	-7.068017000	1.187476000	1.867399000
1	-7.804854000	1.962087000	1.661112000
6	-7.161907000	0.427322000	3.031287000
1	-7.968100000	0.608737000	3.739498000
6	-6.222238000	-0.565675000	3.282326000

1	-6.291074000	-1.166264000	4.187774000
6	-5.192722000	-0.805119000	2.375510000
1	-4.469643000	-1.593733000	2.583130000
6	-4.415928000	-0.482302000	-1.580422000
6	-5.719756000	-0.955838000	-1.764471000
1	-6.360007000	-1.140413000	-0.901583000
6	-6.207567000	-1.185034000	-3.046784000
1	-7.223706000	-1.552334000	-3.180285000
6	-5.399229000	-0.949469000	-4.155350000
1	-5.784947000	-1.128779000	-5.157341000
6	-4.101703000	-0.477663000	-3.981584000
1	-3.468495000	-0.285935000	-4.845931000
6	-3.614747000	-0.236858000	-2.701574000
1	-2.601680000	0.149116000	-2.569878000
1	-0.968072000	0.163467000	-1.121573000

[Re(LH)₂L]

0 1

75	0.001887000	0.522349000	-0.151905000
16	-0.053024000	0.170602000	-2.464628000
16	-0.168218000	2.947928000	-0.676510000
16	0.235228000	0.982632000	2.249003000
1	-0.078752000	-0.110550000	2.999021000
15	0.064739000	-1.839301000	0.025067000
15	-2.439968000	0.764165000	0.031527000

15	2.429160000	0.825934000	-0.104875000
6	-0.301468000	-1.577539000	-2.716189000
6	-0.556521000	-2.025037000	-4.018084000
1	-0.575283000	-1.302804000	-4.834265000
6	-0.803553000	-3.369352000	-4.258760000
1	-1.010875000	-3.707084000	-5.272736000
6	-0.795043000	-4.284222000	-3.206110000
1	-0.995787000	-5.337287000	-3.392194000
6	-0.526709000	-3.844709000	-1.915438000
1	-0.526242000	-4.559284000	-1.091063000
6	-0.270658000	-2.494077000	-1.656259000
6	1.613029000	-2.687870000	0.573505000
6	2.238949000	-3.691270000	-0.169394000
1	1.855648000	-3.967596000	-1.150047000
6	3.367705000	-4.339723000	0.324353000
1	3.841212000	-5.117524000	-0.272559000
6	3.893235000	-3.997206000	1.565189000
1	4.771049000	-4.513236000	1.950104000
6	3.298881000	-2.977879000	2.302993000
1	3.711237000	-2.678761000	3.266054000
6	2.176162000	-2.327649000	1.805212000
1	1.745128000	-1.514887000	2.389742000
6	-1.179490000	-2.731939000	1.074363000
6	-0.932203000	-2.986628000	2.430355000
1	0.039883000	-2.762528000	2.865459000

6	-1.899778000	-3.577639000	3.236756000
1	-1.677885000	-3.777433000	4.283962000
6	-3.134379000	-3.934001000	2.702217000
1	-3.887891000	-4.407141000	3.329047000
6	-3.389557000	-3.696825000	1.356096000
1	-4.346479000	-3.978451000	0.919431000
6	-2.425280000	-3.096296000	0.550612000
1	-2.650255000	-2.922079000	-0.500889000
6	-1.904631000	3.298883000	-1.047041000
6	-2.211759000	4.526884000	-1.627125000
1	-1.415910000	5.237700000	-1.845356000
6	-3.535280000	4.826753000	-1.928924000
1	-3.782502000	5.784282000	-2.382684000
6	-4.537204000	3.897085000	-1.663032000
1	-5.572722000	4.127569000	-1.905125000
6	-4.217527000	2.667565000	-1.099171000
1	-5.004051000	1.939035000	-0.901592000
6	-2.892279000	2.352936000	-0.784987000
6	-2.971189000	1.040659000	1.764975000
6	-3.173051000	2.327691000	2.270983000
1	-3.152166000	3.190254000	1.604393000
6	-3.406147000	2.517360000	3.630416000
1	-3.562726000	3.523518000	4.014881000
6	-3.444556000	1.428211000	4.494972000
1	-3.629630000	1.581746000	5.556491000

6	-3.251644000	0.141593000	3.997067000
1	-3.288099000	-0.721392000	4.660717000
6	-3.008874000	-0.050896000	2.642408000
1	-2.847951000	-1.058285000	2.260735000
6	-3.693431000	-0.360336000	-0.694248000
6	-4.824866000	-0.790762000	0.001785000
1	-4.993143000	-0.471241000	1.029348000
6	-5.741539000	-1.641759000	-0.610803000
1	-6.620419000	-1.971006000	-0.058855000
6	-5.535450000	-2.069420000	-1.918199000
1	-6.249257000	-2.741712000	-2.390573000
6	-4.422751000	-1.621240000	-2.627136000
1	-4.266030000	-1.935452000	-3.657435000
6	-3.511869000	-0.764223000	-2.022597000
1	-2.650858000	-0.406584000	-2.586327000
6	1.993805000	1.035542000	2.661036000
6	2.351666000	1.176395000	4.001720000
1	1.582001000	1.184349000	4.773014000
6	3.689518000	1.328199000	4.340708000
1	3.974222000	1.426527000	5.386205000
6	4.655948000	1.402548000	3.339346000
1	5.698742000	1.573337000	3.598264000
6	4.286999000	1.276995000	2.006891000
1	5.041755000	1.376832000	1.227325000
6	2.953554000	1.038507000	1.647089000

6	3.554628000	-0.421858000	-0.863119000
6	3.297504000	-0.804214000	-2.187684000
1	2.422550000	-0.416356000	-2.708412000
6	4.135443000	-1.695966000	-2.847752000
1	3.917255000	-1.971348000	-3.878076000
6	5.238018000	-2.234946000	-2.193887000
1	5.896651000	-2.930855000	-2.710072000
6	5.480417000	-1.892276000	-0.868921000
1	6.321967000	-2.331009000	-0.334982000
6	4.647080000	-0.995926000	-0.207248000
1	4.846659000	-0.778804000	0.838883000
6	2.995063000	2.420758000	-0.832613000
6	3.238245000	2.536798000	-2.204155000
1	3.237226000	1.653785000	-2.840767000
6	3.492878000	3.780314000	-2.771394000
1	3.684891000	3.853136000	-3.840184000
6	3.507567000	4.924266000	-1.980002000
1	3.707829000	5.895897000	-2.427456000
6	3.270966000	4.819435000	-0.613479000
1	3.290951000	5.707730000	0.015613000
6	3.012520000	3.577085000	-0.043616000
1	2.824596000	3.513512000	1.029318000
1	-0.147353000	3.612050000	0.512809000

Table D9. Computational input coordinates for CuL¹ and related compounds.CuL¹

0 2

Cu	1.431847450	-0.488032580	0.446112510
S	2.332615610	-0.119942340	2.552696700
S	2.858402730	-1.722415690	-0.909505780
N	-0.257435500	0.971116720	2.468152050
N	-0.172027540	0.534274340	1.177021620
N	0.574079220	-1.034389140	-2.391256330
N	0.223704470	-0.461096440	-1.204115870
C	0.866804360	0.696900310	3.160702940
C	-1.156654600	0.726779040	0.313291070
C	1.780157800	-1.630949380	-2.329823970
C	-0.928456430	0.172470660	-1.041194200
C	-2.430852170	1.445672040	0.707410510
C	-1.949721220	0.325466600	-2.151313540
N	0.905903760	1.099112750	4.470338340
N	2.249331710	-2.229486700	-3.469048500
C	1.542073250	-2.300940750	-4.757663730
C	-0.256906930	1.621968390	5.210058210
H	-0.736089590	2.427871470	4.633939270
H	0.095862870	2.020878310	6.174487110
H	-1.009760380	0.833110030	5.396764760
H	-3.052880760	1.693994160	-0.164430810
H	-2.187359810	2.369822740	1.257044200
H	-3.027972700	0.817502200	1.394048690

H	2.232241150	-2.034661770	-5.577035900
H	0.709065320	-1.588742850	-4.742827890
H	1.143750430	-3.316026930	-4.940576080
H	-1.595749020	-0.186808630	-3.055724620
H	-2.117801900	1.390722990	-2.392856600
H	-2.924379830	-0.103170090	-1.856998090
H	1.714229460	0.779113230	5.003296850
H	3.143979070	-2.710111620	-3.380991940

[CuL¹H]⁺

1 2

Cu	1.431847450	-0.488032580	0.446112510
S	2.332615610	-0.119942340	2.552696700
S	2.858402730	-1.722415690	-0.909505780
N	-0.257435500	0.971116720	2.468152050
N	-0.172027540	0.534274340	1.177021620
N	0.574079220	-1.034389140	-2.391256330
N	0.223704470	-0.461096440	-1.204115870
C	0.866804360	0.696900310	3.160702940
C	-1.156654600	0.726779040	0.313291070
C	1.780157800	-1.630949380	-2.329823970
C	-0.928456430	0.172470660	-1.041194200
C	-2.430852170	1.445672040	0.707410510
C	-1.949721220	0.325466600	-2.151313540
N	0.905903760	1.099112750	4.470338340

N	2.249331710	-2.229486700	-3.469048500
C	1.542073250	-2.300940750	-4.757663730
C	-0.256906930	1.621968390	5.210058210
H	-0.736089590	2.427871470	4.633939270
H	0.095862870	2.020878310	6.174487110
H	-1.009760380	0.833110030	5.396764760
H	-3.052880760	1.693994160	-0.164430810
H	-2.187359810	2.369822740	1.257044200
H	-3.027972700	0.817502200	1.394048690
H	2.232241150	-2.034661770	-5.577035900
H	0.709065320	-1.588742850	-4.742827890
H	1.143750430	-3.316026930	-4.940576080
H	-1.595749020	-0.186808630	-3.055724620
H	-2.117801900	1.390722990	-2.392856600
H	-2.924379830	-0.103170090	-1.856998090
H	1.714229460	0.779113230	5.003296850
H	3.143979070	-2.710111620	-3.380991940
H	0.002279216	-1.014134076	-3.211399298

CuL¹H

0 1

Cu	1.431847450	-0.488032580	0.446112510
S	2.332615610	-0.119942340	2.552696700
S	2.858402730	-1.722415690	-0.909505780
N	-0.257435500	0.971116720	2.468152050

N	-0.172027540	0.534274340	1.177021620
N	0.574079220	-1.034389140	-2.391256330
N	0.223704470	-0.461096440	-1.204115870
C	0.866804360	0.696900310	3.160702940
C	-1.156654600	0.726779040	0.313291070
C	1.780157800	-1.630949380	-2.329823970
C	-0.928456430	0.172470660	-1.041194200
C	-2.430852170	1.445672040	0.707410510
C	-1.949721220	0.325466600	-2.151313540
N	0.905903760	1.099112750	4.470338340
N	2.249331710	-2.229486700	-3.469048500
C	1.542073250	-2.300940750	-4.757663730
C	-0.256906930	1.621968390	5.210058210
H	-0.736089590	2.427871470	4.633939270
H	0.095862870	2.020878310	6.174487110
H	-1.009760380	0.833110030	5.396764760
H	-3.052880760	1.693994160	-0.164430810
H	-2.187359810	2.369822740	1.257044200
H	-3.027972700	0.817502200	1.394048690
H	2.232241150	-2.034661770	-5.577035900
H	0.709065320	-1.588742850	-4.742827890
H	1.143750430	-3.316026930	-4.940576080
H	-1.595749020	-0.186808630	-3.055724620
H	-2.117801900	1.390722990	-2.392856600
H	-2.924379830	-0.103170090	-1.856998090

H	1.714229460	0.779113230	5.003296850
H	3.143979070	-2.710111620	-3.380991940
H	0.002279216	-1.014134076	-3.211399298

CURRICULUM VITA

Andrew Z. Haddad
University of Louisville | Department of Chemistry
2320 South Brook Street, Louisville, KY 40202
Tel. (502) 370-8358
DOB. 03/19/1990; Citizenship: United States
azhaddad1@gmail.com | andrew.haddad@louisville.edu

Education

B.A., Chemistry
University of Louisville
2008-2012

M.S., Chemistry
University of Louisville
2012-2015

Ph.D., Chemistry
University of Louisville
2012-2017

Honors and Awards

- **2017:** John Richard Binford Memorial Award
- **2017:** Graduate Deans Citation Award
- **2017:** Awarded ITRI-Rosenfeld Postdoctoral Fellowship at Lawrence Berkeley National Laboratory: research proposal on new technologies for desalination of brackish water using capacitive deionization.
- **2016:** Awarded first place in the graduate student oral presentation category at the Kentucky Academy of Sciences Annual Meeting
- **2016:** Awarded Council on Postsecondary Education Fellowship Award
- **2016:** School Of Interdisciplinary Studies Tuition Award

- **2016:** Intellectual Property and Preliminary Patent's filed through the University of Louisville Patent Office, *Co-Inventor*. <http://www.flintbox.com/public/project/29807/>
- **2015:** Winner of the Merck International Student Research Poster Presentation (Inorganic Division) Competition at the International Chemical Congress of Pacific Basin Societies (Pacifi-Chem) Conference. Honolulu, HI. December 2015
- **2014:** Kentucky Science & Engineering Research Grant #148-502-15-350; *Research (student) and Co-Author*
- **2013:** National Science Foundation Research Grant Funding Grant #1361728; *Research (student) and Co-Author*
- **2011:** Summer Research Opportunity Program (SROP), *Selected Applicant*, University of Louisville
- **2010:** Univ. of Louisville STEM-UTA-Program: Undergraduate Teaching Assistantship Appointment (*Instructed three classes per week or two labs per week each semester until graduation*)
- **2008:** University of Louisville Trustees Scholar (*4yrs tuition and fees*)
- **2007:** Kentucky Governor's Scholars Program, *participant and alum* – Major in International Relations; Minor in Integrated Mathematical Relationships

Publications and Presentations

1. **Proposed Ligand-Centered Electrocatalytic Hydrogen Evolution and Hydrogen Oxidation at a Noninnocent Mononuclear Metal–Thiolate**
Andrew Z. Haddad, Davinder Kumar, Kagna Ouch Sampson, Anna M. Matzner, Mark S. Mashuta, and Craig A. Grapperhaus.
Journal of the American Chemical Society **2015** *137* (29), 9238-9241.
 DOI: [10.1021/jacs.5b05561](https://doi.org/10.1021/jacs.5b05561)
2. **Beyond Metal-Hydrides: Non-Transition Metal and Metal-Free Ligand-Centered Electrocatalytic Hydrogen Evolution and Hydrogen Oxidation**
Andrew Z. Haddad, Brady D. Garabato, Pawel M. Kozlowski, Robert M. Buchanan, Craig A. Grapperhaus
Journal of the American Chemical Society **2016** *138*, 7844
 DOI: [10.1021/jacs.6b04441](https://doi.org/10.1021/jacs.6b04441)
3. **Compounds, Their Preparation, Related Compositions, Catalysts, Electrochemical Cells, Fuel Cells, and Uses Thereof**
Andrew Z. Haddad, Robert M. Buchanan, Craig A. Grapperhaus
 U.S. Provisional Patent Application No. 62/348,420. Filed: June 10, **2016**
 ULRF 16082-02, <http://www.flintbox.com/public/project/29807/>

4. Materials, Compounds, Their Preparation, Related Compositions, Catalysts, Electrochemical Cells, Fuel Cells, and Uses Thereof

Andrew Z. Haddad, Robert M. Buchanan, Craig A. Grapperhaus
U.S. Provisional Patent Application No. 62/348,490. Filed: June 10, 2016

ULRF 16082-02(P2),

<http://www.flintbox.com/public/project/29807/>

5. Translation of Ligand-Centered HER Activity and Mechanism of a Rhenium-Thiolate from Solution to Modified Electrodes: A Combined Experimental and DFT Study

Andrew Z. Haddad, Wuyu Zhang, Brady D. Garabato, Pawel M. Kozlowski, Robert M. Buchanan, Craig A. Grapperhaus
Inorganic Chemistry **2017** 56 (4), pp 2177–2187

DOI: <http://dx.doi.org/10.1021/acs.inorgchem.6b02829>

6. Ligand-Centered Hydrogen Evolution upon Reduction of a Bis(thiosemicarbazonato)Cu(II) Complex

Andrew Z. Haddad, Robert M. Buchanan, Craig A. Grapperhaus
Journal of the American Chemical Society **2017** Submitted

1. American Chemical Society International Conference
September 2013 Indianapolis, Indiana

- **Presentation 1: Inorganic Chemistry:** *Homogeneous Ligand-Centered Proton Reduction* (Presenter)
- **Presentation 2: Invited Sci-Mixer:** *Homogeneous Ligand-Centered Proton Reduction* (Presenter)

2. Gordon Research Conference: Inorganic Reaction Mechanisms

March 1-6, 2015 Galveston, Texas.

- **Presentation:** *Homogeneous Ligand-Centered Hydrogen Evolution and Oxidation at a Mono-Nuclear Metal Thiolate.* (Presenter)

3. Pacifi-Chem Research Conference

December 14-22, 2015 Honolulu Hawaii.

- **Presentation 1:** *Redox Active Ligands: Ligand-Centered Electrocatalytic Proton Reduction and Hydrogen Oxidation* (Presenter; Winner Inorganic Division)
 - **Presentation 2:** *Synthesis, Characterization and Electrochemical Properties of New Tetra Coordinated Ni(ii) and Zn(ii) Complexes with New P₂S₂ type Ligand Framework* (Co-Author)
 - **Symposium Talk:** *Redox-active metal-thiolates: Ligand-centered Electrocatalytic Proton Reduction/Hydrogen Oxidation* (Co-Author)
4. **Kentucky Academy of Sciences Annual Meeting**
November 4-5, **2016** Louisville, KY (University of Louisville)
- **Talk:** Homogeneous Ligand-Centered Electrocatalytic Hydrogen Evolution and Oxidation: *Exploiting Redox Non-Innocence to Drive Catalysis* (Presenter; *1st Place*)
5. **Lawrence Berkeley National Laboratory: Energy and Technology Area Guest Lecturer**
January 5, **2017** Berkeley, CA
- Talk: Ligand-Centered Electrocatalytic Hydrogen Evolution and Oxidation: *Applying Water-Splitting for LBNL's Advanced CDI Technology* (Presenter)
6. **University of Louisville Graduate Research Conference: *Three Minute Thesis Competition***
March 24, **2017** Louisville, KY
- Talk: Transition metal and Metal Free Hydrogen Production and Oxidation: A viable Path for the Future